RIGA TECHNICAL UNIVERSITY
Faculty of Civil Engineering
Institute of Materials and Structures

Edgars EGLĪTIS

DYNAMIC BUCKLING OF COMPOSITE SHELLS

A dissertation submitted in partial fulfilment
of the requirements for the degree of
Doctor of Philosophy (Solid Mechanics)
in Riga Technical University

Scientific supervisor
Dr. sc. ing.
Kaspars KALNIŅŠ

Riga 2011

This work has been supported by the European Social Fund within the project "Support for the implementation of doctoral studies at Riga Technical University"

ANOTĀCIJA

Promocijas darbs ir veltīts kompozīto čaulu dinamiskās noturības pētījumiem. Šobrīd pielietotā projektēšanas prakse paredz pieņemt slodzes kā kvazistatiskas, ievērtējot dinamiku ar konservatīviem drošuma koeficientiem. Līdzšinējie pētījumi parāda, ka pie dažādiem īslaicīgiem dinamiskajiem slogojumiem, konstrukcijām kritiskie spēki var būt gan augstāki, gan zemāki nekā statiska slogojuma gadījumā. Tādēļ, īslaicīga slogojuma dinamiskā rakstura precīza ievērtēšana projektēšanas gaitā nākotnē ļautu samazināt konstrukciju svaru, vienlaicīgi nodrošinot nestspēju. Lai realizētu īslaicīgi dinamiski slogotu kompozīto konstrukciju svara samazināšanas potenciālu, nemazinot to drošumu, nepieciešams radīt ticamu, eksperimentāli validētu aprēķinu metodoloģiju. Promocijas darbā veiktā literatūras analīze parāda, ka šobrīd ir pieejami tikai daži kompozīto konstrukciju dinamiskās noturības eksperimentālu pētījumu rezultāti šādu eksperimentu sarežģītības dēļ. Šajā promocijas darbā eksperimentāli un skaitliski tiek pētīta kompozīto čaulu noturība pie īslaicīgiem, dinamiskiem slogojumiem, un tiek piedāvāta atbilstoša, eksperimentāli validēta modelēšanas metodika. *Pirmajā nodaļā* ir sniegts apskats par līdzšinējos pētījumos uzkrātajām zināšanām plānsienu konstrukciju dinamiskās noturības jomā. Svarīgākie agrīnie pētījumi ir tikuši apskatīti līdz ar jaunākajām publikācijām, kas iezīmē šī brīža zinātnes sasniegumus. Papildus dinamiskās noturības pētījumiem, ir aprakstīta arī kompozīto konstrukciju noturība pie statiska slogojuma. *Otrajā nodaļā* ir aprakstītas promocijas darbā izmantotās eksperimentālās un skaitliskās metodes. Eksperimentālie pētījumi ir tikuši veikti ar kompozītām cilindriskām čaulām, izmantojot hidrauliskas slogošanas iekārtas, kā arī triecientorni. Visi skaitliskie aprēķini šajā promocijas darbā veikti ar ABAQUS/Explicit galīgo elementu programmatūru. *Trešajā nodaļā* eksperimentāli un skaitliski pētīta izvēlēto paraugu noturību pie statiska slogojuma, lai vēlāk to salīdzinātu ar noturību pie dinamiska slogojuma. Cilindrisko čaulu jutības pret ģeometriskajām nepilnībām problēma risināta, izmērot šīs nepilnības pielietotajiem paraugiem un papildinot skaitliskos modeļus ar iegūtajiem datiem. *Ceturtā nodaļa* ir veltīta īslaicīgi, dinamiski slogotu cilindrisku kompozīto čaulu eksperimentāliem un skaitliskiem pētījumiem. Apskatītas vienmērīgi un pēkšņi pieliktas slodzes, kā arī pulsveida slodzes, un ir noteikta to parametru ietekme uz cilindrisko kompozīto čaulu noturību. *Piektā nodaļa* paplašina pētījumu, apskatot liektu, ribotu kompozīto paneļu dinamisko noturību. Iegūti rezultāti pie dažādiem slogojuma veidiem ar skaitliskiem modeļiem, kas validēti ar statiskās noturības eksperimentu rezultātiem.

ABSTRACT

This thesis is focused on the investigation of the changes in the buckling behaviour of various composite shells due to dynamic, rapid loading. Currently, the structural design procedures of lightweight structures incorporate assumption of the loads as quasistatic, while maintaining reliability by applying conservative safety coefficients. Different investigations show that in various cases of dynamic loading the buckling loads can be both higher and lower than the static buckling load. Therefore, correct consideration of the load dynamics in the design procedure would lead to safer and more efficient structures. A reliable, experimentally validated analysis approach is required in order to benefit from the weight-saving potential of dynamically loaded composite structures, while maintaining the reliability. However, only few experimental investigations on dynamic buckling of composite structures have been performed because of the complexity of such experiments. In present thesis, the dynamic buckling of composite shells has been investigated experimentally and numerically, and an appropriate experimentally validated modelling approach has been proposed. *Chapter 1* gives review of the accumulated knowledge in dynamic buckling of thin-walled structures. The key pioneering research has been reviewed along with the publications describing the current state-of-the-art in the field. It has been revealed that surprisingly few experimental studies have been attempted in dynamic buckling of composite shells, with most researchers resorting to the analytical and numerical investigations only. *Chapter 2* contains the relevant information about the experimental and numerical methods used within this thesis. The experimental investigations have been performed on cylindrical composite shells using hydraulically actuated loading frames and a drop tower. The main numerical tool used in this thesis is the ABAQUS/Explicit finite element software. *Chapter 3* describes the static buckling behaviour of the selected specimens as a reference for the comparison with the dynamic buckling behaviour. The imperfection sensitivity of the cylindrical shells has been addressed by measuring the geometrical imperfections of the specimens and using this data in the numerical analyses. *Chapter 4* contains the results of experimental and numerical investigations of dynamic buckling of composite cylinders. Gradually and suddenly applied loads, as well as half-sine shaped pulse loads have been considered and the influence of the load parameters on the buckling behaviour of the shells has been revealed. *Chapter 5* expands the research to stiffened curved composite panels. The results have been obtained for various loading patterns using numerical models validated with the results of static buckling experiments.

ACKNOWLEDGEMENTS

I would like to thank my supervisor dr. Kaspars Kalniņš for providing me with the opportunity to complete my PhD studies under his guidance. His ambitious, energetic and creative approach to research inspired me, and his encouragement was essential for me to successfully finish this work. I also thank prof. Chiara Bisagni for welcoming to the Politecnico di Milano and her kind guidance, useful advice and generous help in my research. The assistance of other employees of Politecnico di Milano involved in my experimental work is also acknowledged.

I am grateful to my colleagues from the Institute of Materials and Structures. Firstly, prof. Andris Čate for the financial support he has provided me and for admitting me to the research work at the Institute of Materials and Structures that allowed me to grow professionally. I would also like to thank my fellow PhD students Oļģerts Ozoliņš and Kārlis Dzelzītis with whom I have collaborated while working on my PhD thesis and my colleagues prof. Evgeny Barkanov and dr. Sergey Gluhih for introducing me to the research on composite structures.

The financial support provided for presentation of the results at scientific meetings and conferences by EC 6th Framework Programme projects Advanced Low Cost Aircraft Structures (ALCAS) and Improved Material Exploitation at Safe Design of Composite Airframe Structures by Accurate Simulation of Collapse (COCOMAT) is gratefully acknowledged, as well as the experimental results of German Aerospace Centre (DLR) and Israel Institute of Technology (Technion) obtained within the project COCOMAT that have been used in this thesis.

Finally, my parents and closest relatives deserve my deepest appreciation for always supporting and encouraging my academic and professional development.

LIST OF TABLES

LIST OF FIGURES

TABLE OF CONTENTS

INTRODUCTION

The use of composites in aerospace, wind turbine, automotive and sports industries has been steadily increasing over the last three decades. Their high stiffness and strength characteristics make composites the material of choice in many applications requiring weight-efficiency. However, the composite structures still lack vast amount of knowledge that has been accumulated for traditional metal structures. Therefore, the composites have a weight-saving potential that could allow tailoring of light-weight structures to suit the consumer needs better.

Several areas have been identified which are not fully exploited and restrict potential improvement of weight-efficiency of composite structures: post-buckling capabilities, damage tolerance, imperfection robustness and also loading dynamics. Post-buckling and collapse of stiffened composite shells are being investigated in order to create reliable simulation tools and improve design guidelines. Research on the robustness of the composite shells is being performed to improve the obsolete knock-down factor approach. This outdated approach has been defined for metallic shells in the sixties, and updating it according to modern production methods and capabilities of modern composites present a significant potential. Different investigations show that in various cases of dynamic loading the buckling loads can be both higher and lower than the static buckling load. However, the current structural design procedures incorporate assumption of the loads as quasistatic, while maintaining reliability by applying conservative safety coefficients. Therefore, considering the load dynamics in the design procedure would lead to safer and more efficient structures.

A reliable analysis approach is needed in order to benefit from the weight-saving potential of dynamically loaded composite structures, while maintaining the reliability. The analysis approach has to be experimentally validated to be considered reliable. However, as it was concluded from the literature review, very few experimental results on dynamic buckling of composite shells have been published this far. Moreover, there are only some numerical studies where experimentally validated numerical models are used for simulation of the dynamic buckling behaviour of composite shells. Therefore, dynamic buckling of composite shells has been investigated experimentally and theoretically in this thesis. An experimentally validated approach has been developed for buckling analysis of dynamically loaded stiffened and unstiffened composite shells.

Motivation and background

The broad range of the research activities at Riga Technical University (RTU) include analysis and optimisation of lightweight composite structures, performed at the Institute of Materials and Structures (IMS). The experience of the IMS in the field of lightweight structures allowed it to enter the EU FP-5 project POSICOSS and FP-6 projects COCOMAT and ALCAS, all of which deal with stiffened lightweight structures for use in the Aerospace industry. I have joined the team of IMS already during my MSc studies and had the honour to work on the FP-6 research projects ALCAS and COCOMAT, where the buckling behaviour of the lightweight composite structures was in the centre of the research. In scope of the EC FP-7 project Improved Design Methodology for Dynamically Loaded Composite Aerospace Structures (DEDYCAS) proposal, I have chosen the problem of dynamic buckling as the topic for my further research work.

Problem statement

The current design procedures for the composite structures, which are often subjected to highly dynamic loads, simplify the designing process by assuming the loads as quasistatic and applying conservative safety factors. Considering the loading dynamics would allow to produce lighter, cheaper and also more reliable composite structures for the future. The aim of this thesis is the development and physical validation of reliable dynamic buckling and post-buckling analysis approaches suitable for engineering applications.

Research objectives

- Development of a stability analysis procedure for composite structures under the dynamic loading;
- Elaboration of a composite shell production method for experimental validation of the developed analysis procedure;
- Establishment of a testing procedure for composite shells under quasi-static and dynamic loads;
- Validation of the developed analysis approach against the experimental results;
- Experimental evaluation of the loading rate influence on buckling behaviour of the composite shells;
- Numerical evaluation of the dynamic loading type and duration influence on dynamic buckling behaviour of composite structures using the validated models.

Research approach

The buckling phenomena have been investigated analytically, numerically and experimentally for decades. The analytical investigations may serve as a good reference to understand the buckling behaviour of simple structural elements well. However, the use of contemporary numerical methods and structural analysis software packages is much more efficient in case of complex structures and allows modelling virtually any configuration and obtaining reasonably accurate results.

Explicit dynamic finite element analysis has been widely used in various research and engineering applications for buckling behaviour simulation of different structures. It is based on equations of motion approach and is especially efficient for simulation of structures under loads with short durations. Therefore, explicit dynamic finite element analysis is a reasonable choice of a tool for numerical studies of dynamic buckling of various structures.

No matter how elaborate and exact are the theoretical models of structures, they have to be validated by experimental results, to make sure that all the assumptions made within the modelling are valid and the phenomenon modelled actually corresponds to the one encountered in the real world. A good example is the linear perturbation buckling theory – while it produces reasonable results for bars, plates and other structures, it is producing result that can never be observed in the experiments in case of cylindrical shells. Therefore, the experimental investigations account for significant part of this thesis, and all the numerical models used are validated using experimental results.

Thesis overview

The flowchart of the research performed within this thesis is presented in Figure 1 describing the interconnections between the research steps.

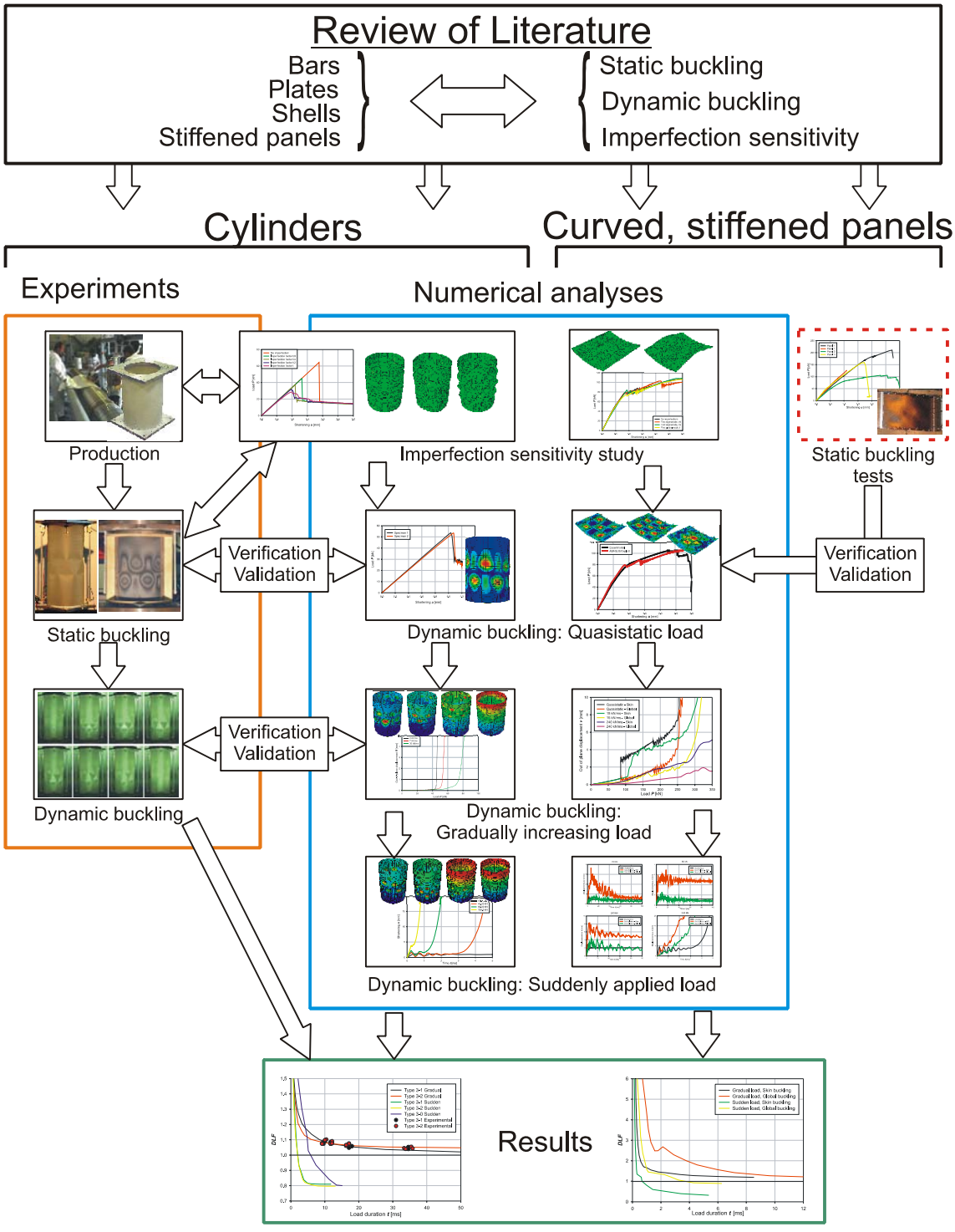

Figure 1.1. Structure of the research work

1. REVIEW OF THE LITERATURE

1.1. Concepts of elastic stability

A general role of design in engineering of structures is accounting for satisfaction of two basic criteria, namely:

1. *the strength criterion*, which states that under the specified (foreseeable) loading conditions the maximums stresses may not exceed the allowed stresses anywhere in the structure;
2. *the stiffness criterion*, which specifies the maximum allowable deflections under the different loading conditions in order not to hinder proper orientation or to avoid undesirable and potentially dangerous behaviour such as flutter or mechanical vibrations.

What often is overlooked is that by carrying out the usual linear stress and deformation analysis by finite element codes the designer may obtain no information concerning the stability behaviour of the structure. It is by now well known that thin-walled slender structures, or structures, which contain slender members subject to compressive stresses, may initially fail in one of the many possible instability modes, which in turn may significantly affect the strength or stiffness behaviour of the whole structure. This is especially true for the current trends in design where with the use of structural optimization techniques often result in highly stressed structures of very slender proportions.

With the sudden and often unexpected occurrence of partial or total structural failure due to different forms of initially elastic instabilities, one has to rely on buckling tests to provide the data for the development of safe and reliable design. However, before one can transform buckling test results into the reliable design, it is necessary to understand the basic phenomenon of structural instability and recognize the different types of buckling behaviour that may occur during the experiment.

The problem of a slender, perfectly straight, centrally compressed column, clamped at the base and free at the upper end has been first solved by Leonard Euler (1744). He found the equation to determine the smallest critical load:

$$P_{cr} = \frac{\pi^2 EI}{4L^2}, \tag{1.1}$$

where E is Young's modulus, I is moment of inertia of the cross-section and L is the length of the column. Euler has assumed in his work that the cross-section of the section does not distort and that the wavelength of the buckling mode is of the order of the column length.

For thin-walled columns Euler's assumptions that the cross-section does not distort during buckling and that the wavelength of the buckle is in order of column length must be re-examined. Such columns can be thought of as an assemblage of thin plates.

The buckling of a simply supported rectangular thin flat plate subjected to a uniform compressive force on two opposite sides has first been derived by G.H. Bryan (1891). Using sinusoidal deflection shape he found the smallest critical stress

$$\sigma_c = k_c \frac{\pi^2 E}{12(1-\nu^2)}\left(\frac{b}{h}\right)^2, \tag{1.2}$$

where k_c is the plate buckling coefficient, dependant on plate aspect ratio. Using a large deflection theory and an initial sinusoidal imperfection Coan (1951) obtained solutions for the buckling and post-buckling behaviour of rectangular plates with uniformly displaced edges and either undistorted or stress-free unloaded edges. The axial compressive stress is no longer uniformly distributed over the loaded edges (Singer et al., 2004).

1.2. Buckling of cylindrical shells

Axially compressed cylinder may be one of the last classical problems in structural mechanics for which it remains difficult to obtain close agreement between careful experiments and the best predictions from numerical modelling, therefore this remains a subject of continuous research (Teng and Rotter, 2004), including the current thesis.

Buckling and post-buckling of axially compressed, homogenous isotropic cylinders has been investigated since it was first identified in the beginning of the last century by "wrinkling" or "secondary flexure" in columns (Lilly, 1906). In practice, buckling of cylindrical shells under axial compression became important as their use in aircraft structures broadened as thin-walled columns and stressed-skin construction of fuselages and wings, introduced in the late twenties. Since then the shell buckling phenomena became the central design constraint for aerospace structures (Hoff, 1967).

According to the well-known and accepted linear classical theory, the linear bifurcation buckling stress for a perfect isotropic cylindrical shell under ideal conditions (the shell is of medium length and boundaries that restrain circumferential displacements during buckling) is:

$$\sigma_{cr} = \frac{E}{\sqrt{3(1-\nu^2)}}\frac{t}{r}, \tag{1.3}$$

where E is the elastic modulus of the material, ν is the Poisson ratio, t is wall thickness and r is the radius of the cylinder. This buckling stress equation was independently found by Lorenz

(1908), Timoshenko (1910) and Southwell (1914) and is known as the "classical elastic critical stress".

At this buckling stress, a very large number of different buckling modes or eigenmodes are all simultaneously critical, sometimes over 100 modes within 1% above the first one. Moreover, the steeply falling post-buckling path is associated with the proximity of these many modes (Teng and Rotter, 2004).

1.2.1. Imperfection sensitivity of cylindrical shells

As mentioned before, significant effort has been applied to understand the buckling and postbuckling phenomena for axially compressed cylinders, though it is still difficult to obtain good accordance of experimental results and numerical predictions. When reviewing the shell buckling and correlation between experimental and theoretical results, the single most important problem outlined by all authors is the imperfection sensitivity of shells, and axially compressed cylinders particularly.

The initial imperfections are dependant on production technology and post-processing, therefore producing cylinders with no imperfections that would compromise the buckling strength is still a challenge. Imperfections are mainly associated with in the shell geometry, thickness variations, residual stresses and poor definition of boundary conditions. It is widely accepted that the most important factor contributing to the discrepancy between theory and experiment for axially compressed cylinders is initial imperfections in the shell geometry (Teng and Rotter, 2004; Eglitis et al., 2007).

The awareness of the imperfection influence on shell buckling behaviour has been rising since the results of experimental studies performed in the 1930ties (Lundquist, 1933; Donell, 1934; Wilson and Newmark, 1933) were compared to the predictions of the linear classical theory, which showed great scatter in experimental results with experimental values being much lower than theoretical ones. This led to the establishment of "knock-down" factors based on the experimental results, which where applied while designing shells. For example, the *knock-down* factor function from NASA SP-8007 guideline is presented on Figure 1.1 along with experimental results for buckling of isotropic shells available at that time. This guideline has been established in 1965 and is still being used in practical applications. Nevertheless, the discrepancy between the theory and experimental results was too great for researchers to accept and it became the motivation for development of large deflection theories. Von Kármán and Tsien (1941) made the reason for this behaviour become evident by considering the postbuckling equilibrium paths for axially compressed cylinders,

calculated using a nonlinear theory (Figure 1.2). However, a considerable progress in analysis and measurement of imperfect shells has been achieved only during last two decades.

Since initial imperfections are obviously random by nature, stochastic stability analysis can be used. The buckling of imperfection sensitive structures with small random imperfections has been studied by several investigators, such as Bolotin (1957), Faser and Budiansky (1969) and Amazigo (1969). However, considering the absence of experimental evidence about type of imperfections that occur in practice and in order to reduce the mathematical complexity of the problem, all the above-named investigators have been working with some form of idealized imperfection distribution. (Singer et al., 2004)

Singer and Abramovich (1995) from Technion, Israel reviewed the development of imperfection measurement techniques since sixties until mid-nineties. It is outlined that until late sixties only partial imperfection measurements have been made and *out-of-roundness* criterion was established as a measure of imperfection of the shell. Complete imperfection measurement systems were developed at California Institute of Technology (Arbocz and Babcock, 1969) and Stanford University (Shover, 1968) in the late sixties, however, for the next decade, imperfection measurements were still usually considered useless and bothersome. In the late seventies some type of geometric imperfection measurement became an integral part of a properly carried out shell buckling test, be it on a laboratory scale or full scale structures. With the realization of the importance of the shape and amplitude of initial imperfections, various measurement systems were developed in different aerospace research laboratories worldwide.

Singer and Abramovich (1995) also discussed the establishment of the International Imperfection Data Bank. They stated that if the initial imperfection shapes are known, or can be reliably predicted, and the boundary conditions (including the load eccentricity) are well defined, adequate analytical tools and computer codes are available for calculation of the buckling load of the shell structure. However, if the imperfections and the boundary conditions are unknown, the predictions of the buckling loads cannot be improved, no matter how sophisticated the analysis codes are and how large and fast the computers become. Therefore, branches of the Imperfection Data Bank has been established at TU-Deft, the Netherlands, and Technion, Israel, and contained imperfection data of 148 different shells at that time.

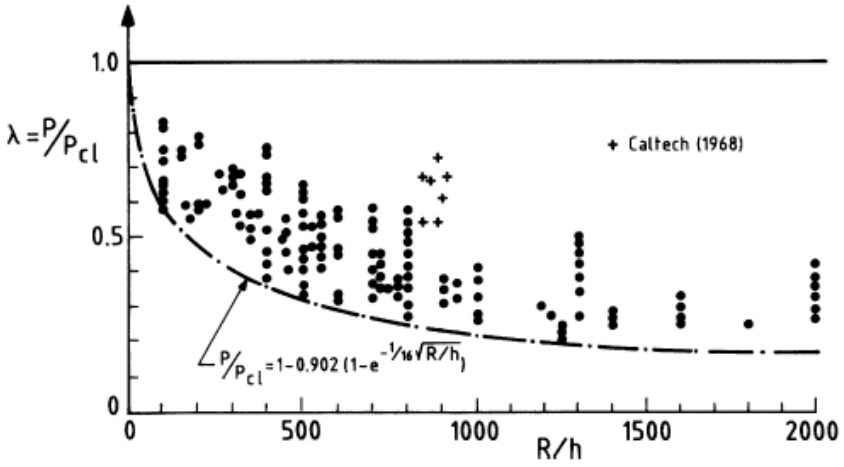

Figure 1.1. Test data for isotropic cylinders under axial compression (from Singer et al., 2004, Volume 2)

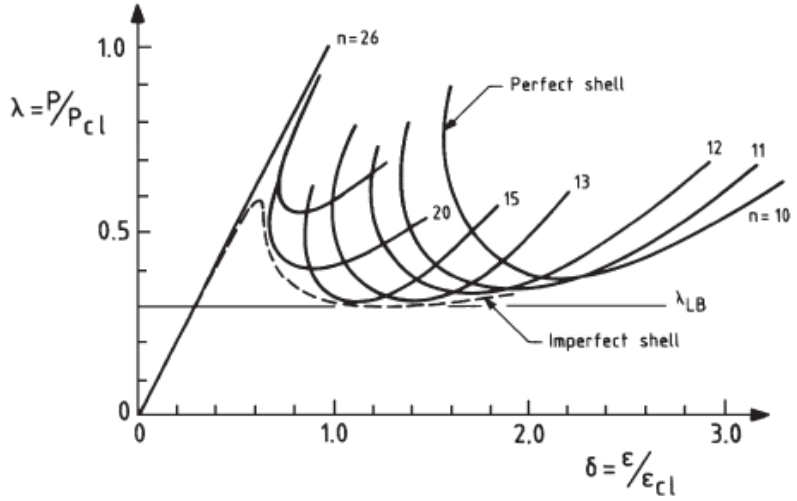

Figure 1.2. Theoretical post-buckling curves for axially compressed cylinders (from Singer et al., 2004, Volume 2)

In the end, Singer and Abramovich (1995) presented their considerations on a future shell design procedure based on the imperfection data collected in the Imperfection Data Banks. The designer would have to take into account the typical imperfections caused by the chosen production method and proceed with buckling analysis using one of the available non-linear codes. According to the procedure, a full-scale imperfection scanning would be an integral part of quality control routine and the measured imperfection pattern – one of the cardinal quality control parameters.

J. Arbocz and J.M. Hol (1995) from Deft University of Technology, another co-founding institution of the International Imperfection Data Bank, present their considerations on improvement of the *knock-down* factor based design approach. An improvement to the presently recommended design procedures is offered, which would allow use of *knock-down*

factors derived by a stochastic approach, considering the accuracy of the shell production technology, instead of the conservative lower-bound value of all known experiments.

It was stated, that use of the modern computer codes can lead to accurate buckling load prediction, given complete information on shell imperfections. This is only reasonable for prototypes, but cannot be implemented in industrial manufacturing of full scale parts. Instead, the characteristic initial imperfection distribution which a given fabrication process is likely to produce should be established beforehand, and then this information combined with statistical analysis of both the initial imperfections and the corresponding critical loads.

Furthermore the authors emphasized that the imperfection distributions are directly associated with the production technology. Two shells, AS-2, machined out of seamless heavy-wall 6061-T6 aluminium tube and tested at California Institute of Technology, and KR-1, produced using same technology and material, and tested at Israel Institute of Technology, were compared. Their imperfection data was decomposed in half-wave sine Fourier series and the plots of coefficients showed a striking similarity (Figure 1.3), generally decaying with the increase of the circumferential wave number.

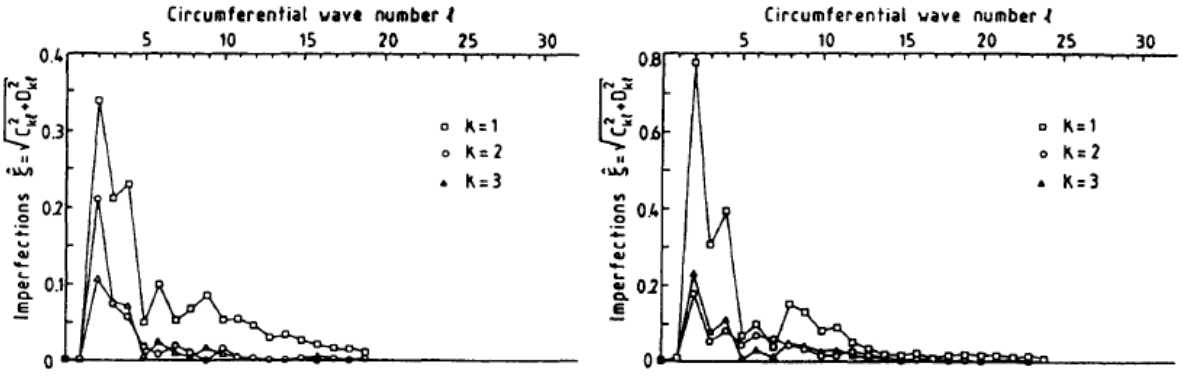

(a) (b)

Figure 1.3. Fourier coefficients of shells AS-2 (a) and KR-1 (b)
(from Arbocz and Hol, 1995)

Further, a method for stochastic shell stability analysis has been presented that uses statistical measures of initial imperfections as input. The example analysis of a shell with two different boundary condition sets (simply supported and clamped) gave somewhat different results in the probability distribution, which brought the authors to conclusion that the key to the success of any stochastic stability analysis lies in the reliability and accuracy of the buckling load predictions made by the deterministic buckling analysis used. The authors also stressed the fact that only a shell design specialist, who is aware of the latest theoretical developments and who is familiar with the theories upon which the nonlinear structural

analysis codes he uses are based, can achieve the accurate results while applying the method described in that study. In the end the need for the collection of the measured imperfections in Imperfection Data Banks to make the proposed design procedure available to designers has been emphasized.

Another significant experimental study on buckling of axially compressed shells is presented by Abramovich et al. (2002). The authors consider that the scatter produced by damage due to repeated buckling in carefully conducted tests is much less than that resulting from the initial differences in shape and properties of separate specimens, even if they are manufactured rather accurately. Hence, repeated buckling of the same specimen can provide a better experimental interaction curve.

The authors presented a test program including six cylindrical stringer stiffened shells on nominally simple supports. Each shell has been subjected to various combinations of axial compression and external pressure. The "repeated buckling" approach has been used applying the VCT (vibration correlation technique (Singer, 1982)) method to redefine the actual boundary conditions and the buckling loads. Initial geometrical imperfections, their growth and the imperfections after buckling under external pressure, axial compression and combined loading were measured in situ. The influence of the geometrical imperfections has been assessed, using the CPIUTAM and CPIUTAMN multimode analyses.

The results showed that the repeated buckling approach to obtain interaction curves for metal shells can be used successfully, while the appropriate sequence of loading is employed. Again, the imperfection measurements have been shown to be an important step in the research of shell buckling. Using the measured geometrical imperfections as an input to the two multimode analyses, CPIUTAM and CPIUTAMN one can calculate the theoretical buckling loads with the "new" imperfections for the shells under external pressure or axial compression, as well as a combination of constant axial compression and varying external pressure till buckling. This capability permits an evaluation of the effect of the growth of imperfections at all the intermediate points, and thus results in further improvement in the interaction curves.

1.2.2. Imperfection measurement methods

Linear variable differential transformers (LVDT) have been used in most imperfection scanning equipment, as stated in the exhaustive review on the topic presented in (Singer et al., 2004). This includes the portable system of California Institute of Technology that had been used to perform series of imperfection surveys at different aerospace companies in the United

States in the late 70ties and the imperfection measurement systems at Israel Institute of Technology, RWTH-Aachen, German Aerospace centre DLR and Politecnico di Milano. These systems have been operated either manually or automatically using servo or stepping motors.

Combination of LVDTs and optical levelling has been used for imperfection measurements of steel tubes at the Western University of Sydney (Pircher and Wheeler, 2003). 12 LVDTs were mounted on a trolley that could be moved along the axis of the cylinder, and optical levelling has been used to align the trolley. The other degree of freedom in this system was rotation of the specimen around the axis.

A noncontact imperfection measurement technique has been developed at University of Leeds, UK, and demonstrated on a diaphragm of a steel girder (Megson and Hallak, 1992). A system consisting of two electronic theodolites with measurement accuracy of 0.1'' and a programmable data recorder has been used. The measurements of the theodolites were recorded at certain points and later transformed into numerical imperfection model. The authors claim that accuracy of ±0.1 mm can be achieved using this method.

Several measurement procedures have been tried on cold-rolled steel panels at University of Western Sydney, Australia (Bernard et al., 1999). One of the methods was close-range photogrammetry, which involved photographing an object from several viewpoints without a change in object geometry within the survey period. A CRC1 close-range photogrammetric camera has been used to take images of the specimen. Kodak Technical Pan film with an image size measuring 230x230 mm, and a Schneider 240 mm lens, have been used to ensure the required image resolution. The accuracy of measurements was estimated to be 50 μm. Another method described in the paper was optical levelling. A Leica NA2 automatic level and a GPM3 parallel plate micrometer have been used to measure out-of-plane geometric imperfections at 10 mm intervals along selected profile lines on the surface of each specimen. Changes in the vertical position of a target resting on the specimen were taken to define the out-of-plane imperfections. In the optical levelling procedure, errors in the out-of-plane measurements could arise from several sources. The most significant of these was due to uncertainties in observing the target. 20 readings have been made in each of five stationary positions to estimate the precision of each observation. The pointing precision of a single measurement has been found from these sets of observations to be 14.6 μm for the trapezoidal specimen, and 13.0 μm for the Bondek specimen (two observers made the observations for the two sets of measurements).

An extensive research program on buckling of axially compressed GFRP cylinders has been performed at the Imperial Colledge, London, UK (Elghazouli et al., 1999; Chryssanthopoulos et al., 1999; Spagnoli et al., 2001, Chryssanthopoulos et al., 2000). The measurement of the thickness variation has been carried out using a grid of 50x50 mm and a vernier micrometer mounted on a specially-designed bracket. The initial imperfections have been measured using an automated laser scanning system with a grid of 20x26.5 mm. A reference surface has been created by scanning an accurately machined steel ring at three different heights and later applied for evaluation of the scan data. This automated scanning system has also been used for the measurements of the buckling modes.

A comprehensive review on techniques used for imperfection measurements of large structures has been presented by Godoy (1996). These techniques include the aforementioned triangulation using theodolites and photogrammetry, as well as measuring by a single laser range-finder device. The review confirms that contact scanning methods are mainly used for laboratory scale shells.

Post-processing of the measured imperfection data and Fourier analysis are described well by Teng et al. (2005). Imperfection data of three 10,000 ton grain silos at Port Kembla in New South Wales, Australia has been used in that study. According to the author, the most effective method of characterizing shell geometric imperfections is a 2D Fourier series: this method has been widely used in other shell applications and has also been applied to the Port Kembla silo measurements. The reference surface relative to which the net imperfections should be defined was first found as the "best-fit cylinder". The original imperfection data were referred to as the nominal imperfections and the corrected set as the net imperfections.

If a surface is perfectly cylindrical, but is not aligned with the reference axes being used, the differences caused by the misalignment would naturally appear to be imperfections. It is therefore necessary that the reference shape of the perfect cylindrical shell should be identified as the best fit to all the measurements, and the net imperfections deduced as the deviations from this notional perfect cylinder (Arbocz and Babcock, 1969; Arbocz and Williams, 1977; Arbocz, 1982). The best-fit perfect reference cylinder was found using the method of least-squares adjustment.

In the following procedure, the best-fit cylinder was defined in the main coordinate system as a tilted cylinder (Figure 1.4 *a*) of mean radius R, with its axis oriented at $(\cos\alpha, \cos\beta, \cos\gamma)$ and eccentricities at the origin of x_0 and y_0. This procedure is necessary if the observations lack such clear axis and the axes of the *O–X'Y'Z'* coordinate system are not necessarily parallel to those of the reference coordinate system *O–XYZ*.

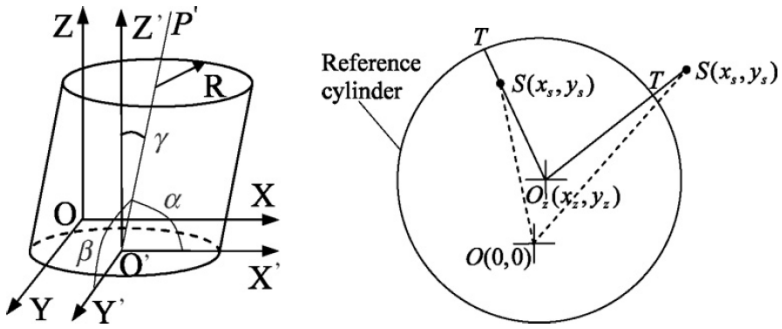

a *b*

Figure 1.4. Best-fit approximation of imperfection measurements
a - Coordinate definition of the best-fit cylinder;
b - Deduction of net imperfection using the best-fit cylinder
(from Teng et al, 2005)

The axis *O'P'* of the reference cylinder may be described as

$$\frac{x - x_0}{\cos\alpha} = \frac{y - y0}{\cos\beta} = \frac{z - z_0}{\cos\gamma} \quad . \tag{2.4}$$

With the arbitrary choice $z_0 = 0$,

$$x_z = x_0 + \zeta z \tag{2.5}$$

$$y_z = y_0 + \rho z \,, \tag{2.6}$$

where x_z and y_z are the coordinates of a point at coordinate z on the cylinder axis *O'P'* and

$$\frac{\cos\alpha}{\cos\gamma} = \zeta \,, \; \frac{\cos\beta}{\cos\gamma} = \rho \,. \tag{2.7}$$

The reference cylinder is given by

$$(x - x_z)^2 + (y - y_z)^2 = R^2 \,, \tag{2.7}$$

or

$$(x - x_0 - \zeta z)^2 + (y - y_0 - \rho z)^2 = R^2 \,, \tag{2.9}$$

and the deviation of a sampling point from the reference cylinder is given by

$$\begin{aligned} f_i(i, x_0, y_0, R, \zeta, \rho) &= (x - x_z)^2 + (y - y_z)^2 - R^2 = (x - x_0 - \zeta z)^2 + (y - y_0 - \rho z)^2 - R^2 \\ g_i(i, x_0, y_0, R, \zeta, \rho) &= f_i^2 = [(x - x_0 - \zeta z)^2 + (y - y_0 - \rho z)^2 - R^2]^2 \,. \end{aligned} \tag{2.10}$$

The sum of the squares of the sampling point deviations can be used as an index to express the total deviations of the sampling points from the reference cylinder

$$G = \sum_{i=1}^{N_s} g_i = \sum_{i=1}^{N_s} f_i^2 \,, \tag{2.11}$$

in which N_s is the number of sampling points. To minimize the total deviations, the first partial derivatives of G with respect to x_0, y_0, R, ζ, and ρ should be zero. Writing these five parameters as ξ_1–ξ_5, expressions may be written for the stationary partial derivative:

$$\frac{\partial g_i}{\partial x_0} = -4[(x_i - x_0 - \zeta z_i)^2 + (y_i - y_0 - \rho z_i)^2 - R^2] \times (x_i - x_0 - \zeta z_i) \tag{2.11}$$

etc. and writing

$$h_{1i} = [(x_i - x_0 - \zeta z_i)^2 + (y_i - y_0 - \rho z_i)^2 - R^2] \times (x_i - x_0 - \zeta z_i). \tag{2.12}$$

The five partial derivatives are zero when

$$\sum_{i=1}^{N_s} h_{1i} = \sum_{i=1}^{N_s} h_{2i} = \sum_{i=1}^{N_s} h_{3i} = \sum_{i=1}^{N_s} h_{4i} = \sum_{i=1}^{N_s} h_{5i} = 0. \tag{2.13}$$

The partial derivatives matrix may be defined as

$$[H] = \sum_{i=1}^{N_s} [h_{1i} \quad h_{2i} \quad h_{3i} \quad h_{4i} \quad h_{5i}]^T = 0. \tag{2.14}$$

Equation (2.14) represents a non-linear system, with the five parameters ξ_1–ξ_5 as unknowns, which can be solved iteratively using the well-known procedure:

$$\{\delta^j\} = \{\delta^{j-1}\} - [J^{j-1}]^{-1}[H^{j-1}], \tag{2.15}$$

where $\{\delta^j\}$ is the j^{th} approximation of the five unknowns given by

$$\{\delta^j\} = [x_0^j \quad y_0^j \quad R^j \quad \zeta^j \quad \rho^j]^T, \tag{2.16}$$

in which $[H^{j-1}]$ is the matrix $[H]$ at the $(j-1)^{\text{th}}$ iteration given by

$$[J^{j-1}] = \sum_{i=1}^{N_s} \begin{bmatrix} \frac{\partial h_{1i}}{\partial x_0} & \frac{\partial h_{1i}}{\partial y_0} & \frac{\partial h_{1i}}{\partial R} & \frac{\partial h_{1i}}{\partial \zeta} & \frac{\partial h_{1i}}{\partial \rho} \\ \frac{\partial h_{2i}}{\partial x_0} & \frac{\partial h_{2i}}{\partial y_0} & \frac{\partial h_{2i}}{\partial R} & \frac{\partial h_{2i}}{\partial \zeta} & \frac{\partial h_{2i}}{\partial \rho} \\ \frac{\partial h_{3i}}{\partial x_0} & \frac{\partial h_{3i}}{\partial y_0} & \frac{\partial h_{3i}}{\partial R} & \frac{\partial h_{3i}}{\partial \zeta} & \frac{\partial h_{3i}}{\partial \rho} \\ \frac{\partial h_{4i}}{\partial x_0} & \frac{\partial h_{4i}}{\partial y_0} & \frac{\partial h_{4i}}{\partial R} & \frac{\partial h_{4i}}{\partial \zeta} & \frac{\partial h_{4i}}{\partial \rho} \\ \frac{\partial h_{5i}}{\partial x_0} & \frac{\partial h_{5i}}{\partial y_0} & \frac{\partial h_{5i}}{\partial R} & \frac{\partial h_{5i}}{\partial \zeta} & \frac{\partial h_{5i}}{\partial \rho} \end{bmatrix}^{j-1}. \tag{2.17}$$

The convergence od the iteration procedure can be determined using the parameter

$$\Delta = \left\| [J^{j-1}]^{-1}[H^{j-1}] \right\|_{\max} \le Tol, \tag{2.18}$$

where Tol is the required tolerance. When this tolerance is achieved, the values of parameters x_0, y_0, R, ζ, and ρ are obtained and the reference cylinder is given by Eq. (2.9). The

orientation (cos α, cos β, cos γ) of the reference cylinder axis *O'P'* can be deduced from the values of ρ and ζ, with $\cos^2\alpha + \cos^2\beta + \cos^2\gamma = 1$.

1.2.3. Buckling of composite cylinders

Buckling of laminated shells has been investigated since the introduction of the laminated composites in the 1960ties. Dong et al. (1962) and Cheng and Ho (1963) were among the first to develop the analysis approaches within the framework of the classical buckling theories. Tennyson (1975) reviewed theoretical and experimental investigations on buckling of composite cylinders with focus on initial geometrical imperfections and boundary conditions, and their influence on the buckling load of the cylinders.

Extensive experimental and analytical studies on the buckling of composite cylinders made of carbon fibre reinforced plastics (CFRP) have been conducted at the University of Toronto in the seventies and eighties (Tennyson and Muggeridge, 1973). Special emphasis has been given in these studies to the effect of initial geometrical imperfections of the cylinders. The random distributions of the geometrical imperfections of the shells have been determined by mounting the shell in a transversing device equipped with two, diametrically opposed low pressure, linear contracting transducers. The imperfection data has been processed using Fourier analysis program, and imperfection amplitudes and an estimated line of power spectral density as a function of special frequency has been computed. The data recorded by transducers has also been used to compute the average shell thickness. The cylinders were tested with their ends clamped into fitted aluminium plates and bonded.

The analytical estimates of the buckling capacity of the imperfect shells have been based on the maximum value of the imperfection amplitude, which has been obtained from the statistical representation of the measured initial geometrical imperfection. The magnitude of the imperfection amplitude was in the order of the shell wall thickness, and resulted in significantly lower buckling strength compared to the perfect cylinders. It has been reported that the agreement between the predicted response and the experiments was consistently good, with discrepancy not exceeding 20 percent.

More recently, buckling tests on composite cylinders manufactured from CFRP prepreg tapes were conducted at the German Aerospace centre DLR, Brauschweig, Germany (Zimmermann, 1996). One study has been devoted to experimental confirmation of the computed large difference between the buckling loads of optimum and pessimum designs, where the one of optimum may be as high as 2.8 times that of the worst one, for laminates consisting of the same number of plies. The comparison with the analytical predictions

yielded in “knock-down” factors ranging from 0.80 – 1.03, their scatter was small and they were not significantly smaller for the optimal cylinders (about 0.8) than the pessimal ones (about 0.9).

Geier et al. (1991), also from DLR, have performed search for imperfection tolerant laminate lay-up. The results have shown that imperfection sensitivity of composite cylinders depends on lay up. A knockdown factor of 0.68 has been experienced with the [±75°/±75°] laminates, while a knockdown factor of 0.91 has been found for the [$0°_2$/±19°/±37°/±45°/±51°] laminates.

Probabilistic approach to the buckling of axially compressed composite shells has been used by Degenhardt et al. (2010) at DLR. Static buckling tests have been performed on 10 CFRP shells with radius to shell wall thickness ratio R/t of 500. The geometric and thickness imperfections have been measured prior the test, using photogrammetry to measure the geometry and ultrasonic scanning to find the thickness variations. The *knock-down* factors from 0.68 to 0.82 have been obtained in the experimental study. In the numerical part of the investigation, deterministic stability analyses have been performed first. Inclusion of the geometrical and thickness imperfections decreased the numerically obtained buckling loads, but not to the level of the experimental values. To include additional imperfections, as inclination of the compression load and the deviations of the stiffness of a CFRP ply, probabilistic analysis based on Monte Carlo simulations has been performed. The lower limiting quantiles with probability of 0.5% have been found for both experimental and numerical *knock-down* factors, being 0.646 and 0.648, respectively. For comparison, the knock-down factor according to the NASA SP-8007 guideline should be taken as 0.32.

Another path to the improvement of the *knock-down* approach has been proposed by Hühne et al. (2008). They pointed out that a large number of test data are needed for the probabilistic approaches, but often such data is not available. Motivated by this lack of data, a new deterministic approach has been presented for determining the lower bound of the buckling load of a thin-walled cylinder. This approach is based on the application of a single radial perturbation load before application of the compressive load. The physical experiments have been carried out on cylindrical CFRP shells with effective length L of 510 mm, inner radius R of 250 mm and radius to wall thickness ratio R/t of 500. These shells have been composed of four 0.125 mm thick layers of unidirectional pre-preg CFRP tapes, and the test results have been presented for a shell with lay-up of [±24°/±41°], which is near to optimum. The perturbation load levels, further increase of which did not result in further decrease of the buckling loads, have been found experimentally for various shells. Each shell has been tested

repeatedly and a total of 4000 tests have been performed. Further, the numerical analyses have been performed, excluding the initial geometrical and thickness imperfections, but including the perturbation loads and good correlation with the experimental results have been achieved. Based on the results of this study, a deterministic design approach has been proposed which would be less conservative than the *knock-down* factor approach of NASA-SP 8007 guideline.

Chryssanthopoulos and Poggi (1995) from Imperial Colledge, London and Politecnico di Milano performed imperfection sensitivity analysis of Kevlar/epoxy composite cylinders. Imperfections of 16 nominally identical cross-ply and 14 nominally identical angle-ply cylinders were measured and decomposed in Fourier series. On the basis of the statistical analysis, a characteristic imperfection model for both cross-ply and angle-ply cylinders has been proposed for the particular manufacturing method. Random imperfection samples were generated using this model for further probabilistic analysis, which was used to obtain knock-down factors for this particular production method. However, the authors admitted that the obtained knock-down factors were not severe enough.

Few years later, Chryssanthopoulos (1998) extended this probabilistic approach for thin anisotropic plates and shells, including examples of its application in a variety of problems dealing with partial factors, rationalization of imperfection tolerances, code calibration and assessment as well as more specific design-oriented studies.

Significant experimental and analytical imperfection sensitivity studies on graphite/epoxy composite cylinders have been performed at NASA Langley Research Center (Hilburger and Starnes, 2004). The effects of initial imperfections on the buckling response and failure of unstiffened thin-walled axially compressed cylindrical shells have been presented. The response of shells with shell-radius-to-thickness ratios R/t of 100 and 200 has been studied. The thicker cylinders represented thin-walled shells that exhibit material failures before or during buckling. The thinner ones represented contrasting examples of thin-walled shells that exhibit significant post-buckling load carrying capacity and material failures occur in the post-buckling range of loading. Three-dimensional imperfection surveys of the inner and outer shell-wall surfaces of the specimens were made prior to testing the specimens to determine their initial geometric shell-wall imperfection shapes and shell-wall thickness distributions. Measurements have been taken over a uniform grid with increments of 3.2 mm in the axial direction and 3.5 mm in the circumferential direction over the exposed surfaces of the specimens. These results indicated that the shell-wall thickness, and hence the laminate stiffness, varied significantly over a short distance. The thickness varied from 0.928 to 1.321

times average laminate thickness. Most of the thickness variation has been attributed to local variations in the resin content of the laminate, however, small gaps have been observed between adjacent pieces of graphite-epoxy tape in some of the laminate plies that were generated during the lay-up and curing processes. These locally thin shell-wall regions had a significant shell-wall mid-surface eccentricity and reduced stiffness relative to the rest of the shell wall.

The shells considered in that study were analyzed with the STAGS shell analysis code. The pre-buckling responses were determined using the geometrically nonlinear quasi-static analysis capability of STAGS. The Riks pseudo arc-length path-following method has been used to compute the initial shell response until just before buckling occurred. Then the unstable buckling response of the shell has been predicted using the nonlinear transient analysis option of the code. Geometrically perfect and imperfect shells have been considered. Nominal shell geometry, laminate thickness, lamina mechanical properties, and boundary conditions have been used for the finite-element models. Subsequently, the geometrically perfect finite-element models have been modified to include the effects of the measured shell imperfections in order to simulate the response of the specimens more accurately. These modelling modifications included the effects of the measured initial geometric shell-wall mid-surface imperfections, shell-wall thickness variations, local shell-wall lamina ply-gaps, thickness-adjusted lamina properties, elastic boundary conditions, shell-end geometric imperfections, and non-uniform end loads. A common Tsai-Wu tensor failure criterion has been used to predict material failure in the shells.

The numerical results confirmed that the effects of the various imperfection types and selected parameter uncertainties considered can be important for predicting the buckling loads of composite shells since they can significantly affect the nonlinear response and buckling loads of the shells. According to the results, the measured imperfections can couple with the in-plane compressive stress resultants in a nonlinear manner to affect the shell response. In particular, typical results that illustrate the response of a compression-loaded quasi-isotropic shell have been presented and indicated that a complex nonlinear interaction between localized shell-wall pre-buckling deformations in the bending boundary region of the shell and compressive axial and circumferential stresses caused the overall buckling of the shell to occur.

The experimental results indicated that, for the most part, the measured response of the shells fell mid-way between the predicted upper and lower bounds to the response that has been associated with the uncertainties or variations in the shell parameters considered in the

numerical study. In addition, numerically predicted material failure initiation agreed well with experimentally observed failure trends. These results indicated that the developed nonlinear analysis procedure can be used to determine accurate, high-fidelity design *knock-down* factors and response bounds for predicting composite shell buckling and failure loads in the design process.

Kriegesmann et al. (2010) described the measured imperfections of several composite shells with double Fourier series and performed the probabilistic analysis treating the Fourier coefficients as random variables. Considering the geometrical imperfections only, the 99.9% quantile of the probabilistic analysis results was higher than the experimental results for all of the shells considered, from where it was concluded that other imperfection types, as the inclination of the loaded edge of the cylinder must be considered. The probabilistic analysis has been repeated with inclusion of the inclination of the loaded edge as an additional random variable. This time, the 99.9% quantile was always slightly lower than the experimental buckling loads, but still significantly higher than the design load according to the *knock-down* approach of the NASA SP-8007 guideline.

Extensive experimental, analytical and numerical investigations on the buckling behaviour of composite cylindrical shells under compression, torsion and combined loadings have been carried out at the Politechnico di Milano, Italy (Giavotto, 1991). The cylinders investigated were 700 mm long, with 350 mm radius and reinforced at the ends to facilitate their fixing into loading rig. Cross-ply $[0°/90°]_S$, angle-ply $[\pm 45°]_S$ and eight-ply quasi-isotropic lay-ups have been used in these investigations. Particular attention has been paid to the boundary conditions. The employed testing rig had elaborate clamping devices providing accurate application of the combined loading. The inner and outer surfaces have been scanned using non-contact measuring device to record the initial geometrical imperfections and their growth during the loading. The results have been compared to theoretical predictions and knockdown factors ranging from 0.86 for angle-ply cylinders to 0.88 for cross-ply cylinders have been obtained.

Bisagni and Cordisco (2003) extended the studies on buckling of composite shells under combined loads with focus on the post-buckling behaviour. All the shells exhibited a completely linear pre-buckling behaviour. A sudden drop after buckling under axial compression has been experienced in case of all shells except for a shell composed of unidirectional layers of CFRP with stacking sequence $[0°/90°]_{2S}$ that exhibited a gradual reduction of the stiffness after buckling. In contrary, under torsion load, the buckling under torsion loading occurs very smoothly for all of the tested shells.

1.3. Buckling of stiffened shells

The aeroplane shell structure of the thirties was typified by a very thin skin, which often buckled during the flight, supported by much stiffer longitudinal and transverse reinforcing elements. The structural element that buckled was therefore a plate, or an unstiffened shell segment, supported by relatively rigid stiffeners. With increase of speed of flight, skins became thicker and stiffeners closer until skin and reinforcements were of similar rigidity and interacted during buckling. Therefore, the buckling behaviour of the modern aerospace structure is predominantly global buckling (Singer et al., 2004).

Few results of experimental and theoretical investigations on buckling and postbuckling behaviour of stiffened composite shells are available in the scientific literature. Some of the early published results include those by Agarwal (1982) and Knight and Starnes (1985). McGowan et al. (1994) has presented results of a study aimed at demonstrating that, as in design practice of metal aircraft structural components, the design of postbuckled composite curved, stiffened panels is viable and even more efficient.

Bisagni and Cordisco (2006) used the combined loading testing set-up created at Politecnico di Milano to investigate post-buckling and collapse of stiffened composite cylinders under axial loading and torque. The three specimens were designed to be able to work in the post-buckling range. Consequently, the number of stiffeners and their lay-up were optimized so as to guarantee a local skin buckling and a large post-buckling range before the collapse. The geometrical imperfections of the specimens have been measured using a scanning device based on LVDT transducers. Two of the stiffened shells have been tested in axial compression and one shell has been tested in torsion, all of them until collapse. In case of axial compression tests, the collapse load was 2.8 to 3.7 times higher than the skin buckling load, and in case of torsion 3.0 times higher. The skin buckling did not influence the stiffness of the shell significantly under axial load, because the load was predominantly supported by the stiffeners. Meanwhile, the skin buckling resulted in notable decrease of the stiffness under torsion loading. The test results clearly showed the strength capacity of stiffened composite cylinders to work in the post-buckling range, as neither failure mechanisms nor any other hazards were visible in the post-buckling range. On the other hand, the collapse due to the failure of the stringers was sudden and destructive. It caused extensive fracture in the skin and in the stringers, so the shell was not able to support any load any more after the collapse.

The post-buckling and collapse behaviour of stiffened, curved composite panels has been investigated within the projects POSICOSS (Zimmermann and Rolfes, 2006) and

COCOMAT (Degenhardt et al., 2006) supported by the European Commission. Degenhardt et al. (2008) reported on the experience gained within these projects by the German Aerospace Centre DLR. Numerical models of the stiffened CFRP panels have been created using finite element software ABAQUS, and user sub-routines have been developed for simulation of the degradation and the skin-stiffener separation, and the results have been validated experimentally. Orifici et al. (2008) reported on the software benchmarking studies, comparing the capabilities of Nastran and ABAQUS software for modelling of the curved, stiffened panels under axial compression until collapse. The numerical results have been compared to the results of preliminary experiments, where the testing procedure was still in the development. ABAQUS model also updated according to a methodology developed at DLR that uses the USDFLD user subroutine for modelling of the material degradation. It was concluded that the modelling of collapse in Nastran was very time consuming and had significant convergence problems. The use of the USDFLD user subroutine in ABAQUS gave very close prediction of the load-carrying capacity of the panel; however, it misrepresented the actual damage mechanism. Araico et al. (2010) presented the results of further developed ABAQUS modelling technique. In addition to the use of the USFLD user subroutine for modelling of the material degradation, the so-called 'cohesive elements' were employed in the finite element models to capture the skin-stiffener separation. Intact panels and panels with artificially induced initial delaminations have been tested for the validation of the analysis method developed. The comparison of the analysis results and the experimental data revealed that the proposed analysis methodology finds the buckling loads and the stiffness of a panel well, and the collapse loads were predicted accurately. Nevertheless, for some of the panels tested, the deformed shapes in the deep post-buckling were somewhat different in the experimental and numerical results.

Results of cyclic buckling experiments on curved stiffened CFRP shells performed at German Aerospace Center DLR and Israel Institute of Technology have been presented by Wilckens et al. (2010) and Abramovich and Weller (2010). Undamaged panels and panels with artificially introduced skin-stiffener delaminations have been subjected to repeated tests relatively deep in the post-buckling and the propagation of the delaminations has been monitored. The common finding in both studies was that the skin-stiffener delaminations did not propagate during the cyclic tests. The propagation started only after the global, stiffener-based buckling during the final collapse tests. Wilckens et al. (2010) observed the decrease of the axial stiffness and collapse loads of the panels after 4001 cycles of buckling, while Abramovich and Weller (2010) did not observe any stiffness degradation as a result of the

cyclic tests. Nevertheless, both studies confirm that curved stiffened composite can be designed to operate in the post-buckling region safely.

Cordisco and Bisagni (2010) presented on the work performed at Politecnico di Milano under the project COCOMAT. The experimental setup used in several investigations mentioned before has been adjusted to perform buckling tests on stiffened composite box under combined axial compression and torque. To explore the post-buckling capabilities of the stiffened composite structures, the box assemblies have been designed to collapse at 3 times the axial buckling load or 2 times the buckling torque. First, the specimens have been loaded until 125% of buckling load in axial compression and torsion in clockwise and counter-clockwise directions. Next, the axial load has been applied at constant levels before the buckling and then the torque has been introduced until buckling, thus obtaining buckling compression-torque interaction curves. Finally, the axial compression equal to 50% of the buckling load has been applied and then the torque is introduced in counter-clockwise direction until collapse. The buckling loads predicted in the design process using ABAQUS/Explicit overestimated the buckling load by 78% and the buckling torque by 46%, and therefore the modelling approach has been reconsidered and some over-constraining assumptions have been changed. In the finite element analyses, the first-ply-failure load according to the Tsai-Wu criterion has been considered as the collapse load. As a result, the buckling and collapse torques of the final collapse test have been predicted with accuracy within 5%. The tests and analyses of the same boxes, but with artificial initial skin-stiffener delaminations, have been presented by Karachalios et al. (2010). Both experimental and numerical results showed that at the given configuration of initial delaminations, the crack does not start propagate until the collapse torque. These studies confirm once more that the ultimate load for stiffened composite structures can be allowed in the post-buckling region.

A metamodelling methodology has been proposed by Kalnins et al. (2010) for simulation of stiffened composite structures with integrated degradation scenarios. This methodology can be used for fast design of such structures and is based on response surface methodology and design and analysis of computer experiments. The metamodels have been created using ANSYS/LS-DYNA finite element models validated with the tests performed within the COCOMAT project. The proposed methodology resulted in accurate metamodels with the cross-validation error within 10% margin.

Buckling and post-buckling behaviour of stiffened composite panels has also been in focus of interest of number of other research projects, including ALCAS (Barkanov et al.,

2010), also supported by European Commission, and aimed at development of all-composite primary structures for commercial aircraft such as Airbus A350.

1.4. Dynamic buckling of lightweight structures

The need to design lightweight structures that have to withstand time dependent dynamic loads, sometimes quite severe, has led to the increasing interest in dynamic buckling, also referred in literature as dynamic stability/instability (Yaffe and Abramovich, 2003).

The phenomenon of dynamic buckling has been investigated by Koning and Taub (1933) in the early thirties and has been studied experimentally and theoretically by many researchers since. However, only within the last three decades a basic understanding of buckling under impulse loads has been developed. The introduction of high-speed electronics and photographic instrumentation has facilitated that made this development possible (Singer et al., 2004).

In the last decades dynamic buckling with emphasis on crashworthiness (Johnson and Mamalis, 1978), energy absorption and nuclear containment structures (Johnson and Reid, 1978) has been investigated. In these studies the emphasis has focused on the plastic response to the dynamic plastic buckling. Despite the numerous investigations on dynamic buckling hardly any suitable experimentally verified criteria for the determination of dynamic buckling loads or for presentation of design information for prediction of the dynamic buckling load of a given structure and loading have appeared in the open literature. The need for such criteria and such a design database motivated the extensive dynamic buckling tests carried out by Ari-Gur and Singer (1981) and Ari-Gur et al. (1982). at the Aerospace Structures Laboratory, Technion, Israel.

A monograph on dynamic buckling of bars, plates and cylindrical shells, covering research on this topic from 1960 to 1980 has been published by Lindberg and Florence (1987). The focus has been kept on loads much higher than the static buckling loads with very short durations, and only isotropic materials have been considered. Both analytical and experimental investigations have been presented in the review.

Another monograph on dynamic buckling of basic structural elements and structures has been written by Simitses (1990). Buckling behaviour of suddenly loaded beams, frames, arches, spherical caps and cylinders has been described analytically in this work. However, no experimental work has been presented.

1.4.1. Dynamic buckling of beams

Dynamic buckling of columns has been investigated both experimentally and theoretically in Israel Institute of Technology in the 1980ties. Ari-Gur et al. (1982) investigated the dynamic response of columns under impulsive axial compression. The investigation has been carried out on clamped specimens, made of metals and composite materials, loaded impulsively by a striking mass. In the theoretical study Rayleigh-type beam equations were assumed for a geometrically imperfect column of a linear-elastic anisotropic material, and the numerical solution, yielded buckling behaviour that correlated well with the experimental results. The results have shown that initial geometrical imperfections, duration of impulse and effective slenderness have a major influence on the buckling loads, whereas the effect of the material is secondary.

Weller et al. (1989) investigated the dynamic buckling of metal beams, along with metal plates, subjected to in-plane axial impact. A computer code ADINA has been used to obtain Dynamic Load amplification Factors (DLFs) of the specimens and the results have been compared to experimental results. As anticipated, the DLFs were usually higher than unity. However, in a few cases, in the presence of certain magnitudes of initial geometric imperfections and for loading durations close to the first natural period in bending, DLFs less than unity have also been observed.

Some theoretical studies in dynamic buckling of columns have been performed at Western Michigan University, Kalamazoo, Michigan (Ari-Gur and Elishakoff, 1996; Kadandale and Ari-Gur, 1997). Isotropic and viscoelastic columns under compressive pulses have been considered, with pulse frequencies varying from quasistatic to impulsive. An appropriate dynamic instability criterion has been defined and utilized and the corresponding buckling results have been compared with those for isotropic columns, as well as with results obtained by the classical beam theory. The results have shown that the classical theory predicts the dynamic buckling strength of isotropic columns accurately. However, for columns with low transverse shear rigidity, buckling loads predicted by the refined theory may be as low as two thirds of those estimated via the classical theory. As for viscoelastic columns, the material viscous damping has a significant effect on the buckling load only for short duration pulses, where higher buckling loads and smoother deflection shapes occur. It has also been concluded that buckling under impulsive loading is very sensitive to the initial geometrical imperfection of the column and, for moderately slender columns, rotary inertia terms may be neglected in the analysis.

More recently, the dynamic buckling of "quasi-ductile" laminated composite beams with laminate sequence of $[(\pm 67.5)_n]_s$ has been investigated by Zhang and Taheri (2004) at Dalhousie University, Canada. Post-impact deformations have been observed rather than buckling loads. Both carbon/epoxy and E-glass/epoxy laminates exhibited post-impact residual deformation, while no obvious delamination has been observed. The numerical investigation showed that both the top and bottom surfaces would fail due to the excessive magnitude of the transverse tensile stress (i.e., normal to the fibre direction).

Dynamic buckling of elastic columns under fluid-solid slamming has been investigated by Cui et al. (2000; 2001a; 2002). The experiments have been performed employing a drop-tower, where a specimen is being dropped on a water surface, resulting in a compression wave very close to the half-sine. Analytical model for the analysis of column under impact load has been developed, and the obtained DLFs were in good agreement with the experimental results, with an average error of 8.4% for the 12 tested columns. It was concluded that the dynamic buckling critical load of the column approaches the static buckling load as its duration approaches infinity, but is always larger than the static buckling load.

Recently, lots of research has been devoted to the dynamic plastic buckling/crash tests of structural elements. Kenny et al. (2002a; 2002b) investigated dynamic plastic buckling of slender beams both numerically and experimentally. In the numerical investigation, direct implicit integration has been employed in ABAQUS/Standard, and the results have been compared to results obtained in finite element software NISA and experimentally. The author concluded that for the parameters investigated, the modelled boundary conditions and element formulation had the most significant influence on the computed buckling response. The element aspect ratio, imperfection model and contact mechanics were of secondary importance on the computed modal behaviour.

Gladden et al. (2005) performed an experimental study on dynamic buckling and fragmentation of brittle rods in Penn State University. The authors present experiments on the dynamic buckling and fragmentation of slender rods axially impacted by a projectile. By combining the results of Saint-Venant and elastic beam theory, they derived a preferred wavelength λ for the buckling instability, and experimentally verified the resulting scaling law for a range of materials including teflon, dry pasta, glass, and steel. For brittle materials, buckling leads to the fragmentation of the rod. Measured fragment length distributions have shown two peaks near $\lambda/2$ and $\lambda/4$. The non-monotonic nature of the distributions reflected the influence of the deterministic buckling process on the more random fragmentation processes.

1.4.2. Dynamic buckling of plates

Dynamic buckling of plates has been comprehensively investigated at Israel Institute of Technology by Abramovich and Grunwald (1995). Experimental studies with axially impacted laminated composite plates having various edge aspect ratios and boundary conditions have been performed to determine the DLF. The static and the dynamic buckling loads have been determined using a modified Donnell approach to yield consistent results. As anticipated from earlier theoretical results, the DLF's were usually above unity. However, for loads having duration in the vicinity of the first natural bending period of the plate, DLF's below unity were observed.

About the same time, dynamic buckling of rectangular composite plates has been investigated numerically by Ari-Gur and Simonetta (1994; 1997) in Western Michigan University. Specifically, the effects of fibre orientations of angle-ply laminated panels have been studied, and geometric non-linearities due to large deflections, as well as wave propagation effects due to in-plane inertia terms, were included in the analysis. The authors found that the dynamic buckling loads were not always higher than the static ones; in some cases there was a range of loading frequencies near the fundamental frequency of the plate where dynamic buckling occurs for lower load (which confirms to the experimental results obtained by Abramovich and Grunwald (1995)). Buckling under a displacement pulse occurs at a load higher than that for a force pulse of similar duration. Also, the critical axial displacement is not sensitive to the material configuration.

More recently, Cui et al. (1999; 2001a) and Cheong et al. (2000) investigated dynamic buckling of plates under fluid-solid slamming, both experimentally and numerically. The experiments were performed employing a drop-tower, where a specimen is being dropped on a water surface, resulting in a compression wave very close to the half-sine. The author determined corresponding critical impulse from the experimental results for each tested plate. The effect of different boundary conditions on the elastic-plastic dynamic buckling properties of plates was also examined and the authors concluded that the boundary conditions strongly affect the plastic collapse load and collapse mode of the plates, and therefore strengthening plate boundary constraints is a very effective way to enhance its load bearing capacity for in-plane impact loads. On the other hand, it was found that different loading sequences strongly affect the plastic deformation of plates, but they basically have very little effect on the load bearing capacity of a plate under fluid-solid slamming. In (Cui et al., 1999) the results indicated that dynamic buckling always took place elastically for the types of rectangular

plates tested under fluid-solid slamming. The dynamic buckling modes of the plates were governed by the plate fundamental transverse free vibration mode. It was also found that boundary conditions strongly affect the dynamic buckling properties of plates subjected to fluid–solid slamming loads. Results from numerical parametric study indicated that initial imperfection and load duration have significant influence on the dynamic buckling of the plates, the smaller the initial imperfection and the load duration, the higher the dynamic buckling critical loads of the plates.

The dynamic stability behaviour of imperfect simply supported plates subjected to in-plane pulse loading has been investigated by Petry and Fahlbusch (2000) at Bundeswehr University, Munich. For the calculation of dynamic buckling loads a stress failure criterion has been applied. The large-deflection plate equations have been solved by a Galerkin method by using Navier's double Fourier series. Parametric studies have been performed in which the influences of the pulse duration, shock function, imperfection, geometric dimensions and limit stress of the material have been discussed. The authors concluded that the dynamic elastic limit loads, which were computed by the stress failure criterion, were more useful for the design of lightweight structures than the commonly used criterion of Budiansky and Hutchinson (1964).

1.4.3. Dynamic buckling of shells until 1980ties

Since the World War II, following the appearance of advanced technologies of large-scale, high-speed, weight-efficient military and civilian vehicle structures, dynamic buckling of shells has received serious attention.

Extensive studies on dynamic buckling have been performed at the Harvard University and Avco Corporation in the beginning of 60ties. Budiansky and Roth (1962) have investigated axisymmetric dynamic buckling of spherical shells analytically. The non-linear elastic shallow shell theory has been employed to study the response of shallow spherical cap to a uniform transient pressure with rectangular loading history. The authors presented a qualitative criterion for the determination of critical parameters for dynamic buckling. According to that criterion, the buckling point is identified from the pressure – maximum displacement plot.

A more general study of dynamic buckling phenomena using simple imperfection-sensitive models has been presented by Hutchinson and Budiansky (1966) and Budiansky (1966). The results have been presented in such form that the dynamic buckling loads of an imperfect structure were related to its static buckling load, therefore bypassing the explicit

dependence on the initial imperfections. Application of this approach to the real structures has also been discussed, and the attention has been paid to axially compressed cylinders. It has been assumed that the dynamic buckling mode shape is the same as the static one; however, the authors admitted that for short load application times the buckling mode shape may differ.

Roth and Klosner (1964) have performed a study on the dynamic instability of long, circular cylindrical shells having initial imperfections subjected to time-dependent axial compressive loads. By using a nonlinear shell theory and including the radial inertia terms, Karman-Tsien (von Karman and Tsien, 1941) type equations have been derived. An approximate four-term deflection function having time-dependent coefficients has been assumed, and by appealing to Hamilton's principle a system of four coupled, second-order differential equations relating these coefficients has been obtained. A numerical-integration scheme has been used to solve these equations as a function of five parameters; namely, two initial imperfection parameters, two parameters governing the time dependent geometrical configuration of the shell (equivalent to selecting the number of waves in the axial and circumferential directions), and the applied axial compressive load. It has been found that the critical load is highly dependent on the initial imperfections and little effect is found from small outside disturbances. The effect of applying a load over a short time has been studied, and a significant increase in the dynamic buckling stress with a reduction of time duration of loading has been observed.

The dynamic buckling of cylindrical shells under axial compression has been also studied at the Avco Corporation (Humphereys and Sve, 1966). A comparison of experimental data with the theory of Roth and Klosner (1964) has been presented by Humphereys and Zatlers (1965) for dynamic buckling of axially loaded circular cylindrical shells. The experiments have been performed in the Air Force six-foot diameter shock tube, operated by the University of New Mexico. The purpose of these tests was not to simulate any specific blast environment, but rather to duplicate as closely as possible the conditions that were assumed in the analysis. Comparison then provided simply a test of validity of the method, not a proof of applicability of specific results to any actual engineering situation. In that series of tests, four identical cylinders with wall thickness of 0.851 ±0.076 mm, machined from heavy-wall 6061-T6 grade aluminium extruded seamless tube, have been subjected to blast loads of successively increasing magnitude until an instability condition has been reached.

At loading levels below the buckling point the response was elastic and consisted basically of the damped harmonic vibration of the rather heavy end plate on the cylinder acting as a spring. This was attenuated to zero in about 50 ms with little change of shape. At

the critical buckling level, however, drastic changes occurred and the following events took place. The initial stress wave resulting from the shock pulse moved in a quite uniform fashion down the cylinder, at a level too low to cause buckling by itself. When, however, the wave hit and reflected off the relatively rigid clamping fixture, the initial stress level was effectively doubled. As the wave reflected, this region of roughly uniform higher stress would grow in size, with steadily decreasing stress amplitude. For the right combination of wavelength and stress amplitude, dynamic buckling would occur in a short section near the clamped end.

A good correlation between experiment and theory has been found for the particular shell shape tested. The effect of the initial imperfections could not be ignored and in this analysis, a double cosine function has been used for initial imperfections. Although the models had imperfections that did not obey this formula but had a random distribution. According to the authors, this double cosine distribution represented the imperfection influence sufficiently well to provide results that were reasonable, when compared to the tests.

Stability of axially-loaded thin cylindrical shells under dynamic lateral pressures has been investigated both analytically and experimentally at Space Technology Laboratories, Redondo Beach, California (Koval and O'Neill 1963; 1964). The theoretical study used nonlinear shallow shell theory to investigate the coupling between an axisymmetric "ring-type" mode and the asymmetric "breathing mode" into which the shell would initially buckle. It has been shown that, under certain conditions, when the ring mode has been dynamically excited, it might be possible to induce buckling at a dynamic critical pressure that is smaller than the static buckling pressure for shells having R/t ratios less than 200. It was stated that the possibility of a dynamic buckling pressure lower than the static value appears to be a significant design factor only for thicker shells ($R/t<200$, especially $R/t<100$) and only under the conditions described below. To show this dynamic effect, the static buckling modes must be tuned to the axisymmetric ring-type mode, i.e., the ratio of frequency of the buckling mode to the frequency of the ring mode must be about 1/2. The degree to which a mode is tuned is critical. For a shell to show a lower dynamic buckling pressure, the dynamic critical pressure for at least one mode must fall below the static buckling pressure of the shell. It was concluded that the rise times of the suddenly applied pressures must be shorter than the half-period of the ring mode in order to induce "dynamic buckling". According to that study, the initial imperfections affect the dynamic buckling pressures to a lesser extent then the static values.

The authors concluded that a supercritical load could be applied without leading to collapse if the load would be removed sufficiently soon. It has also been outlined that in the

case of very short durations, the governing factor on buckling appears to be the impulse given to the shell. It was noted that the rectangular pulse used had zero rise time; consequently, the horizontal asymptote of the critical pressure curve was the critical pressure for a suddenly applied pressure rather than that for static loading.

A parallel experimental investigation has also been reported in which an electrostatic loading system has been developed for the purpose of producing the necessary high rates of loading on the cylinder. The technique of loading the structural models electrostatically was entirely new and its feasibility has been established. Advantages offered by this new procedure were very high rates of loading (measured in microseconds), possibilities for tailoring time histories and spatial distributions of loads, and operation in a vacuum to allow the structural responses to be unimpeded by a fluid in contact with the surfaces. The tests conducted on very thin (R/t = 800) mylar cylinders did not detect a difference in buckling pressures between slow and rapid loading rates. This was consistent with theoretical predictions. Thicker shells could not be tested because the necessary pressures for buckling of the cylinder could not be generated electrostatically.

Experimental and theoretical studies on cylindrical shells have been carried out at the University of Toronto. The basic objective of these studies was to obtain reliable experimental data on the behaviour of near-perfect and imperfect cylindrical shells subjected to dynamic loading. Zimick and Tennyson (1980) studied the buckling response of thin-walled circular cylindrical shells subjected to dynamic, transient, axial square-wave loading of varying time duration. Both geometrically perfect and imperfect shells have been tested. The geometrically near-perfect circular cylindrical shells have been manufactured from a liquid epoxy plastic using the spincasting technique. The imperfect cylindrical shell specimens have been machined from a near-perfect cylinder on a lathe using a hydraulic tracer tool and a suitable template. All specimens were of uniform thickness but contained a geometric shape imperfection in the form of an axisymmetric cosine function in the axial direction or an asymmetric "checkerboard" pattern. Due to the material's high ratio of yield strength to modulus of elasticity, the shell models buckled entirely elastically and thus could be retested many times.

Dynamic transient square-wave axial loading of the shell specimens has been performed on an impact testing machine designed and constructed at the University of Toronto. A gas gun has been used to propel a hardened steel projectile down at 2500 mm barrel to impact on a striker shell. A restraint on the displacement of the piston ring assembly limited the contact time with the striker shell, which was then free to move in the axial

direction on bearings to impact upon the test specimen that was also free to travel axially. After the event had been recorded, the test specimen was eventually brought to rest by an end stop. An important feature which rendered that machine unique was the independent control of time duration of loading τ and input stress magnitude σ, which were governed by the length of the striker cylinder and its velocity, respectively. Duration of loading ranged 200-450 μs, which physically corresponds to an input pulse of about 0.55-1.35 of the length of the shell specimen.

Several small (1.59 mm) foil strain gages were bounded to the inner and outer cylinder surfaces and the dynamic strain histories have been recorded on two dual-beam oscilloscopes. To supplement the strain gauge data, high-speed framing photography using a 16 mm Hycam camera has been used to record the deformation of the shell on impact for selected specimens at filming rates of 1500-6500 fps. Because of the elastic behaviour of the shells during loading, each specimen could be tested multiple times to give repeated results. The test procedure involved impacting the striker shell against the specimen at increasing velocity with each run. A series of response curves were thus obtained showing the strain as a function of time which were then used to define a dynamic buckling load for a given input pulse time duration. Each cylinder has been subjected to a number of such sequences of varying time duration to outline the trend of the dynamic buckling loads.

The analytical treatment of this problem was based on the Karman-Donnell large-deflection equilibrium equations, modified to include effects of initial shape imperfections and radial inertia, together with the corresponding compatibility equation. The focus of the investigation was buckling on first passage of the input pulse. Therefore, no account has been made for reflections of the stress pulse from the end of the shell. Analytically, the shell has been assumed to be very long in order to neglect the effect of boundary conditions.

Buckling stiffness increased dramatically for short durations of loading due to the shell inertia in the radial direction. For short time durations (less than the period of free vibration in the static buckling mode), the dynamic buckling stress was increased above static for even relatively imperfect models. However, the presence of initial geometric shape imperfections could lead to substantial reductions in the dynamic buckling stress, particularly, if their wavelengths would be close to the classical buckling modes. In addition, increasing imperfection amplitude decreased the pulse duration for which dramatic increases in buckling strength could be expected. These two quantities, dynamic buckling load and pulse duration, could be combined as a finite time buckling impulse to provide a conservative dynamic buckling design criterion. It has also been observed that in the time domain investigated, the

dynamic buckling modes differed from the classical static asymmetric mode, tending rather to be axisymmetric for some thin-walled cylinders. Because of the good agreement obtained between experiment and analysis, it was concluded that the simplified analytical buckling model adequately accounted for the principal mechanisms governing the dynamic response of circular cylinders.

1.4.4. Dynamic buckling of shells since 1980ties

With the development of computers and numerical analysis methods and software, as well as advances in the measurements of geometrical imperfections of shells, the experimental investigations in dynamic buckling could be supported by accurate and comprehensive numerical studies. The limitations and simplifying assumptions of the analytical methods could be avoided and buckling behaviour of shells of virtually any shape could be modelled, and the initial imperfections of real shells could be included in the analyses.

Yaffe and Abramovich (2003) investigated dynamic buckling of cylindrical stiffened shells within the extensive research on dynamic buckling of thin-walled structures performed at Israel Institute of Technology. It is one of the few recent experimental investigations in dynamic buckling of cylindrical shells. Buckling of aluminium cylindrical stringer stiffened shells under axial dynamic applied loading has been investigated, both numerically and experimentally. Like in the previous studies, the Hutchinson–Budiansky (Hutchinson and Budiansky, 1966) dynamic buckling criterion has been applied to determine the DLF.

A finite element model for a shell has been built using the ADINA finite element code to simulate the experimental case used throughout the test series. The shell was impacted through the upper end plate and pairs of strain gages glued circumferentially at the mid-height measured its response. The amplitude of the impact was governed by the height of the dropping mass, while the duration depended on the ratio of striking mass to the upper end plate mass. During the tests, the load-time curve was nearly a half-sine, and numerical predictions have been computed for a rectangular shape and half-wave sine. A parametric investigation has been performed to find the dynamic buckling loads of the impacted shells and their respective loading durations to yield a DLF less than unity (see Figure 1.5).

It has been shown numerically that when the period of the applied loading (half-wave sine) equals half the lowest natural period of the shell, there is a slight drop in the DLF. This factor drops below unity, when the ratio of the given sound speed in solids, c, to the velocity developed axially due to the applied dynamic loading, approaches unity. It means that, for this particular loading period, the dynamic buckling load would be lower than the static one.

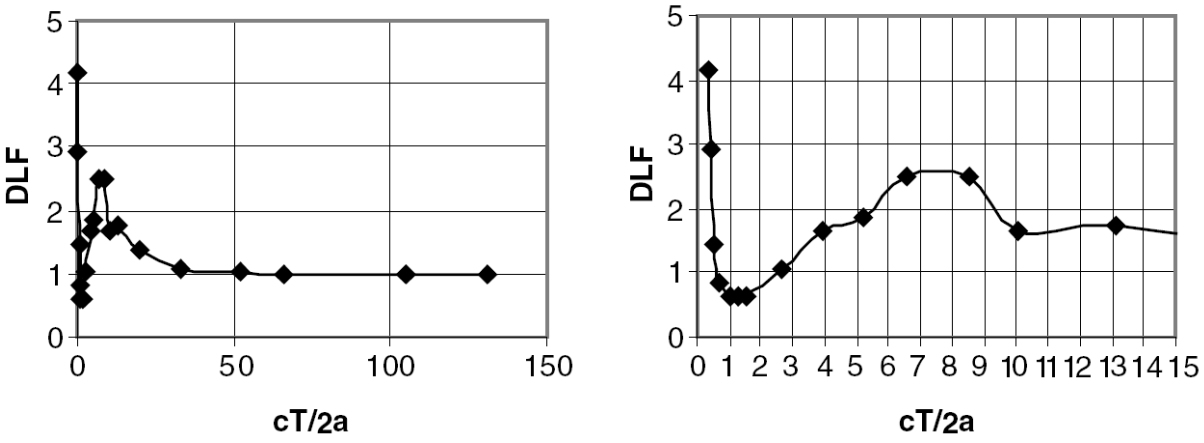

Figure 1.5. DLF versus non-dimensional time parameter *T*'
(from Yaffe and Abramovich, 2003)

It has also been shown numerically that the shape of the load-time curve, the half-wave sine, a shape encountered during the tests, as well as the initial geometric imperfections have a great influence on the dynamic buckling of the shells.

The initial geometric imperfection shape used to calculate the buckling loads due to imperfections had the shape of the calculated static buckling mode. Including the initial imperfections with magnitude 1/10 of the skin thickness in the non-linear buckling analysis resulted in 13% lower buckling load than obtained from the linear buckling analysis. The numerically obtained dynamic buckling mode shapes were very similar to the higher natural mode shapes, like the static buckling mode is similar to the lowest natural mode shape.

The experimental test setup used was following: the shell was clamped to two loading plates and placed under the loading tube, in which a dropping mass would impact the upper loading plate of the shell. To measure the response of the shell, three pairs of strain gages were bonded face to face on each side of the circumferential mid-plane of the shell. The responses of the strain gages were stored on a PC using a data logger for the dynamic strain acquisition. The dynamic buckling strain of the tested shell has been evaluated by plotting a graph of the bending strains vs. the compression strains and applying the Hutchinson–Budiansky dynamic buckling criterion (Hutchinson and Budiansky, 1966). The length of the loading period, which had a shape similar to a half-sine, was altered by increasing/decreasing the dropping mass, by changing the mass of the upper loading plate and by adding a rubber layer on top of the upper loading plate.

The relatively simple test set-up design to cause a shell to buckle dynamically did not fulfil the authors' expectations. Although, the process leading to eventually the dynamic

buckling of the shell worked properly, still no test results have been obtained to form a sound experimental database for this phenomenon.

Dynamic buckling of thin-walled CFRP shell structures due to impulsive loading has been investigated by Bisagni and Zimmermann (1998). Computations for axially compressed cylindrical shells have been performed by commercially available finite element codes. The effect of the laminate set-up on the buckling load of cylindrical shells, the influence of boundary conditions, and their sensitivity to geometric imperfections have been analyzed for static and dynamic buckling loads. The time history of impulsive loading with finite duration and constancy in magnitude was varied, and the corresponding dynamic buckling loads have been related to the quasi-static buckling loads. It was found that the dynamic buckling loads are strongly dependent on the load duration. For short periods of time, the dynamic buckling loads are larger than the static ones. By increasing the load time, the dynamic buckling loads decrease quickly and become significantly smaller than the static loads. In addition, the dynamic buckling loads, like the static ones, decrease with increasing imperfection amplitude.

Bisagni (2004) also performed experimental study on dynamic buckling of carbon fibre composite shells under impulsive axial compression at Politecnico di Milano. CFRP shells with length L of 700 mm, radius R of 350 mm and radius to shell wall thickness ratio R/t equal to 265 with have been tested in the experimental investigation. These shells were composed of bi-directional carbon fibre fabric with stacking sequence [0°/45°/-45°/0°]. The displacement-controlled static buckling tests of the shells resulted in buckling load of 140 kN, which dropped to 50 kN after buckling. The post-buckling mode was diamond-shaped, 10 half waves around the circumference and 2 half waves along the length. The dynamic buckling tests have been conducted using typical crash test equipment, a horizontal deceleration sled. The choice of this equipment has been justified by the difficulties of setting up an ad-hoc testing machine able to provide the high loads coupled with short application times that are required for dynamic buckling tests. The length of the loading period was adjusted by altering the deceleration of the system through hydro-pneumatic brake, while the load intensity was adjusted by choosing the appropriate mass of the sled. The load has been estimated from accelerometer measurements on the sled, and the shortening has been measured using an extensometer. Two tests have been performed on nominally identical cylinders. The buckling loads of 83 kN and 74 kN have been estimated for the two tests, and maximum shortening of the specimen of 6 mm has been registered. The duration of the pulse in the both tests was around 100 ms. The DLFs equal to 0.58 and 0.52 have been obtained in that study, showing that the dynamic buckling loads can get significantly lower than static

ones. However, the author admits that the reported results were not complete at that moment and must be considered as a feasibility study of the test set-up proposed.

A parallel numerical investigation has been carried out along the experimental one (Bisagni, 2005). The approach adopted for the numerical studies was based on the equations of motion, which were numerically solved using a finite element code (ABAQUS/Explicit). The numerical models of two shells with different lay-ups included the imperfection data of the real shell specimens and have been validated by experimental static buckling results. Instead of applying the load at a certain rate, the load has been applied suddenly in that study, and the critical load durations have been found for each load level. The lowest DLFs for the two shells were equal to 0.54 and 0.57. Exclusion of the imperfections from the analyses resulted in drop of the DLF to 0.48 in case of the shell with [0°/45°/-45°/0°] layup, but for the shell with $[45°/-45°]_S$ the lowest DLF was 0.67. That study confirmed the results of (Bisagni and Zimmermann, 1998) that for short loading time duration, the dynamic buckling loads are larger than the static ones. However, at longer application time of the sudden load, the buckling load was significantly lower than the static buckling load. Therefore, taking the static buckling load as the design point for dynamic problems might be misleading.

Numerical and some experimental results on dynamic buckling of axially impacted composite cylindrical shells have been presented by Abramovich et al. (2007). Particular attention has been given to the dynamic buckling criteria and initial imperfections to be used in the numerical analyses. It was pointed out that the dynamic buckling can only be identified by using an arbitrary value of critical response of the structure (displacement, stress, strain). The inclusion of initial imperfections measured on real specimens has been discussed and use of artificial imperfections with shape of the first eigenmode of the shell has been justified. The numerical simulations have been performed using ABAQUS/Explicit finite element software on models with and without the initial imperfections. The results showed that for the models without the imperfections, the DLF can get lower than unity when the duration of the applied load is close to the half natural bending period of the shell. However, the DLF was always greater than unity when the numerical model was updated with the geometrical imperfections. Thus, it was concluded that the dynamic buckling load of a shell is somewhat less sensitive to the initial imperfections than the static buckling load. The experimental results confirmed this finding and no dynamic buckling loads lower than the static buckling loads have been obtained.

Similar problem has been investigated for case of isotropic cylindrical shells by Wei et al. (2005) at the University of Science and Technology of China and Virginia Polytechnic

Institute and State University. The axial velocity has been prescribed at cylinder end faces through the analytical and numerical study. Cubic algebraic equations for the maximum initial growth rate of infinitesimal perturbations superimposed upon a homogeneously deformed state and for the corresponding wavelength have been obtained. It was concluded that the buckled shape corresponds to this wavelength. The buckling behaviour of the shell under relatively low impact speed and containing initial imperfections has been studied using the finite element method. Two mechanisms of buckling initiation have been observed for the shell geometry analyzed: dynamic plastic buckling, when the entire length of the shell wrinkles before the development of large radial displacements, and dynamic progressive buckling, when the shell folds develop sequentially.

Pegg (1994) performed a numerical study of dynamic pulse buckling of cylindrical structures under lateral pressure loads. The study concerned thick cylinders, cylinders with varying radius-to-thickness ratios, a ring-stiffened cylindrical segment that could be applied in the civil and naval marine structures. The finite difference solution has been formulated from existing theory to investigate the non-linear effects of elasto-plasticity and strain rate and curvature rate reversal on the dynamic buckling behaviour. Buckling failure during dynamic response has been shown to occur at peak loads that are much higher, and in modes which consist of much smaller wavelengths, than static buckling loads. The buckling mode shape also changes significantly during its formation due to the effects of strain rate and curvature reversal.

Lindberg et al. (1987) has performed an experimental and theoretical investigation of dynamic buckling of thin cylindrical shells under oscillating stress waves following axial impact. The investigation shows that hoop-breathing response induced by the Poisson effect plays a strong role in buckling initiation, and that the stress oscillations allow buckling initially localized near the impacted end to propagate up the shell toward the free end. As a result of this energy spreading, the total compressive impulse of multi-pulse loading can be substantially larger than the critical impulse for a single pulse.

Number of numerical investigations on static and dynamic buckling of metallic and laminated composite cylindrical shells has been performed at the University of Cincinnati, USA (Simitses and Tabiei, 1997; Tanov and Tabiei, 1998). The dynamic stability of metallic and laminated cylindrical shells has been investigated by Huyan and Simitses (1996). The cylinders were geometrically imperfect and subjected to axial compression or pure bending moment. These loads were suddenly applied with constant magnitude and finite or infinite duration. The finite element method has been employed to generate dynamic responses and

the Budiansky-Roth criteria to determine dynamic critical loads. ANSYS computer code has been chosen to discretize the system and obtain the response of the cylindrical shell under dynamic load. Numerical results have been presented for two distinctly different structure types. The first one is an isotropic cylindrical shell and the second is a laminated shell. The dynamic critical loads decreased with increasing load duration in all the cases and converged to those corresponding to the case of infinite duration. The convergence rate depended on the fundamental frequencies. The higher the fundamental frequency, the faster the critical loads converged. For metallic and laminated cylindrical shells, the static and dynamic critical loads reduced with increasing imperfection amplitude in both cases of compression and bending.

Performance of the two major time-integration techniques used, namely, the implicit integration operator in its Newmark method implementation and the explicit central difference scheme, has been compared (Tabiei et al., 1999) using cylinders under impulsive lateral pressure. ABAQUS/Standard and ABAQUS/Explicit has been used in these studies. The results demonstrated that the explicit method is very attractive when investigating the dynamic buckling of cylindrical laminated shells, combining both good accuracy and excellent computational efficiency. Additionally, the effects of initial preload have been studied by Tanov et al. (1999). It was concluded: as the time duration of the applied dynamic pressure is increased the critical load approaches that of the infinite duration; the imperfection amplitude has virtually the same effect on static critical load as on the dynamic critical load of infinite duration; for thin and for longer shells the static critical load is virtually the same as that of infinite duration.

There are also a number of analytical investigations in dynamic buckling of cylindrical shells, including studies of imperfection sensitivity, probabilistic analyses, and variable shell properties. Shaw et al. (1993) has studied imperfection sensitivity of composite cylindrical shells under dynamic loading. The study considered axial and/or torsional impulsive load in the form of a step function. Two buckling criteria have been used for comparison and critical loads were calculated for different imperfection parameters. A significant reduction of the dynamic buckling load in axial direction compared to the static case has been found, but no significant reduction for the torsional load buckling. Another conclusion was that the Simitses criteria gave more conservative results than the Budiansky and Roth criteria.

Numerous studies in probabilistic dynamic buckling analysis of composite shells have been performed by Chamis and Abumeri (2003; 2005a; 2005b) at NASA Glenn research centre. The objective of these investigations was to describe one approach that has been successfully used to perform probabilistic dynamic buckling analysis of composite shells. A

secondary objective specific and centerpiece to the approach was to use conventional finite elements, available composite mechanics and elementary probabilistic methods. In essence, the approach consisted of the judicious combination and use of all three and coupled with an incremental updated Lagrangian solution algorithm. The emphasis of the investigation was on developing the method and demonstrating its effectiveness by using a cylindrical composite thin shell.

The dynamic buckling load has been obtained at each time step by first satisfying the dynamic structural response equation, including iteration when necessary, and then by solving for the buckling load by available eigenvalue extraction routines in conventional structural analysis computer codes, such as NESSUS and IPACS5 modules. The probabilistic evaluation has been performed using an integrated computer code Integrated Probabilistic assessment of Composite Structures (IPACS). The probabilistic composite mechanic module generated the properties at each node of the finite element model of the structure. This information was used by probabilistic composite mechanics to generate 42 variable probabilistic properties that are needed to probabilistically describe the composite laminate at each finite element node. Subsequently, these properties have been combined with the structural probabilistic information to probabilistically describe the composite shell.

The developed method was generic and not restricted to any special class of shells and/or loading conditions. Typical results obtained included deterministic and probabilistic dynamic buckling loads, buckling modes, affects of uncertainties and respective sensitivities. The effectiveness of the method was demonstrated to evaluate the probabilistic dynamic buckling load of a specific thin composite shell. A universal plot which shows the buckling load at different probability levels and at different loading rates has been developed.

A similar approach has been employed by Abumeri and Chamis (2003a; 2003b) and Chamis (2008) for probabilistic dynamic buckling analysis of adaptive composite shells. The adaptation of the intraply hybrid composite concept to the smart shell composite structure is depicted schematically in Figure 1.6. Note that the intraply hybrid composite consisted of plies that have strips of a regular (host) composite material and interspersed strips of material for sensor/control devices. Actuators, made of control materials such as piezoelectric ceramic fibre, have been used to control the behaviour of the composite structure by expanding (positive-induced strain) or contracting (negative-induced strain) the sensor/control strips to achieve the requisite design and operational goals. The induced control strains have been simulated using equivalent variables principles. Temperature loads representing the electric field strength have been applied to the plies that include smart fibres. The thermal expansion

coefficients have been used to represent the strain coefficients. At the end of each time step, linear buckling analysis has been performed. The smart shell geometry has been updated at the end of each time step to include time dependent deformations.

The dynamic buckling load of the smart composite shell was 7.43 GN compared to 6.85 GN for the conventional composite shell. The 8.5% improvement in the dynamic buckling load for the shell that comprised the smart material was resulting from field strength of 25 400 V/m, a strain coefficient of 1.22×10–10 m/V, smart fibre volume ratio of 0.65, and a smart material volume fraction of 0.5%. For any time *t*, the buckling load of the smart shell was consistently higher than the one of the conventional composite shell. Also, the dynamic buckling of the smart composite shell required longer time before it occured. Weight analysis of the smart and conventional composite shells indicated that the smart shell was about 9% heavier than the conventional one. The weight of the smart shell was estimated at 276.8 N compared to 209.1 N for the conventional graphite epoxy shell. It is concluded that for the shell considered, benefits obtained from the use of smart material can be surpassed by the simple re-arrangement of the fibre orientation of the outer plies.

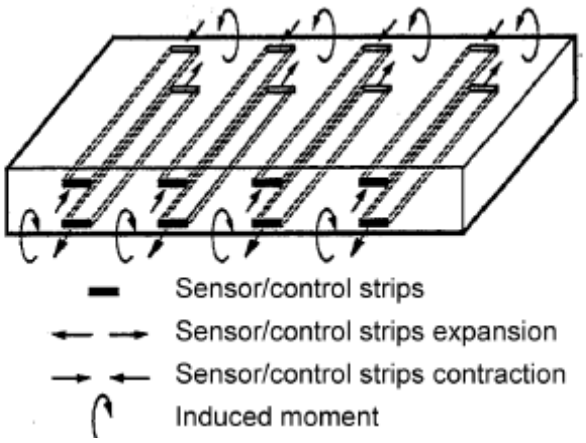

Figure 1.6. Sensor/control configuration of an adaptive shell
(from Chamis (2008))

Rahman and Jansen (2009) from Delft University of Technology, the Netherlands implemented a modified form of Koiter's perturbation approach proposed by Byskov and Hutchinson (1977) in finite element code DIANA. Single mode dynamic bucking analysis has been carried out for unstiffened and ring-stiffened composite cylindrical shells. Results have been compared with available results computed in a similar, semi-analytical analysis and also with full model finite element based explicit dynamic analysis. A good agreement has been

observed in case of external pressure when compared to full model explicit dynamic analysis done with ABAQUS.

One of the analytical studies in dynamic buckling of functionally graded shells has been carried out by Sofiyev (2007) at Suleyman Demirel University, Turkey. The material properties of functionally graded shells were assumed to vary continuously through the thickness of the shell. The fundamental relations, the dynamic stability and compatibility equations of functionally graded truncated conical shells have been obtained first. Applying Galerkin's method, these equations have been transformed to a pair of time dependent differential equation with variable coefficient and critical parameters obtained using the Runge–Kutta method. It was found that critical parameters are affected by the configurations of the constituent materials, compositional profile variations, loading speed variations and the variation of the shell geometry.

Teter (2007) from Technical University of Lubin, Poland performed another analytical study in dynamic buckling of shell structures with varying properties. Static and dynamic buckling of thin-walled closed columns with variable thickness has been considered. Koiter's asymptotic method in the second-order approximation has been used for the static solution, and the non-linear equations of dynamic stability have been solved with the Runge-Kutta method.

1.4.5. Crash tests

A special attention has been paid to elastic-plastic dynamic buckling of isotropic shells under high velocity impact with focus on energy absorption and there are several authors who have performed research in this field in the last decade. Karagiozova from Bulgarian Academy of Sciences in collaboration with Jones from University of Liverpool and Alves from University of Sao Paulo has been investigating these phenomena experimentally, numerically and analytically. Effects of stress wave propagation on formation of dynamic plastic buckling (when the entire length of the shell wrinkles before development of large radial displacements) and dynamic progressive buckling (when the shell folds form sequentially) have been analysed (Karagiozova and Jones, 2001; 2002). The numerical analysis (Karagiozova and Jones, 2001) revealed that the material properties together with the geometrical characteristics of the shell determine the particular type of response for high velocity impacts, and it has been concluded by Karagiozova and Jones (2002) that high velocity impact causes an instantaneously applied load with the maximum value at t=0 and whether or not this load causes inelastic collapse depends on the magnitude of the initial

kinetic energy. Transition from progressive buckling to global bending has been investigated experimentally and analysed numerically and analytically by Karagiozova and Jones (2004a; 2004b).

Another experimental investigation in elastic-plastic dynamic buckling has been performed by Kenny et al. (2002). In this study, a 10 kg free-fall impact hammer applied an axial impulsive load to aluminium and cold rolled steel beams with fixed-slide bearing boundary condition. A total of 94 tests were conducted and the deformed buckled geometry for each impact event has been profiled. A normalized response parameter has been defined to characterize the observed dynamic buckling behaviour, which related the axial position and transverse amplitude of the peak buckle with respect to local stiffness and natural frequency characteristics. Simplified theoretical expressions defining the critical buckle wavelength provided a reasonable bound limit with respect to the experimental data.

1.4.6. Other related research

A numerical procedure for analysis of dynamic delaminations buckling in composites has been developed at the NASA Lewis Research centre (Grady et al., 1987, Aiello and Grady, 1989). Experimental observations of dynamic delamination buckling in transversely impacted laminates were reported, using high-speed photography and simultaneous strain measurements of transversely impacted laminates. A related numerical analysis indicated that the buckling behaviour must be accounted for in the computational model in order to accurately assess the damage tolerance capability of the laminate. Linear buckling analysis requires solution of the eigenvalues problem. In terms of the buckling analysis, the eigenvector represents the buckling mode shape, and the associated eigenvalue indicates the multiple of the stress stiffness matrix needed to make equation singular, that is, to cause buckling. In the dynamic case, the terms of stress stiffness matrix vary with time as the stress waves propagate through the structure. The eigensolution then becomes time dependent, and can be used to track the buckling stability as a function of time. A modified direct-time integration solution sequence has been presented (Figure 1.7) in which the updated stress stiffness matrix is formed after each time step, and the associated eigenvalue problem is solved. The eigenvalue is then a function of time, and it indicates the onset of buckling when it reaches the critical value of unity.

Experimental and numerical investigation in dynamic collapse of CFRP square tubes has been performed at National Technical University of Athens. Mamalis et al. (2006) investigated the compressive properties and crushing response of the tubes numerically, using

LS-DYNA finite element code. The development of simulation focused on modelling the three modes of collapse observed in the series of the static and dynamic experiments. A satisfactory reproduction of the collapse modes, which range from mid-length unstable collapse mode (the predominant collapse mode), to local tube-wall buckling and stable progressive end crushing with tube wall splaying (the mode of collapse featured by the higher crash energy absorption), has been obtained. However, the existing formulation of material models was inadequate due to lack of strain rate effects that justify the strength increase of the tested composite tubes that was recorded in the case of impact tests. Thus, these effects had to be considered when calibrating the material parameters for simulation of dynamic problems.

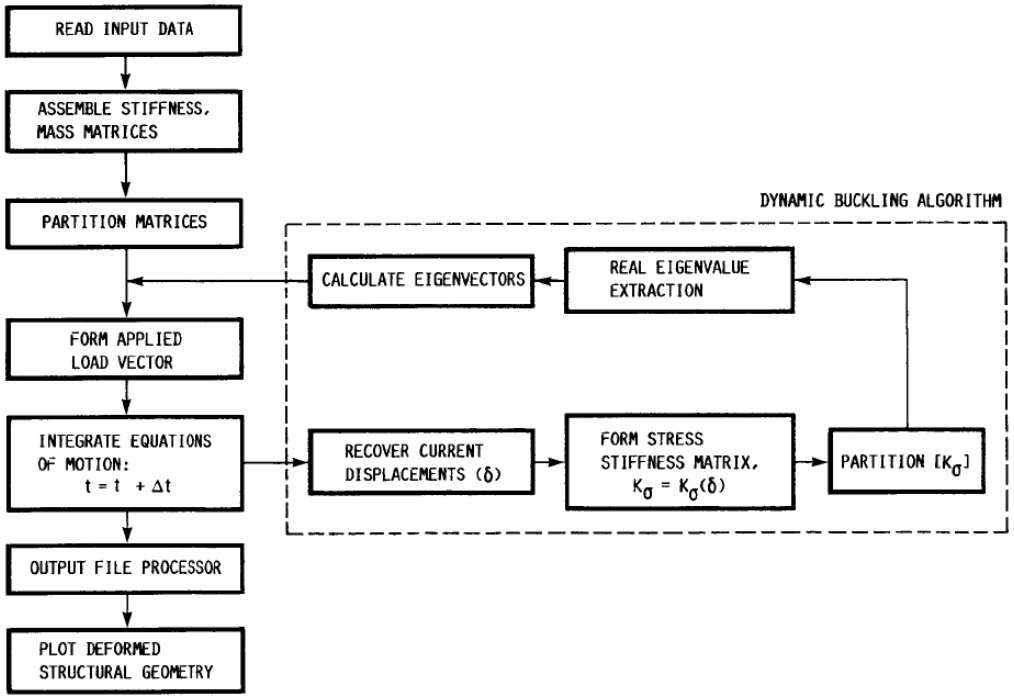

Figure 1.7. The dynamic buckling analysis flow chart
(from Grady et al., 1987)

Tsai and Sun (2005) investigated the aforementioned problem of dynamic compressive strength of polymeric composites at Purdue University, USA. Both the strain rate and shear stiffness effects on the compressive strength were considered in the experimental and numerical study. Off-axis S2/8552 glass/epoxy composite specimens were tested at various strain rates to provide the experimental data with the presence of shear stresses. It has been shown that, by including fibre misalignments and matrix non-linear behaviour, the microbuckling model can be extended to predict compressive strengths of polymeric composites under low and high strain rate loadings. From model predictions as well as

experimental results it was concluded that the compressive strength of polymeric composites is rate-sensitive and that the presence of in-plane shear stress can appreciably lower the compressive longitudinal strength.

1.5. Concluding remarks

Lightweight composite structures are of importance in many fields, including aerospace, wind energy, automotive and sports industries. Buckling of these structures has received lots of research attention over the last 50 years. Various configurations of these structures have been investigated and different loadings considered, but still composite structures lack vast amount of knowledge that has been accumulated for traditional metal structures.

Imperfection sensitivity is one of the main problems still affecting the design efficiency of composite shells. The *knock-down* factor approach defined for metallic shells in the 60s with the NASA SP-8007 guideline is still being used; however, significant advancements have been made. First of all, the lay-ups of composite shells can be tailored in order to decrease the imperfection sensitivity. Secondly, number of studies has shown that probabilistic approaches can be used to find the lower bound of the buckling loads of composite shells confidently. The experimental results show that the buckling loads in actual tests are in the range of confidence predicted by a properly carried out probabilistic analysis. It must be noted though, that the probabilistic approaches are relatively computationally expensive and need statistical data on the various imperfections the structures can have. Alternatively, other methods, like single perturbation approach can be used. It has been shown that application of a relatively small radial perturbation load would result in decrease of the buckling load to a certain level, which was in good agreement with experimental results. Even though this approach is relatively simple, reliable *knock-down* factors can be obtained for the composite shells with improvement over the ones set in the NASA SP-8007 guideline.

Stiffened composite shells are less sensitive than unstiffened ones; however, there are other problems that arise with use of such structures. The buckling of stiffened composite shells can lead to debonding of the stiffeners and thus reduction of the stiffness and strength. Nevertheless, number of studies show that properly designed and produced composite shells can be safely exploited with the ultimate load being in the post-buckling range of the structure. Significant achievements have been made in the field of numerical modelling of the stiffened composite structures, allowing accurate modelling of the buckling behaviour, structural degradation and collapse. Number of commercially available finite element

software is available, but it seems that in most studies the ABAQUS software package has been used more successfully.

The dynamic buckling has been studied extensively over the last five decades. Many of the experimental investigations have been performed in the 60s on isotropic shells, using elaborate and expensive experimental set-ups. With the development of the computers and software, the researchers have been tempted to resort to the numerical simulations instead of tests, and there are only few studies on dynamic buckling of composite structures that include physical experiments. All of the studies on dynamic buckling of composite structures outline the trend of increase of the buckling load with the decrease of the time of the load application. However, there are certain conditions when the dynamic buckling load is lower than the static one, e.g. suddenly loaded cylindrical shell, a plate loaded with a pulse that is as long as half of the plate's bending period etc. On the other hand, there are some investigations where it has been demonstrated that dynamic buckling load can be higher than the static one across the whole spectrum of the dynamic loading.

Based on the findings of the literature review, the dynamic buckling of unstiffened and stiffened composite shells has been studied numerically and experimentally in the present thesis. Particular attention has been given to the effect of the initial imperfections and accurate specimen production and execution of the experiments, so that the numerical results could be validated by the experimental data.

2. MATERIALS AND METHODS

2.1. Specimens

2.1.1. Type 0 cylindrical specimens

The first cylindrical glass fibre reinforced plastic (GFRP) specimens produced in 2008 at Riga Technical University for the investigations of static and dynamic buckling of composite cylinders are called Type 0 specimens in this thesis. Two cylinders with length of 700 mm, nominal radius of 150 mm and nominal wall thickness of 1.1 mm have been produced of four layers of 290 g/m2 E-glass fabric and polyester resin. The ends of the cylinders were reinforced with 70 mm wide strips of same GFRP material, and the total thickness at the ends was 2.5 mm.

The cylinders have been designed for repetitive buckling tests, so they would undergo the buckling deformations without damage occurring. However, for unknown reasons, the matrix of one of the Type 0 specimens was much more brittle than of the other, and already the first static buckling test had damaged the cylinder (Figure 2.1), so the results are presented for only one Type 0 specimen.

Figure 2.1. The damage of the Type 0 specimen

Initially, it has been assumed that the end reinforcements are sufficiently stiff to distribute the load non-uniformities due to limited accuracy of the specimen geometry. However, after obtaining the buckling load of 27.3 kN instead of the numerically predicted 48.8 kN, additional measures have been taken to improve the load distribution. A strip of polyester filler has been placed on a flat surface and the cylinder ends embedded in it. This simple modification (Figure 2.2) increased both the stiffness response and the buckling load of the cylinder (Figure 2.3). However, to assure consistent boundary conditions and load distribution, another approach has been used for Type 1, Type 2 and Type 3 specimens, as described in Chapters 2.1.3 – 2.1.5.

(a) (b)

Figure 2.2. The edge of the specimen without filler (a) and with polyester filler (b)

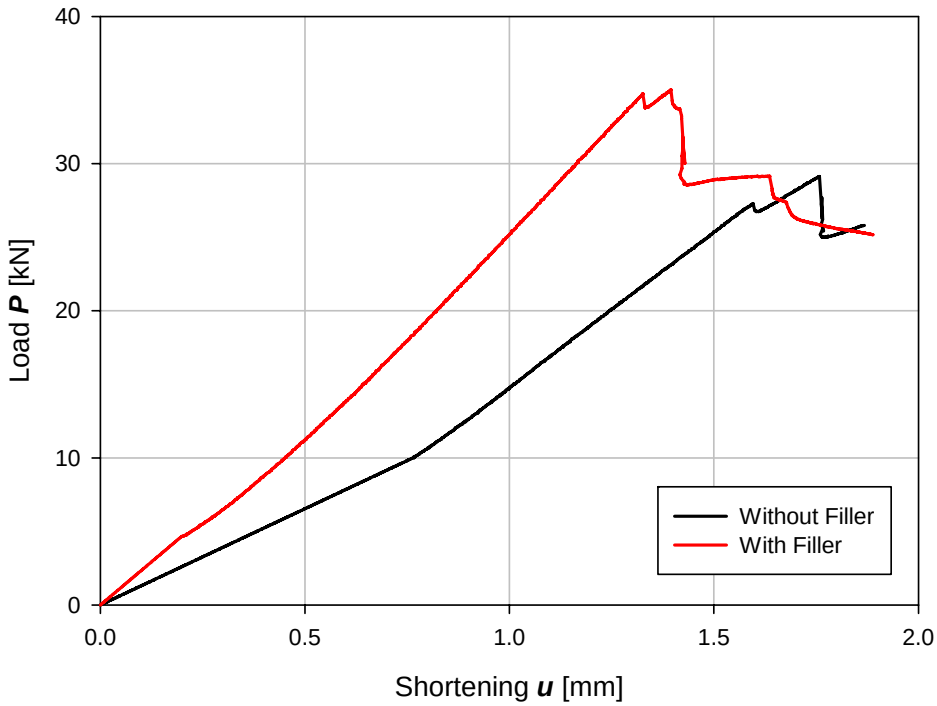

Figure 2.3. Load-shortening curves of quasistatically loaded Type 0 specimen

2.1.2. Type 1 cylindrical specimens

The next series of GFRP cylindrical specimens produced in 2008 at Riga Technical University and "Valmiera-Andren, Ltd." are called Type 1 specimens. 20 specimens with various diameters and lengths have been produced of four layers of 290 g/m2 E-glass fabric and polyester resin, providing nominal wall thickness of 1.1 mm. The dimensions and designations of the specimens are summarized in

Table 2.1.

The specimens with radius of 150 mm were produced at Riga Technical University and cured in an autoclave with 80˚C temperature. These specimens were produced employing cylindrical, slightly conical mould for easy removal of the specimens without damage. The specimens with radius of 250 mm were produced at "Valmiera-Andren, Ltd." and cured in ambient temperature of about 20˚C. Vacuum bag moulding was employed to remove excess resin and ensure more consistent material properties, excluding specimens RTU #1-5, RTU #1-6 and RTU #1-7.

Following the conclusions drawn from the Type 0 specimen tests, the boundary conditions on the edges of the cylinders were provided the following way: After curing the specimens were cut to their lengths and the ends were potted into gaps of circular plates using mixture of aluminium powder and epoxy resin (Figure 2.4). The plates were cut out of MDF and plywood boards for specimens of 250 mm and 150 mm radius, respectively. However, the

relatively low stiffness response of the specimens with the MDF board ends lead to development of Type 2 specimens with aluminium end plates.

All Type 1 specimens were painted white using acrylic spray paint for post-buckling shape monitoring using moiré fringes.

The Type 1 specimens have been designed for repetitive buckling tests, so they would undergo the buckling deformations without damage occurring. However, some of the Type 1 specimens were damaged (Figure 2.5) due to different circumstances during the investigations and were excluded from further tests.

Table 2.1. Dimensions and designations of specimens

		Radius *R*	
		150 mm	**250 mm**
Free length *L*	**400 mm**	RTU #6 RTU #12 RTU #13 RTU #16	-
	560 mm	RTU #3 RTU #4 RTU #5 RTU #7 RTU #8	-
	660 mm	RTU #9 RTU #10 RTU #11	RTU #1-1 RTU #1-5 RTU #1-2 RTU #1-6 RTU #1-3 RTU #1-7 RTU #1-4 RTU #1-8

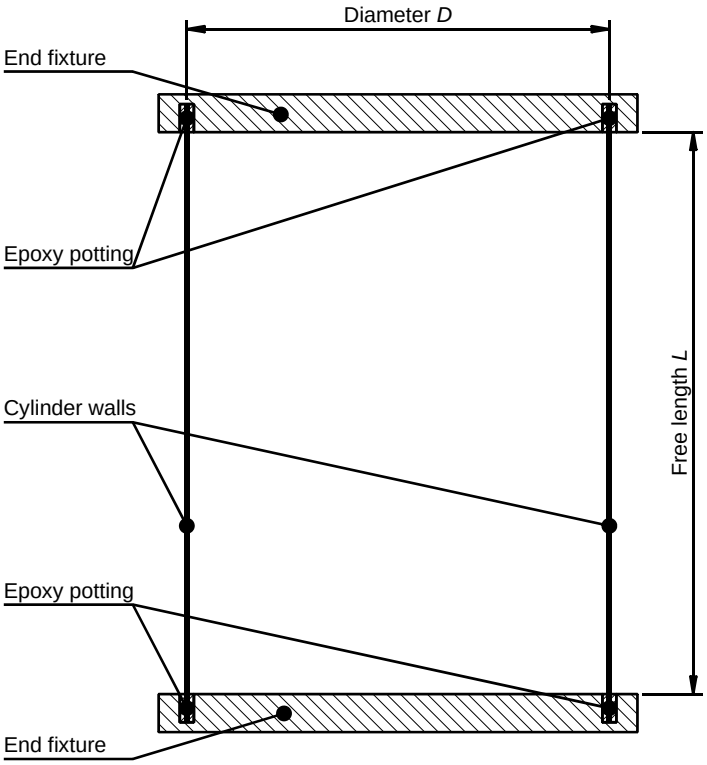

Figure 2.4. Type 1 specimen

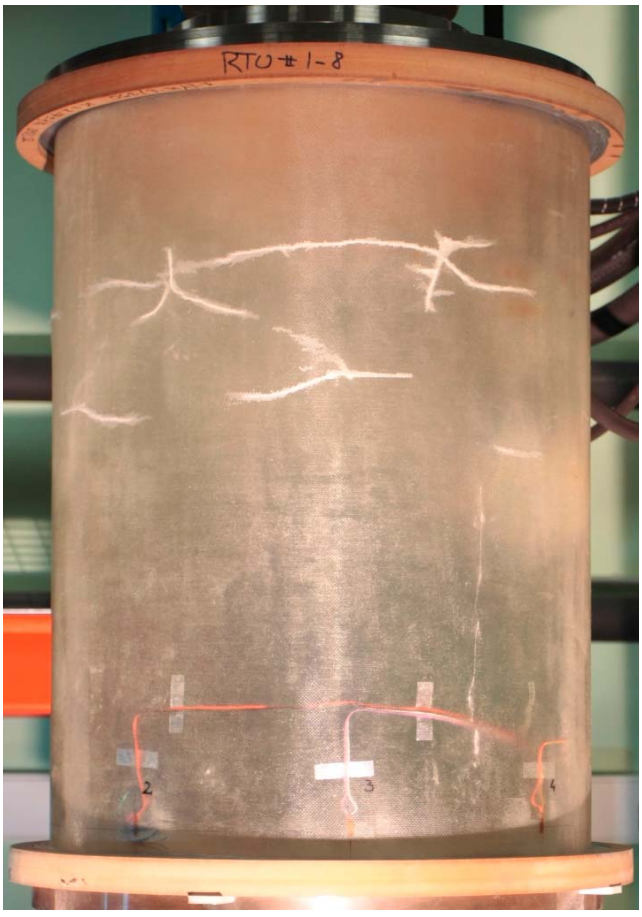

Figure 2.5. The damaged specimen RTU #1-8

2.1.3. Type 2 cylindrical specimens

Type 2 GFRP cylindrical specimens have been produced in 2009 at Riga Technical University. Two specimens with nominal radius of 150 mm and free length of 660 mm have been produced of six (Type 2-1) and eight (Type 2-2) layers of 80 g/m2 E-glass fabric and Polylite 440 polyester resin, providing nominal wall thickness of 0.62 mm and 0.85 mm, respectively. The specimens were cured in an autoclave with 80˚C temperature. These specimens were produced employing cylindrical, slightly conical mould for easy removal of the specimens without damage. Vacuum bag moulding produced folds on top layer of fabric, and therefore wasn't used.

To ensure even more consistent load distribution and boundary conditions than for Type 1 specimens, aluminium was used for production of the end plates (Figure 2.6). After curing the specimens were cut to their lengths and the ends were potted into gaps of the aluminium plates using mixture of aluminium powder and epoxy resin. The plates were CNC milled out of 20 mm thick aluminium. To keep the plates parallel and concentric while placing the GFRP cylinder and curing the epoxy potting, four columns precision machined to the same length were fastened to the corners of the plates.

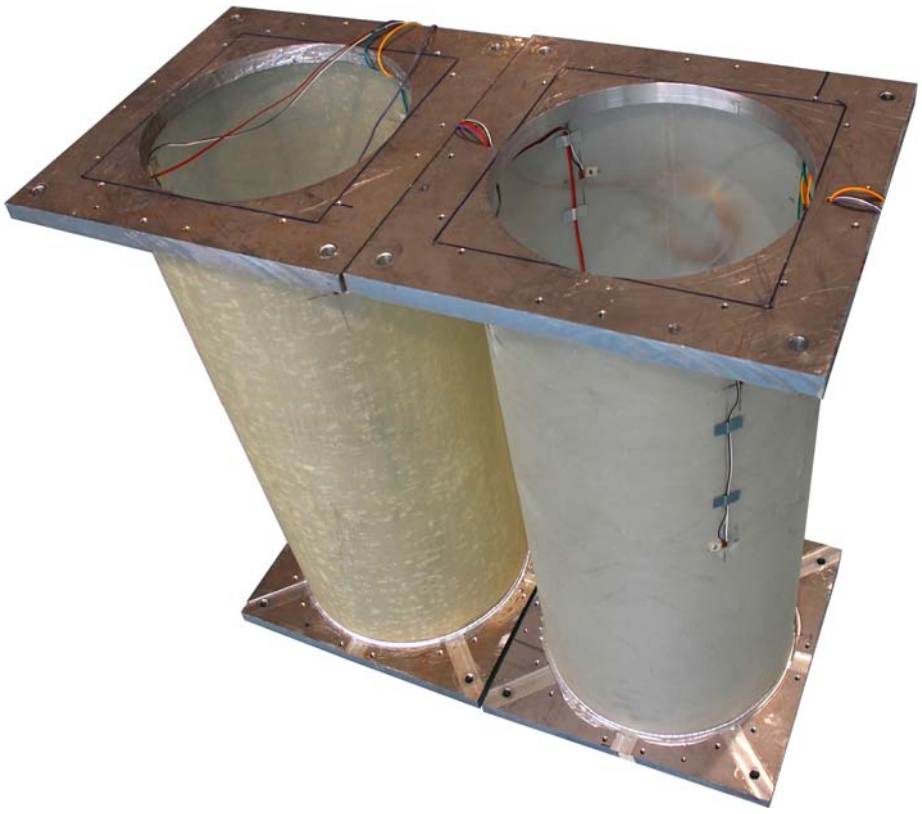

Figure 2.6. Type 2 specimens

2.1.4. Type 3 cylindrical specimens

After the testing of Type 2 specimens that still resulted in significant discrepancy between the experimental and numerical data, Type 3 cylinders were introduced in 2010. 2 specimens with nominal radius of 150 mm and free length of 400 mm have been produced of four layers of 290 g/m2 E-glass fabric and epoxy resin, providing nominal wall thickness of 1.2 mm. Unlike in case of all the cylindrical specimens produced previously for this study, aviation grade E-glass fabric has been used, and polyester resin has been substituted by epoxy resin, this way contributing to more consistent material properties and smaller residual stresses after curing.

The production technology has been altered and tested on 8 other 'scratch' specimens before producing the actual Type 3 specimens. To have the two Type 3 specimens as identical as possible, they have been cut out of a single GFRP cylinder.

The same aluminium plates as in case of Type 2 specimens have been used to reinforce the ends of the cylinders, and particular attention has been paid to keep the initial stresses and deformations in the cylinder as low as possible.

The Type 3 specimens are presented on Figure 2.7.

Figure 2.7. Type 3 specimens

2.1.5. Stiffened CFRP panels

The experiments used in this thesis for the benchmarking of Finite Element software and for validation of ABAQUS/Explicit models of stiffened shells were performed on curved stiffened carbon fibre reinforced plastic panels. Panel 1 has been manufactured by Israel Aircraft Industries (IAI) and Panels 2 and 3 have been manufactured by Aernnova within the EC FP-6 project COCOMAT (Degenhardt et al, 2006; www.cocomat.de). The first two of selected panels have been assembled using 5 blade stiffeners symmetrically attached to the shell curvature, while Panel 3 had 5 stiffeners. The benchmark panel are given in Table 2.2, where 0° direction is parallel to the stiffeners. Typical cross-section of a panel is shown in Figure 2.8. The stiffener and skin are joined using a flange, where the stiffener plies are continued over the web and half the stacking lay-up on each side. The flange plies are cut symmetrically.

The all of the panels during the buckling tests were clamped at the loaded ends. The unloaded edges of Panel 1 and Panel 3 were simply supported, with axial displacement allowed, while the unloaded edges of Panel 1 had no boundary conditions applied.

Table 2.2. Panel specifications

	Panel 1	Panel 2	Panel 3
Free length, L_f	660 mm		520 mm
Panel radius, R	938 mm	848 mm	1000 mm
Arc length, a	680 mm	560 mm	624 mm
Distance between stringers, d	136 mm	132 mm	156 mm
Distance between stringers and longitudinal edge, e	68 mm	16 mm	78 mm
Material		IM7 8552	
Laminate lay-up of the skin	$[0,\pm45,90]_s$	$[90,\pm45,0]_s$	$[\pm45,0,90]_s$
Laminate lay-up of the stiffener:			
Blade	$[(\pm45,0_2)_3]_s$	$[\pm45_3,0_6]_s$	$[\pm45,0_2,90_2]_s$
Flange	$[(\pm45,0_2)_3]$	$[\pm45_3,0_6]$	$[\pm45,0_2,90_2]$
Ply thickness, t	0.125 mm		0.152 mm
Skin thickness, t_s	1.0 mm		1.22 mm
Stringer thickness, t_h	3.0 mm		1.82 mm
Stringer height, h	20.5 mm	14.3mm	28 mm
Stringer flange width, f	40.0 mm	32.0 mm	56 mm

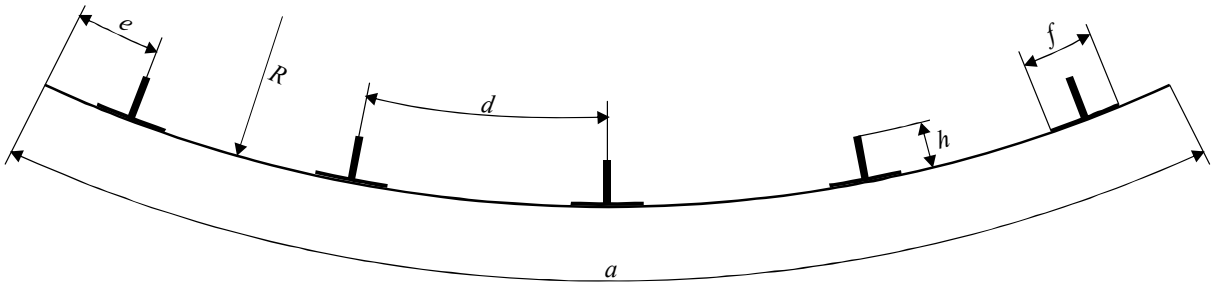

Figure 2.8. Panel cross-section

2.2. Materials

The term "composite material" can be related to a wide range of materials, as the definition of composite material is "material made from two or more constituent materials with significantly different physical or chemical properties which remain separate and distinct on a macroscopic level within the finished structure" (Kaw, 2006). This includes materials as concrete, sandwich plates and fibre reinforced plastics. Exclusively fibre-reinforced plastic composites are considered in this thesis and therefore terms "composite" and "fibre-reinforced plastic laminate" are being used interchangeably.

The use of composite materials is consistently increasing in different industries. The expansion of composite materials started from space applications in 60ties, and now composites are important class of materials in aerospace, road, rail and marine transports, general mechanical applications, sports equipment, electrical industries and also construction.

The properties of fibrous composites are dependant on the proportions of reinforcement and matrix, the form of reinforcement, the fabrication process etc. Some remarkable common properties include brittle fracture without yielding, fatigue and corrosion resistance, good fire resistance comparing to light alloys, aging, and medium to low impact resistance.

Glass fibre reinforced plastics (GFRP) and carbon fibre reinforced plastics (CFRP) are the most widely used composites. The main advantage of GFRP is low cost, while CFRP can have much higher strength and modulus. Composites usually have lower modulus to strength ratios than steels and lightweight alloys, and therefore stiffness problems, including buckling, are more constraining the design than in case of traditional materials (Gay and Hoa, 2007).

The specimens produced and tested for this thesis are GFRP cylinders made of woven fabrics and polyester resin. Vacuum bag moulding technology has been used for most of the specimens. Experimental buckling test results for stiffened CFRP shells obtained in Technion, and DLR (German Aerospace Center) are also used for benchmarking the Finite Element

codes and validation of numerical models. These stiffened shells were made of prepreg unidirectional carbon fibre.

2.2.1. Materials used in Type 0 and Type 1 specimens

All Type 0, Type 1 specimens have the same nominal wall thickness of 1.1 mm and the same material, E-glass fibre fabric / polyester resin matrix composite. Four layers of 290 g/m^2 fabric with nominal fibre volume ratio of 35% were applied manually on a purpose-made mandrel to achieve the specified wall thickness.

Small coupon material property identification tests have been performed at Riga Technical University RTU, Institute of Materials and Structures according to the relevant ISO 527-4:1997 standard. Flat composite plate has been produced using the same technology and materials as the cylinders for the identification of material properties.

Tensile tests have been performed using Zwick Z100 universal testing machine. The tests were displacement-controlled, a load cell has been used to measure the load and the strains were registered using a laser extensometer. The identified material properties are summarized in the Table 2.3.

Table 2.3. Properties of the material used for Type 0 and Type 1 specimens

Property	Direction	Mean value
Elastic modulus (GPa) in tension	E_1	18.66
	E_2	18.28
Poisson's ratio	υ_{12}	0.16
Shear modulus (GPa)	G_{12}	4.56
Tensile strength (MPa)	σ_1	219
	σ_2	296

2.2.2. Materials used in Type 2 specimens

Type 2 specimens have nominal wall thickness of 0.85 mm and they are made of E-glass fibre fabric / polyester resin matrix composite. Six layers of 80 g/m^2 fabric with nominal fibre volume ratio of 35% were applied manually on a purpose-made mandrel to build up the 0.62 mm wall thickness of the specimen Type 2-1 and eight layers of the same materials have been used to form the specimen Type 2-2 with the nominal wall thickness of 0.85 mm.

Small coupon material property identification tests have been performed at Riga Technical University RTU, Institute of Materials and Structures according to the relevant ISO 527-4:1997 standard. Flat composite plate has been produced using the same technology and materials as the cylinders.

Tensile tests were performed using Zwick Z100 universal testing machine. The tests were displacement-controlled, the load was measured by a load cell and the strains were registered by a laser extensometer and strain gauges. The identified material properties are summarized in the Table 2.4.

Table 2.4. Properties of the material used for Type 2 specimens

Property	Direction	Mean value
Elastic modulus (GPa) in tension	E_1	16.04
	E_2	15.52
Poisson's ratio	υ_{12}	0.13
Shear modulus (GPa)	G_{12}	2.59
Tensile strength (MPa)	σ_1	233.8
	σ_2	202.9
	τ_{12}	34.05

2.2.3. Materials used in Type 3 specimens

The Type 3 specimens have nominal wall thickness of 1.2 mm and the same material, E-glass fibre fabric / epoxy resin matrix composite. Four layers of 290 g/m^2 aviation grade fabric with nominal fibre volume ratio of 35% were applied manually on a purpose-made mandrel to achieve the specified wall thickness.

Small coupon material property identification tests have been performed at Riga Technical University RTU, Institute of Materials and Structures according to the relevant ISO 527-4:1997 standard. The specimens for material property identification have been cut out of one of the 'scratch' specimens produced within the same series as the actual Type 3 specimens, using the same materials and technology.

Tensile tests have been performed using Instron 8872 hydraulic testing machine. The tests were displacement-controlled, a load cell has been used to measure the load and the strains were registered using a mechanical extensometer (Figure 2.9). The identified material properties are summarized in the Table 2.5.

Table 2.5. Properties of the material used for Type 3 specimens

Property	Direction	Mean value
Elastic modulus (GPa) in tension	E_1	18.40
	E_2	17.11
Poisson's ratio	υ_{12}	0.14
Shear modulus (GPa)	G_{12}	4.12
Tensile strength (MPa)	σ_1	245
	σ_2	203

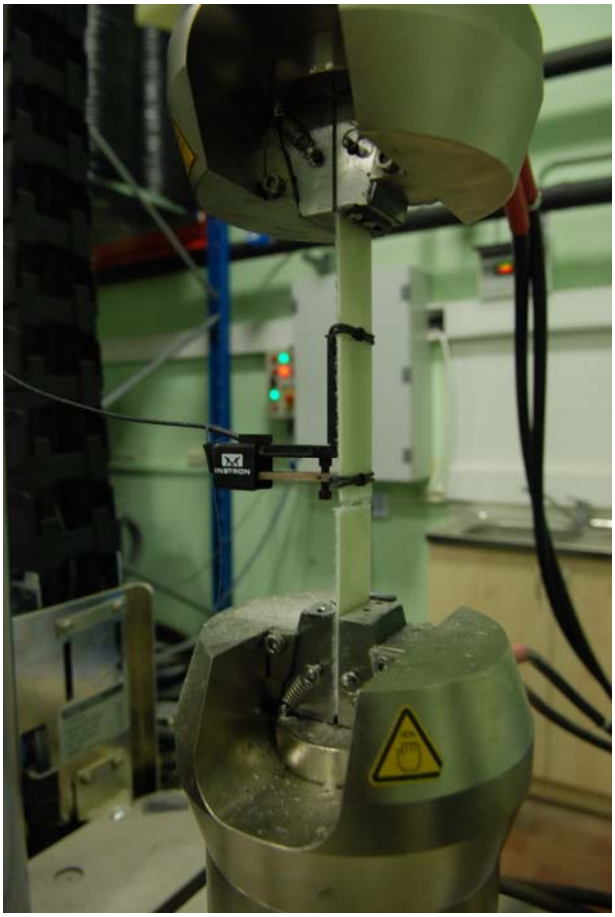

Figure 2.9. Material property identification test

2.2.4. Materials used in CFRP panels

Both CFRP panels were produced of IM7/8552 prepreg tapes. Small coupon identification tests in tension, compression and shear have been performed at Riga Technical University within the COCOMAT project according to the ASTM guidelines. The results of these identification tests are summarized in Table 2.6.

Table 2.6. Properties of the IM7/8552 prepreg composite

Property	Direction	Mean value
Elastic modulus (GPa) in tension	E_1^T	168
	E_{22}^T	9.1
Tensile strength (MPa)	σ_{11}^T	2414
	σ_{22}^T	51.0
Elastic modulus (GPa) in compression	E_{11}^C	145
	E_{22}^C	8.9
Compressive strength (MPa)	σ_{11}^C	972.3
	σ_{22}^C	269
Poisson's ratio	υ_{12}	0.33
Shear modulus (GPa)	G_{12}	5.58
Shear strength (MPa)	τ_{12}	116

2.3. Experimental methods

2.3.1. Imperfection measurement setup

A simple set-up has been created at Politecnico di Milano for measuring imperfections of the Type 2 and Type 3 specimens (Figure 2.10). The set-up consists of rotating table for measuring geometry in circumferential direction and vertical axis for measuring in longitudinal direction. The radial imperfections are recorded using Keyence LK-501 CCD laser displacement sensor, attached to the vertical axis. The resolution of this sensor is listed as 10 μm.

The set-up has been operated completely manually, performing series of radial imperfection scans along the circumference with 7.5 mm steps, and with vertical steps of 7.5 mm. This measurement grid corresponds to the finite element model used for numerical analysis and therefore the imperfect shape can be applied to the model directly, without employing any interpolation.

It should be noted that only the external surface of the cylinder could be measured, leaving the thickness variations unknown.

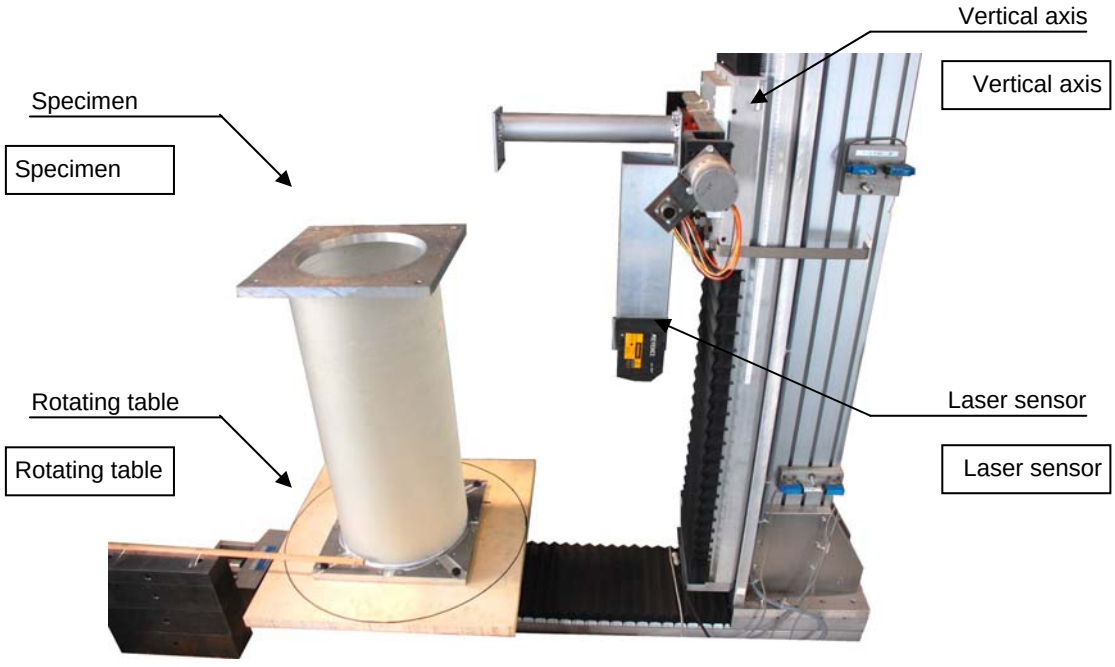

Figure 2.10. The set-up for imperfection measurements

2.3.2. Buckling tests at Riga Technical University

The experimental rig prepared at the laboratory of the RTU Institute of Materials and Structures consists of Instron 8802 hydraulic frame, Instron 3520 hydraulic pump, Instron 8800 Fast Track controller and a computer (see Figure 2.11). The load is being introduced through pair of grips and two steel plates. The top plate is fixed to the grip, while the bottom plate is spherically supported to distribute the load evenly when the specimen end plates aren't strictly parallel. The use of the spherical bearing also allows introduction of an eccentric load. The rotation centre of the spherical support is 150 mm above the bottom plate. The load cell that registers the axial load of the cylinder is located between the lower grip and the frame. This experimental rig also allows cyclic and pulse loading of the test specimens.

In order to monitor the post-buckling shapes of the cylinders, a basic interferometry set-up has been created. A moiré fringe with both line thickness and distance between lines of 1 mm was placed in front of the specimens. Placing a spotlight and a camera at different angles resulted in pictures with moiré patterns clearly indicating post-buckling shapes on the taken pictures (see Figure 2.12).

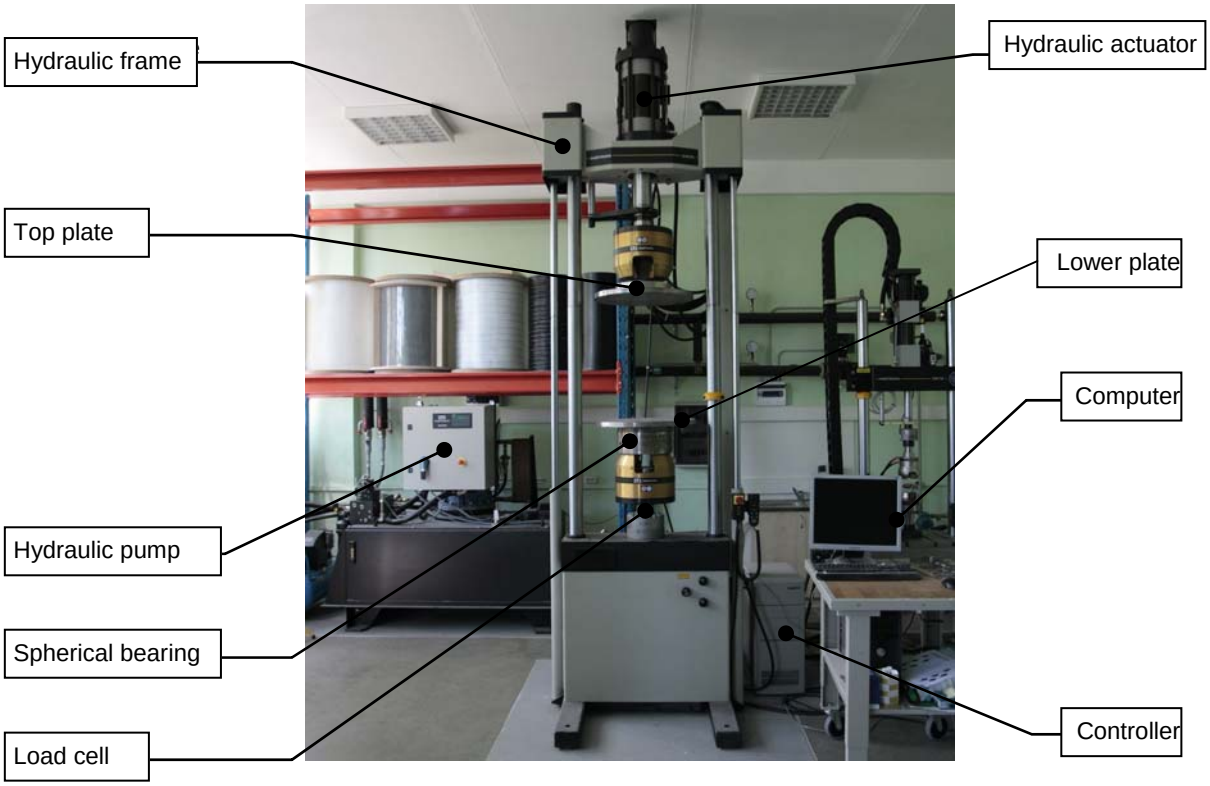

Figure 2.11. The set-up for buckling experiments at RTU

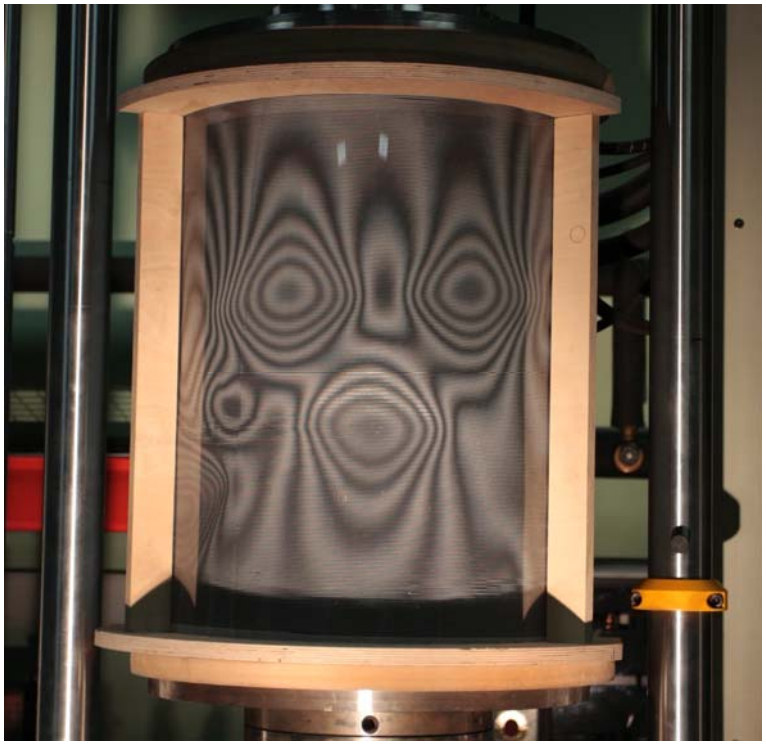

Figure 2.12. Buckling pattern of a cylinder registered by interferometry

2.3.3. Static buckling tests at Politecnico di Milano

The experimental rig prepared at the laboratory of the Politecnico di Milano consists of MTS 810 hydraulic frame, MTS TestStar IIs controller, Vishay A2 strain gauge signal conditioner, a custom built LVDT signal conditioner and a computer (see Figure 2.13). The load is being introduced through two steel plates. Bottom plate is resting on the actuator, while the top plate is spherically supported to distribute the load evenly when the specimen end plates aren't strictly parallel. The rotation centre of the spherical support is 40 mm above the top plate. The load cell that registers the axial load of the cylinder is located between the upper loading plate and the frame. This experimental rig also allows cyclic and pulse loading of the test specimens.

The displacement is being recorded by two LVDT displacement sensors, attached to the upper plate using purpose-made aluminium arms in opposite sides of the specimen. This way, the LVDT transducers measure the change in distance between the upper and lower plates. Seven back-to-back pairs of strain gauges are used to monitor the strains in axial direction.

The same interferometry technique has been used at Politecnico di Milano as at RTU.

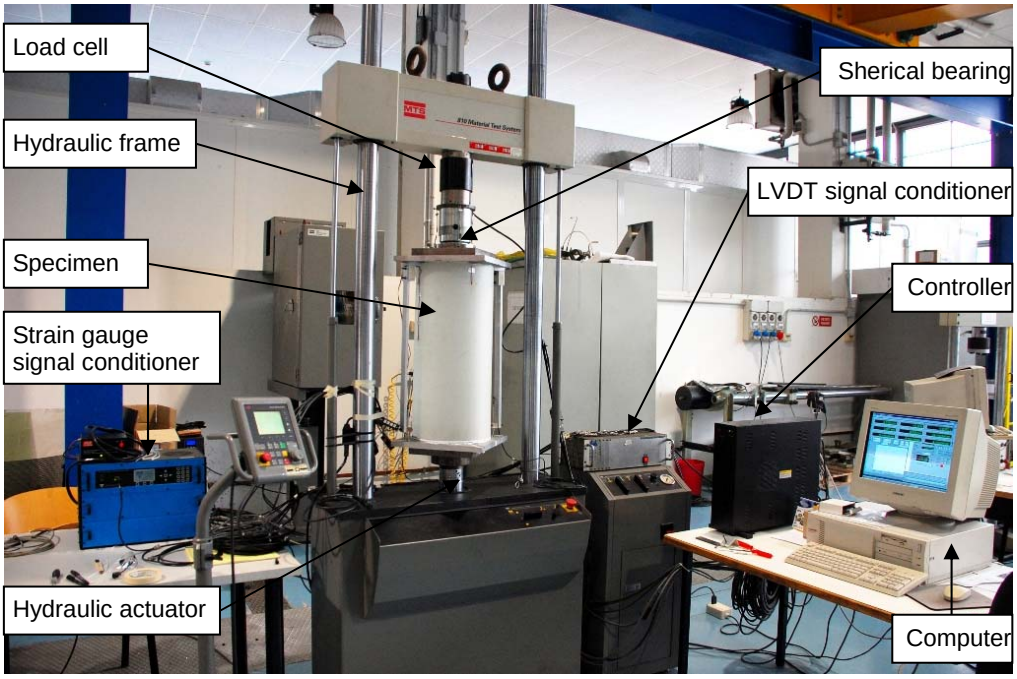

Figure 2.13. The set-up for buckling experiments at Politecnico di Milano

2.3.4. Dynamic buckling tests at Politecnico di Milano

There were two essentially different methods for dynamic buckling testing that were used at Politecnico di Milano. The hydraulic experimental rig that has been used for the static buckling tests could also be used for dynamic buckling tests with loading rate up to 70 mm/s. This moderate loading rate could be used for dynamic buckling tests with load durations of 50 ms and more. The other type of the dynamic buckling tests has been performed at the LAST crash laboratory facilities of Politecnico di Milano, using a drop tower. This method turned out to be less accurate, however, pulse durations of 10 ms could be achieved using this method. The simple drop-tower based dynamic buckling test setup is presented on Figure 2.14 and Figure 2.15. It consisted of the drop-tower columns and the dropping mass, with the release mechanism. The specimen has been clamped to the hard floor, and a load cell has been placed on top of it. To decrease the peak load during the test, a piece of steel honeycomb has been placed on top of the load cell. An accelerometer has been attached to the bottom of the load cell to monitor the movement of the upper end of the cylinder. A dropping mass of 42.2 kg has been used for the tests, and the total mass of the load cell and the plates resting on the end of the cylinder was 57.6 kg. The strain gauge, load cell and accelerometer measurements have been recorded with frequency of 12.5 kHz, and the tests have been filmed using a high-speed camera with frame rate of 2000 fps.

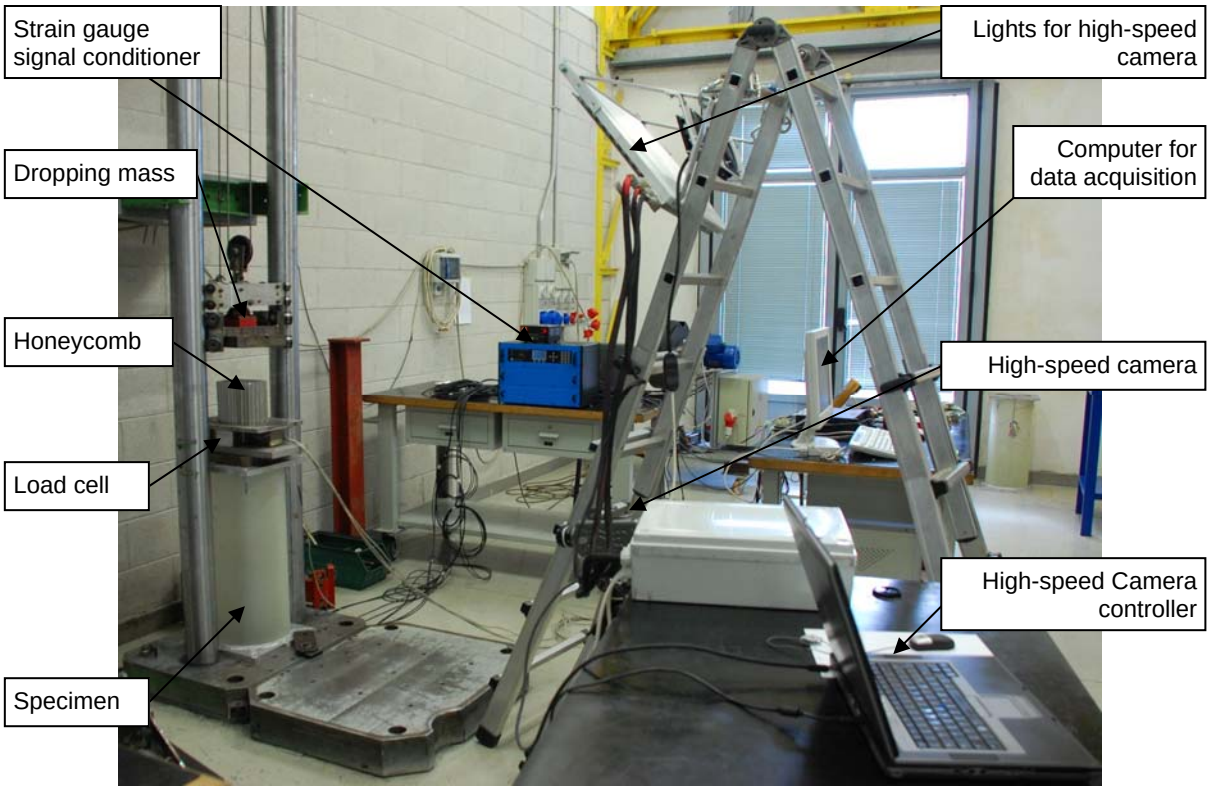

Figure 2.14. The set-up for dynamic buckling experiments at Politecnico di Milano

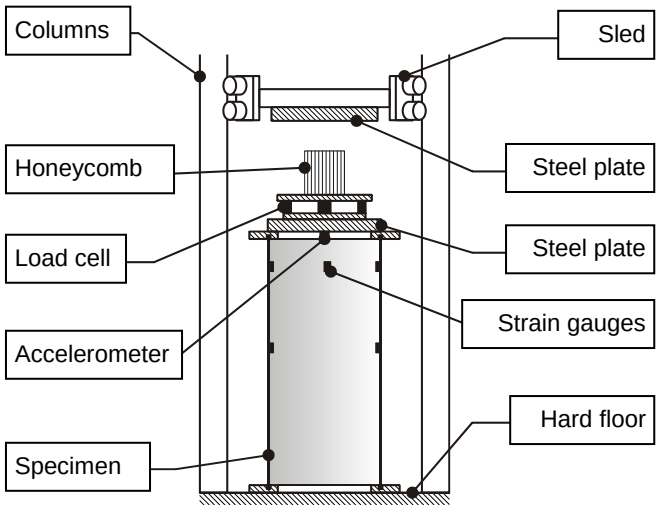

Figure 2.15. The set-up for dynamic buckling experiments at Politecnico di Milano

2.4. Numerical methods

Finite element analysis has shown its versatility and efficiency in vast number of studies. The classical analytical methods are constrained by the need to describe the structures, loads and fields with mathematical functions, and can be efficiently used only in case of simple structures. The numerical methods involving discretization of the structure in small elements allow analysis of structures of virtually any shape and complexity.

Development of the computers and finite element software over the decades has allowed not only linear stress, strain and deformation estimations, but also elaborate non-linear simulations that account for geometrical and material non-linearities, material degradation and fracture. Use of the linear analyses is very computationally efficient and can provide useful information about the loaded structure. However, non-linear simulations can capture the buckling and post-buckling behaviour even if it occurs as a snap-through. Explicit dynamic analyses can be especially efficient compared to the implicit solution methods in case of such sudden snap-through buckling, and are preferred buy many researchers for buckling analysis of shells. In present thesis, the non-linear ABAQUS/Explicit is the main numerical tool for buckling simulations of the unstiffened and stiffened composite shells. The linear capabilities of ABAQUS have been employed for linear buckling analyses and calculation of the eigenmodes that were used as imperfection shapes in some steps of the research.

2.4.1. Linear eigenvalue buckling analysis

Eigenvalue buckling analysis:

- is generally used to estimate the critical (bifurcation) load of "stiff" structures;
- is a linear perturbation procedure;
- can be the first step in an analysis of an unloaded structure, or it can be performed after the structure has been preloaded—if the structure has been preloaded, the buckling load is calculated from the preloaded state;
- can be used in the investigation of the imperfection sensitivity of a structure.

In an eigenvalue buckling problem we look for the loads for which the model stiffness matrix becomes singular, so that the problem $K^{MN}v^{M} = 0$ has nontrivial solutions. K^{MN} is the tangent stiffness matrix when the loads are applied, and the v^{M} are nontrivial displacement solutions. The applied loads can consist of pressures, concentrated forces, nonzero prescribed displacements, and/or thermal loading.

Eigenvalue buckling is generally used to estimate the critical buckling loads of stiff structures (classical eigenvalue buckling). Stiff structures carry their design loads primarily by axial or membrane action, rather than by bending action. Their response usually involves very little deformation prior to buckling. A simple example of a stiff structure is the Euler column, which responds very stiffly to a compressive axial load until a critical load is reached, when it bends suddenly and exhibits a much lower stiffness. However, even when the response of a

structure is nonlinear before collapse, a general eigenvalue buckling analysis can provide useful estimates of collapse mode shapes.

The buckling loads are calculated relative to the base state of the structure. If the eigenvalue buckling procedure is the first step in an analysis, the initial conditions form the base state; otherwise, the base state is the current state of the model at the end of the last general analysis step. Thus, the base state can include preloads ("dead" loads), P^N. The preloads are often zero in classical eigenvalue buckling problems.

If geometric nonlinearity was included in the general analysis steps prior to the eigenvalue buckling analysis, the base state geometry is the deformed geometry at the end of the last general analysis step. If geometric nonlinearity was omitted, the base state geometry is the original configuration of the body.

An incremental loading pattern, Q^N, is defined in the eigenvalue buckling prediction step. The magnitude of this loading is not important; it will be scaled by the load multipliers, λ_i, found in the eigenvalue problem:

$$(K_0^{NM} + \lambda_i K_\Delta^{NM}) v_i^M = 0, \tag{3.1}$$

where K_0^{NM} is the stiffness matrix corresponding to the base state, which includes the effects of the preloads, P^N (if any); K_Δ^{NM} is the differential initial stress and load stiffness matrix due to the incremental loading pattern, Q^N; λ_i are the eigenvalues; v_i^M are the buckling mode shapes (eigenvectors); *M* and *N* refer to degrees of freedom *M* and *N* of the whole model; and *i* refers to the *i*th buckling mode.

The critical buckling loads are then $P^N + \lambda_i Q^N$. Normally, the lowest value of λ_i is of interest. The preload pattern, P^N, and perturbation load pattern, Q^N, may be different. For example, P^N might be thermal loading caused by temperature changes, while Q^N is caused by application of pressure. The buckling mode shapes, v_i^M, are normalized vectors and do not represent actual magnitudes of deformation at critical load. They are normalized so that the maximum displacement component has a magnitude of 1.0. If all displacement components are zero, the maximum rotation component is normalized to 1.0. These buckling mode shapes are often the most useful outcome of the eigenvalue analysis, since they predict the likely failure mode of the structure.

Abaqus/Standard can extract eigenvalues and eigenvectors for symmetric matrices only; therefore, K_0^{NM} and K_Δ^{NM} are symmetrized. If the matrices have significant

unsymmetric parts, the eigenproblem may not be exactly what is expected to solve (ABAQUS Documentation).

2.4.2. Non-linear static buckling analysis

Post-buckling analysis is a nonlinear problem that usually involves thousands of variables. In terms of these variables the equilibrium equations obtained by discretizing the virtual work equation can be written symbolically as

$$F^N(u^M) = 0, \tag{3.2}$$

where F^N is the force component conjugate to the N^{th} variable in the problem and u^M is the value of the M^{th} variable. The basic problem is to solve the equation (3.2) for the u^M throughout the history of interest.

Newton's method is being generally used as a numerical technique for solving the nonlinear equilibrium equations. The basic formalism of Newton's method is as follows. Assume that, after iteration *i*, an approximation u_i^M, to the solution has been obtained. Let c_{i+1}^M be the difference between this solution and the exact solution to the discrete equilibrium equation (3.2). This means that

$$F^N(u_i^M + c_{i+1}^M) = 0. \tag{3.3}$$

Expanding the left-hand side of this equation in a Taylor series about the approximate solution u_i^M then gives

$$F^N(u_i^M) + \frac{\partial F^N}{\partial u^P}(u_i^M)c_{i+1}^P + \frac{\partial^2 F^N}{\partial u^P \partial u^Q}(u_i^M)c_{i+1}^P c_{i+1}^Q + \ldots = 0. \tag{3.4}$$

If u_i^M is a close approximation to the solution, the magnitude of each c_{i+1}^M will be small, and so all but the first two terms above can be neglected giving a linear system of equations:

$$K_i^{NP} c_{i+1}^P + -F_i^N, \tag{3.5}$$

where $K_i^{NP} = \frac{\partial F^N}{\partial u^P}(u_i^M)$ is the Jacobian matrix and $F_i^N = F^N(u_i^M)$.

The next approximation to the solution is then $u_{i+1}^M = u_i^M + c_{i+1}^M$, and the iteration continues. Convergence of Newton's method is best measured by ensuring that all entries in F_i^N and all entries in c_{i+1}^N are sufficiently small. (ABAQUS Documentation)

2.4.3. Non-linear dynamic buckling analysis

An explicit dynamic analysis:

- is computationally efficient for the analysis of large models with relatively short dynamic response times and for the analysis of extremely discontinuous events or processes;
- allows for the definition of very general contact conditions;
- uses a consistent, large-deformation theory—models can undergo large rotations and large deformation;
- can be used to perform an adiabatic stress analysis if inelastic dissipation is expected to generate heat in the material;
- can be used to perform quasi-static analyses with complicated contact conditions;
- allows for either automatic or fixed time incrementation to be used.

The explicit dynamics procedure performs a large number of small time increments efficiently. An explicit central-difference time integration rule is used; each increment is relatively inexpensive (compared to the implicit direct-integration dynamic analysis procedure) because there is no solution for a set of simultaneous equations. The explicit central-difference operator satisfies the dynamic equilibrium equations at the beginning of the increment, *t*; the accelerations calculated at time *t* are used to advance the velocity solution to time $t + \Delta t/2$ and the displacement solution to time $t + \Delta t$.

The explicit dynamics analysis procedure is based upon the implementation of an explicit integration rule together with the use of diagonal ("lumped") element mass matrices. The equations of motion for the body are integrated using the explicit central-difference integration rule

$$\dot{u}^N_{(i+\frac{1}{2})} = \dot{u}^N_{(i-\frac{1}{2})} + \frac{\Delta t_{(i+1)} + \Delta t_{(i)}}{2} \ddot{u}^N_{(i)}, \tag{3.6}$$

$$u^N_{(i+1)} = u^N_{(i)} + \Delta t_{(i+1)} \dot{u}^N_{(i+\frac{1}{2})}, \tag{3.7}$$

where u^N is a degree of freedom (a displacement or rotation component) and the subscript *i* refers to the increment number in an explicit dynamics step. The central-difference integration operator is explicit in the sense that the kinematic state is advanced using known values of $\dot{u}^N_{(i-1/2)}$ and $\ddot{u}^N_{(i)}$ from the previous increment.

The explicit integration rule is quite simple but by itself does not provide the computational efficiency associated with the explicit dynamics procedure. The key to the computational efficiency of the explicit procedure is the use of diagonal element mass matrices because the accelerations at the beginning of the increment are computed by

$$\ddot{u}_{(i)}^{N} = \left(M^{NJ}\right)^{-1}\left(P_{(i)}^{J} - I_{(i)}^{J}\right), \tag{3.8}$$

where M^{NJ} is the mass matrix, P^{J} is the applied load vector, and I^{J} is the internal force vector. A lumped mass matrix is used because its inverse is simple to compute and because the vector multiplication of the mass inverse by the inertial force requires only *n* operations, where *n* is the number of degrees of freedom in the model. The explicit procedure requires no iterations and no tangent stiffness matrix. The internal force vector, I^{J}, is assembled from contributions from the individual elements such that a global stiffness matrix need not be formed.

The explicit integration scheme requires nodal mass or inertia to exist at all activated degrees of freedom unless constraints are applied using boundary conditions. More precisely, a nonzero nodal mass must exist unless all activated translational degrees of freedom are constrained and nonzero rotary inertia must exist unless all activated rotational degrees of freedom are constrained. Nodes that are part of a rigid body do not require mass, but the entire rigid body must possess mass and inertia unless constraints are used. Nodes that belong to Eulerian elements also do not require mass, since the surrounding Eulerian elements may be void at some time during the simulation. When degrees of freedom at a node are activated by elements with a nonzero mass density (e.g., solid, shell, beam) or mass and inertia elements, a nonzero nodal mass or inertia occurs naturally from the assemblage of lumped mass contributions. (ABAQUS Documentation)

2.4.4. Benchmarking of Finite element codes

Benchmarking of commercially available finite element analysis codes ANSYS, ABAQUS and LS-DYNA, capable of nonlinear buckling and post-buckling analysis, has been performed and results presented in (Eglitis and Kalnins, 2007). Results of two post-buckling experiments have been used for this task. Both experiments were performed on stiffened, curved carbon fibre reinforced plastic panels. One of the experiments (Panel 1) was performed by Israel Institute of Technology (Technion) (Abramovich et al., 2003; Abramovich and Weller, 2005), and the other experiment (Panel 2) was tested at the German

Aerospace Center (DLR) (Degenhardt et al., 2006; 2008) within the EC FP-6 project COCOMAT (www.cocomat.de).

There were three FE models created for each of the panels using commercially available FE software ABAQUS, ANSYS and LS-DYNA. S4, S4R and S8R elements have been used for this benchmark to evaluate performance of ABAQUS/Standard implicit non-linear analysis. Four-node Shell181 and eight-node Shell281 elements have been used to test ANSYS, and Shell163 element has been used for explicit analysis in ANSYS/LS-DYNA.

To avoid convergence problems in ABAQUS non-linear analysis a stabilization using dissipated energy fraction was used. ANSYS did not have such damping stabilization option and therefore another approach was used to deal with convergence problems at bifurcation points: a geometrical imperfection is introduced before the non-linear analysis to induce the buckling shape. First local and first global eigenmodes were used as the imperfection to obtain solution. However, ANSYS solution remained unstable in all cases. For benchmark verification of LS-DYNA the ANSYS pre-processor has been utilised therefore saving the modelling time and avoiding human errors due transformation of the input data. ANSYS/LS-DYNA automatically converts the implicit Shell181 elements into explicit thin structural Shell163 elements. After performing the implicit analysis, redefinition of the shell real constants and loading configurations was performed in order to run the explicit analysis.

Load-shortening curves obtained by FE simulations and experimentally obtained curve of Panel 1 are presented in Figure 2.16 (a). The implicit solvers all gave very similar results, overestimating panel's stiffness and subsequently critical load for 10%. However, the critical displacement predictions were more accurate. The explicit ANSYS/LS-DYNA also resulted in overestimation of stiffness, yet the critical force obtained was 13% underestimated. It was necessary to increase dissipated energy fraction above the one found as optimal in preliminary studies performed on Panel 2 to maintain stability of solution in ABAQUS.

Results of implicit FE predictions and experiment of Panel 2 are presented in Figure 2.16 (b). The accuracy of implicit analysis is much higher in this case, predicting global buckling modes at 5% higher load than obtained experimentally. ABAQUS S8R element produced most accurate prediction of critical displacements. Explicit ANSYS/LS-DYNA was even less accurate predicting critical load, underestimating it by 27%. It was impossible to solve the problem past the buckling point with ANSYS Shell181 element because of convergence problems. However, it produced accurate results before the stop of solution.

The typical obtained buckling mode shape sequence for Panel 2 is presented in Figure 2.17. The same buckling mode shape sequence was observed during the experiment.

ABAQUS finite element package and its element S4R, which can be used with both implicit and explicit solvers proved to be the most versatile finite element package for modelling of the buckling phenomena. It allows achieving the highest accuracy obtained in the benchmarking study at relatively low computing time.

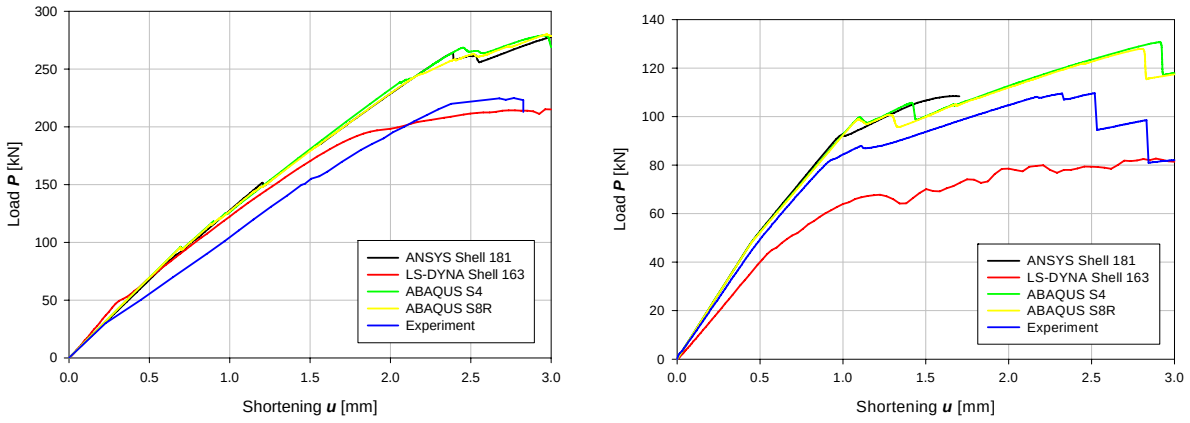

Figure 2.16. Comparison of experimental and numerical results
(a) – Panel 1; (b) – Panel 2

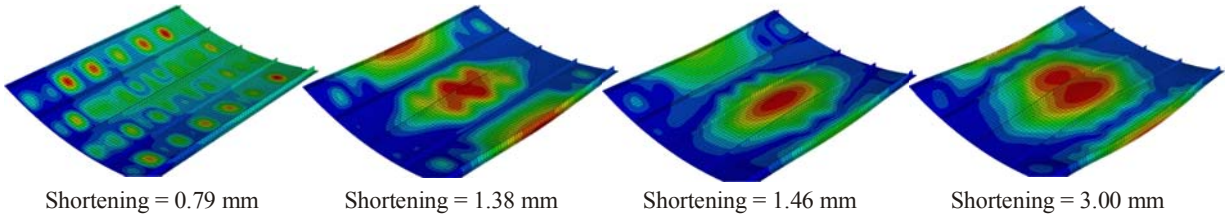

Figure 2.17. Buckling mode shape sequence for Panel 2

3. STATIC BUCKLING OF GFRP CYLINDERS

3.1. Imperfection sensitivity of GFRP cylinders

3.1.1. Sensitivity to eigenmode-shaped imperfections

Imperfection sensitivity analysis of composite cylinders has been performed numerically and presented in (Eglitis et al., 2007; 2009). Numerical models corresponding to the four designs of Type 1 specimens have been created for this imperfection sensitivity study. Linear eigenvalue analysis has been used for calculation of eigenmodes that were applied to the model as "worst case scenario" imperfections. Eigenmodes were calculated for all of the specimens, and their shapes were used to introduce geometrical imperfections. A representation of the spherical bearing used in the experiments was included in the finite element models and therefore the buckling modes cover only one side of the cylinder. As the eigenvalues are very closely spaced, one of the first 10 eigenmodes was chosen for introduction of the imperfections, so the buckling pattern would cover largest part of the shell surface. Imperfection amplitudes were 1/1, 1/2, 1/4 and 1/8 of the skin thickness t.

Adding initial imperfections to the model decreases the numerically obtained buckling loads and confirms that the drop of the critical load depends on the shape and the magnitude of the imperfections. Fractions of the shell thickness were used as the amplitudes in this study. Imperfection amplitude of $t/8$ resulted in a 30 % drop comparing to the intact model, and drop up to 59 % has been observed with the imperfection amplitude equal to the skin thickness t. The buckling loads for all models of Type 1 specimen with different imperfection amplitudes are summarized in Table 3.1. An example of numerically obtained load-shortening curves for Type 1 composite cylinders with different imperfection amplitudes is presented in Figure 3.1, and change of buckling mode shapes with increase of the initial imperfection amplitude is presented in Figure 3.2.

Table 3.1. Critical loads for the models considered

	Model 150-400	**Model 150-560**	**Model 150-660**	**Model 250-660**
Analytical result	84.09 kN	84.09 kN	84.09 kN	84.09 kN
No imperfections	63.14 kN	64.36 kN	64.52 kN	66.94 kN
Imperfection amplitude *t*/8	44.39 kN	44.99 kN	45.27 kN	48.46 kN
Imperfection amplitude *t*/4	37.09 kN	37.15 kN	36.90 kN	39.54 kN
Imperfection amplitude *t*/2	34.12 kN	31.82 kN	32.47 kN	34.80 kN
Imperfection amplitude *t*	33.31 kN	28.59 kN	28.18 kN	31.97 kN

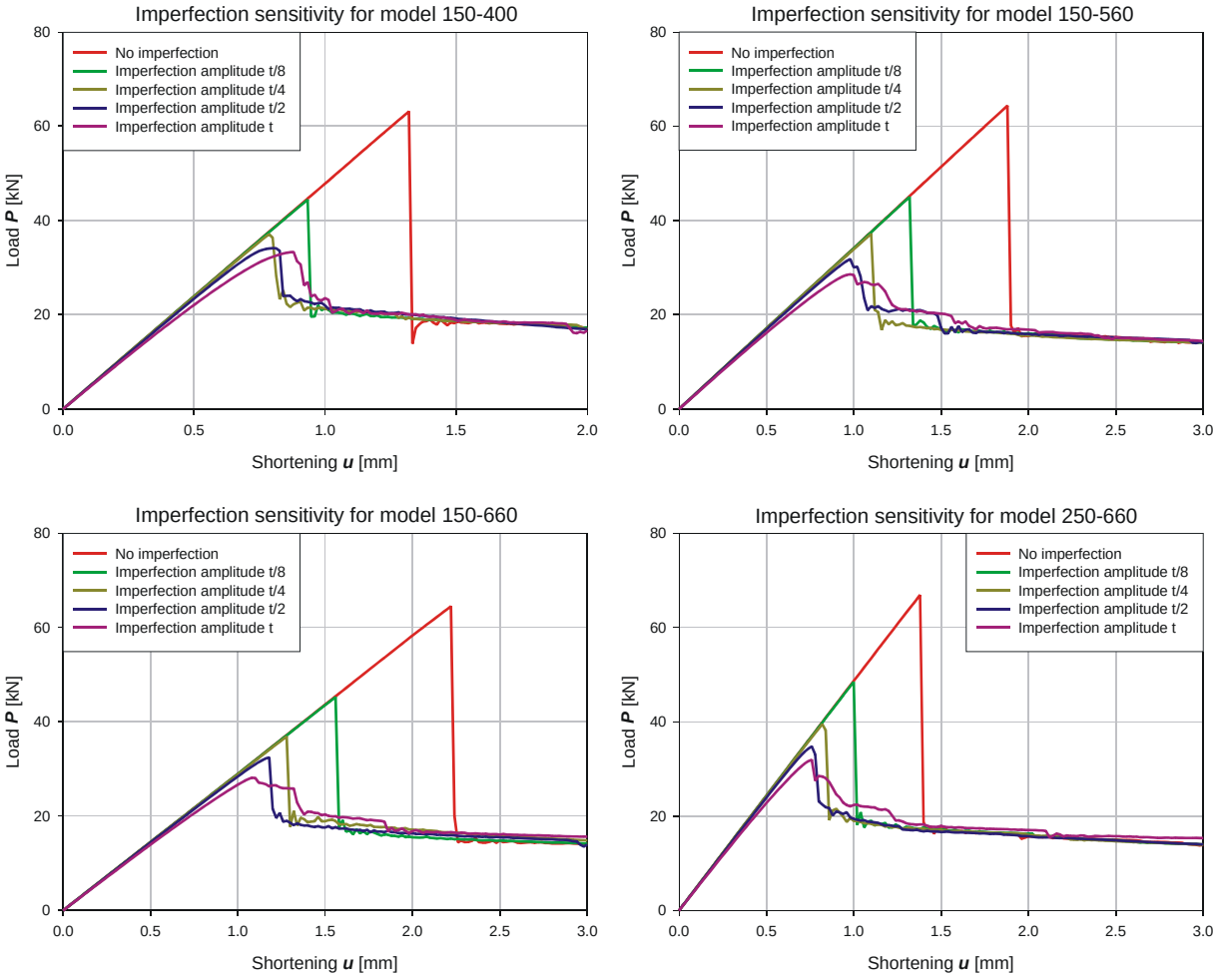

Figure 3.1. Numerical load-shortening curves for different imperfection magnitudes

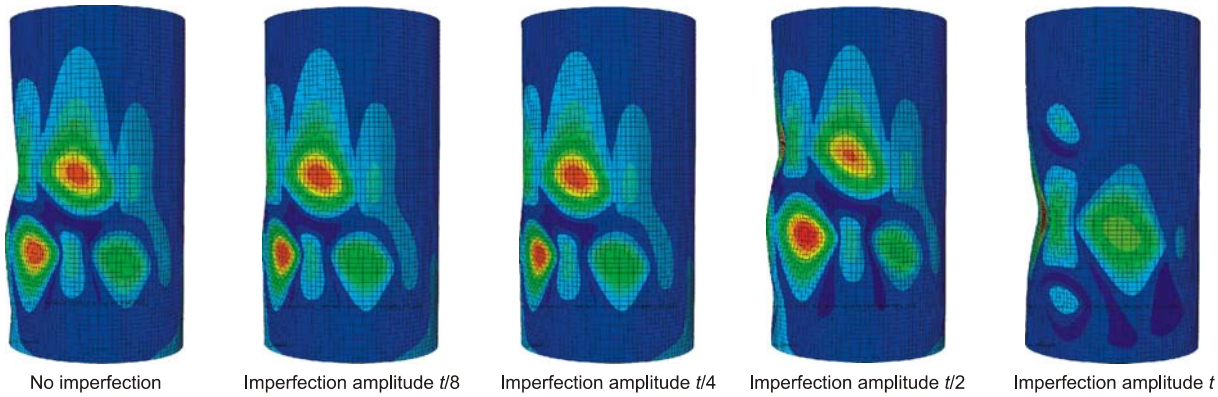

Figure 3.2. Influence of boundary conditions and magnitude of initial imperfections on post-buckling shape of the cylinder (results shown only for model 150-560)

3.1.2. Measurement of Type 2 specimen imperfections

Imperfections of the Type 2 specimens have been measured using the set-up described in Chapter 2.3.1. First, the measured data points are transformed in Cartesian coordinate system. To suppress the noise that arises from different random factors influencing each measurement, the data is smoothed, calculating the radial imperfection of each point as the average of this point and eight closest points.

Then, a computer code written in MATLAB is used to perform the best-fit cylinder approximation described in the Chapter 1.2.2. A modified version of this code is used to find the best-fit cone approximation, as the Type 2 specimens have been produced using slightly conical, machined mandrel. The parameters of the approximations and the deviations of the measured imperfection data are summarized in Table 3.2, and the linear buckling loads for the corresponding best-fit shapes are presented as well. The raw measured imperfection data is presented in Figure 3.3, the measured imperfection data related to the best-fit cylinders and best-fit cones is plotted in Figure 3.4 and Figure 3.5 respectively.

Table 3.2. Imperfection statistics for Type 2 specimens

	Nominal cylinder		**Best Fit cylinder**		**Best Fit cone**	
	Type 2-1	Type 2-2	Type 2-1	Type 2-2	Type 2-1	Type 2-2
R_1 [mm]	150	150	148.7	149.4	150	150.6
R_2 [mm]	150	150	148.7	149.4	147.4	148.2
t [mm]	0.85	0.85	0.85	0.85	0.85	0.85
E_1=E_2 [GPa]	15.75	15.75	15.75	15.75	15.75	15.75
ν	0.13	0.13	0.13	0.13	0.13	0.13
Δ_{max} [mm]	3.57	1.3776	2.48	1.47	2.14	0.51
Δ_{min} [mm]	-8.09	-2.81	-3.75	-1.59	-2.41	-0.54
$\Delta_{average}$ [mm]	2.23	0.84	0.79	0.62	0.52	0.14
P_{cr} [kN]	41.54	41.54	41.52	41.53	41.52	41.53
u_{cr} [mm]	2.17	2.17	2.19	2.18	2.19	2.18

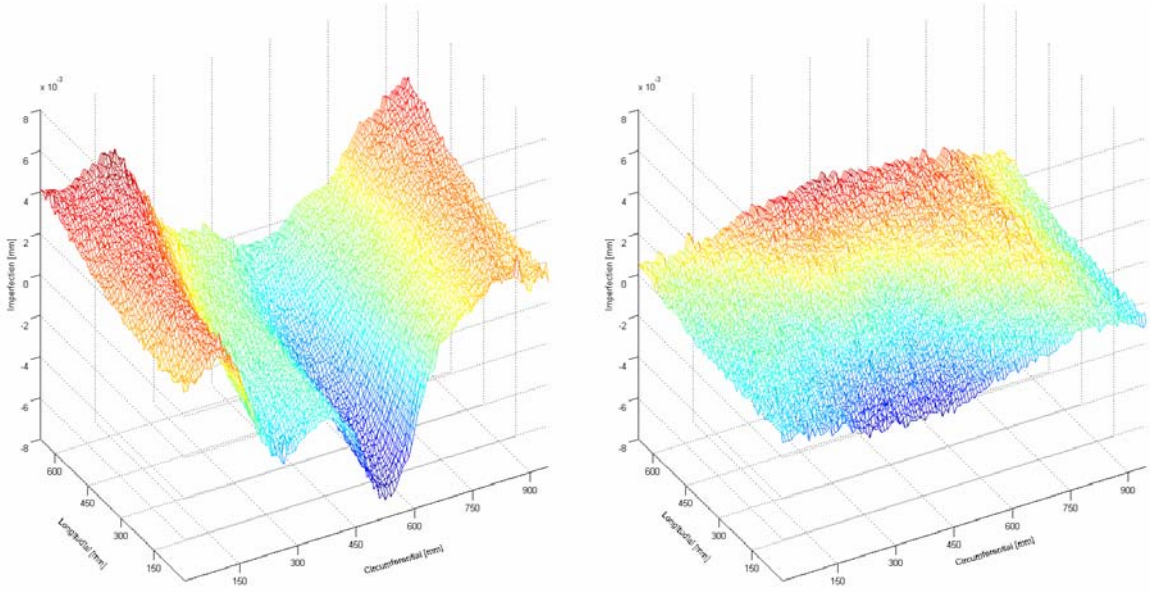

(a) (b)

Figure 3.3. Raw imperfection data
(a) – specimen **Type 2-1** and (b) – specimen **Type 2-2**

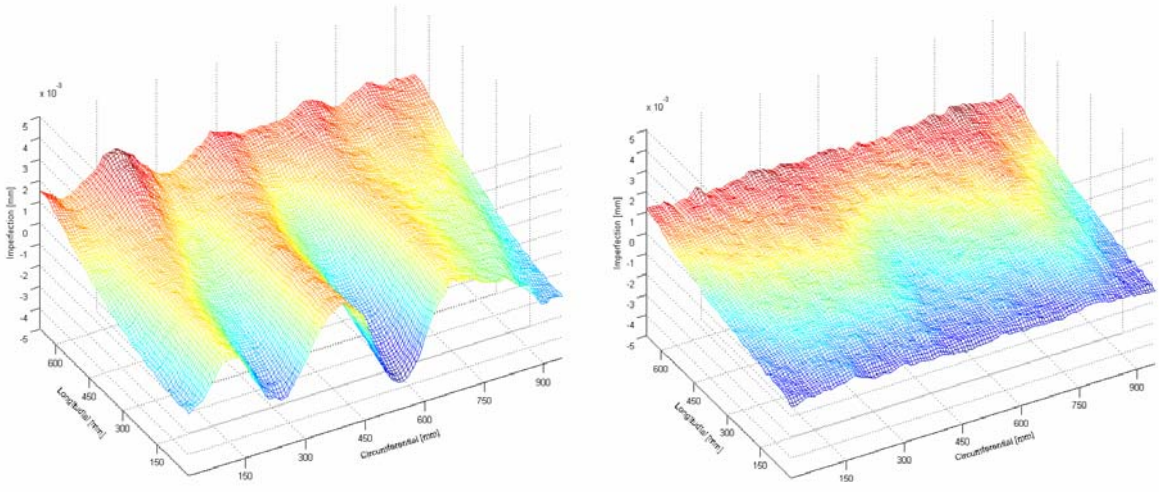

(a) (b)

Figure 3.4. Imperfection data related to the best-fit cylinder
(a) – specimen **Type 2-1** and (b) – specimen **Type 2-2**

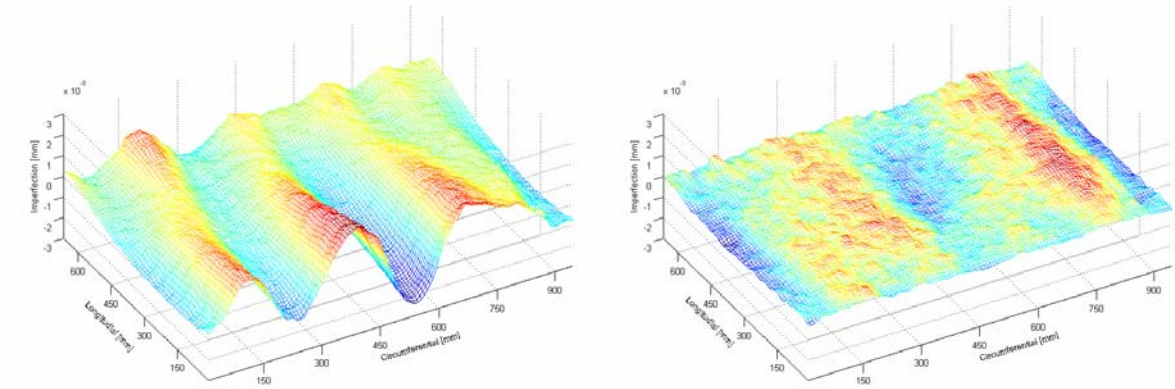

(a) (b)

Figure 3.5. Imperfection data related to the best-fit cone
(a) – specimen **Type 2-1** and (b) – specimen **Type 2-2**

3.1.3. Measurement of Type 3 specimen imperfections

Imperfections of the Type 3 specimens have been measured using the set-up described in Chapter 2.3.1 and processed in the same manner as in case of the Type 2 specimens. The parameters of the approximations and the deviations of the measured imperfection data are summarized in Table 3.3, and the linear buckling loads for the corresponding best-fit shapes are presented as well. The raw measured imperfection data is presented in Figure 3.6, the measured imperfection data related to the best-fit cylinders and best-fit cones is plotted in Figure 3.7 and Figure 3.8 respectively.

Table 3.3. Imperfection statistics for Type 3 specimens

	Nominal cylinder		**Best Fit cylinder**		**Best Fit cone**	
	Type 3-1	Type 3-2	Type 3-1	Type 3-2	Type 3-1	Type 3-2
R_1 [mm]	150	150	150.6	149.2	150.0	148.8
R_2 [mm]	150	150	150.6	149.2	151.2	149.6
t [mm]	1.22	1.2	1.22	1.2	1.22	1.2
E_1 [GPa]	18.66	18.66	18.66	18.66	18.66	18.66
ν	0.16	0.16	0.16	0.16	0.16	0.16
Δ_{max} [mm]	3.72	4.71	1.06	0.77	0.83	0.44
Δ_{min} [mm]	-2.02	-4.64	-0.87	-1.29	-0.50	-0.89
$\Delta_{average}$ [mm]	0.88	2.34	0.34	0.21	0.12	0.09

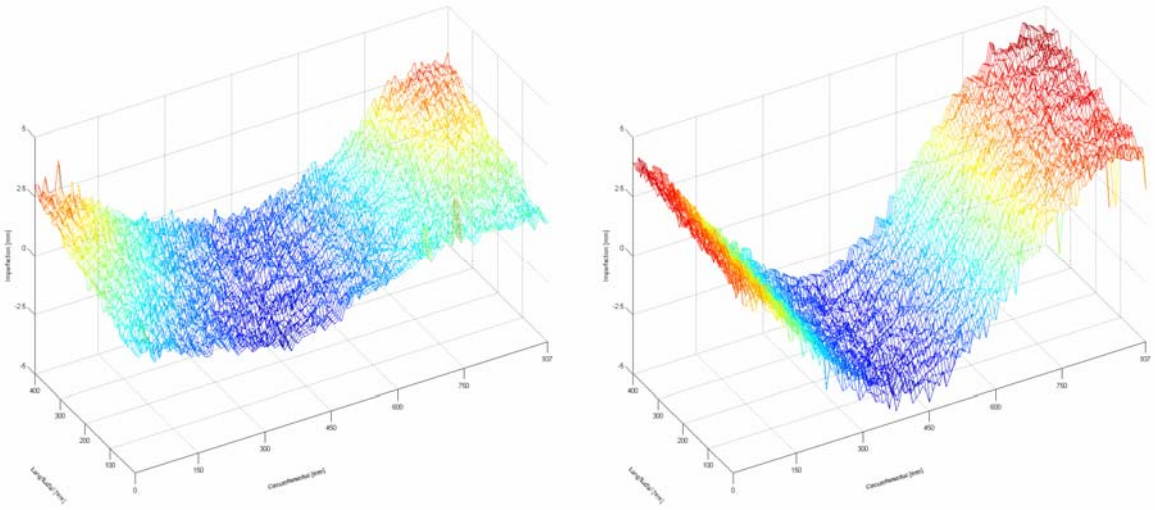

(a) (b)

Figure 3.6. Raw imperfection data
(a) – specimen **Type 3-1** and (b) – specimen **Type 3-2**

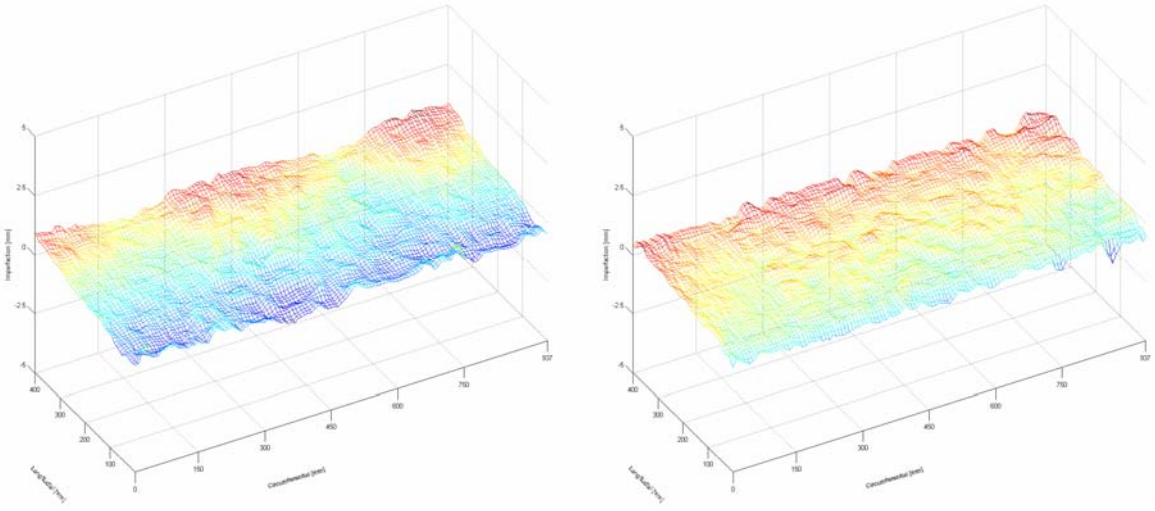

(a) (b)

Figure 3.7. Imperfection data related to the best-fit cylinder
(a) – specimen **Type 3-1** and (b) – specimen **Type 3-2**

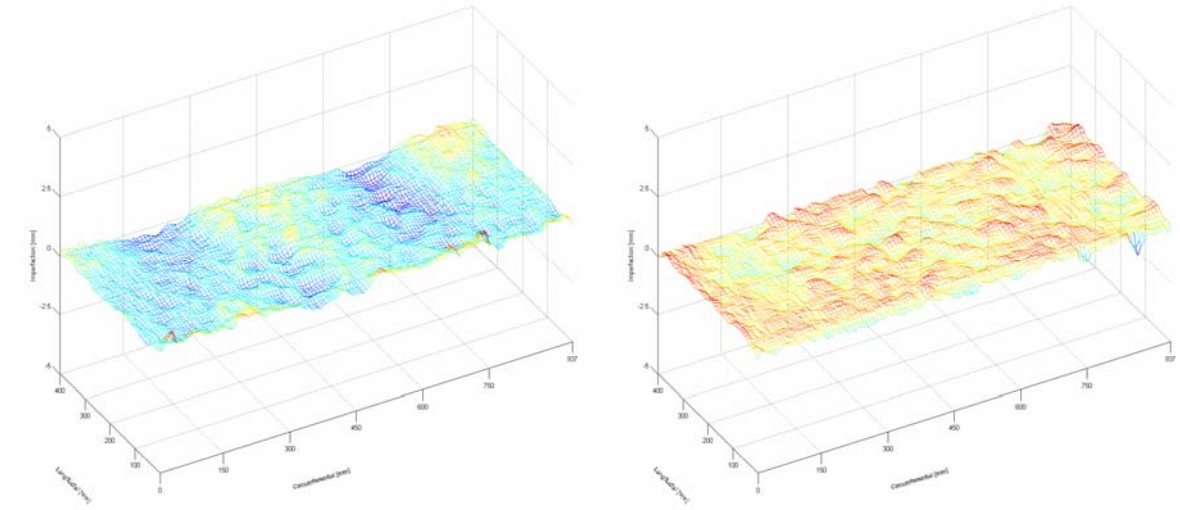

(a) (b)

Figure 3.8. Imperfection data related to the best-fit cone
(a) – specimen **Type 3-1** and (b) – specimen **Type 3-2**

3.1.4. Sensitivity to the measured imperfection shapes

The measured imperfections of Type 2 specimens were used to update the ABAQUS numerical models of the cylinders. First, a conical approximation of the measured imperfections has been found. From the Table 3.2 it can be seen that this conical component of the imperfections has virtually no influence on the buckling loads.

As the lowest calculated eigenmode for the cylinders under consideration has an axisymmetric shape, a hypothesis has been made that the imperfections varying along the vertical axis have much more influence than the imperfections varying along the circumference. To verify this hypothesis, the imperfection data has been also decomposed in two components: one component is created by approximating each vertical line of measurements as a straight line, therefore eliminating the curvature along the axial direction. The second component is the rest of imperfections, so that the combination of both components results in the measured imperfect shape. The 'straight line' components of the Type 2 specimen imperfections are plotted in Figure 3.9 and the components of remaining imperfections are plotted in Figure 3.10.

The non-linear buckling analysis has been performed for numerical models with perfect shape, imperfect shape and each of the imperfection components mentioned before. The load-shortening curves for both shapes are presented in Figure 3.11. The buckling load for nominal, perfect cylinders is 41.44 kN. When the measured imperfections are included in

the numerical model, the buckling load is 25.14 kN for the specimen Type 2-1 and 27.69 kN for the specimen Type 2-2, which is 39% and 32% lower than in case of a perfect shape. The inclusion of the straight line imperfection component only in the numerical model results in buckling loads of 37.41 kN and 40.42 kN respectively, which means the drop in buckling load of 9.7% and 2.5% comparing to the 'perfect' model, while the second component of the imperfections, which has much lower amplitude, results in buckling loads of 26.46 kN (36% lower) and 27.65 kN (32% lower).

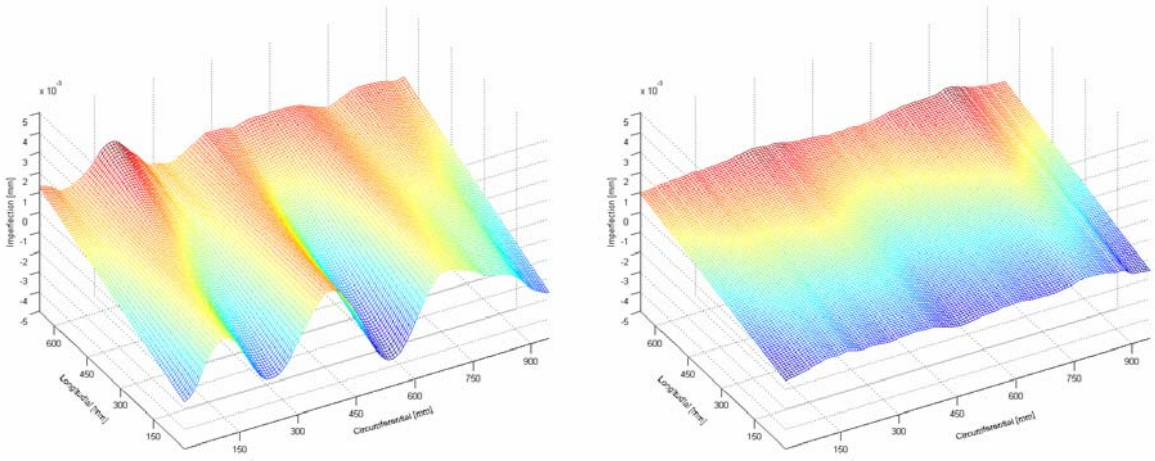

(a) (b)

Figure 3.9. Imperfection data approximated as straight lines
(a) – specimen **Type 2-1** and (b) – specimen **Type 2-2**

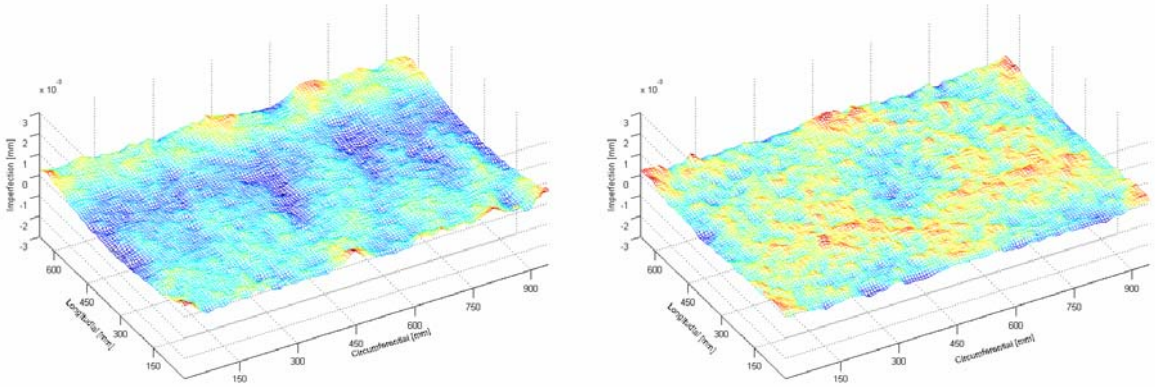

(a) (b)

Figure 3.10. The remaining component of the imperfections
(a) – specimen **Type 2-1** and (b) – specimen **Type 2-2**

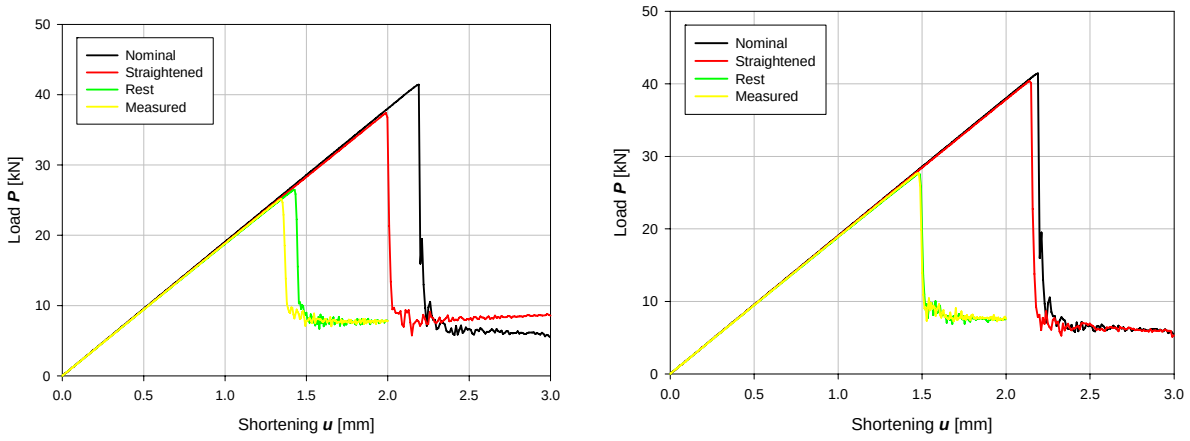

(a) (b)

Figure 3.11. The load-shortening curves for numerical models of the specimens (a) – specimen **Type 2-1** and (b) – specimen **Type 2-2**

3.1.5. Concluding remarks

The numerical imperfection sensitivity studies reveal the important effect of the initial imperfections on the buckling behaviour of axially compressed cylinders. As it is seen in Figure 3.1, adding imperfections with amplitude of 1/8 cylinder wall's thickness decreases the numerically obtained buckling load by 30% and further increase of the imperfection amplitude can lower the buckling load as to 41% of the buckling load for perfect cylinder, in case under consideration. This extreme imperfection sensitivity can be considered the most important reason for such a discrepancy between the experimental and numerical results for Type 1 GFRP specimen.

The imperfection sensitivity study performed numerically using the imperfection data of the Type 2 specimens shows that the imperfection shape influences the buckling behaviour of a cylinder even more than the imperfection magnitude. The substantially different imperfection shapes of the specimens Type 2-1 and Type 2-2 resulted in similar knock-down factors, despite the difference in the magnitudes of the shapes (see Table 3.4).

Furthermore, the imperfections of the Type 2 specimens have been decomposed in several components and the influence of these components on the buckling behaviour has been assessed. The conical component of the imperfection did not alter the buckling load, as did not the slight change in the radius of the cylinder. Decomposition of the measured imperfection in two components, of which one had greater magnitude, but no curvature in axial direction, while the other had smaller magnitude and contained all of the curvature in axial direction proved that the imperfection shapes that does not incorporate the mentioned

curvatures have virtually no influence on the buckling load (see Figure 3.9, Figure 3.10 and Figure 3.11).

Finally, the measurement of the geometric imperfections of the Type 3 specimens combined with careful preparation of the specimens and executions of the experiments allowed to obtain good agreement between the experimental and numerical results, both in terms of buckling loads and buckling shapes, with difference of numerically and experimentally obtained buckling loads not exceeding 2 %.

3.2. Axial compression of GFRP cylinders

3.2.1. Type 1 specimens

Series of cylindrical GFRP Type 1 specimens with wall thickness of 1.1 mm, diameters from 300 mm to 500 mm and lengths from 400 mm to 660 mm have been produced and subjected to buckling tests using the test rig described in Chapter 2.3.2. The results of these experimental investigations are presented in (Eglitis et al, 2009).

All the specimens were repeatedly loaded until post-buckling to determine their buckling loads and corresponding buckling shapes within a timeframe of 6 months. The scatters of obtained critical load values for specimens with diameters of 300 mm and 500 mm are summarized in Figure 3.12, respectively. It should be noted that the results for specimens with different lengths are presented on the same figure, as according to the linear classical theory the buckling load for a perfect cylindrical shell is not dependent on its length, as the shells under investigation are of medium length (Teng and Rotter, 2004).

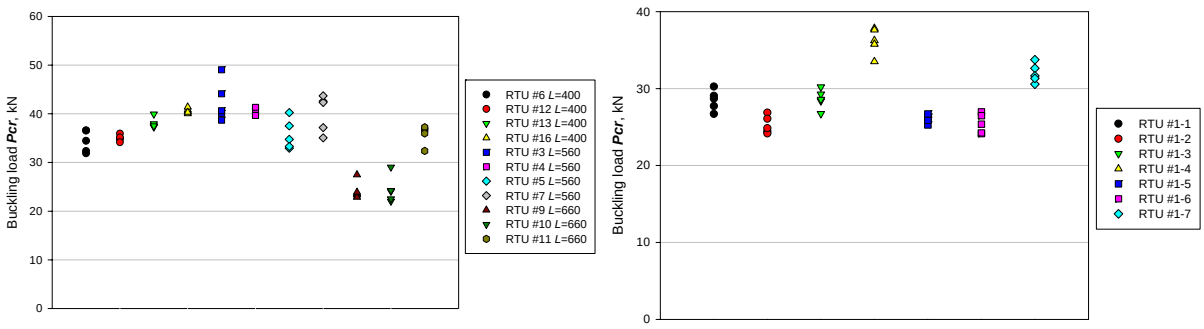

(a) (b)

Figure 3.12. Buckling loads for R = 150 mm (a) and R = 250 mm (b) specimens

As it is seen from the scatter plots, there is significant discrepancy between the maximum and minimum buckling loads. Comparing all the results for the cylinders of the same diameter, the observed difference is 60% for 300 mm specimens and 40% for 500 mm

specimens. The differences are significantly smaller when comparing only the results for each cylinder. Average experimentally obtained buckling loads and their standard deviations for each cylinder configuration are summarized in Table 3.4.

For some cylinders the buckling loads had a smaller scatter during the repeated loading, as for cylinders RTU #1-5, RTU #7, RTU #12, RTU #13, RTU #16. However, for some cylinders, the buckling load and also post-buckling behaviour did vary significantly, as in case of cylinders RTU #3, RTU #5 and RTU #7. However, no visible damage has been observed on these specimens.

Not only the buckling loads differ, but the registered post-buckling mode shapes of the cylinders as well. Pictures of the typical post-buckling mode shapes for the 300 mm and 500 mm cylinders are summarized in Figure 3.13 and Figure 3.14. The load-shortening curves with the maximum and minimum obtained buckling loads for each specimen configuration are presented in Figure 3.15 along with the numerical results.

After performing the ABAQUS/Explicit finite element analysis and obtaining the buckling modes, it is clearly evident that the specimens having the buckling modes close to the numerically obtained ones have the highest buckling loads. The specimen with the highest load-carrying capacity for each configuration, namely, RTU #1-4, RTU #3, RTU #11 and RTU #16 all have fairly similar buckling mode shapes (see Figure 3.13 and Figure 3.14) comparing to the buckling mode shapes obtained numerically (see Figure 3.35). It should be also noted that the pre-buckling stiffness, recorded during the experiments, is significantly lower than the calculated one in case of D = 500 mm specimens. It can be explained by the low elastic modulus of the MDF end fixture used for these specimens and the fact that the shortening has been measured between the steel loading plates. These issues have been addressed when testing the Type 2 and Type 3 specimens.

Suitable approach for finite element modelling has been elaborated, and simulations of the physical experiments have been performed. The finite element models were also updated with initial imperfections in shape of eigenmodes. The results of mesh sensitivity, boundary conditions and imperfection sensitivity studies are presented in detail in (Eglitis et al., 2009). The comparison of experimentally and numerically obtained load – shortening curves is presented in Figure 3.15, and the average critical loads are summarized in Table 3.4.

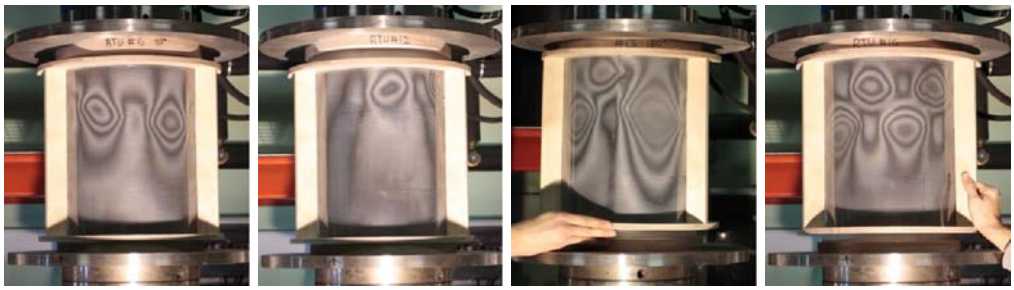

RTU #6 RTU #12 RTU #13 RTU #16

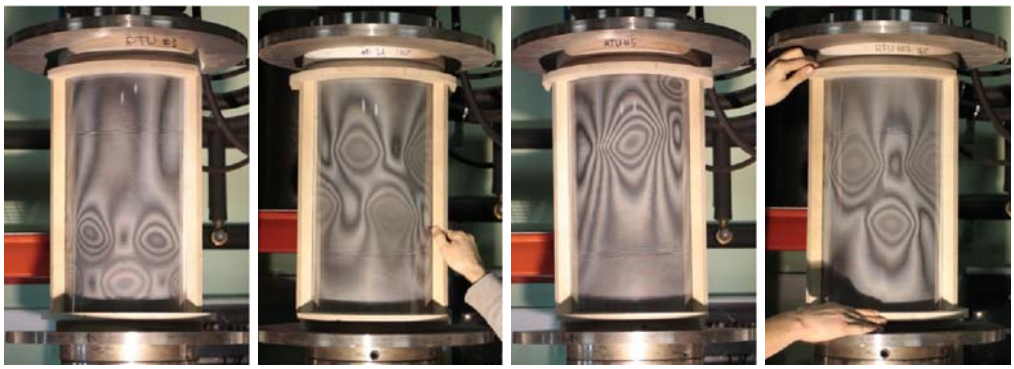

RTU #3 RTU #4 RTU #5 RTU #7

RTU #9 RTU #10 RTU #11

Figure 3.13. Experimental buckling mode shapes of D = 300 mm specimens

Table 3.4. Comparison of experimental and numerical results

Specimen configuration	Average experimental P_{cr} [kN]	Standard deviation [kN]	Closest numerical P_{cr} [kN]	Imperfection magnitude
300-400	36.99	2.84	37.09	$t/4$
300-560	39.73	3.90	37.15	$t/4$
300-660	28.15	6.00	28.18	t
500-660	28.87	3.93	31.97	t

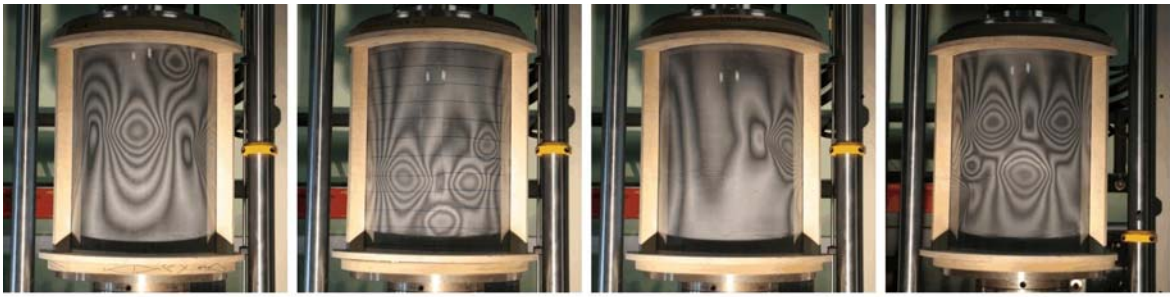

RTU #1-1 RTU #1-2 RTU #1-3 RTU #1-4

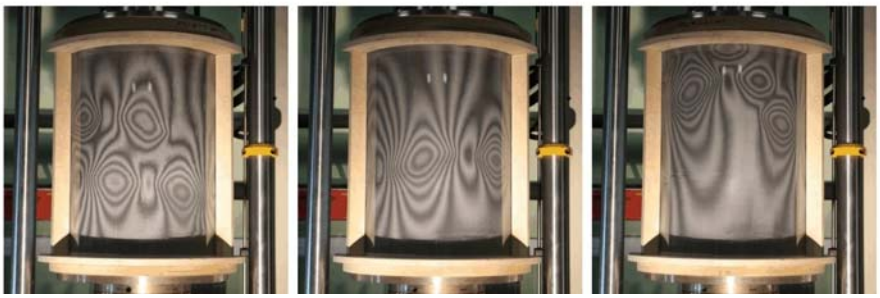

RTU #1-5 RTU #1-6 RTU #1-7

Figure 3.14. Experimental buckling mode shapes of D = 500 mm specimens

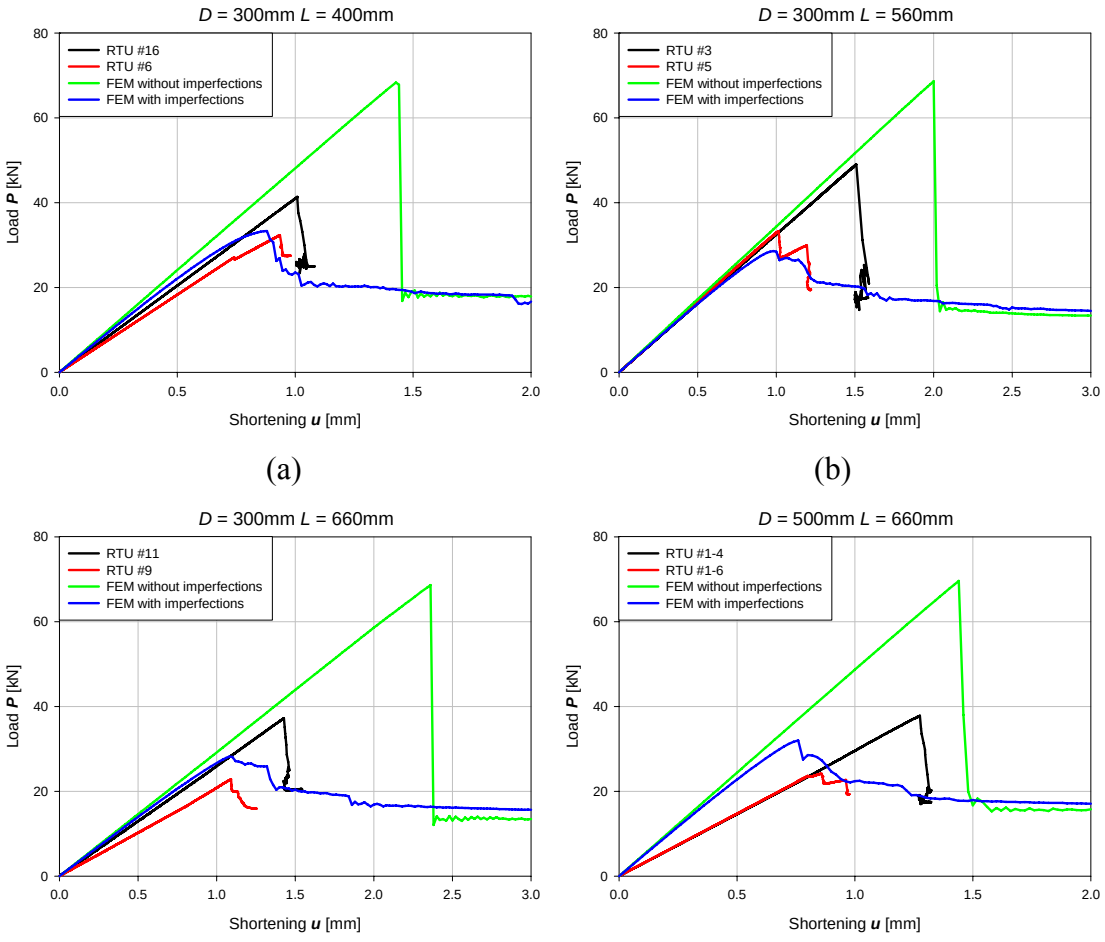

Figure 3.15. Experimental and numerical load-shortening curves

3.2.2. Type 2 specimens

Static buckling tests of Type 2 specimens have been performed using the test set-up described in Chapter 2.3.3.

Both specimens were first loaded until buckling and the buckling side and typical buckling pattern determined. Then, the LVDT displacement transducers were installed on appropriate sides, and the strain gauges applied. A picture of the specimen fully prepared for the buckling test is presented on Figure 3.17.

The specimen Type 2-1 has been subjected to static buckling loads 8 times in total: The first was the preliminary test, and three more tests with LVDT displacement sensors were carried out. The typical buckling shape was marked on the cylinder and 7 pairs of strain gauges in back-to-back configuration were applied. The locations of the strain gauges are schematically indicated on Figure 3.16. After the application of the strain gauges, four more tests were performed on this specimen. Load-shortening curve was recorded only during the loading for all tests, except the last two, when it was recorded also during the unloading. The load-shortening curves of the specimen Type 2-1 are presented on Figure 3.18(a) and the corresponding buckling modes are shown on Figure 3.19. Typical strain gauge measurements (Test 5) are presented in Figure 3.21.

The specimen Type 2-2 has been subjected to static buckling loads 6 times; two preliminary tests have been performed to observe the buckling mode before attaching the LVDT transducers and strain gauges. In case of Type 2-2 specimen, only 5 pairs of strain gauges have been applied to the specimen, as shown in Figure 3.16. Four tests have been preformed on fully equipped Type 2-2 specimens; the obtained load-shortening curves are presented in Figure 3.18(b), corresponding buckling shapes in Figure 3.20 and typical strain gauge readouts (Test 5) are presented in Figure 3.22.

The use of Type 2 specimens did increase the repeatability of the experimental results, and the standard deviations of the repeated static buckling loads are 3.3% in case of specimen Type 2-1 and 2.8% in case of specimen Type 2-2. The specimen Type 2-1 exhibited slightly lower buckling load with each following buckling test, but after removing it from the test rig and repeating the test sequence about a month later, the first buckling load was as high as the first one in the first test sequence, and repeated tests of the specimen kept this tendency (Figure 3.23 (a)). However, such tendency could not be observed in case of the specimen Type 2-2, as it can be seen in Figure 3.23 (b).

Not only the buckling loads of the cylinders varied from test to test, but the buckling shapes as well, as can be seen from the Figure 3.19 and Figure 3.20. The change in buckling loads and shapes indicates the sensitivity of the cylindrical shells to the slight changes in initial shape of loading conditions between consecutive tests.

The differences in the strain gauge measurements prior to buckling can be explained by local thickness or stiffness variations, as the load is distributed evenly by the spherical bearing. It can also be observed that, for example, on specimen Type 2-1, the opposite pairs of strain gauges (1-2 and 5-6) measure 720 and 760 μm/m strains at the buckling load, while the other opposite pairs (3-4 and 7-8) measure 950 and 940 μm/m, respectively.

One of the purposes of the strain gauge measurements is verifying the load measurements and estimating the loads acting on the cylinder during various dynamic tests. To verify the accuracy of the estimations of the axial load based on the strain gauge measurements, these estimations are compared to the load cell measurements of the static tests. The load is estimated in the following way:

$$P^* = \bar{\varepsilon} \cdot E \cdot A\,, \tag{3.1}$$

where P^* is the load estimated from strains, $\bar{\varepsilon}$ is the average stain measured by the strain gauges located at the end of the specimen, E is the modulus of GFRP in the axial direction, and A is the nominal cross-sectional area of the specimen. The comparison of estimated and measured loads is presented in Figure 3.24, and the difference between the measured and estimated critical load is 0.8% in case of specimen Type 2-1 and 3.8% in case of specimen Type 2-2.

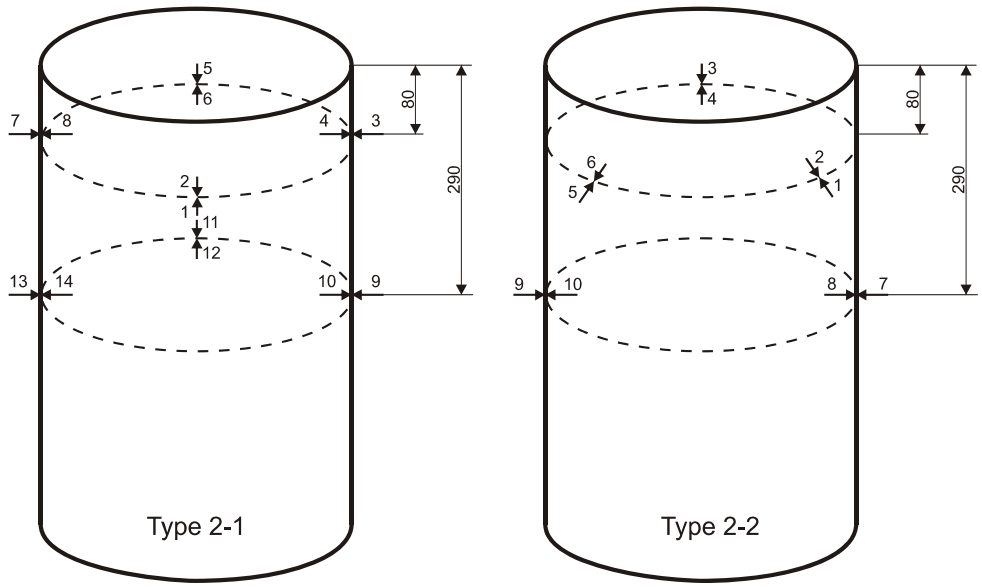

Figure 3.16. Locations and numbering of strain gauges on Type 2 specimens

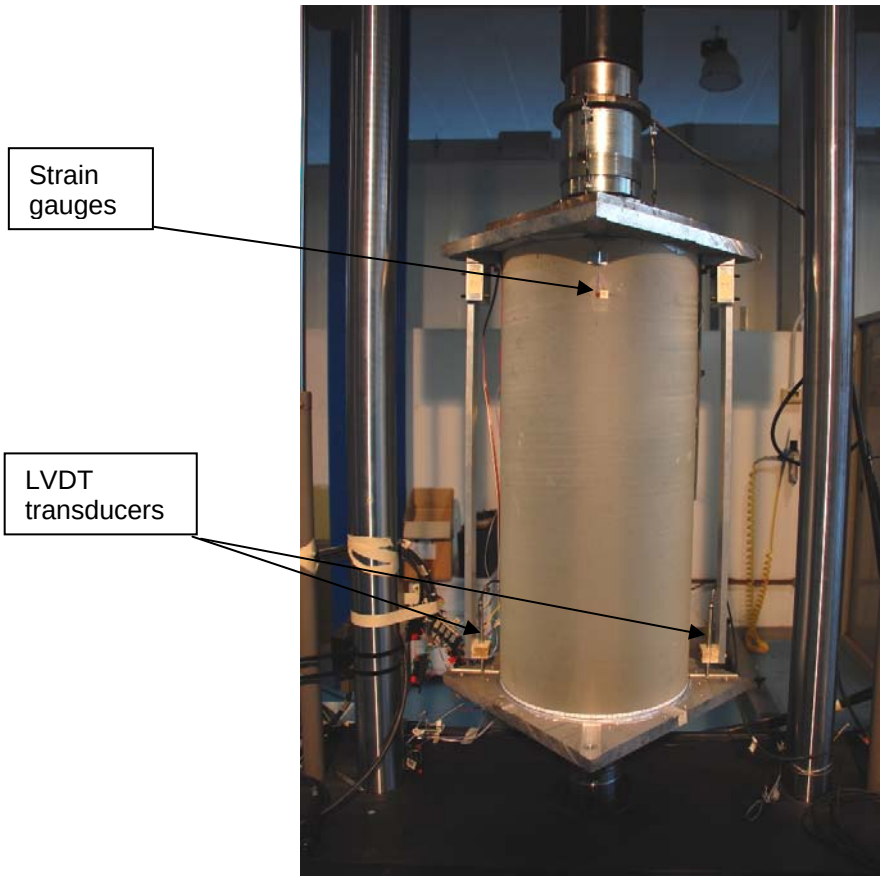

Figure 3.17. Type 2 specimen prepared for the test

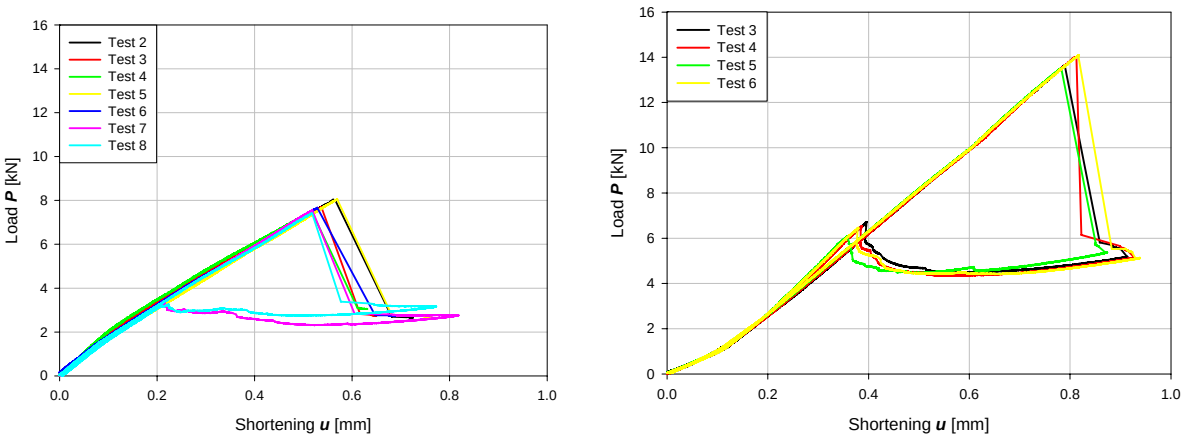

(a) (b)

Figure 3.18. Load-shortening curves of Type 2 specimens
(a) – specimen **Type 2-1**and (b) – specimen **Type 2-2**

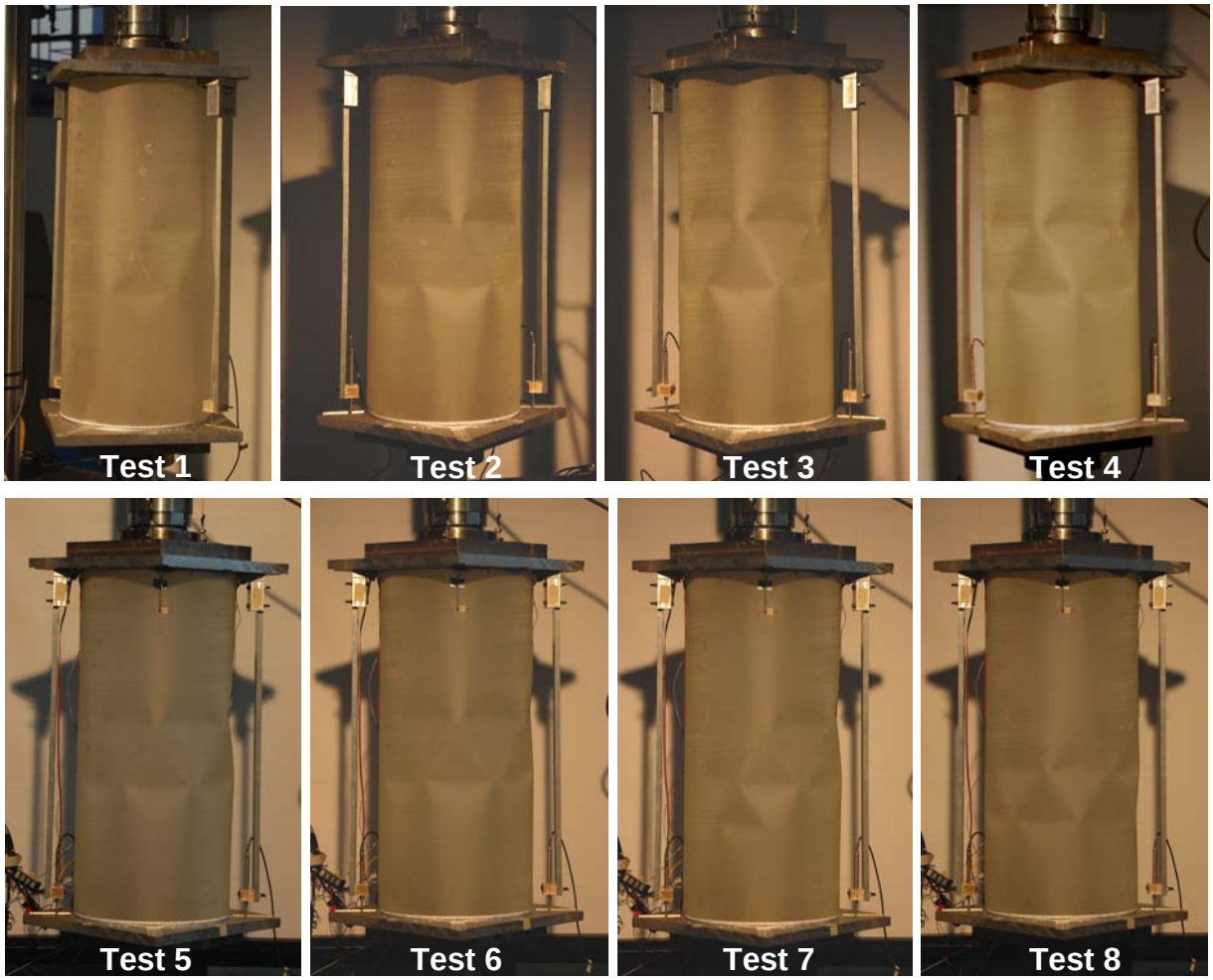

Figure 3.19. Buckling shapes of specimen **Type 2-1**

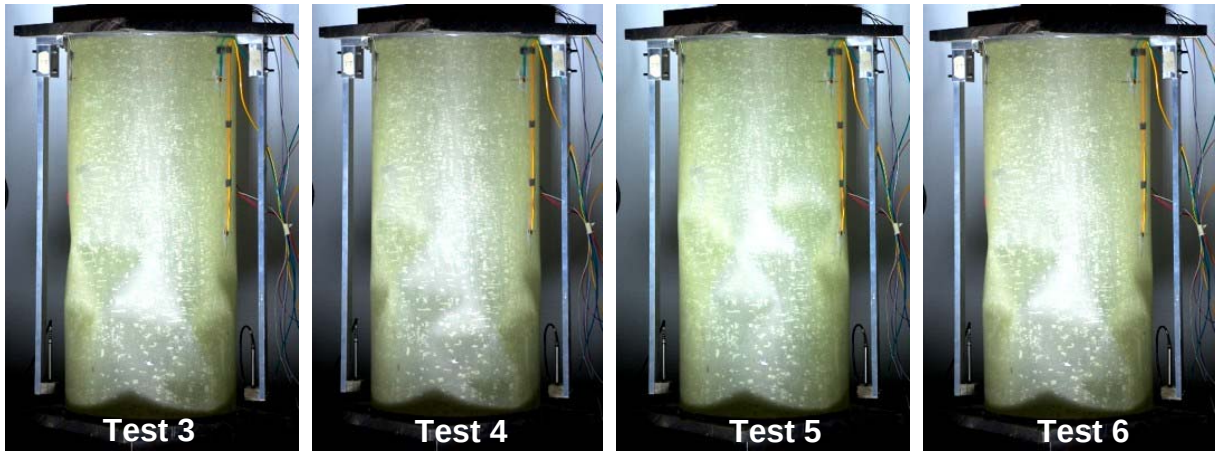

Figure 3.20. Buckling shapes of specimen **Type 2-2**

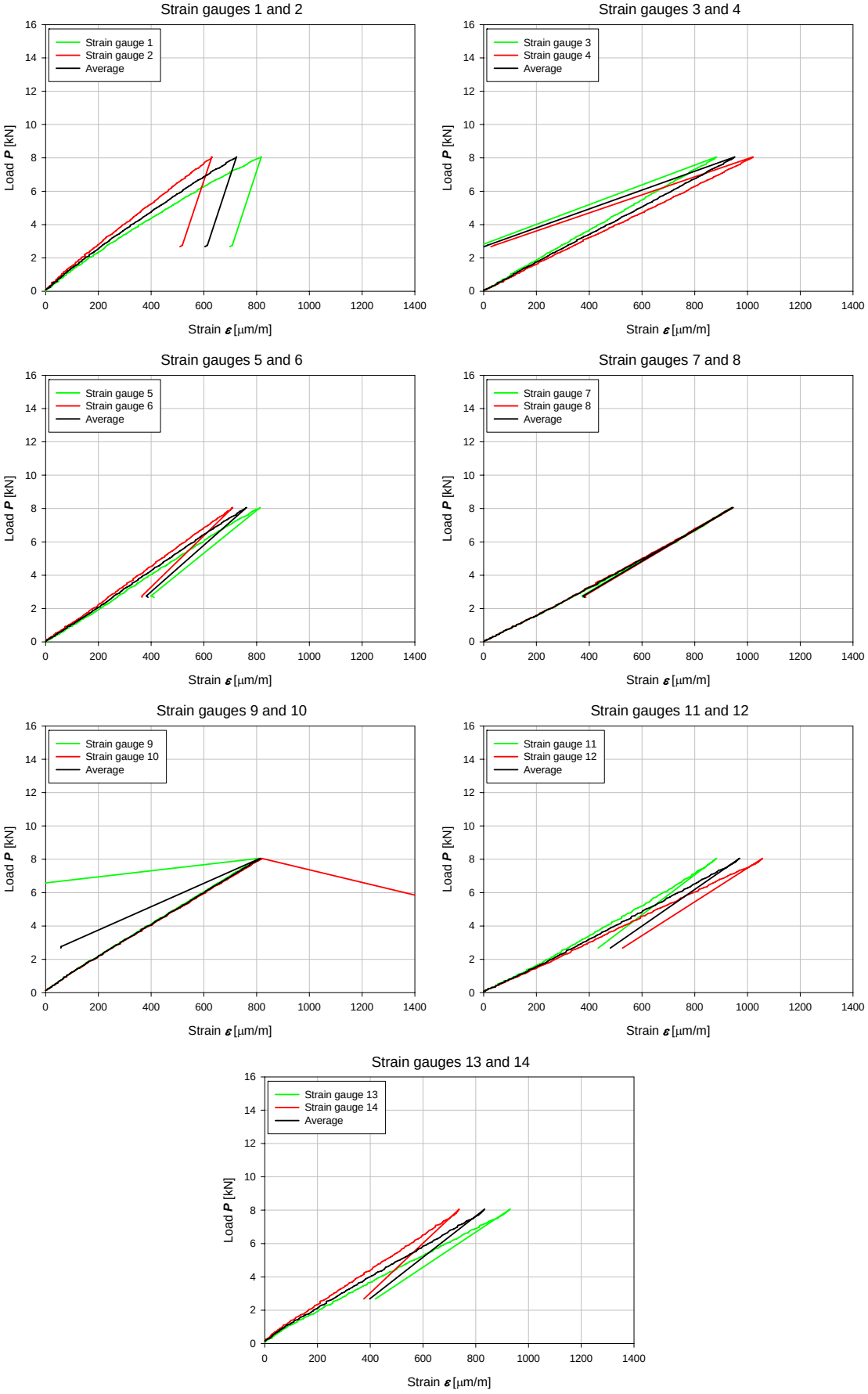

Figure 3.21. Typical strain gauge measurements on specimen **Type 2-1**

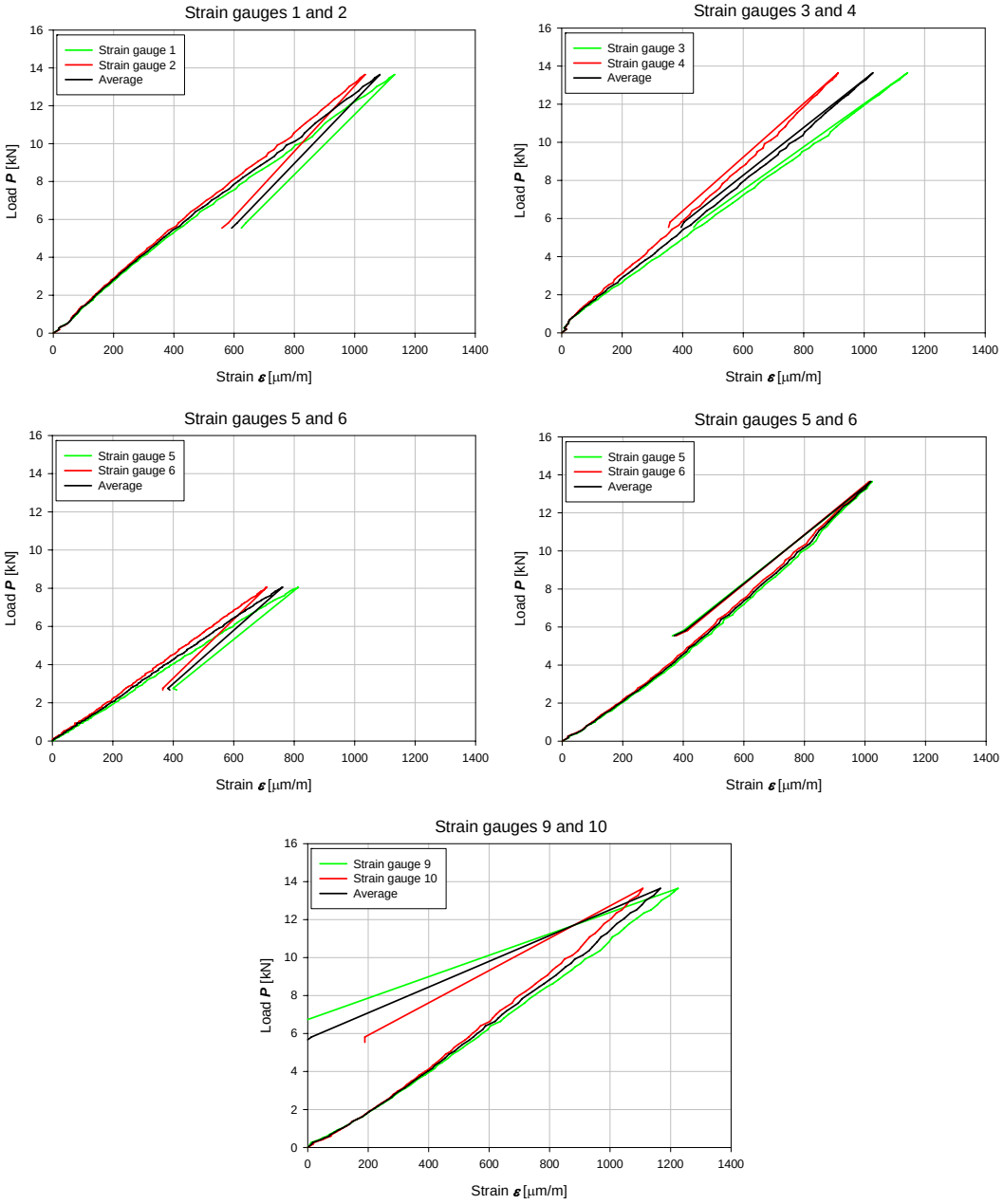

Figure 3.22. Typical strain gauge measurements on specimen **Type 2-1**

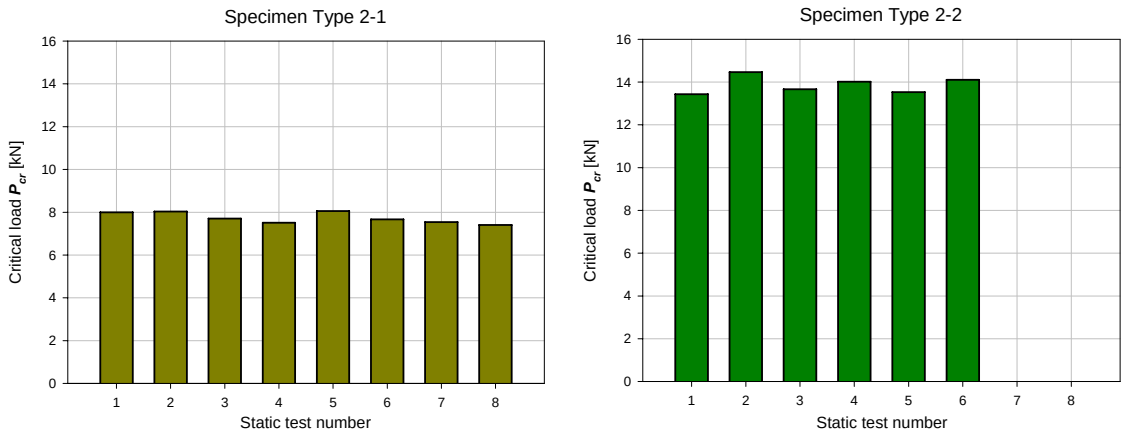

Figure 3.23. Comparison of static buckling loads for Type 2 specimens

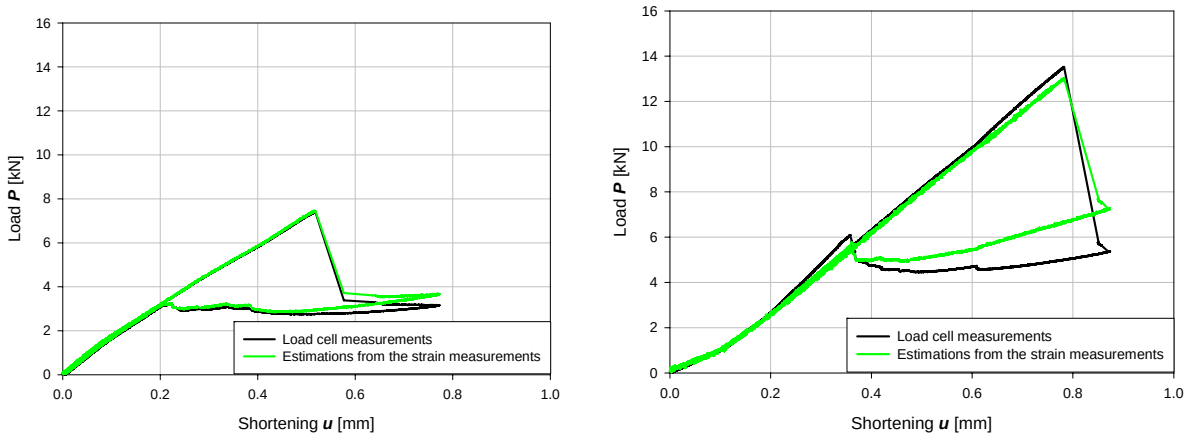

Figure 3.24. Loads measured by load cell and estimated from the strain measurements (a) – specimen **Type 2-1** and (b) – specimen **Type 2-2**

Additionally to the load, displacement and strain measurements that have been performed during the static buckling tests of specimens Type 2, the buckling shape forming process has been filmed using a high-speed camera with frame rate of 1000 frames per second. This allowed observing the formation of the static buckling shape on the cylinders. Sequence of the video frames at the buckling moment of the specimen Type 2-1 is presented in Figure 3.25. The buckling shape initiates as an higher-order shape in a relatively small region of the cylinder and transforms to a lower-order shape in approximately 3 milliseconds.

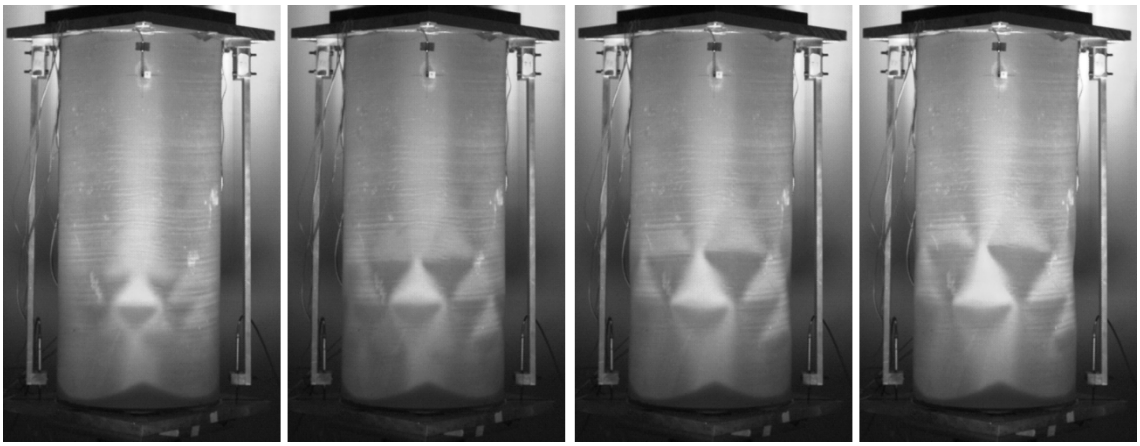

Figure 3.25. Static buckling shape development of specimen **Type 2-1** (1000 FPS)

3.2.3. Type 3 specimens

Static buckling tests of Type 3 specimens have been performed at Riga Technical University, Institute of Materials and Structures. The test set-up is described in Chapter 2.3.2.

The test setup has been updated with LVDT displacement transducers and strain gauges linked to a HBM MGCplus data acquisition system, comparing to the setup used to test the Type 1 specimens. The test set-up with a Type 3 specimen installed is presented in Figure 3.26. Each specimen had three pairs of strain gauges applied in back to back configuration, 50 mm from the lower edge of the specimen and evenly distributed along the circumference, as shown on Figure 3.27.

Each of the two Type 3 specimens has been subjected to static buckling loads 8 times in total, in two sequences of four tests each. The buckling shapes have been recorded using camera and moiré fringe setup, as in case of the Type 1 specimens, and typical buckling shapes are presented on Figure 3.28. The consistent repeatability of the buckling shapes obtained must be noted, and it was regular 'diamond' shape spreading along the whole circumference, with 7 buckles in each row in all of the tests.

The load-shortening curves of the specimens Type 3-1 and Type 3-2 are presented on Figure 3.29. The typical strain gauge measurements for these specimens are presented in Figure 3.31.

Though the repeatability of the test results improved over the Type 2 specimens in terms of buckling shapes, the scatter of the buckling loads remains in the same order. The average buckling load of specimen Type 3-1 was 52.02 kN with standard deviation of 1.8 %, and the average buckling load of the Type 3-2 specimen was 51.83 kN with standard deviation of 3.1 %. Just like in case of the specimen Type 2-1 specimens, a general tendency of slight decrease of the buckling load with each following test in the sequence is observed, while the buckling loads in the second test sequence are not lower than in the corresponding tests of the first sequence. This tendency can be observed in Figure 3.30.

There is significantly less difference in strain gauge measurements than in case of Type 2 specimens, with average strains measured by a strain gauge pair not exceeding 5 % in case of specimen Type 3-1 and 2% in case of specimen Type 3-2. Of course, the thickness variations are inevitable, and therefore the differences in the axial strain can be observed. Moreover, the shape imperfections result in the presence of the pre-buckling bending strains.

Just like in case of Type 2 specimens, the strain gauge measurements have been used for verification of the load measurements during the dynamic tests. Again, to verify the

accuracy of the estimations of the axial load based on the strain gauge measurements, these estimations are compared to the load cell measurements of the static tests using the equation (3.1). The comparison of estimated and measured loads is presented in Figure 3.32, and the difference between the measured and estimated critical load is 1.7% in case of specimen Type 3-1 and 0.8% in case of specimen Type 3-2.

Accurate Finite Element models of the Type 3 specimens, including the measured imperfections, have been elaborated for ABAQUS/Explicit analyses, and the physical tests have been used for the model validation. Good agreement of the experimental and numerical results has been achieved for the static loading, as it can be seen from the agreement of buckling shapes (Figure 3.28) and Load-Shortening curves (Figure 3.29). The explicit dynamic, geometrically non-linear finite element analysis buckling analysis results overestimate the average experimentally obtained buckling loads of the Type 3 specimens less than by 6 % with 95% confidence.

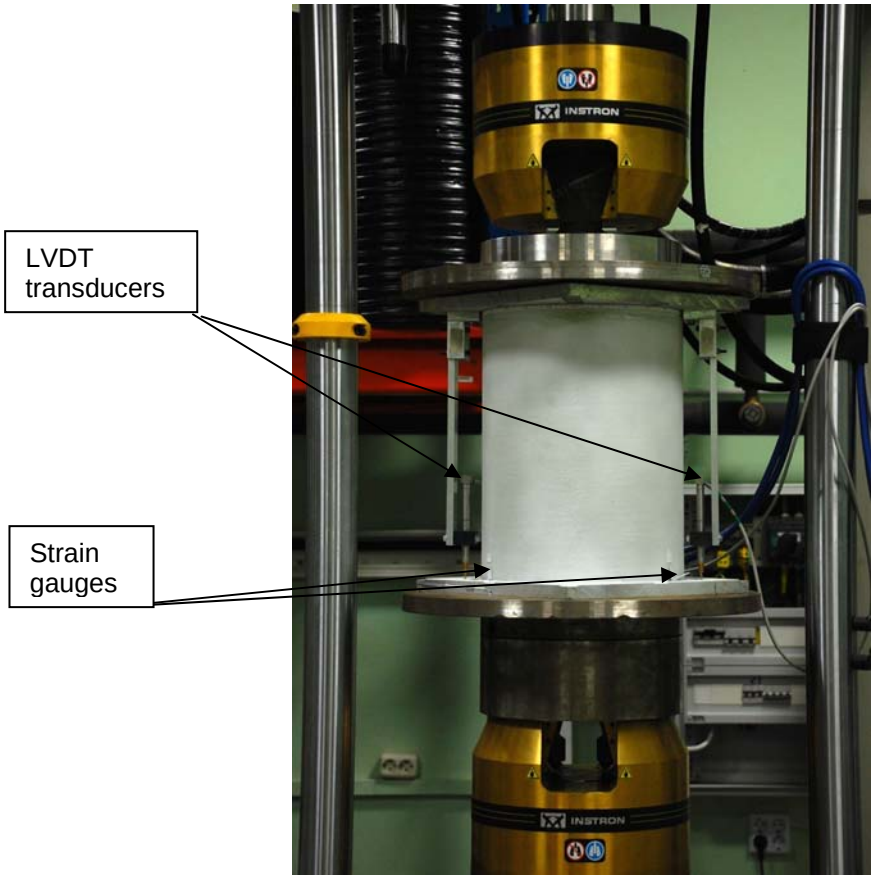

Figure 3.26. Type 2 specimen prepared for the test

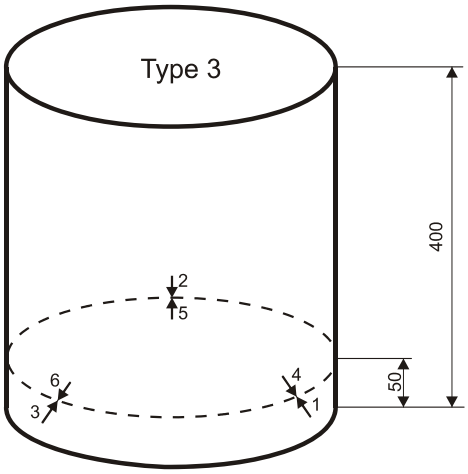

Figure 3.27. Locations and numbering of strain gauges on Type 3 specimens

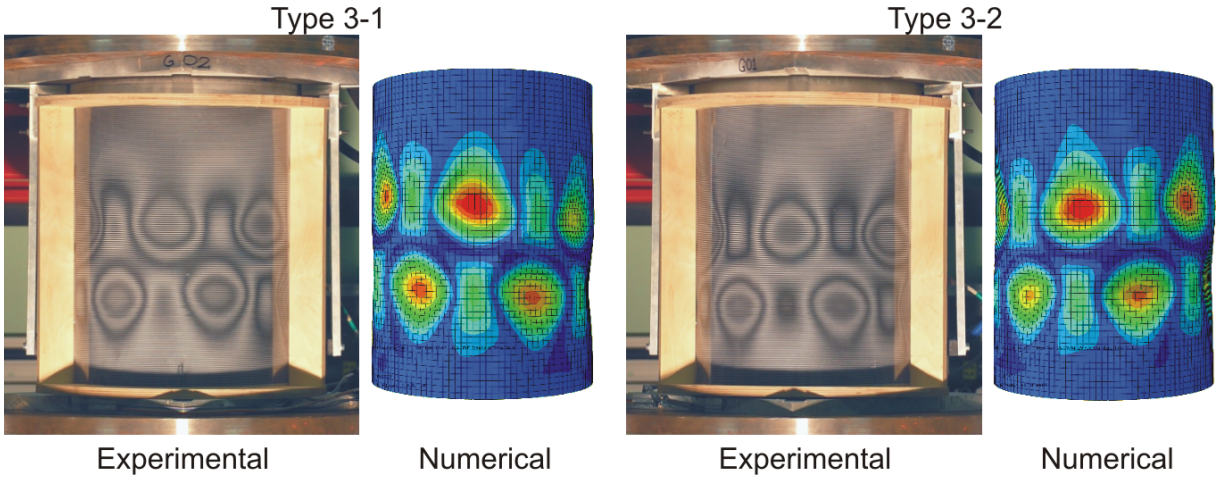

Figure 3.28. Typical buckling shapes of Type 3 specimens

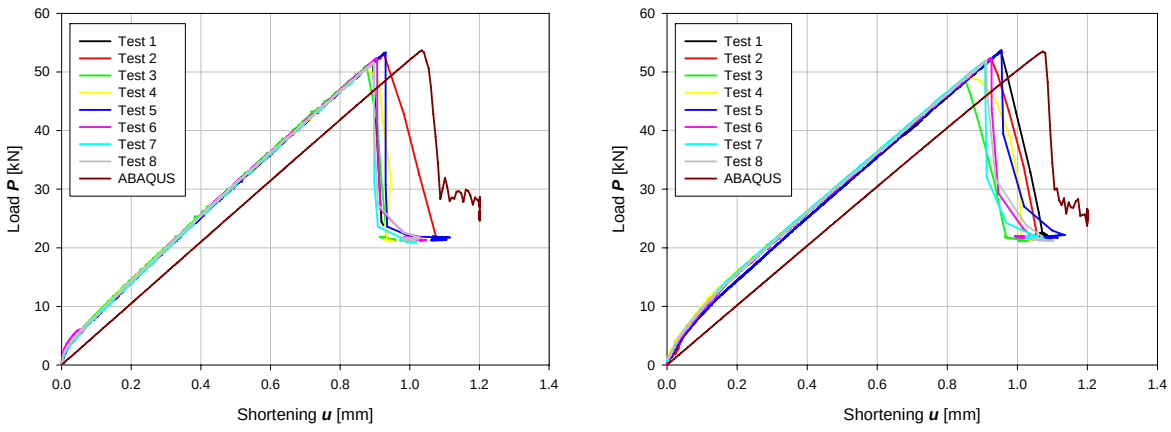

(a) (b)

Figure 3.29. Load-Shortening curves of Type 3 specimens
(a) – specimen **Type 3-1** and (b) – specimen **Type 3-2**

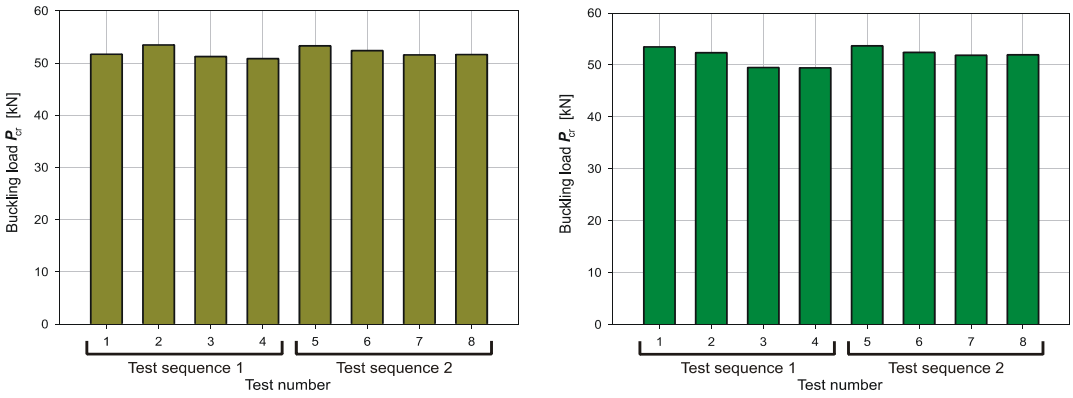

Figure 3.30. Comparison of static buckling loads for specimen Type 3-1 (a) – specimen **Type 3-1** and (b) – specimen **Type 3-2**

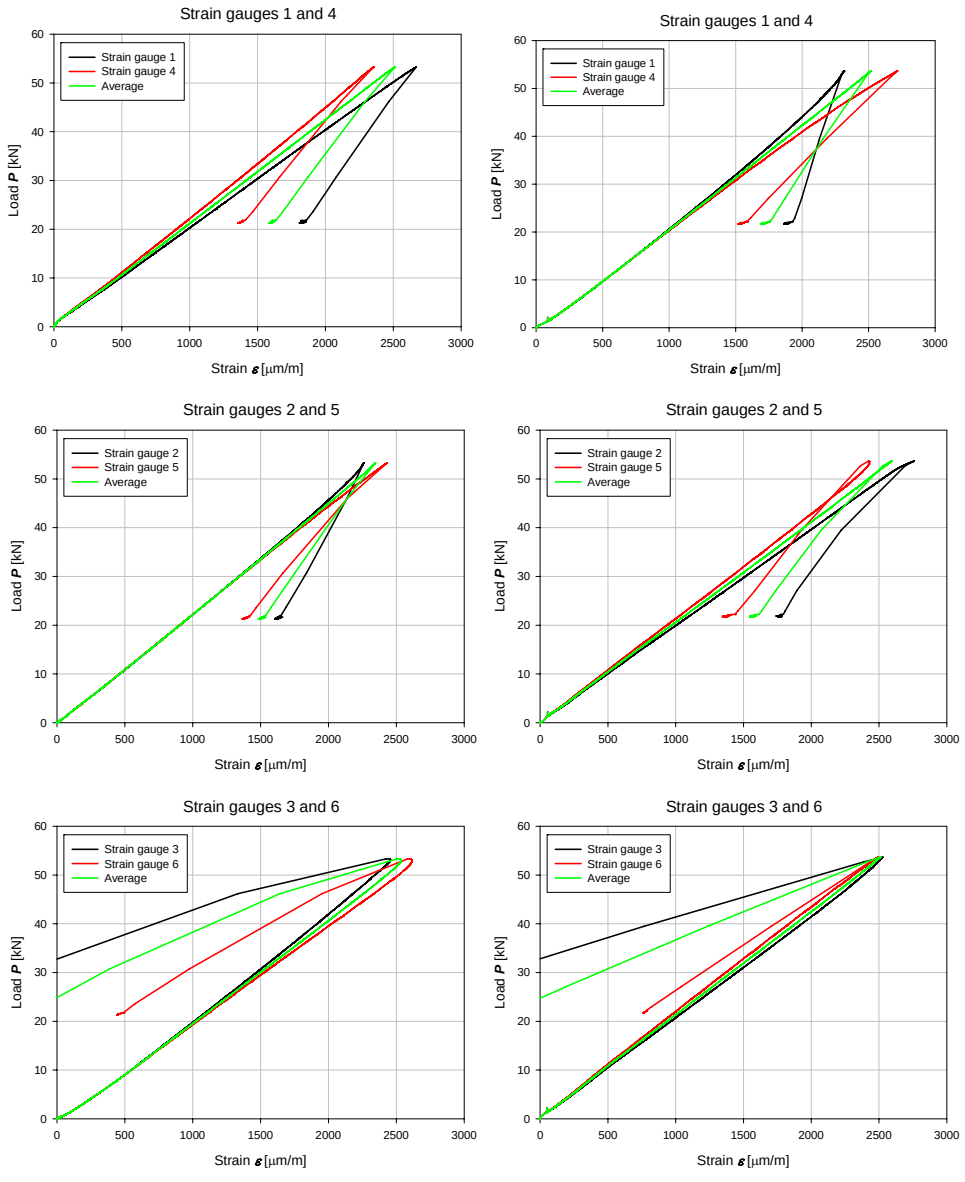

Figure 3.31. Typical strain gauge measurements of specimen **Type 3-1**(a) and **Type 3-2**(b)

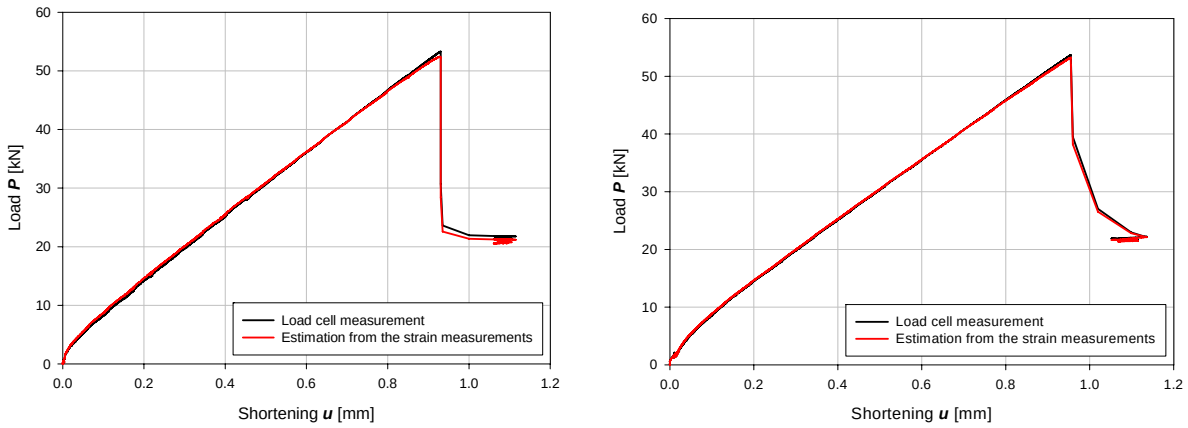

Figure 3.32. Loads measured by load cell and estimated from the strain measurements (a) – specimen **Type 3-1** and (b) – specimen **Type 3-2**

3.2.4. Concluding remarks

The experimental results obtained with Type 1 specimens had significant scatter of critical loads, with standard deviation of up to 21% for nominally identical specimens (see Figure 3.12), while the standard deviation of the results of repeated experiments was ranging from 1.3% to 11%. The knock-down factors obtained in the experiments were ranging from 0.25 to 0.58. These knock-down factors are within the margins observed by Harris et al (1957).

The finite element analysis of geometrically perfect finite element models predicted much higher buckling loads than obtained in the experiments. Applying artificial initial imperfections to the finite element models brought down the numerically obtained buckling loads to the levels of experimental ones (see Table 3.4). However, the imperfection factors needed were different for different specimen series, and further study of initial imperfections in specimen geometry was necessary.

The introduction of the aluminium end plates in Type 2 specimens and more careful experiment execution resulted in significant improvement in the repeatability of the experimental results comparing to the Type 1 specimens, with the standard deviations of the buckling loads measured during repeated tests being 3.3 % for specimen Type 2-1 and within 2.9 % for specimen Type 2-2. However, the method used for alignment of the end plates did not work properly and resulted in significant prestress in the specimens. As a result, no good agreement between the numerical and experimental results could be obtained even considering the measured imperfections of the cylinders. Therefore, only experimental results are presented for Type 2 specimens.

The careful production of the nominally identical specimens Type 3-1 and Type 3-2 resulted in relatively consistent experimental results and good agreement between the static buckling experiments on the two cylindrical specimens. Eight static buckling tests have been performed on each specimen, and the average buckling loads of specimens Type 3-1 and Type 3-2 were 52.02 kN and 51.83 kN, respectively, with the standard deviation of the buckling loads measured during repeated tests being 2.5 % for these nominally identical specimens. In all of the buckling tests for both specimens, the buckling shape was a 'diamond pattern' with 7 waves along the circumference (Figure 3.28).

Numerical models of the both Type 3 specimens have been created for analysis with ABAQUS/Explicit finite element code. Initial imperfections of the specimens have been measured and included in the numerical models. The numerically obtained buckling loads for the specimens Type 3-1 and Type 3-1 are 53.70 kN and 53.49 kN respectively, overestimating the average experimental buckling loads by 3.23 % and 3.19 %. The numerically obtained buckling shapes correspond to the experimentally obtained ones (Figure 3.28)

3.3. Eccentric compression of Type 1 specimens

Eight of the Type 1 specimens have been tested under axial compression with load eccentricity e/R (Figure 3.33) from 0 to 0.67, and the results have been reported in (Eglitis et al., 2010b). First, the specimens have been re-tested under concentric compression. The obtained load-shortening curves are presented in Figure 3.34 and the corresponding buckling mode shapes are shown in Figure 3.35.

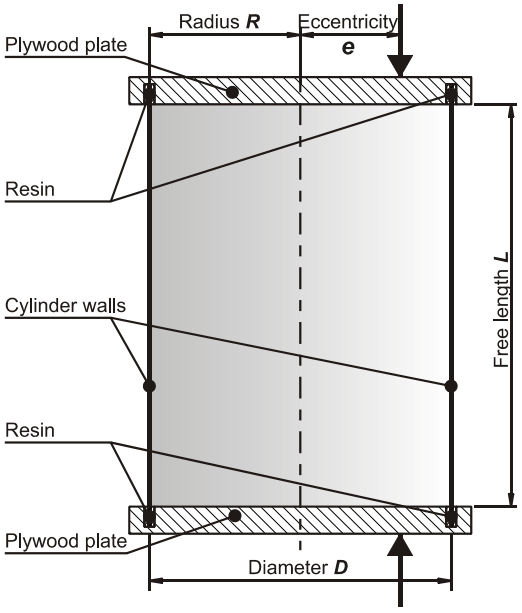

Figure 3.33. Eccentric load application

Following the axial compression tests, eccentric buckling tests have been performed on all of the specimens. The load eccentricities with eccentricity-to-radius ratios e of 1/3 and 2/3 were introduced. Even during the concentric buckling tests, only one side of a cylinder buckled due to presence of the spherical bearing in the test set-up. That side is considered the weakest and the results are presented only for the tests where the weakest side of a cylinder is loaded the most due to the loading eccentricity.

The load-shortening curves obtained during the eccentric buckling tests are presented in Figure 3.36 and Figure 3.38 and the corresponding buckling mode shapes are shown in Figure 3.37 and Figure 3.39.

For the concentric compression, the standard deviation of the experimental results is 7.9% of the average. The scatter of results for cylinders under eccentric compression is even greater than in case of concentric compression. The standard deviation is 9.0% in case of e/R=1/3, and 12.7% in case of e/R=2/3.

This experimental study was supported by a numerical study, where ABAQUS/Explicit finite element code has been used to perform the numerical simulations of the buckling experiments performed. The initial imperfections of the specimens were unknown, so eigenmode-shaped imperfections with amplitude 1/4 of shell thickness t have been introduced to the numerical models. This imperfection magnitude has been chosen to obtain good accordance of buckling loads for concentrically compressed cylinders and kept constant through the whole investigation. The critical loads obtained using linear eigenvalue analyses were used for calculations of the knock-down factors of the experimental and non-linear numerical analysis results.

The experimentally obtained buckling loads and corresponding knock-down factors along with the numerical results are summarized in the Table 4.5. A knock-down factor versus loading eccentricity graph is presented in Figure 3.40.

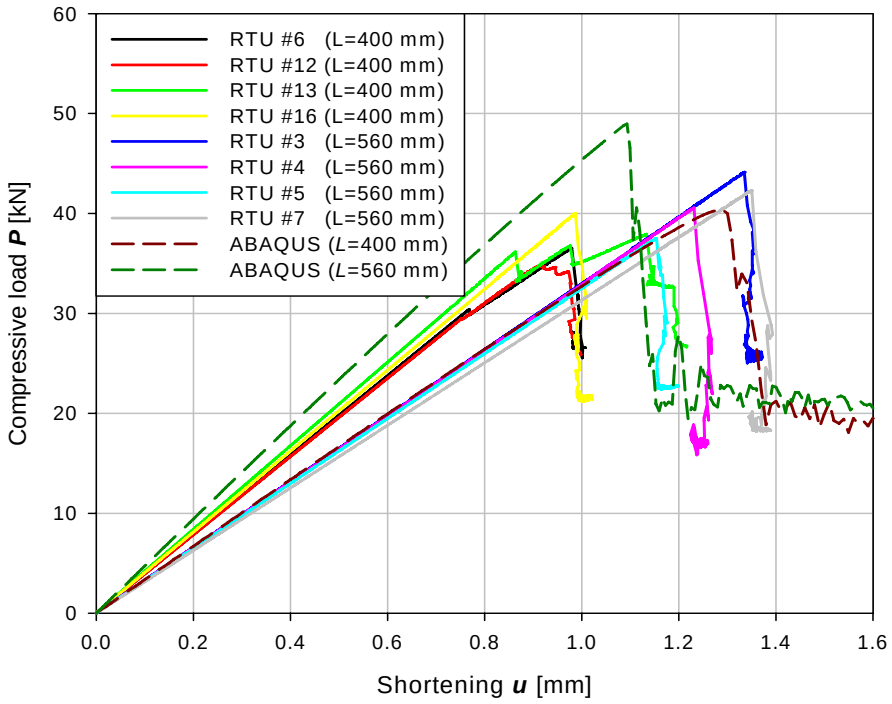

Figure 3.34. Load-shortening curves for $e/R = 0$

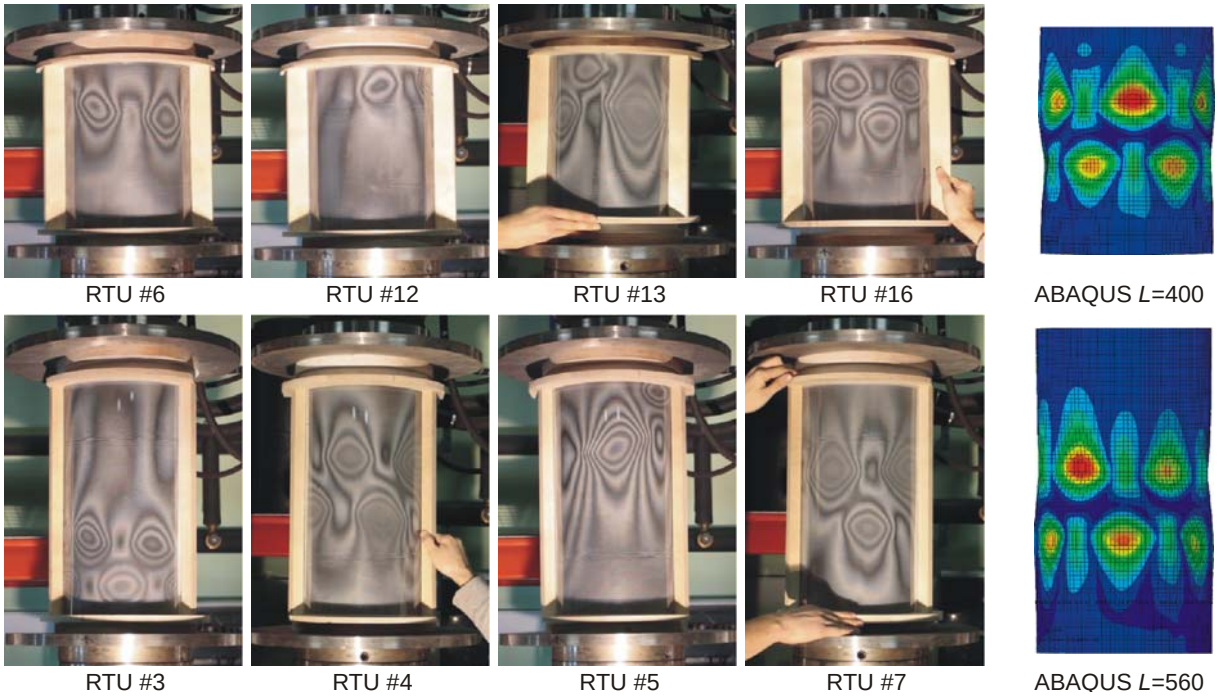

Figure 3.35. Buckling shapes for $e/R = 0$

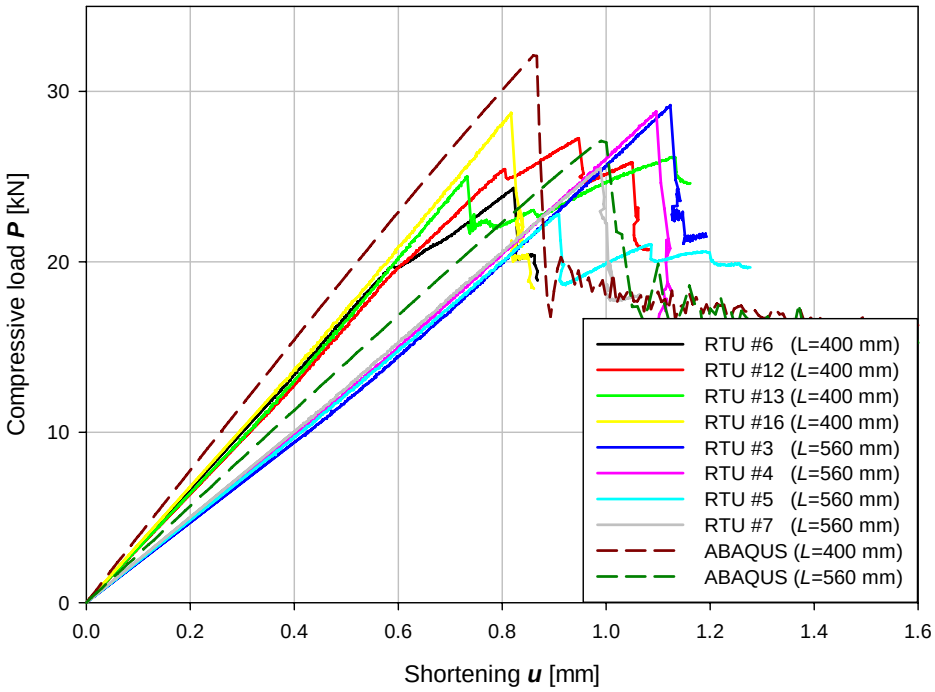

Figure 3.36. Load-shortening curves for $e/R = 1/3$

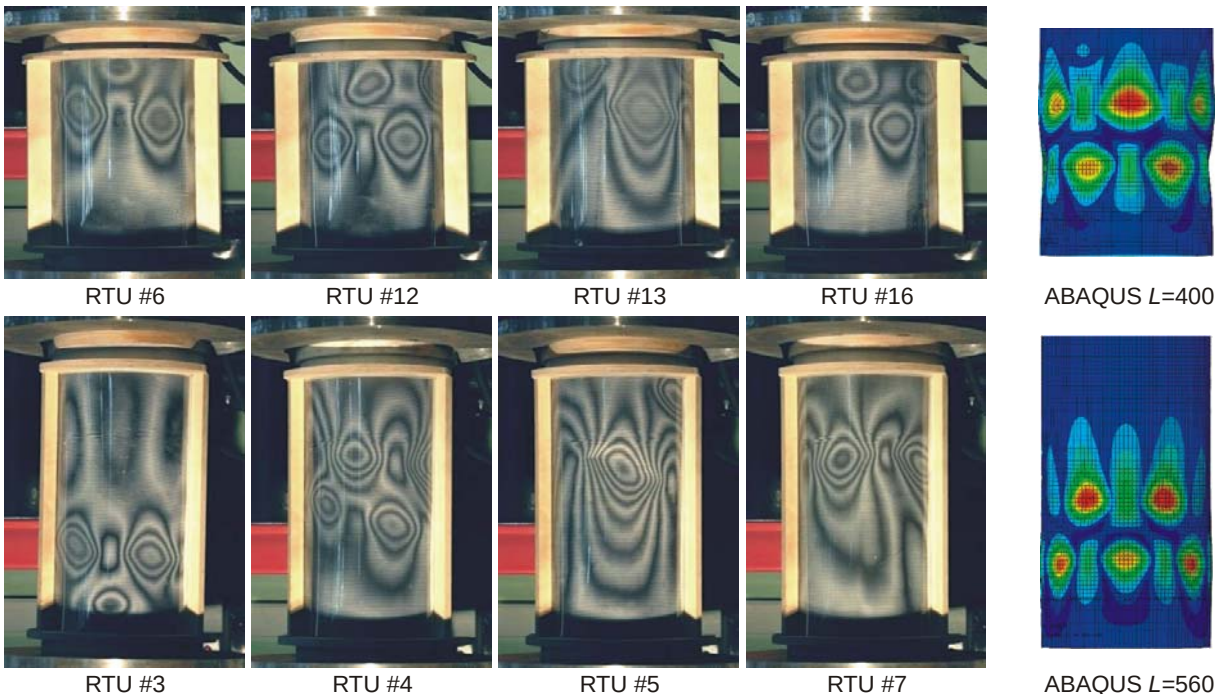

Figure 3.37. Buckling shapes for $e/R = 1/3$

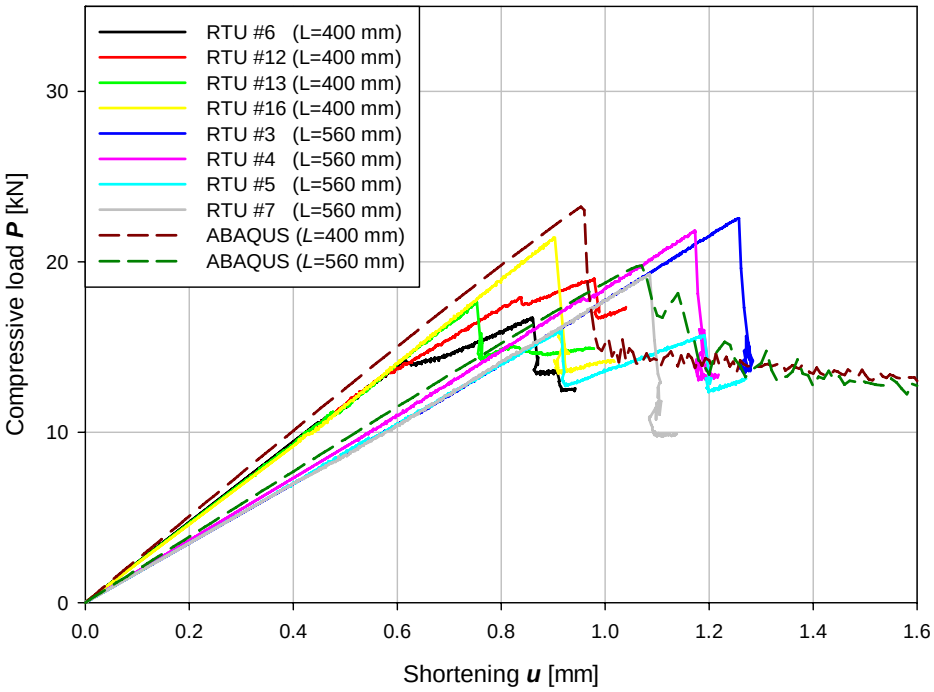

Figure 3.38. Load-shortening curves for $e/R = 2/3$

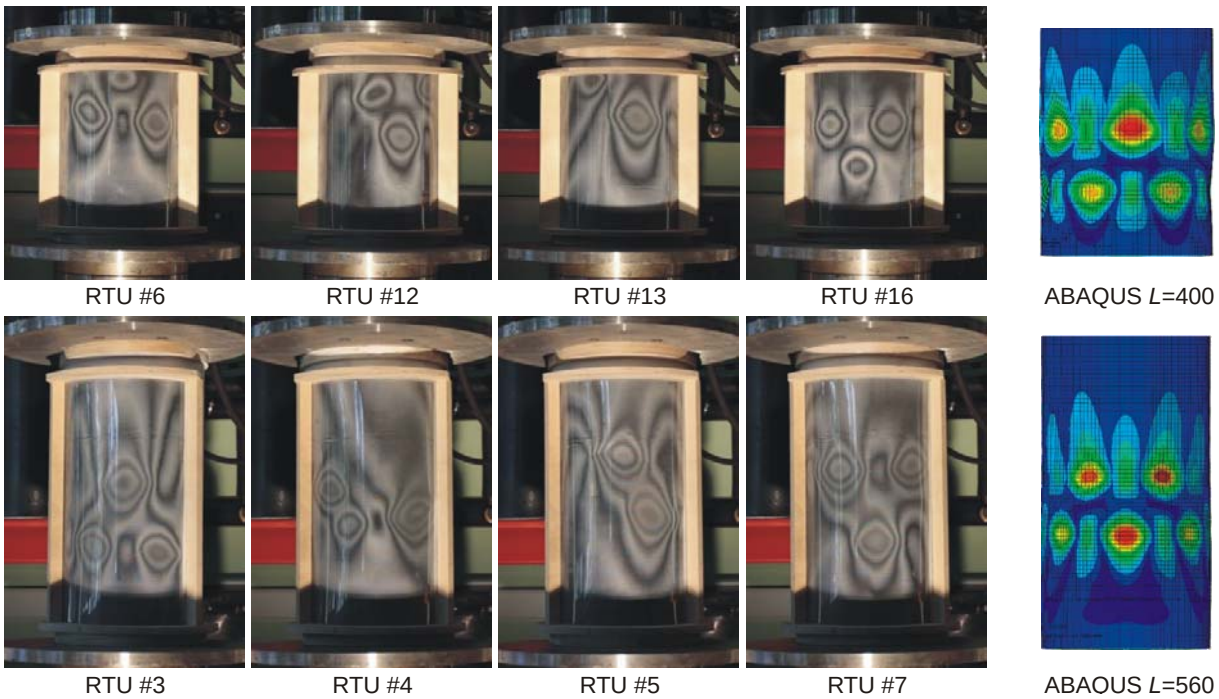

Figure 3.39. Buckling shapes for $e/R = 2/3$

Table 3.5. Comparison of the experimentally and numerically obtained results

Specimen or model	Load type					
	Concentric		Eccentric, e=1/3R		Eccentric, e=2/3R	
	Buckling load P_{cr}, kN	Knock-down factor	Buckling load P_{cr}, kN	Knock-down factor	Buckling load P_{cr}, kN	Knock-down factor
ABAQUS linear	85.02	1.00	51.29	1.00	36.26	1.00
RTU #6 (L=400)	36.55	0.43	24.26	0.47	16.72	0.46
RTU #12 (L=400)	34.75	0.41	27.25	0.53	19.02	0.52
RTU #13 (L=400)	37.95	0.45	24.97	0.49	17.55	0.48
RTU #16 (L=400)	40.03	0.47	28.75	0.56	21.41	0.59
RTU #3 (L=560)	44.13	0.52	29.11	0.57	22.55	0.62
RTU #4 (L=560)	40.57	0.48	28.77	0.56	21.81	0.60
RTU #5 (L=560)	37.52	0.44	22.77	0.44	16.01	0.44
RTU #7 (L=560)	42.33	0.50	25.46	0.50	19.21	0.53
Average	39.23	0.46	26.42	0.52	19.28	0.53
Standard deviation, %	7.9		9.0		12.7	
ABAQUS L=400	48.74	0.57	32.11	0.63	23.23	0.64
ABAQUS L=560	40.35	0.47	27.10	0.53	19.78	0.55

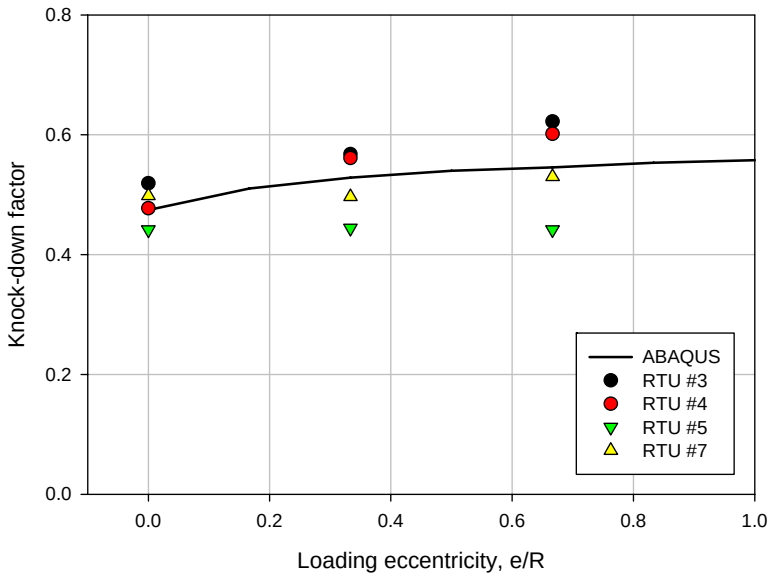

Figure 3.40. Influence of the loading eccentricity on the knock-down factor

According to both experimental and numerical results, the imperfection sensitivity of a compressed composite cylinder slightly decreases, as the load is applied with a greater eccentricity. The numerical results show that the knock-down factor increases with the increase of the loading eccentricity, and the average of the experimentally obtained buckling loads verifies this tendency.

4. DYNAMIC BUCKLING OF COMPOSITE CYLINDERS

4.1. Type 0 specimens

Through a proper experimental setup and testing procedure was still in development stage, some preliminary studies in dynamic buckling of GFRP cylinders have been performed and results presented in (Eglitis et al., 2008).

Static buckling load has been determined for a Type 0 cylindrical GFRP specimen. It must be noted, that preliminary tests have been performed on this specimen too deep in the post-buckling and some visually noticeable damage has occurred. The buckled cylinder is shown in Figure 4.2 (a).

After the static buckling test, the displacement-controlled experiment has been repeated with the velocity 150 mm/s, the listed maximum velocity of the Instron hydraulic frame. With shortening at buckling being approximately 1.5 mm this gives the load duration prior to buckling of 10 ms.

It should be noted that the controlling software failed at stopping the actuator at the specified displacement and the specimen was destroyed after the test (Figure 4.2 (b)).

The experimentally obtained load-shortening curves are presented in Figure 4.1 (a). In this case, the experimentally obtained DLF was 1.33.

Numerical simulations of the static and dynamic tests have been performed using ABAQUS/Explicit dynamic finite element code, and load-shortening curves have been obtained (Figure 4.1 (b)). The numerically obtained DLF was 1.11.

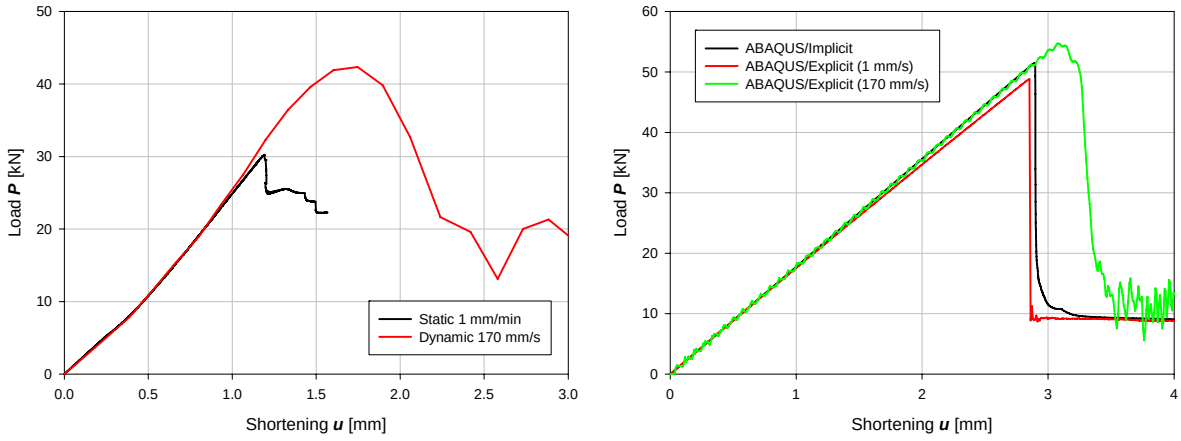

(a) (b)

Figure 4.1. Load-shortening curves of axially impacted Type 0 specimen.
(a) – experimental results; (b) – numerical results

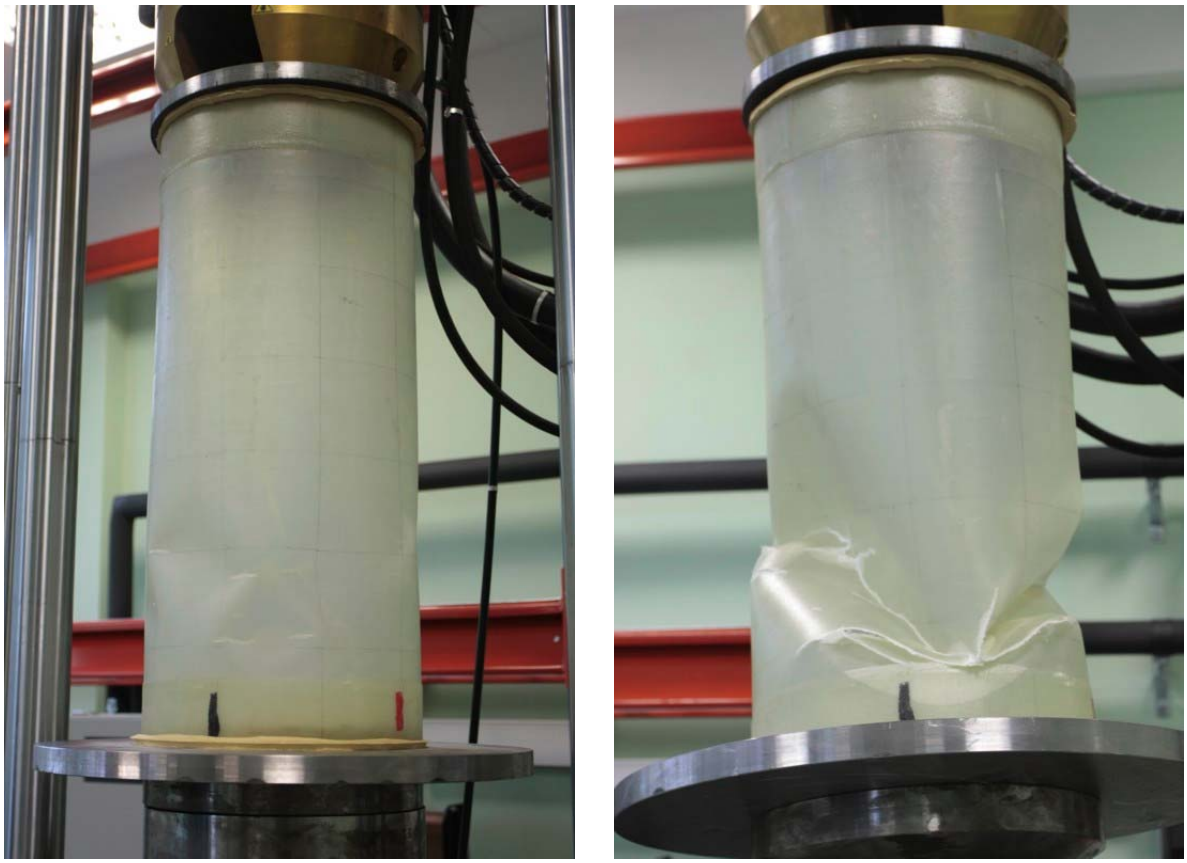

(a) (b)

Figure 4.2. Static buckling test of Type 0 specimen
(a) – Buckling shape; (b) – the collapsed specimen after the dynamic test

Both numerical and experimental results show effect of the higher loading velocity on buckling load of the cylindrical shells. The change in load-shortening curves is present in both cases, with smoother transition to the post-buckling part. However, the obtained DLFs are significantly different. Another drawback in the experimental results is the low data acquisition frequency used, as only about dozen of points have been recorded during the loading period.

Considering the aforementioned facts, the discrepancy between the numerically and experimentally obtained buckling loads and DLFs was too high for qualitative conclusions. However, the increase of the buckling load due to increase in the loading rate was obvious.

4.2. Type 1 specimens

The drawbacks of the Type 0 specimens and the testing procedure were corrected by introducing Type 1 specimens and switching to cyclic buckling software of the Instron test rig, described in Chapter 2.3.2. The use of cyclic software resulted in loading with a half-wave pulse as in impact test, rather than loading with constant velocity into the buckling.

Nevertheless, since the dynamic loading rates were relatively low, the maximum loads registered are considered critical in this part of study. Triangular loading history has been chosen because of the limited maximum velocity and acceleration of the hydraulic actuator on one hand, and need to stop the actuator after the buckling to keep the specimen undamaged on the other hand. The use of the triangular pulse allowed maximizing the loading rate at the moment of buckling and also is somewhat similar to the loading history used in the numerical study. The typical history of actuator position, velocity, acceleration and load on specimen are presented in Figure 4.3.

First, series of quasi-static and dynamic buckling tests have been performed on Type 1 specimens. The quasi-static tests have been performed with constant loading with velocities of 1 mm/min and 3 mm/min. The dynamic buckling tests were displacement-controlled, with initial velocity of 170 mm/s, which is close to the maximum velocity that can be obtained with the Instron equipment. The buckling loads and corresponding DLFs are summarized in Table 4.1 and example load-shortening curves are presented in Figure 4.5 (a).

After collecting results of dynamic buckling of the Type 1 specimens at maximum initial velocity allowed by the equipment, another series of tests were performed on one specimen of each configuration that had displayed most consistent results in previous test series. The loading velocity for the quasi-static test has been kept 3 mm/min and the maximum velocities for the dynamic tests were 40 mm/s, 70 mm/s, 140 mm/s and 170 mm/s. Sample displacement-time histories are presented on Figure 4.4 (b).

The load-shortening curves for each of the considered specimens are presented in Figure 4.5, and the buckling loads at different loading histories and corresponding Dynamic Load Factors (DLF) are summarized in Table 4.2.

The general tendency of increase in DLF along with increase of loading velocity is evident. However, due to the limited maximum loading velocity, additional numerical studies had to be performed.

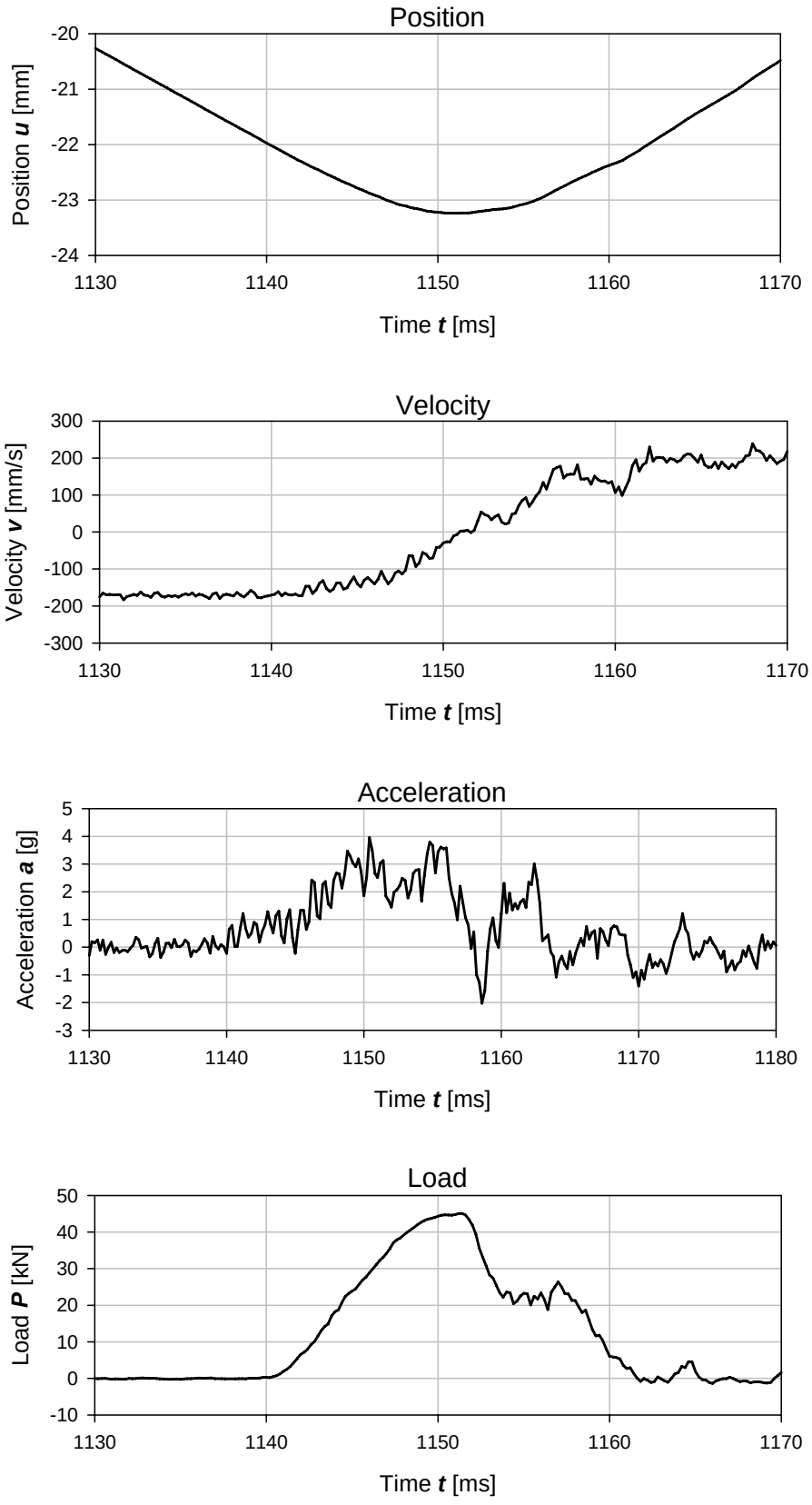

Figure 4.3. Typical time histories of the pulse buckling test

Table 4.1. The static and dynamic buckling loads of Type 1 specimens

	L, mm	D, mm	1 mm/min Pcr, kN	170 mm/s Pcr, kN	170 mm/s DLF	3 mm/min Pcr, kN	170 mm/s Pcr, kN	170 mm/s DLF
RTU #1-1	660	500	29.06	37.92	1.30	30.23	40.00	1.32
RTU #1-2	660	500	27.11	38.58	1.42	27.98	38.10	1.36
RTU #1-3	660	500	30.64	39.73	1.30	31.04	41.10	1.32
RTU #1-4	660	500	37.15	46.31	1.25	38.87	48.00	1.23
RTU #1-5	660	500	30.83	41.60	1.35	27.40	39.23	1.43
RTU #1-6	660	500	25.71	37.52	1.46	26.03	37.28	1.43
RTU #1-7	660	500	32.22	42.92	1.33	31.45	40.69	1.29
RTU #3	560	300	38.58	41.02	1.06	38.21	42.36	1.11
RTU #4	560	300	40.39	44.19	1.09	37.53	48.00	1.28
RTU #5	560	300	33.78	41.31	1.22	32.05	40.60	1.27
RTU #7	560	300	33.03	39.05	1.18	30.07	36.53	1.21
RTU #9	660	300	20.20	27.61	1.37			
RTU #10	660	300	20.24	25.88	1.28	20.26	23.15	1.14
RTU #11	660	300	33.94	41.59	1.23	34.86	42.83	1.23
RTU #6	400	300	36.40	41.79	1.15	35.76	37.28	1.04
RTU #12	400	300	35.80	39.09	1.09	35.36	40.51	1.15
RTU #13	400	300	38.29	42.34	1.11	38.30	41.95	1.10
RTU #16	400	300	40.07	45.09	1.13	40.82	47.66	1.17
StdDev, %			18.88	13.31	9.68	16.69	14.14	9.22

Table 4.2. The dynamic buckling loads at different velocities

		Specimen			
		RTU #1-4	**RTU #4**	**RTU #11**	**RTU #16**
Velocity	**L, mm** **R, mm**	**660** **500**	**560** **300**	**660** **300**	**400** **300**
3 mm/min	Pcr	36.24	40.60	34.64	41.69
40 mm/s	Pcr	42.81	42.68	34.09	45.23
	DLF	1.18	1.05	0.98	1.08
70 mm/s	Pcr	44.74	46.17	35.85	46.74
	DLF	1.23	1.14	1.03	1.12
140 mm/s	Pcr	46.47	48.37	39.28	48.21
	DLF	1.28	1.19	1.13	1.16
170 mm/s	Pcr	46.37	48.53	41.57	47.52
	DLF	1.28	1.20	1.20	1.14

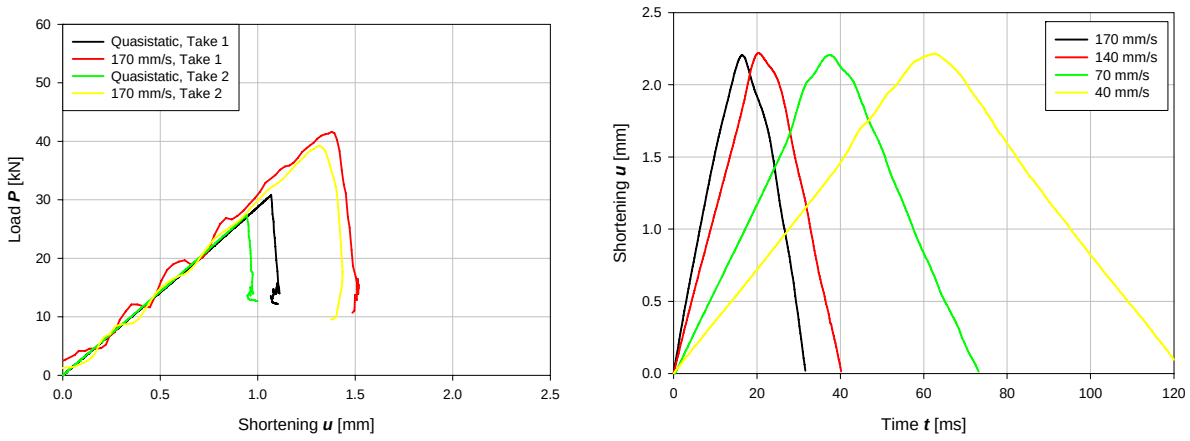

(a) (b)

Figure 4.4. Dynamic buckling test characteristics
(a) – Sample load-shortening curves of static and dynamic buckling tests on specimen RTU #5;
(b) – Shortening-time curves used for specimen RTU #4

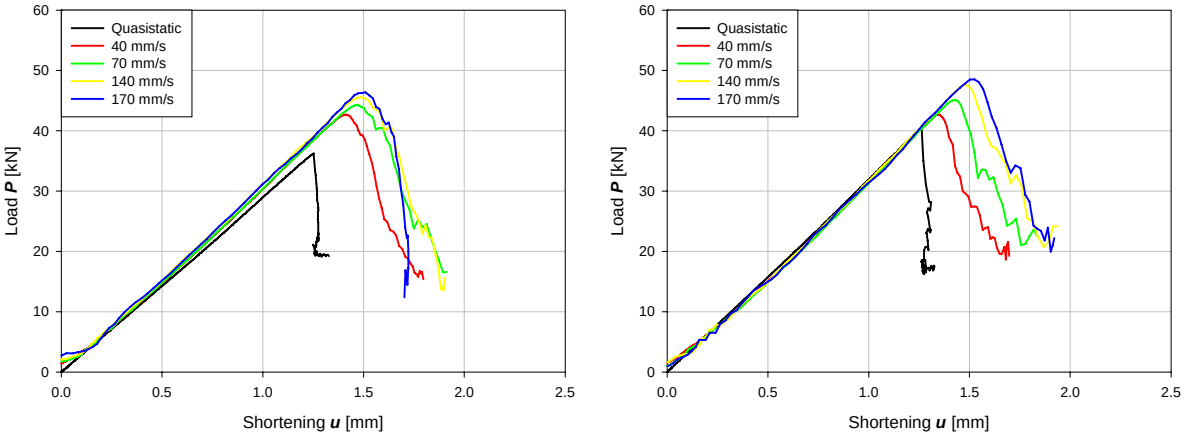

(a) (b)

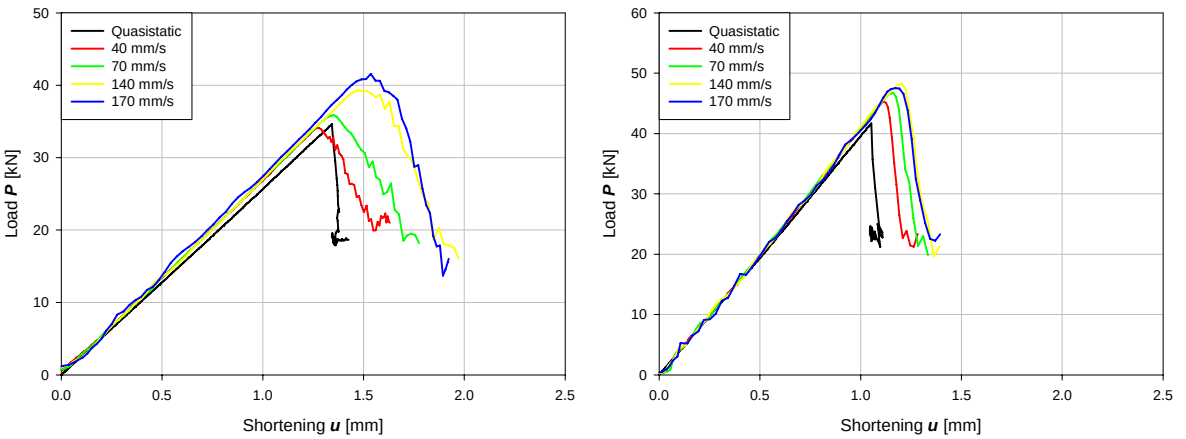

(a) (b)

Figure 4.5. Load-shortening curves at differend loading velocities
(a) – specimen RTU #1-4; (b) – specimen RTU#4; (c) – specimen RTU #11; (d) – specimen RTU #16

ABAQUS/Explicit finite element code has been used to carry out numerical simulations of the buckling experiments performed on Type 1 specimens. Additionally, ABAQUS/Standard has been used for linear buckling and natural frequency analyses. The loading rate of 10 mm/s has been chosen for the simulations of quasi-static tests.

The S4R four node shell elements have been employed and, according to the results of the mesh sensitivity analysis (Eglitis et al., 2009), the nominal dimension of an element was chosen to be 1/20 of the shell radius R.

The spherical bearing, which is present in the experimental set-up, has been modelled as a set of rigid elements that connects the master node located at the centre of rotation of the bearing with the lower edge of the specimen. All the translations are constrained for this master node, but all the rotations are allowed. The only degree of freedom allowed at the upper edge is translation in axial direction, where the load is introduced.

The imperfection sensitivity of axially compressed cylindrical shells has been acknowledged, however, no equipment was available for measurement of Type 1 specimens, therefore imperfection influence on dynamic buckling behaviour has been studied numerically using thee different imperfection shapes:

- First eigenmode of eigenvalue buckling analysis performed on the model ('checkboard' pattern, Figure 4.7 (a))
- First eigenmode of eigenvalue buckling analysis, performed on the model with isotropic material properties (axisymmetric pattern, Figure 4.7 (b))
- Imperfections measured at Politecnico di Milano on Type 2-2 specimen (realistic pattern, Figure 4.7 (c))

The numerical models have been updated with each of the imperfection shapes considered and the experimental shortening-time histories have been simulated using ABAQUS/Explicit. Some of the obtained load-shortening curves for the model of specimen RTU #4 are presented in Figure 4.6. For each specimen, the imperfection shape that resulted in the best correlation with the experimental data (e.g. axisymmetric pattern for specimen RTU #4, in Figure 4.6) is considered to be the best representation of actual imperfections and used further in this study. It can be seen from the Figure 4.6 that dynamic buckling phenomenon is also imperfection sensitive, and for the same shortening-time histories the DLFs are dependent on the initial imperfection shape.

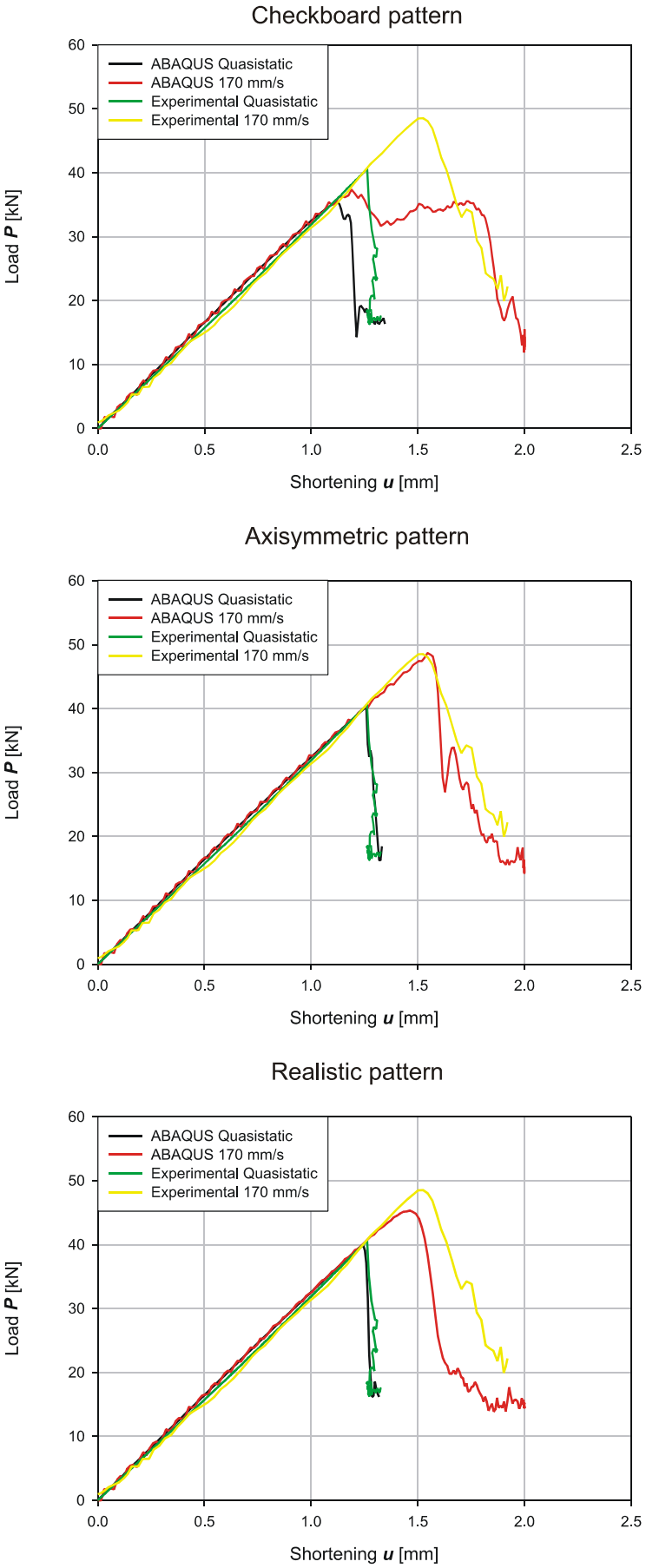

Figure 4.6. Imperfection influence on dynamic buckling

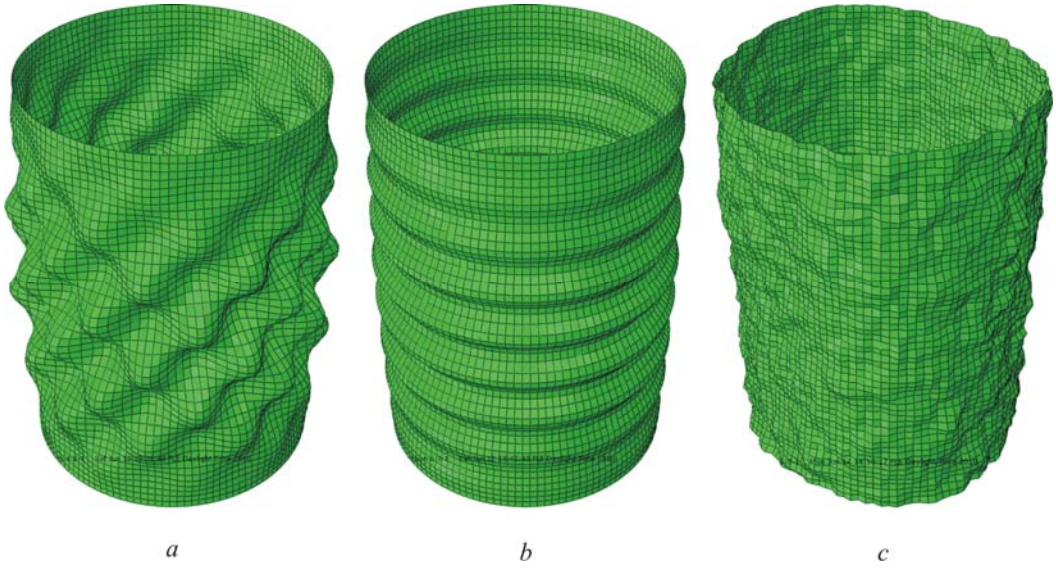

Figure 4.7. Imperfection shapes considered (not to scale)
(a) – checkboard; (b) – axisymmetric; (c) - realistic

The general tendency of increase in DLF along with increase of loading velocity is evident from the experimental results. However, due to the limited maximum loading velocity, additional numerical studies had to be performed. The results of the experimental and numerical investigation of the dynamic buckling behaviour of composite cylinders performed using Type 1 specimens have been reported in (Eglitis et al, 2010a).

Series of simulations have been carried out to construct a dynamic buckling load versus load duration plots for each specimen configuration. The loading rates were ranging from 1 kN/ms to 960 kN/ms, covering the range from 0.26 ms to 43 ms.

For shorter loading durations it is difficult to determine the critical load for a displacement-controlled simulation. Therefore, to study the dependency of DLF on the loading rate, the load is applied at given rates, and the out-of-plane displacements monitored. From these data, a Budiansky-Hutchinson plot (Budiansky and Hutchinson, 1964) is constructed for each simulation, and the load is considered critical when the maximum out-of-plane displacement of a node reaches 1 mm. This tolerance has been selected to exclude oscillations caused by dynamic loading. Example of these plots for specimen RTU #4 and different loading rates are presented in Figure 4.8.

In their study on dynamic buckling of cylindrical stringer stiffened shells Yaffe and Abramovich (2003) expected to obtain DLF<1 with load pulse duration of equal to half of longest natural bending period τ, similarly as in cases of columns and plates. However, their numerical results showed that the DLF could drop below unity, when loading period $T = 2a/c$, where a is the length of the cylinder and c is the speed of sound in the shell.

To make sure the study covers these critical areas, natural bending periods have been calculated using ABAQUS/Standard and speed of sound in the shell evaluated. The load durations that could lead to DLF<1 are summarized in Table 4.3.

The dependency of the dynamic buckling load on the load duration is presented in Figure 4.9 and experimental data is plotted along with the numerical results.

At lowest loading rates considered, buckling modes are similar to the static buckling mode, but with larger number of longitudinal waves (Figure 4.10 (a)). When the load duration approaches the critical $T=\tau/2$, the buckling mode starts to transform to an axisymmetric mode (Figure 4.10 (b)). Further increase of the loading rate and decrease of the load duration leads to axisymmetric buckling mode (Figure 4.10 (c)), and a slight drop of DLF can be observed when the load duration is close to $T = 2a/c$.

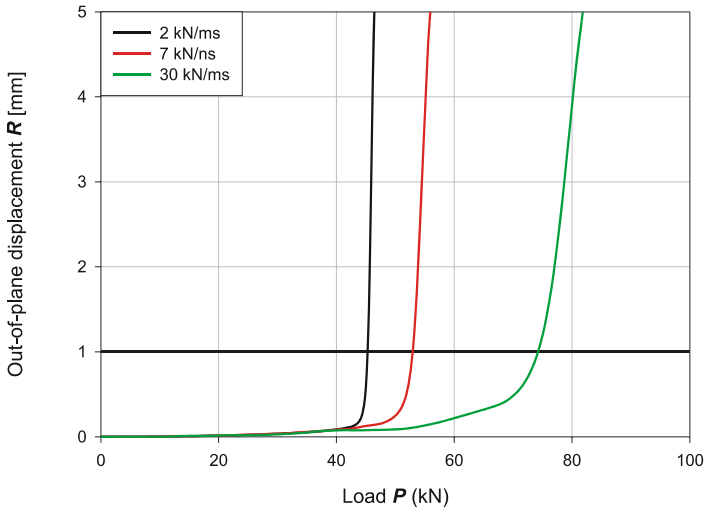

Figure 4.8. Budiansky-Hutchinson plot

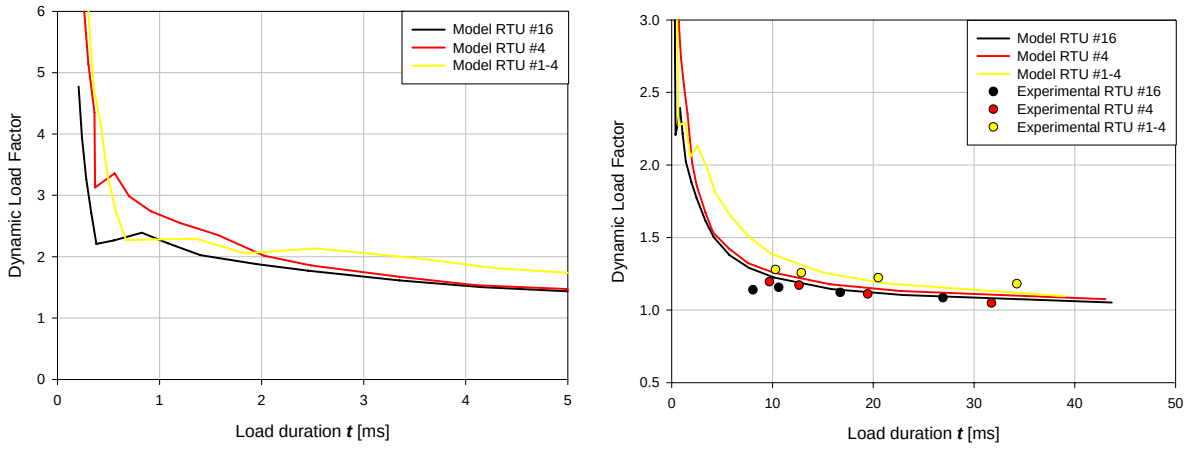

(a) (b)

Figure 4.9. DLF versus load duration, specimens Type 1
(a) – $0 < t < 5$; (b) – $0 < t < 50$

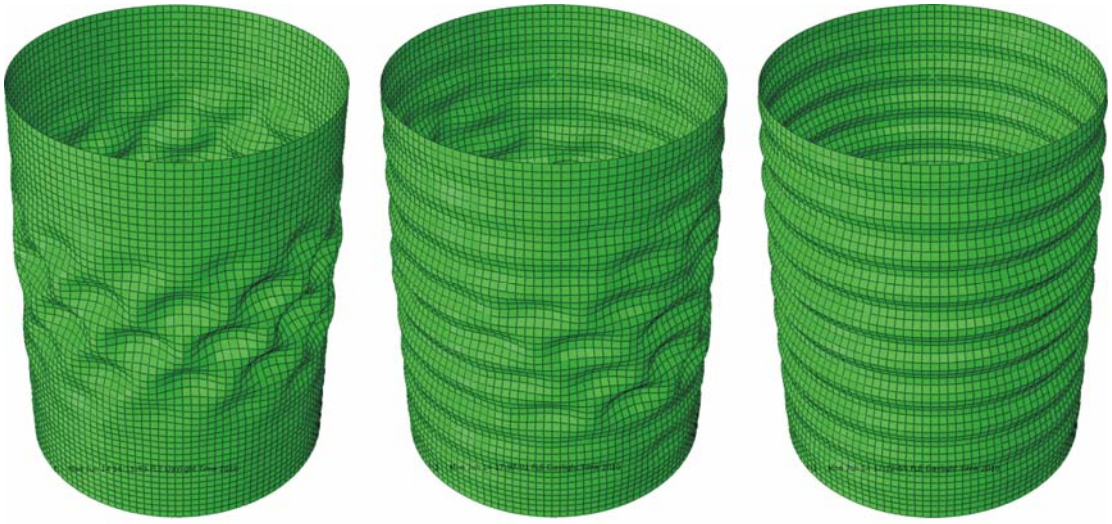

Figure 4.10. Dynamic buckling shapes (not to scale)
(a) – T > τ / 2; (b) – T = τ / 2; (c) – T < τ / 2

Table 4.3. Natural periods of Type 1 specimens

Model	$T=\tau/2$ [ms]	$T = 2a/c$ [ms]
RTU #16	1.46	0.31
RTU #4	2.02	0.43
RTU #1-4	3.03	0.51

4.3. Type 2 specimens

4.3.1. Tests using the hydraulic machine

The Type 2 specimens have been produced at Riga Technical University and brought to Politecnico di Milano for testing. The geometry of Type 2 specimens has been measured as described in Chapter 3.1.2., and the static tests have been performed as described in Chapter 3.2.2. prior the dynamic buckling tests.

There were two different methods used to perform the dynamic buckling tests: The hydraulic test rig was used to perform the tests with load durations of 50 ms and more, and the drop-tower set-up was used to perform the tests with load durations of down to 10 ms.

Due to the limited velocity of the actuator, triangular shape of displacement-time function has been used for the highest velocity at the moment when buckling occurs. In order to study the differences in dynamic buckling behaviour at different load durations, a plateau is introduced in the displacement function or the velocity reduced (Figure 4.11).

The displacement measurements of the actuator are not matching the LVDT measurements of the specimen's shortening (Figure 4.12 (a)). As the LVDT sensors directly

measure the displacement between the end plates of the specimens, their measurements are considered the correct ones. However, due to the inductive principles that the LVDT displacement sensors are based on, they are unable to perform accurate measurements at velocities used in the dynamic buckling tests, as it can be seen from the Figure 4.12 (b), red curve. Therefore, the difference between the actuator displacement and LVDT measurements during the static tests has been approximated as a second-order polynomial, and this function has been used to adjust the actuator displacement measurements to obtain more accurate shortening data (Figure 4.12 (b), brown curve).

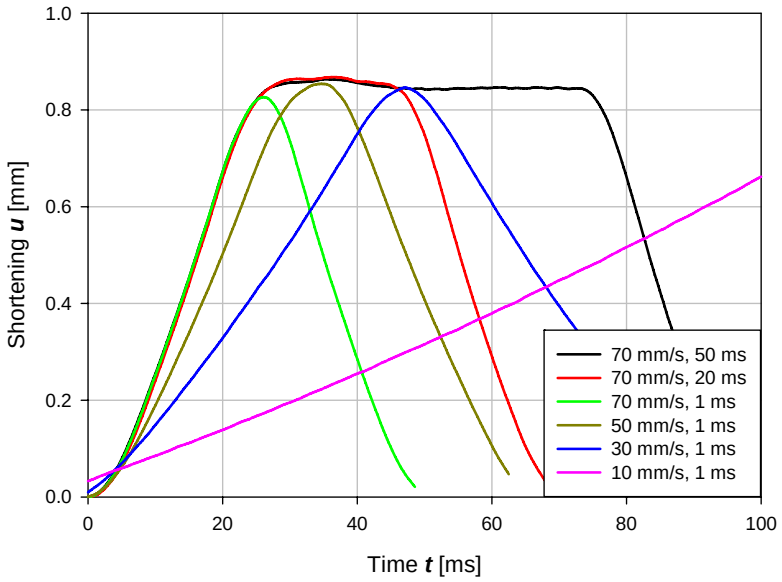

Figure 4.11. Shortening-time histories used for the dynamic buckling tests

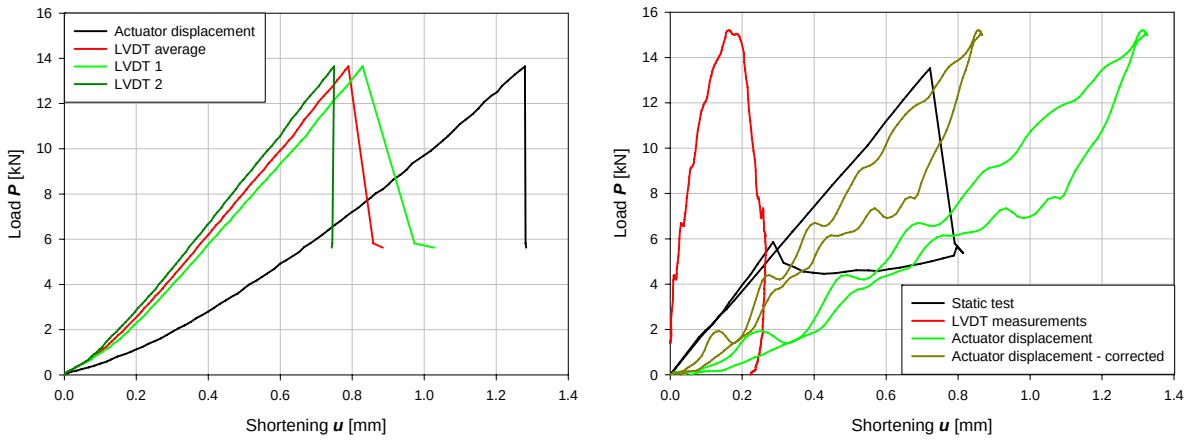

(a) (b)

Figure 4.12. LVDT versus actuator displacement measurements
(a) – static test; (b) – dynamic test

Total of 84 dynamic buckling tests have been performed on specimens Type 2-1 and Type 2-2 with various loading velocities and plateau lengths. For all of the tests the DLFs are calculated and also estimated from the strain measurements using the formula (3.1) to verify if no dynamic effects have influenced the measurements. While the estimated DLFs are within 2.5% of the DLFs calculated from the load cell measurements for the specimen Type 2-2, in case of specimen Type 2-1 the estimated DLFs are in average 8.4% lower than the measured ones. Therefore, the load cell measurements are omitted and the load estimations from strains are used for calculation of the DLFs.

While keeping the maximum velocity of the actuator, the plateau lengths have been varied between 50, 20 and 1 ms, with corresponding load pulse durations of 90, 65 and 50 ms, respectively. The results are presented in the Figure 4.13. It is seen from the graphs that the buckling loads generally are independent of the plateau lengths.

The influence of the prescribed maximum displacement has been studied while keeping the plateau of 1 ms and maximum velocity of the actuator. It is seen from the Figure 4.14 that the higher displacements result in the same load level, while the lowest displacement results in slightly lower buckling loads. This can be explained by different velocities of the actuator at the moment when the buckling occurs.

The tests with varying loading velocity have been performed on specimen Type 2-2 only. The plateau has been kept 1 ms for these tests and the load pulse durations were 50, 60, 90 and 250 ms. Figure 4.15 show that the lowest loading velocities result in lower buckling loads and displacements, however, the difference is within 5%.

Specimen Type 2-2 has been repeatedly tested with maximum velocity and gradually increasing maximum displacement to find the highest non-buckling loads experimentally. The graph of the highest non-buckling loads along with the lowest buckling loads for each velocity considered is presented in Figure 4.16. Because of the imperfection sensitivity of the specimen in some tests the cylinder did not loose stability at higher load than buckling loads measured in other tests. Nevertheless, a slight increase of the highest non-buckling load with the increase of loading velocity can be observed.

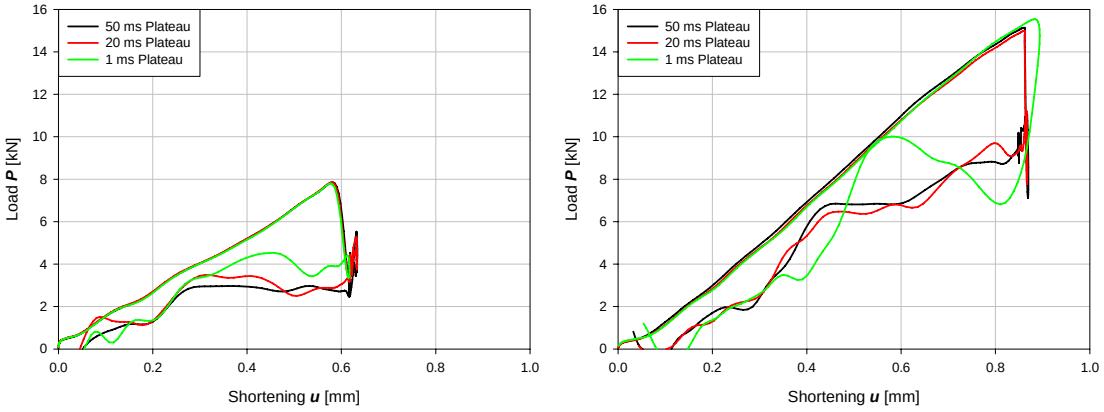

Figure 4.13. Influence of plateau length
(a) – specimen **Type 2-1**; (b) – specimen **Type 2-2**

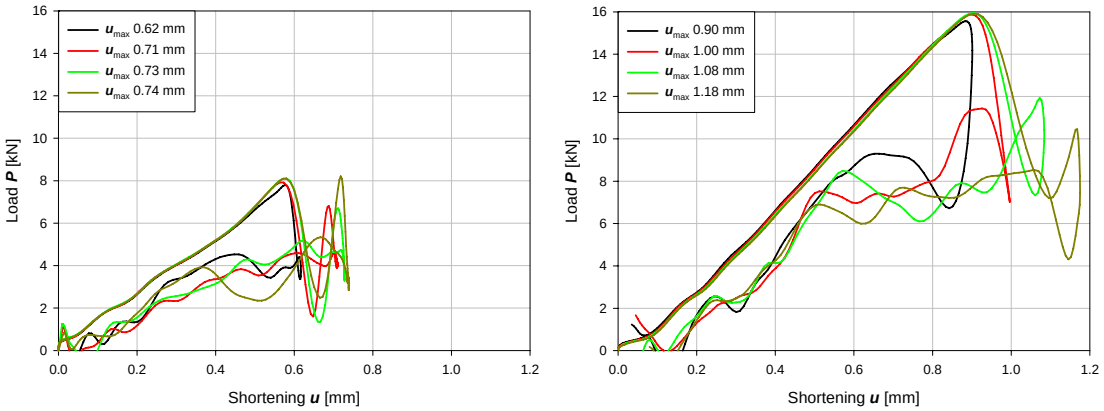

Figure 4.14. Influence of maximum displacement
(a) – specimen **Type 2-1**; (b) – specimen **Type 2-2**

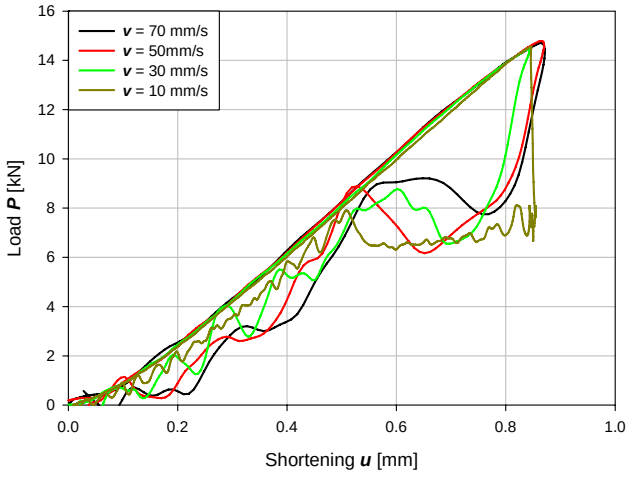

Figure 4.15. Influence of the loading velocity

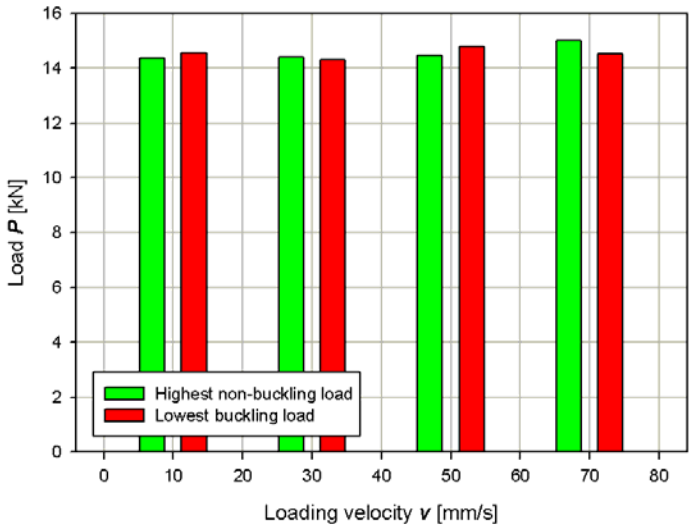

Figure 4.16. Highest non-buckling and lowest buckling loads

Since adequate numerical models of the Type 2 specimens could not be elaborated due to unknown initial stress state in the specimens, only experimental dynamic buckling results are presented.

The use of the hydraulic testing rig allowed performing dynamic buckling tests with loading velocities of 10 to 70 mm/s, which resulted in load pulses with length of 50 ms and more. DLFs from 0.94 to 1.10 have been obtained for specimen Type 2-1 and from 1.08 to 1.21 for specimen Type 2-2.

Different loading parameters have been varied to study their influence on the buckling load of the GFRP cylinders. First of all, keeping the maximum velocity constant (70 mm/s), the assigned maximum displacement of the actuator has been varied. The maximum actual shortening versus DLF scatter plot is presented on Figure 4.17 (a). The DLF is the lowest for the lowest shortening and increases until a constant value soon, and it is true for both specimens. It can be explained by the shape of the shortening-time function of the actuator (Figure 4.11) – at the lowest buckling displacement, the loading velocity is lower at the moment of buckling than in all the cases with higher maximum displacement.

Next, the effect of plateau length in the displacement – time function has been studied wile keeping the loading velocity constant. A scatter plot of load pulse duration versus DLF is presented in Figure 4.17 (b). It must be noted that there have been three plateau lengths used – 1 ms ($\tau \approx 45$ ms), 20 ms ($\tau \approx 65$ ms) and 50 ms ($\tau \approx 90$ ms). The longer the time duration at each plateau length, the higher is the maximum displacement. The trend present in the is

present in this case, too – the lowest displacements result in lower DLFs, because of the lower loading velocity at the bucking moment.

Finally, the tests were conducted on specimen Type 2-2 only with varying the loading velocity while keeping the plateau length of 1 ms and adjusting the maximum displacement to achieve buckling. The average velocity versus DLF plot is presented in Figure 4.17 (c). The slower tests have smaller scatter of the buckling loads, while the tests with velocity of 50 mm/s and 70 mm/s result in DLFs of up to 1.2. However, the lowest DLFs achieved with each velocity are similar.

A sample buckling shape progression of specimen Type 2-1 under the shortest load pulse filmed with a high-speed camera at a frame rate of 1000 fps is presented in Figure 4.18. The similarity with the static buckling shape (Figure 3.19) is obvious, so one must conclude that at the given low loading rates the buckling happens in the same manner as under static loading and only the inertial forces counteracting the 'escaping motion' of the structures are influencing the increase of the buckling load.

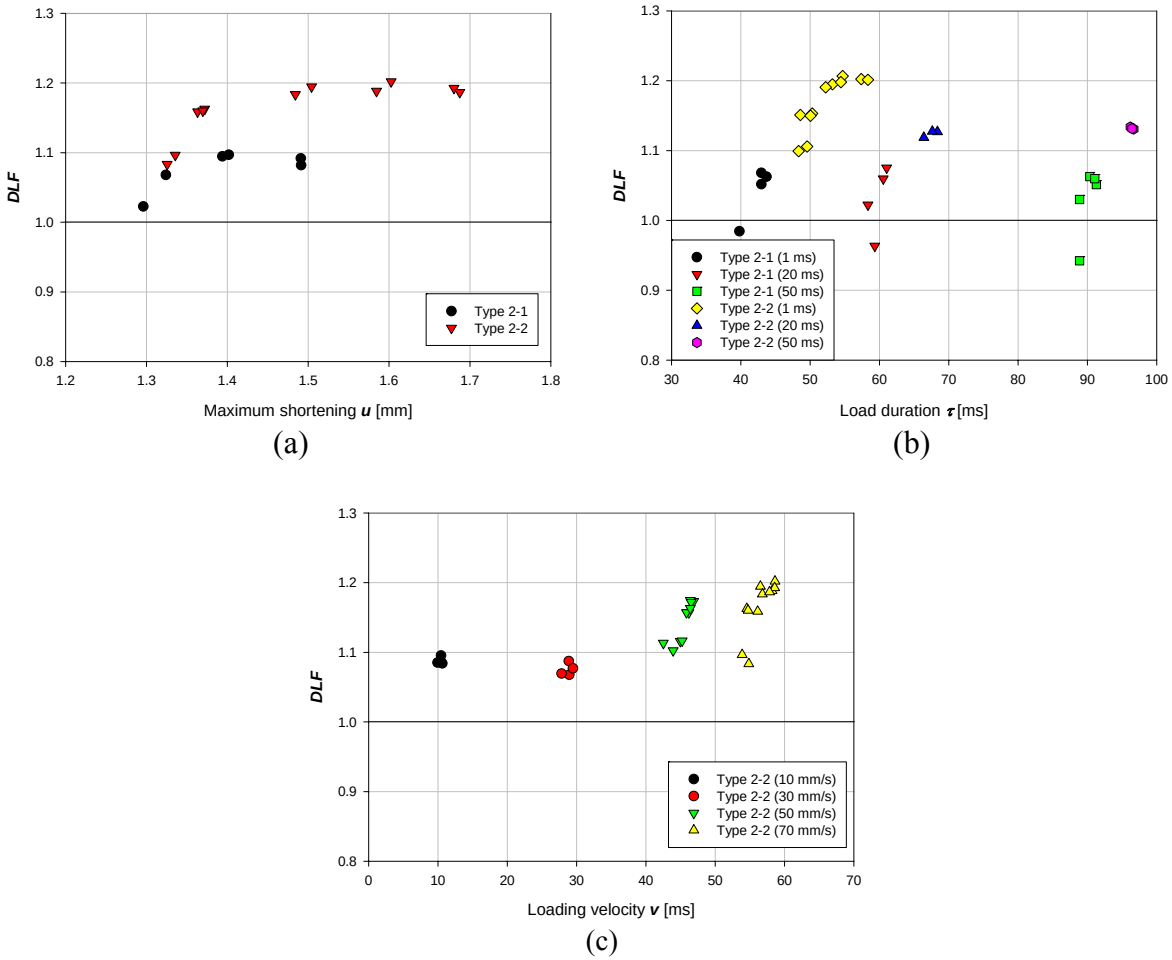

Figure 4.17. Influence of loading parameters on the buckling load
(a) – maximum displacement; (b) – plateau length; (c) – loading velocity

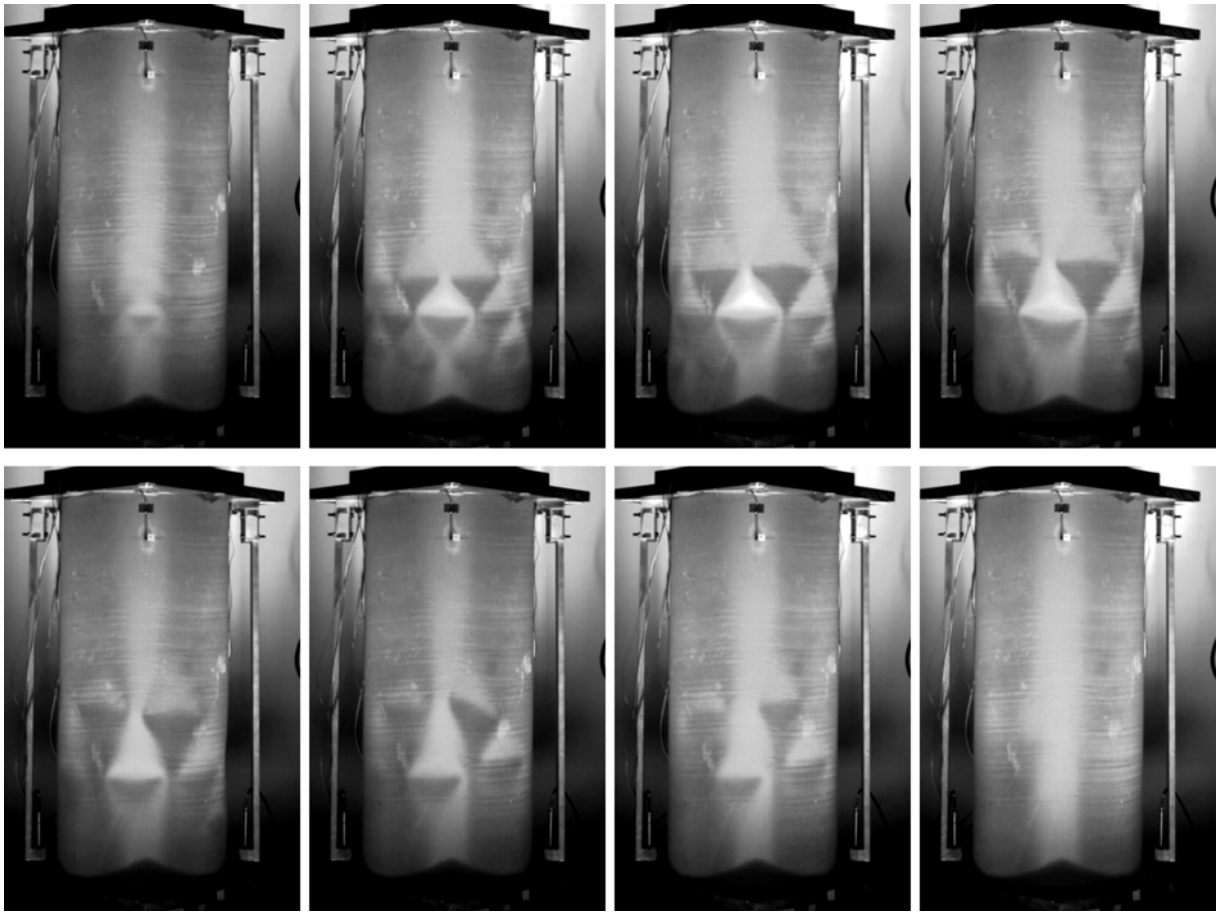

Figure 4.18. Dynamic buckling shape development of specimen **Type 2-1** (1000 FPS)

4.3.2. Tests using the drop tower

In order to achieve shorter load durations than hydraulic test rigs can provide, the specimens have been tested using a drop tower described in Chapter 2.3.4. However, once again the maximum loading rate was constrained by the need to keep the specimen undamaged, and therefore the impacts could be only with the lowest energy.

Load cell, strain gauge and accelerometer measurements have been recorded with frequency of 12.5 kHz during every test, and the evolution of the buckling shape has been filmed using a high-speed camera at 2000 frames per second. Typical strain gauge, accelerometer and load cell measurement histories are presented in Figure 4.19.

Due to the significant mass between the load cell and the loaded end of the specimen, the load cell measurements do not represent the actual load history of the cylinder. The load estimation approach using the strain measurements did not work well, too, because after few impact tests, most of the strain gauges stopped working. However, knowing the mass between the load cell and the accelerometer measurements, it is possible to estimate the reaction history of the cylinder:

$$m \cdot a = P - R;$$
$$R = P - m \cdot a, \tag{4.1}$$

where m is the mass between the load cell and the cylinder, a is the acceleration measured by the accelerometer, P is measured by the load cell and R is the reaction of the cylinder (Figure 4.20 (a)). The end shortening of the specimen is estimated by numerically integrating the accelerometer measurements through time. Sample load-shortening curves, where load is obtained from load cell measurements, estimated from strains and calculated from (4.1) are presented in Figure 4.20 (b).

Dynamic pulse buckling tests have been performed using various dropping masses and cross-sections of energy-absorbing steel honeycomb, therefore changing the magnitude and duration of the load. The higher load magnitude has been achieved by stiffer inserts and longer duration by softer inserts in combination with greater impact energy. Load-shortening curves of Type 2 specimens obtained with different impact energies are shown in Figure 4.21.

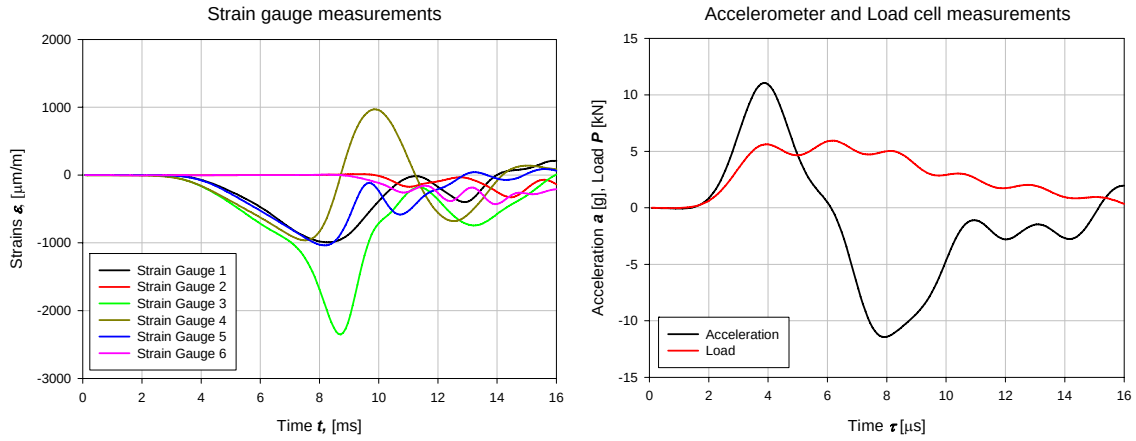

Figure 4.19. Typical measurements during the drop-tower test

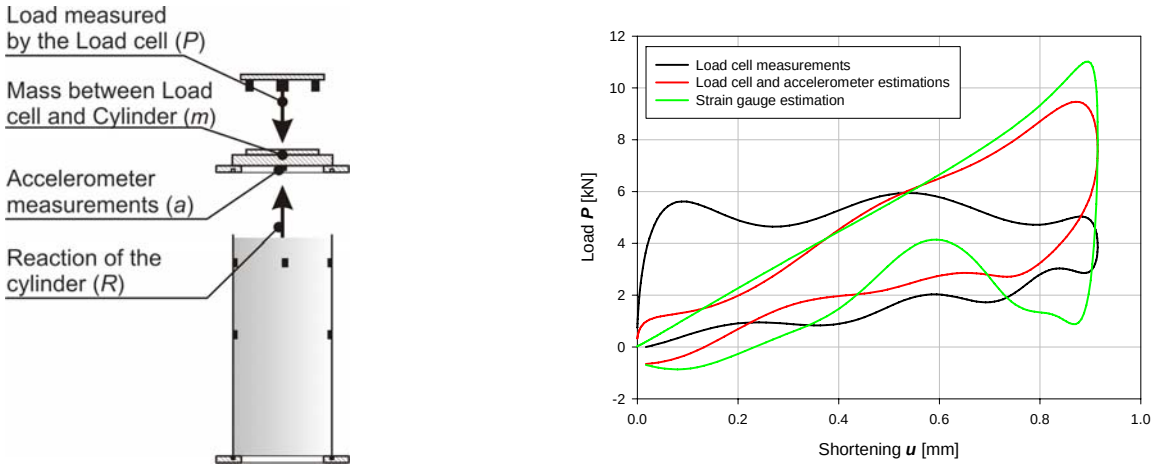

(a) (b)

Figure 4.20. Estimation of the load
(a) – schematic; (b) – load-shortening curves

The tests performed on Type 2 specimens in the drop tower allowed to investigate the buckling of the GFRP cylinders under load durations ranging from 12 to 33 ms. However, due to the many unknown factors influencing the measurements, the results present only the trend and should be regarded with caution. The DLF versus load duration scatter plots are constructed and presented in Figure 4.22 for both specimens.

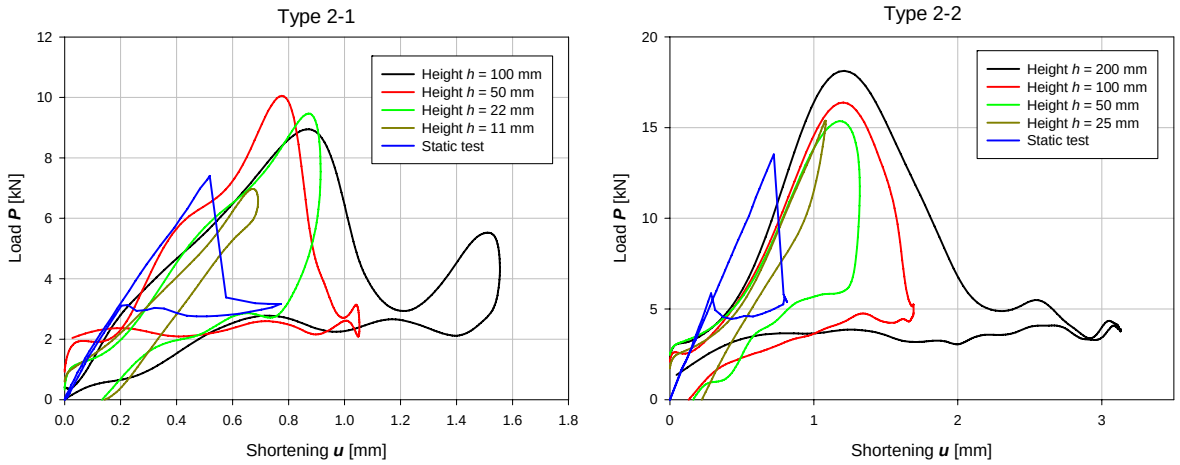

(a) (b)

Figure 4.21. Load-shortening curves of Type 2 specimens from drop-tower experimens (a) – specimen **Type 2-1**; (b) – specimen **Type 2-2**

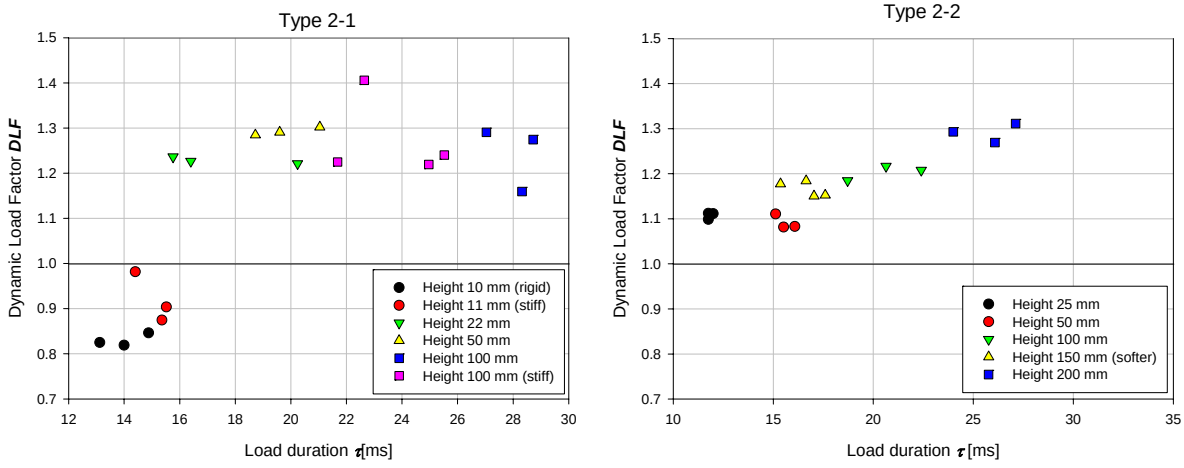

(a) (b)

Figure 4.22. DLF versus load duration plots obtained from drop-tower experiments (a) – specimen **Type 2-1**; (b) – specimen **Type 2-2**

Two result groups can be distinguished among the results of specimen Type 2-1 tests: one with DLF>1 and the other with DLF<1. The DLFs range from 1.16 to 1.41 in the first group and they have been achieved using 'normal' stiffness metal honeycomb inserts and various drop heights. The results obtained with honeycomb insert with 50 % higher stiffness and relatively high impact energy also are within this group, and the resulting load duration is around 24 ms, which is lower than in the tests with the same impact energy, but a 'normal'

stiffness insert. The DLFs range from 0.82 to 0.98 in the second group, and they have been obtained using the lowest impact energies combined with the 50 % stiffer honeycomb or virtually rigid steel insert between the dropping mass and the specimen assembly. These tests also feature the lowest impact durations within the test series. Unlike the seemingly random nature of the load duration – DLF distribution in case of specimen Type 2-1, the tests on specimen Type 2-2 show a trend of increase of the DLF with increase of the load duration. No DLFs lower than 1.0 have been observed with the specimen Type 2-2.

The drop-tower tests have been filmed using a high-speed camera at a frame rate of 2000 FPS. The specimens buckled in a somewhat random way, with buckling shapes not repeating. Unlike the dynamic buckling tests performed with the hydraulic machine, the buckling shape development observed during the drop-tower tests were substantially different than the buckling shape development during the static tests. The buckling shape development during the test with the lowest obtained DLF is presented in Figure 4.23 and the buckling shape development during the test with the lowest pulse duration among those with DLF > 1 is presented in Figure 4.24.

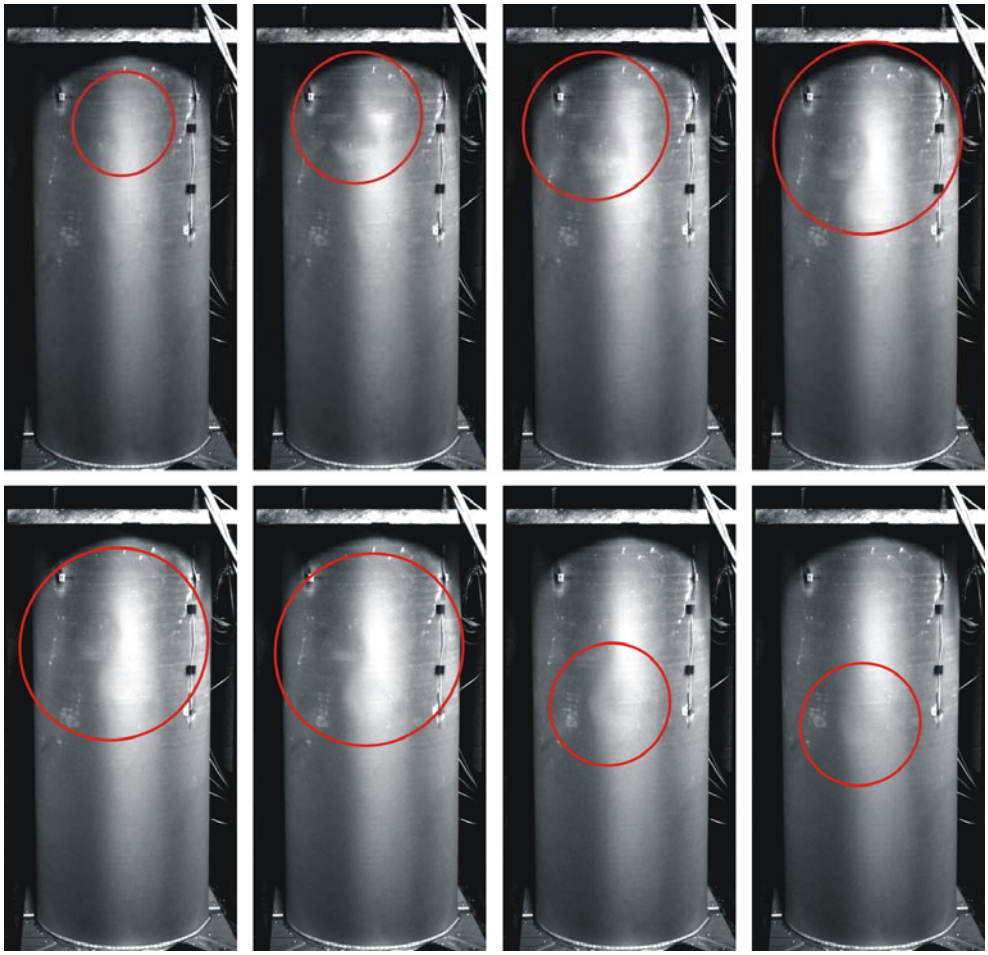

Figure 4.23. Dynamic buckling shape development of specimen **Type 2-1** (2000 fps)

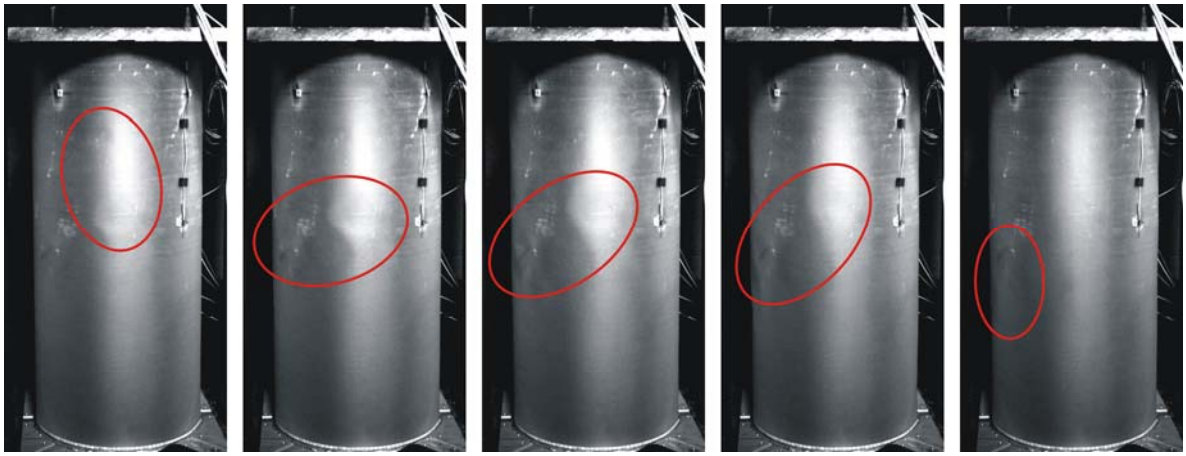

Figure 4.24. Dynamic buckling shape development of specimen **Type 2-1** (2000 FPS)

4.4. Dynamic buckling of Type 3 specimens

The physical dynamic buckling tests of Type 3 specimens have been performed at the laboratory of Riga Technical University, Institute of Materials and Structures, using the test rig described in Chapter 2.3.2. Unlike in the case of Type 1 specimens, the Type 3 specimens had three pairs of strain gauges applied for strain monitoring during the test.

The LVDT displacement sensors could not be used for the reason described in the Chapter 4.3.1. However, the discrepancy between the LVDT measurements and the displacement readouts of the machine is quite significant, as can be seen in Figure 4.25 (a). To obtain more realistic displacement measurements using the actuator displacement readouts, the difference of the displacement measurements using the two methods has been approximated, and the actuator displacement measurement corrected using the approximation.

The dynamic buckling tests have been performed for each Type 3 specimen repeatedly with prescribed velocities of 40, 90, 140 and 190 mm/s. Typical shortening time histories for each of the velocity are presented in Figure 4.26. These shortening time histories have been used for validation of the Finite Element models of the Type 3 specimens under dynamic loading conditions.

The difference between the load cell measurements and the load estimations from the strain measurements also have to be noted. While the difference between the two did not exceed 2% during the static buckling tests (Figure 4.25 (b)), the load estimations from strains were 5.0 % – 8.5 % lower than the load cell measurements during the dynamic buckling tests (Figure 4.25 (b)), depending on loading velocity. The estimations from strains are therefore assumed to be more accurate because the strains are measured directly on the specimen, while there is a significant mass between the shell and the load cell which can influence the measurement results. Therefore, the load cell measurements have been omitted and the

estimations from the strain gauge measurements have been used to calculate the DLFs and presented in the Load – Shortening curves. However, it is obvious that these estimations are inaccurate once the cylinder has buckled, as the load distribution gets non-uniform.

The buckling loads obtained experimentally and numerically and the corresponding DLFs are summarized in Table 4.4. Typical load – shortening curves of Type 3 specimens are presented in Figure 4.27, along with the numerical results. The numerically obtained buckling shapes are presented in Figure 4.28 and Figure 4.29.

The general tendency of increase in DLF along with increase of loading velocity is evident, as in case of all the previously described experimental investigations. In order to study the buckling behaviour of the Type 3 specimens at broader range of loading conditions than the experimental setup could provide, an additional numerical study has been performed. Accurate numerical models incorporated the initial geometrical imperfections of the specimens and were verified and validated against the experimental static and dynamic buckling test results.

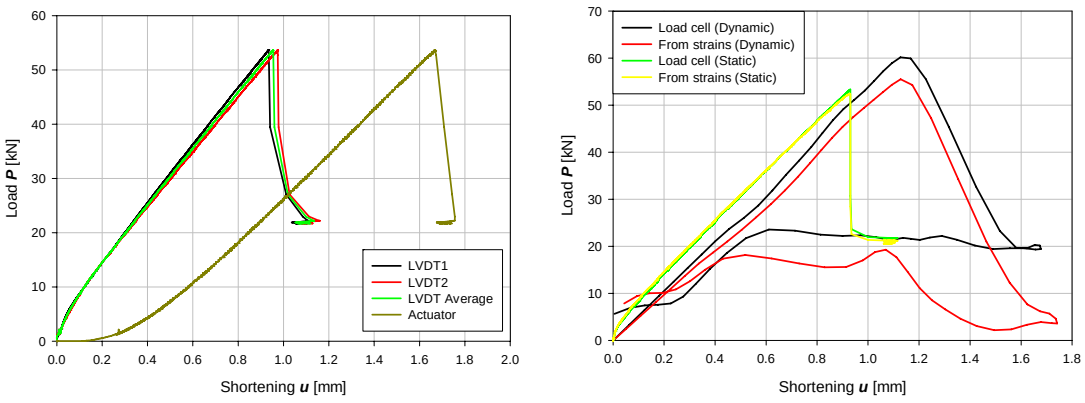

Figure 4.25. Discrepancies between different load and displacement measurements
(a) – the differences of LVDT and actuator displacement measurements;
(b) – the differences in load measurements for static and dynamic tests

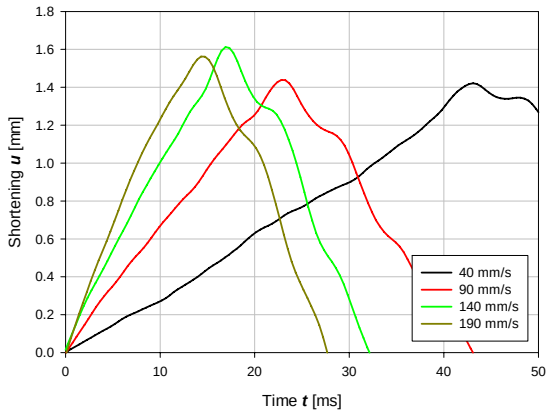

Figure 4.26. Shortening-time histories of the dynamic buckling tests

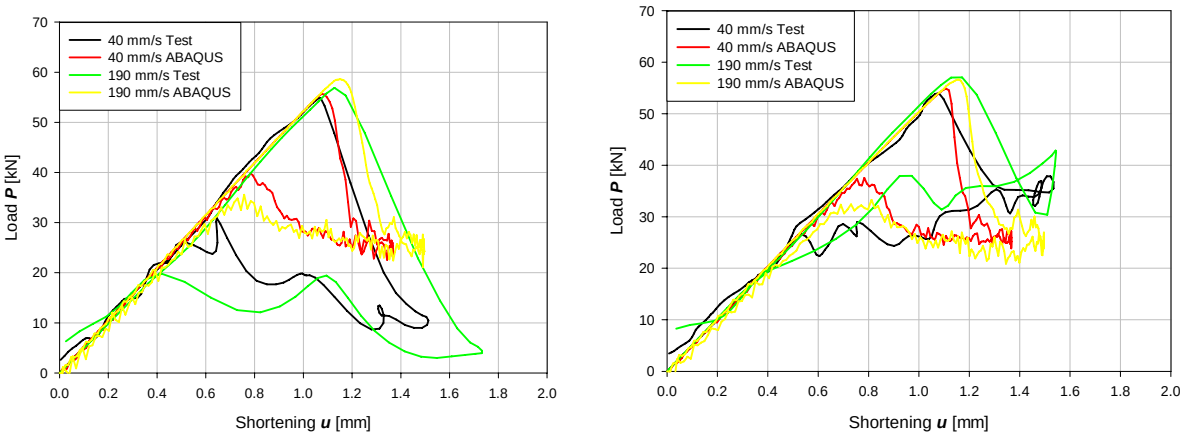

Figure 4.27. Typical dynamic buckling Load-Shortening curves of Type 3 specimens (a) – specimen **Type 3-1**; (b) – specimen **Type 3-2**

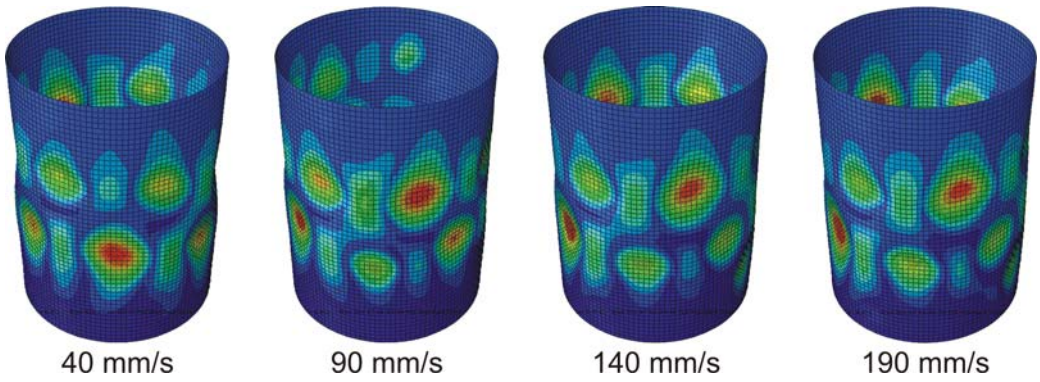

Figure 4.28. Numerical dynamic buckling shapes for specimen Type 3-1

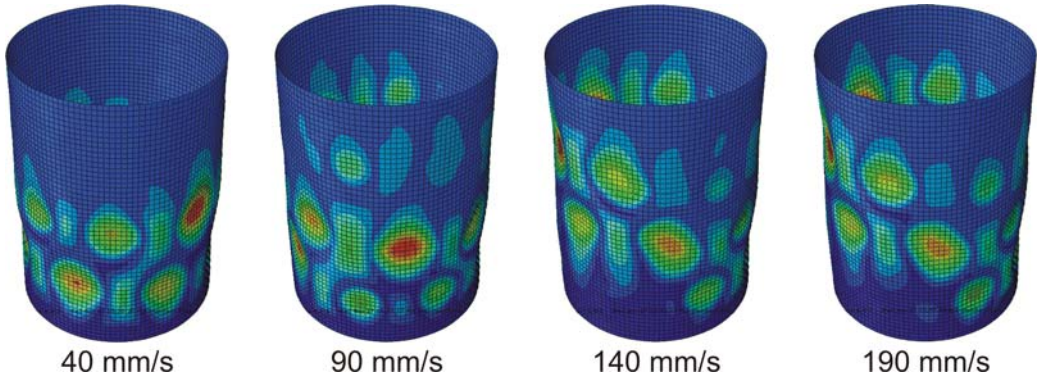

Figure 4.29. Numerical dynamic buckling shapes for specimen Type 3-2

Table 4.4. The dynamic buckling loads of Type 3 specimens

		Experimental			ABAQUS	
Specimen	**Velocity**	**Buckling load P_{cr} [kN]**	**Standard deviation**	**DLF**	**Buckling load P_{cr} [kN]**	**DLF**
Type 3-1	40	54.47	0.37	1.05	55.67	1.04
	90	54.96	0.29	1.06	56.92	1.06
	140	56.34	0.24	1.08	58.47	1.09
	190	56.39	0.39	1.08	58.59	1.09
Type 3-2	40	54.33	0.32	1.05	54.88	1.03
	90	55.54	0.39	1.07	55.63	1.04
	140	56.05	0.42	1.08	56.58	1.06
	190	56.51	0.73	1.09	56.65	1.06

Two types of loading have been considered in the numerical studies performed using the ABAQUS models of Type 3 specimens. Gradually increasing load with loading rates from 1 kN/ms to 1536 kN/ms resulted in DLFs from 1.02 to 4.48 and loading times from 56 ms to 0.14 ms. Suddenly applied load has been considered as well, and ABAQUS/Explicit dynamic simulations have been carried out with loads from 40 kN to 190 kN.

Budiansky-Hutchinson plots have been used to determine the buckling loads of gradually loaded cylinders, as described in Chapter 4.2. Maximum radial displacement tolerance of 1 mm has been used to determine the buckling loads of Type 3 specimens. However, Budiansky-Hutchinson plots could nod be constructed for suddenly applied loads, and the monitoring of maximum radial displacement could be misleading, as the harmonic response of the cylinder to the sudden application of the load results in amplitudes on the same order as buckling deformations. Therefore, the end shortening-time histories have been used to determine the time for which the shell withstands the given loads. Sample shortening-time curves of Type 3 specimens are presented in Figure 4.30.

In addition to the results obtained with the validated models, the buckling behaviour under sudden load has been studied using a Type 3-2 model without the initial imperfections, called model Type 3-0. The DLFs are calculated taking the static buckling load of the validated Type 3-2 model for better comparison.

The half of natural bending period and the period of the stress wave travelling from the one end of the cylinder to the other end and back are estimated numerically for the models of Type 3 specimens and are summarized in Table 4.5. The loading condition range has been chosen so the dynamic buckling in the region of these times is observed.

The dependency of the DLF on the load duration is presented in Figure 4.31. The curves for both gradually and suddenly applied loads are presented for comparison. Experimental results are also included in Figure 4.31 (a).

The general trend of DLF being higher at the shorter loading times is evident. However, there is a region around load duration of 0.60 ms where the growth of the DLF is not consistent in case of gradually applied load. This region does not coincide with the lowest natural periods of the shells in this case. It must be noted that the natural bending frequencies of a cylinder are closely spaced, and this load duration can match some higher-order bending modes. Analysis of the buckling modes associated with each loading time show that the buckling mode shapes also do not change around this region of inconsistent DLF growth. Sample buckling shapes along with the corresponding DLFs and times are presented in Figure 4.32 and Figure 4.33.

The DLF-time curves are more consistent in case of the suddenly applied load. However, the DLFs obtained for suddenly applied loads go as low as 0.8 for both imperfect models. Interestingly, the lowest buckling load increases only by 0.45 % if the imperfections are removed from the model in case of sudden load application, while the static buckling load increases by 55%. Buckling mode progression with increase of the suddenly applied load for models Type 3-1, Type 3-2 and Type 3-0 is presented in Figure 4.34 – Figure 4.36.

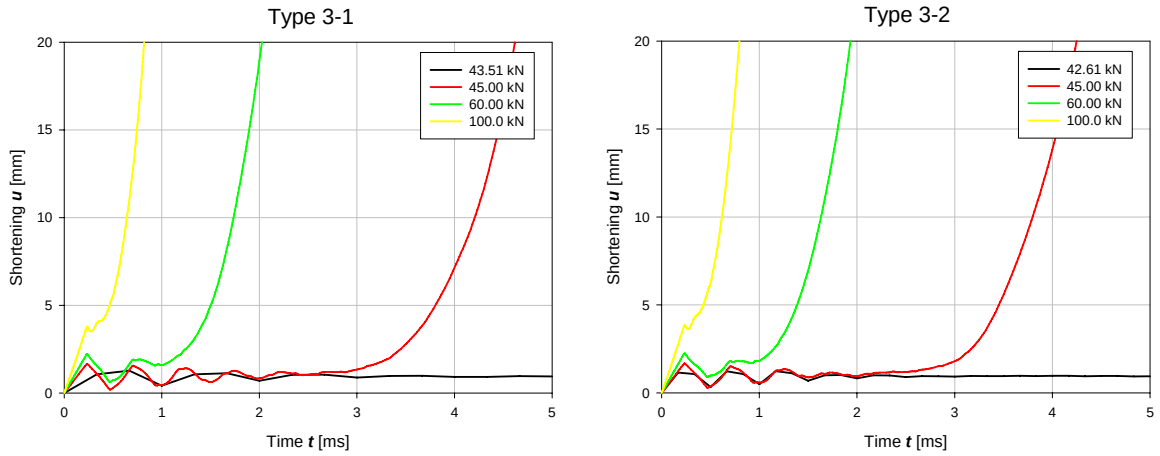

(a) (b)

Figure 4.30. Sample shortening-time histories for Type 3 specimens under sudden load (a) – specimen **Type 3-1**; (b) – specimen **Type 3-2**

Table 4.5. Natural periods of Type 3 specimens

Model	$T=\tau/2$ **[ms]**	$T = 2a/c$ **[ms]**
Type 3-1	1.35	0.24
Type 3-2	1.34	0.24

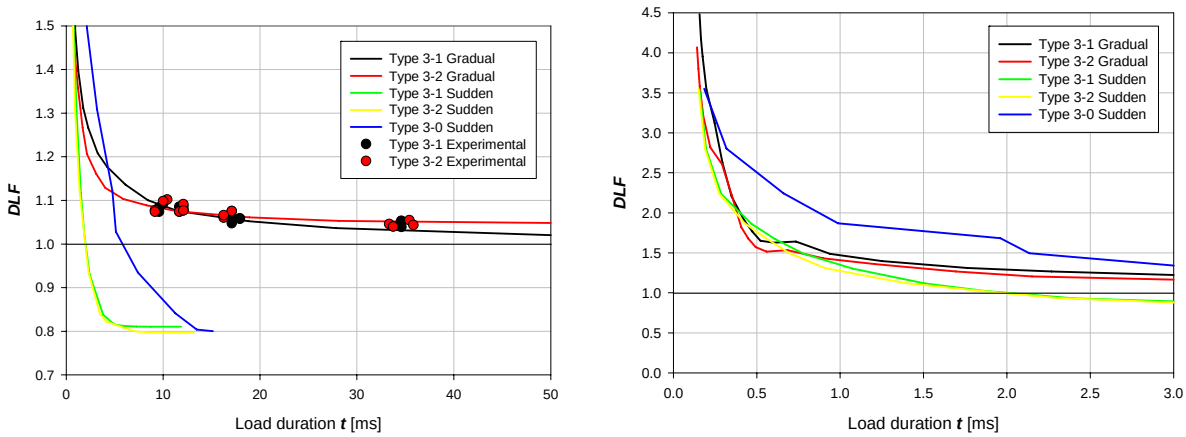

Figure 4.31. DLF versus load duration, Type 3 specimens
(a) – $0 < t < 50$; (b) – $0 < t < 3$

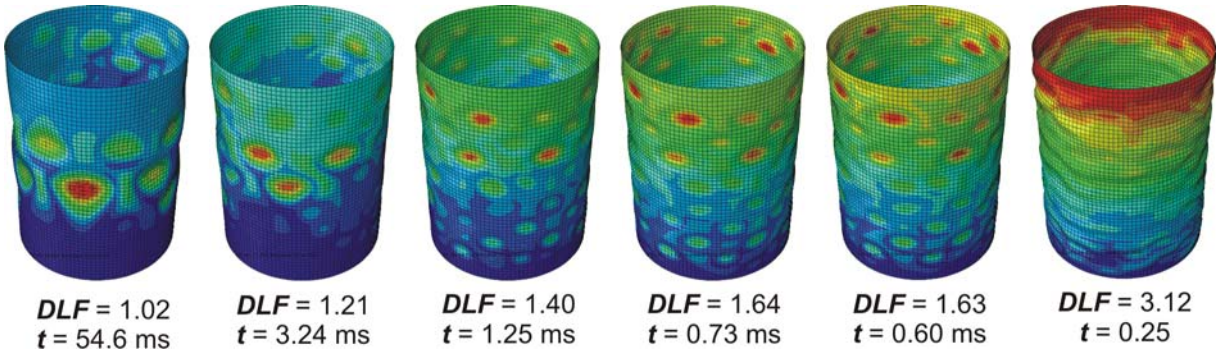

Figure 4.32. Buckling modes of specimen **Type 3-1** at different load durations

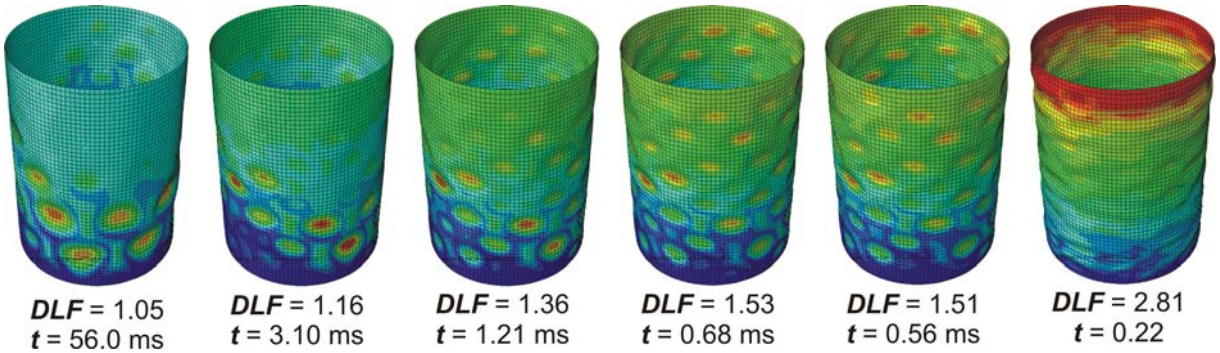

Figure 4.33. Buckling modes of specimen **Type 3-2** at different load durations

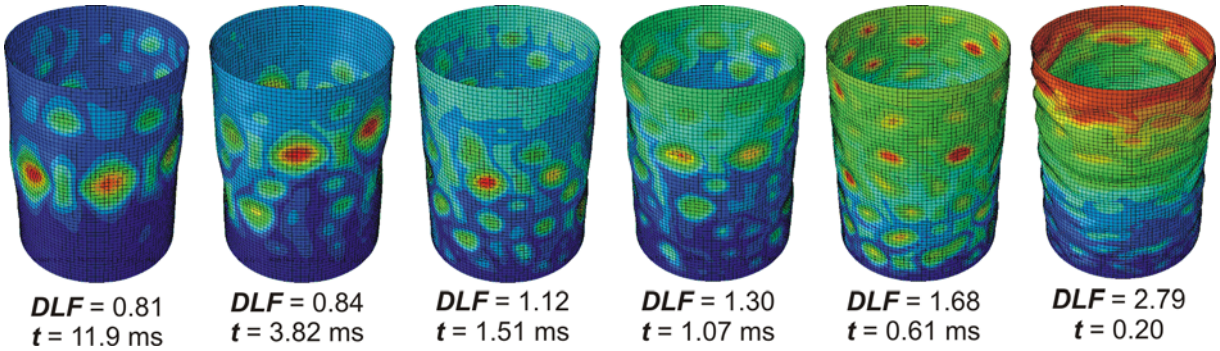

Figure 4.34. Buckling modes of model **Type 3-1** at different sudden load magnitudes

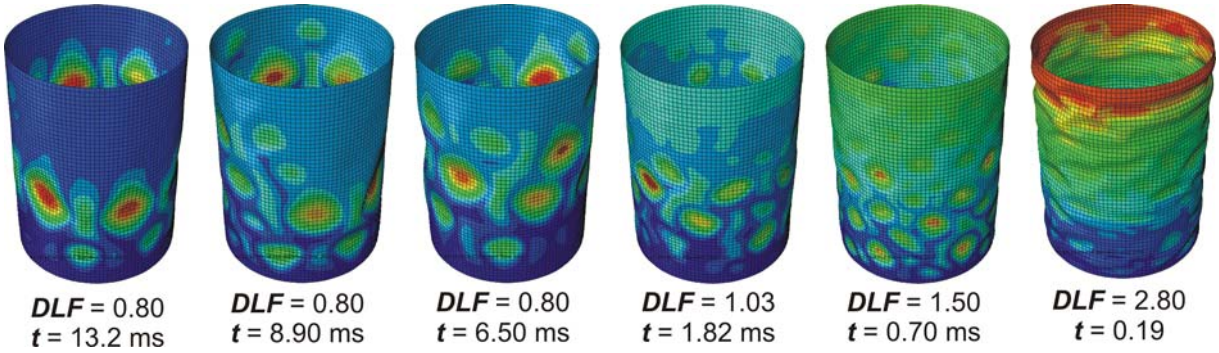

Figure 4.35. Buckling modes of model **Type 3-2** at different sudden load magnitudes

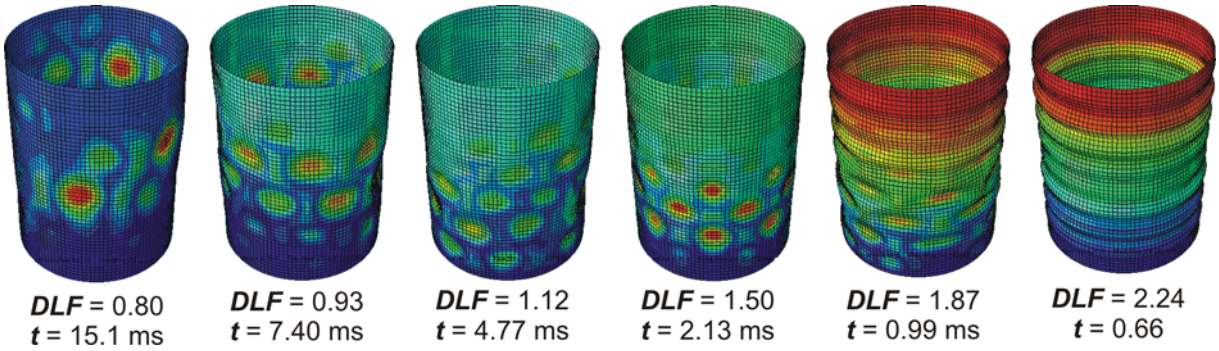

Figure 4.36. Buckling modes of model **Type 3-0** at different sudden load magnitudes

4.5. Concluding remarks

Dynamic buckling of composite cylindrical shells has been studied experimentally and numerically. The dynamic buckling experiments have been performed using hydraulic testing rigs and a drop tower. The hydraulic testing rigs provided relatively low loading rates, but the test conditions were clearly defined and good correlation with the numerical results has been obtained. All of these tests indicated the rise of the buckling load as the loading rate increased. The use of a drop tower resulted in higher loading rates, achieving dynamic buckling loads both higher and lower than the static one. However, the indirect load and displacement measurements could not be interpreted unambiguously and the boundary conditions were unclear due to unrestrained top end of the specimen. The high-speed movies show that the buckles appear and disappear simultaneously in the hydraulic rig tests, which is not the case for the drop-tower tests. The buckling occurs at one location on the specimen and 'moves' along the surfaceof the shell until disappears, confirming the effect of the unrestrained upper end of the specimen. Thus, the results obtained using the drop-tower should be regarded with caution.

The experiments performed with the hydraulic testing rig have been modelled using ABAQUS finite element package, and good correlation of the experimental and numerical dynamic buckling loads has been achieved.

The numerical studies on dynamic buckling of composite cylinders have been carried out at loading conditions unfeasible by the available experimental set-ups. Artificial, eigenmode-shaped imperfections and imperfections, measured on real specimens have been used in this investigation. Imperfection sensitivity study shows that not only the buckling loads, but also the DLFs are sensitive to the magnitude and shape of imperfections. This means that use of eigenmode-shaped imperfections can be misleading in numerical studies of the dynamic buckling behaviour of a shell. Thus, imperfections measured on real structures should be considered instead.

The numerical studies confirmed the results of Abramovich et al. (2007) that for imperfect composite cylindrical shells the DLFs can be higher than unity at any given load duration. Nevertheless, sudden application of the load leads to buckling at a load lower than the static buckling load, confirming the results of Bisagni (2005). On the upside, according to the numerical results, sudden application of the load brings down the buckling load of a geometrically perfect cylinder to the same level as of a nominally identical imperfect cylinder, thus reducing the imperfection sensitivity. The lower imperfection sensitivity in case of dynamic loading has also been outlined by Abramovich et al. (2007).

5. BUCKLING OF STIFFENED CURVED CFRP PANELS

5.1. Imperfection sensitivity of stiffened CFRP panels

No imperfection data of the CFRP panels used in this study was available, so the linear eigenmodes were applied to the model as "worst case scenario" imperfections to check the imperfection sensitivity of these panels numerically. Two types of imperfections have been used for each panel, the first eigenmode (where only the skin of the panel is displaced), and the first mode to feature bending of the stiffeners (the first global mode). The first eigenmode shape imperfections have been applied with amplitudes of 1/8 and 1/2 of skin thickness t, and the global imperfection mode has been applied with the amplitude of skin thickness t.

The buckling loads of the panels with and without the imperfections are summarized in the Table 5.1. The displacement tolerance criterion has been used to determine the buckling load values, as it is used in the dynamic buckling analysis later in the thesis. The example load-shortening curves of the perfect Panel 2 along with the curves obtained using the panel geometry updated with the eigenmode shapes are presented in Figure 5.1. The change in post-buckling shapes due to introduction of imperfections is presented in Figure 5.2.

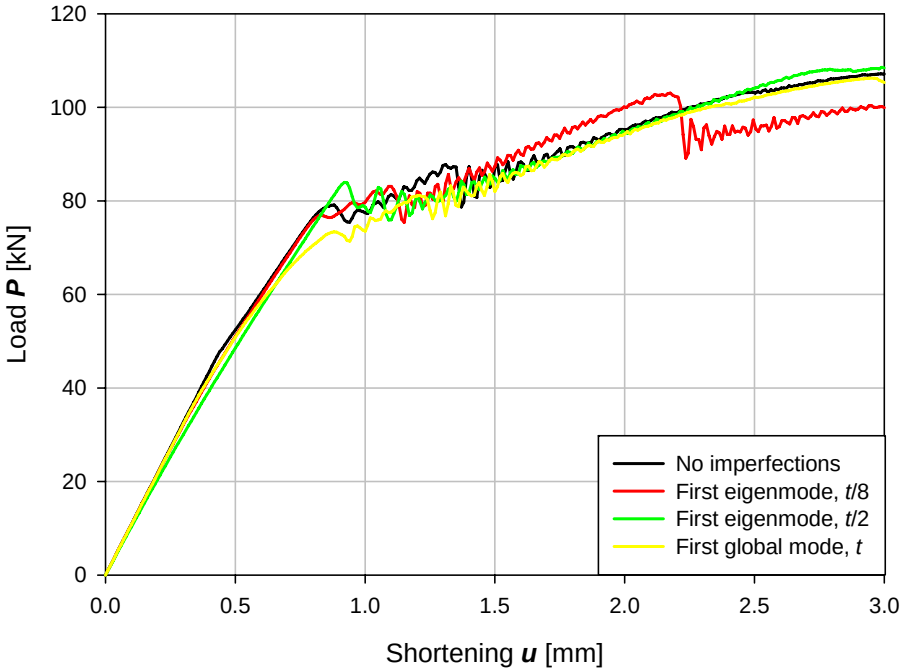

Figure 5.1. The load-shortening curves for numerical models of **Panel 2**

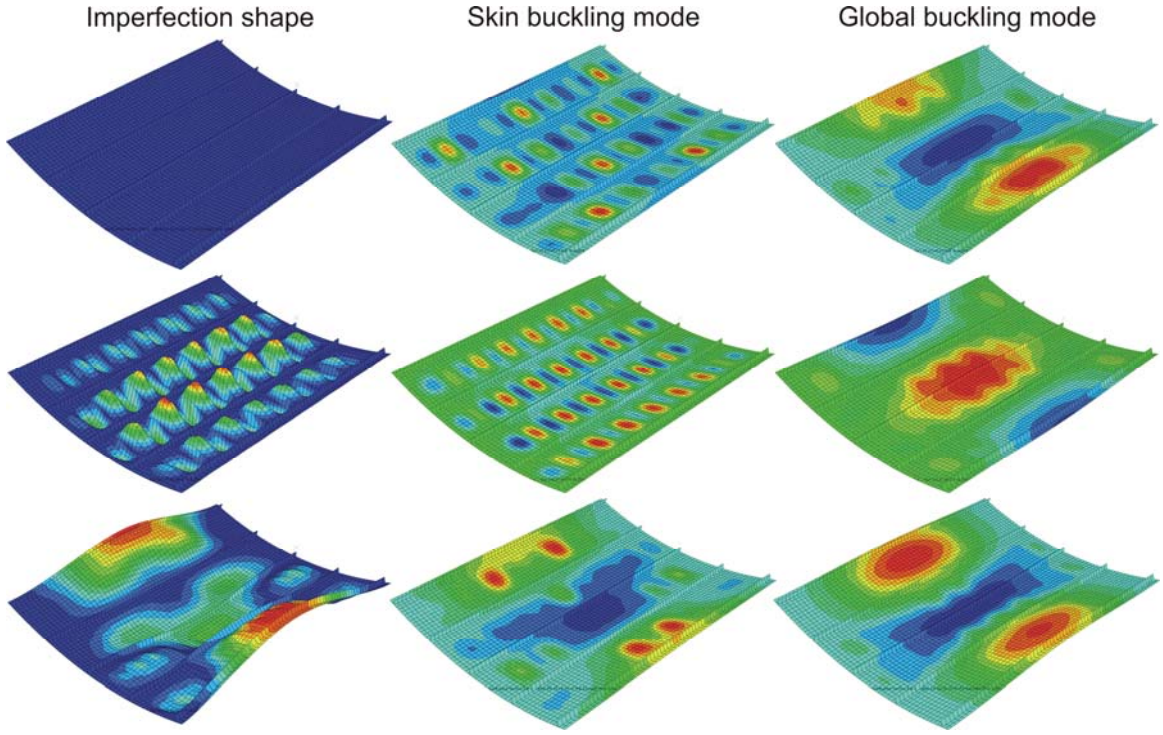

Figure 5.2. The change of buckling shapes due to imperfections for **Panel 2**

Table 5.1. Critical loads for the imperfect stiffened CFRP panels

	Buckling load P_{cr} [kN]					
Panel	**Panel 1**		**Panel 2**		**Panel 3**	
Mode	**Skin**	**Global**	**Skin**	**Global**	**Skin**	**Global**
No imperfections	85.78	253.73	49.27	74.90	63.97	222.74
First eigenmode, *t*/8	61.62	270.45	52.75	74.55	50.71	216.25
First eigenmode, *t*/2	60.95	283.21	48.50	82.83	61.97	214.77
First global mode, *t*	72.23	249.64	35.45	52.45	63.93	227.35

The numerical imperfection sensitivity study performed the validated models of the stiffened CFRP panels show moderate imperfection sensitivity of these structures (see Table 5.1). Namely, the lowest knock-down factors of the skin buckling load obtained in this study are 0.71 (Panel 1) and the lowest knock-down factor of the global buckling load is 0.7 (Panel 2). Nevertheless, the stable post-buckling behaviour of these structures resulted in very subtle changes in the overall stiffness responses of the structures, and therefore the load-shortening curves.

The introduction of the imperfections altered the buckling shapes, and in some cases it resulted in higher buckling loads for imperfect structures than for the perfect structures. For example, the global buckling load of the Panel 1 with first eigenmode shaped imperfection was 12% higher than the global buckling load of a perfect Panel 1.

No imperfections were used in further studies of the stiffened CFRP panels because of the stable post-buckling behaviour of the stiffened CFRP shells, the small influence of the initial imperfections on the load-shortening curves and lack of information about the actual imperfections of the physically tested panels.

5.2. Static buckling

The static buckling tests of the CFRP panels have been performed by the Israel Institute of Technology (Abramovich et al., 2003; Abramovich and Weller, 2005) – Panel 1, and the other panels – Panel 2 and Panel 3 – were tested at the German Aerospace Center DLR (Degenhardt et al., 2006, 2008; Kling et al., 2006) (Panels 2 and 3) within the EU FP6 project COCOMAT (www.cocomat.de). The tests of the panels 1 and 2 have been used in the Finite Element software benchmarking study described in the Chapter 2.4.4. However, the explicit Finite Element method has been represented by LS-Dyna in that study, while the implicit method has been used in ABAQUS. Therefore, the ABAQUS/Explicit solution had to be validated for the models of all the 3 CFRP panels. The validated models have been used in further investigations of dynamic buckling behaviour of stiffened CFRP shells.

Using the results of the mesh sensitivity and boundary condition study from the Finite Element software benchmarking, Finite Element models of the three panels have been elaborated. The four node S4R element has been used in these models, with default element size of 20 mm. The boundary conditions at the panel ends are clamped for all panels, and the side edges of the Panel 1 and Panel 3 are simply supported, with axial displacement allowed. These boundary conditions have been chosen according to the relevant test procedures.

The experimental and numerical load – shortening curves of the Panel 1, Panel 2 and Panel 3 are presented on Figure 5.3. The corresponding sequences of the buckling shape progressions from the ABAQUS/Explicit analyses are presented in Figure 5.4, Figure 5.5 and Figure 5.6, respectively. The post-buckling behaviour of the Panel 1 and Panel 3 are similar, because of the similar boundary conditions, and their stiffness does not decrease significantly after bucking. The unsupported side edges of the Panel 2 lead to more column-like global buckling behaviour, while the skin buckling does not influence the overall stiffness significantly, as in case of the other panels.

It must be noted that this study considers the instability behaviour of the structures only, and neither strength failure criteria, nor any progressive damage models have been implemented in the analyses.

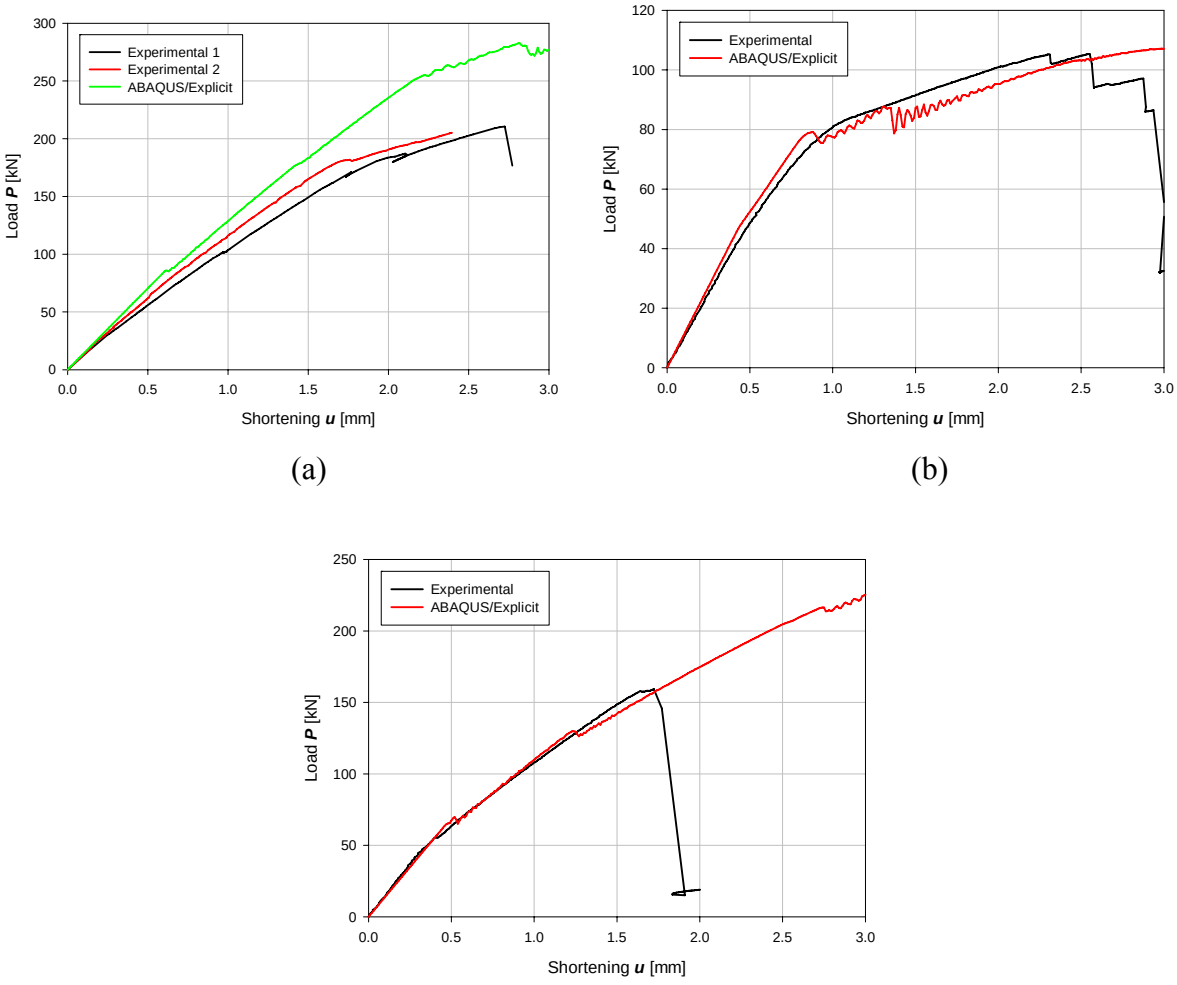

Figure 5.3. Load-shortening curves of stiffened curved CFRP panels
(a) – **Panel 1**; (b) – **Panel 2**; (c) – **Panel 3**

The numerical static buckling analysis results for the stiffened CFRP panels are in fairly good agreement with the available experimental data. In case of the Panel 1, the difference between the experimental and numerical load-shortening curves is the greatest of the three panels considered, and the stiffness of the panel is overestimated by 10 % - 20 % comparing to the experimental data (Figure 5.1 (a)). The pre-buckling and post-bucking stiffness of the Panel 2 and Panel 3 are predicted more accurately, and the buckling loads compare well between the experimental and numerical results (Figure 5.1 (b) and (c)). Therefore, the numerical models of the stiffened CFRP panels are considered to be valid for performing the numerical studies of the dynamic buckling of these structures.

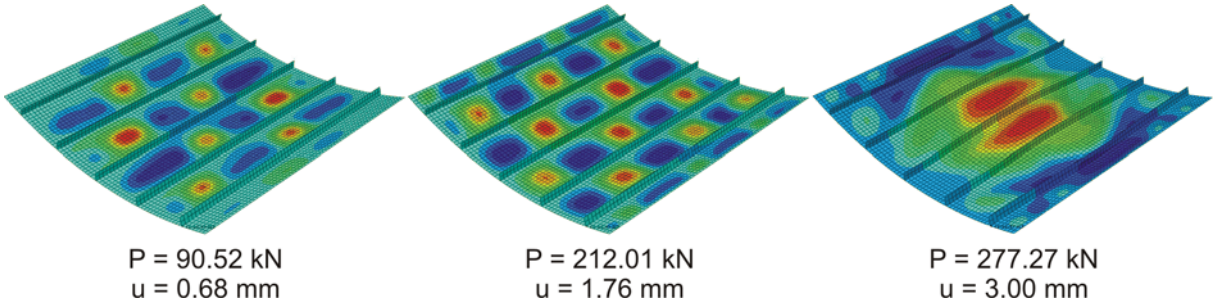

Figure 5.4. Buckling mode progression for Panel 1

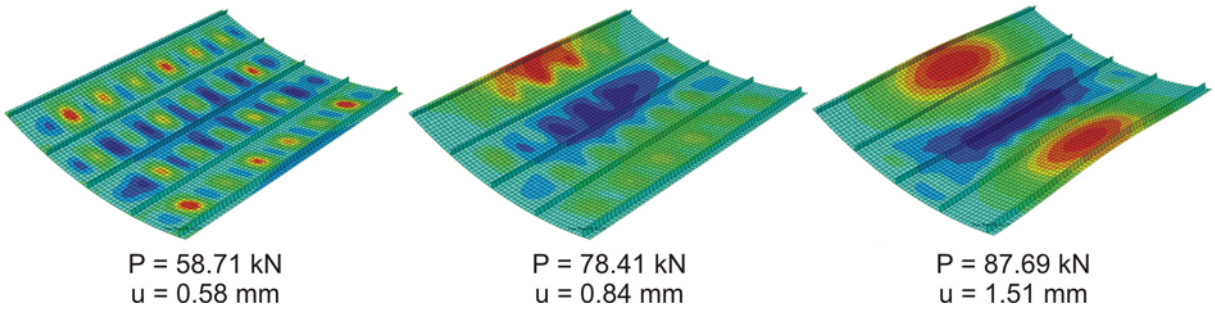

Figure 5.5. Buckling mode progression for Panel 2

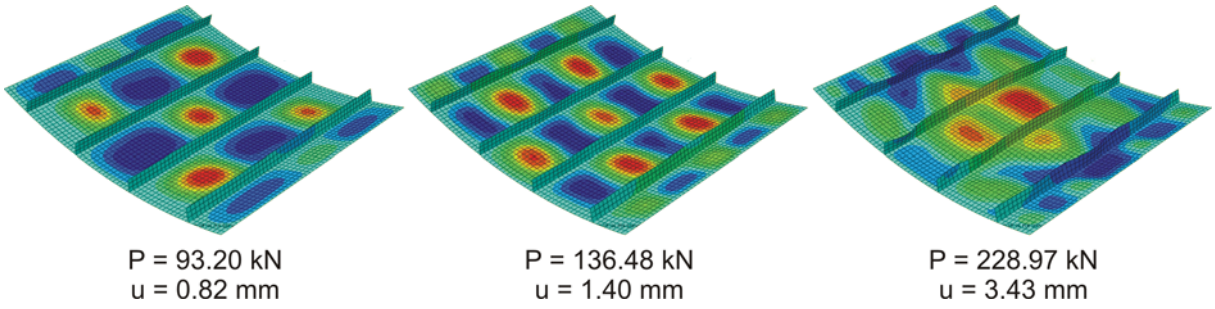

Figure 5.6. Buckling mode progression for **Panel 3**

5.3. Dynamic buckling

The dynamic buckling behaviour of the stiffened CFRP panels has been studied numerically employing the ABAQUS/Explicit models validated as described in Chapter 5.2. Two different loading scenarios have been considered:

- Gradually applied load;
- Suddenly applied load.

In case of gradually applied load, the load is applied with various loading rates, ranging from 7 kN/ms to 2700 kN/ms. Maximum out of plane displacements have been recorded for the whole model and for base of the stiffener from where the buckling loads could be identified using Budiansky-Hutchinson criterion. The maximum out of plane displacement of the base of the stiffener indicates global buckling, while the maximum out of

plane displacements of the whole model indicates the first buckling load, which is always skin buckling for the given models.

Sample Budiansky-Hutchinson plots for Panel 1, Panel 2 and Panel 3 and three different loading rates are given in Figure 5.7. The corresponding local and global buckling shapes are presented in Figure 5.8, Figure 5.9 and Figure 5.10, respectively.

In case of suddenly applied load, the load is applied instantly with various magnitudes and the maximum out of plane displacements and end shortening are recorded to identify the time when the panel buckles and weather the panel has buckled. Sample displacement plots for Panel 1, Panel 2 and Panel 3 and three different loads are given in Figure 5.11, Figure 5.15 and Figure 5.13, respectively. The corresponding buckling shapes are presented in Figure 5.12, Figure 5.16 and Figure 5.14.

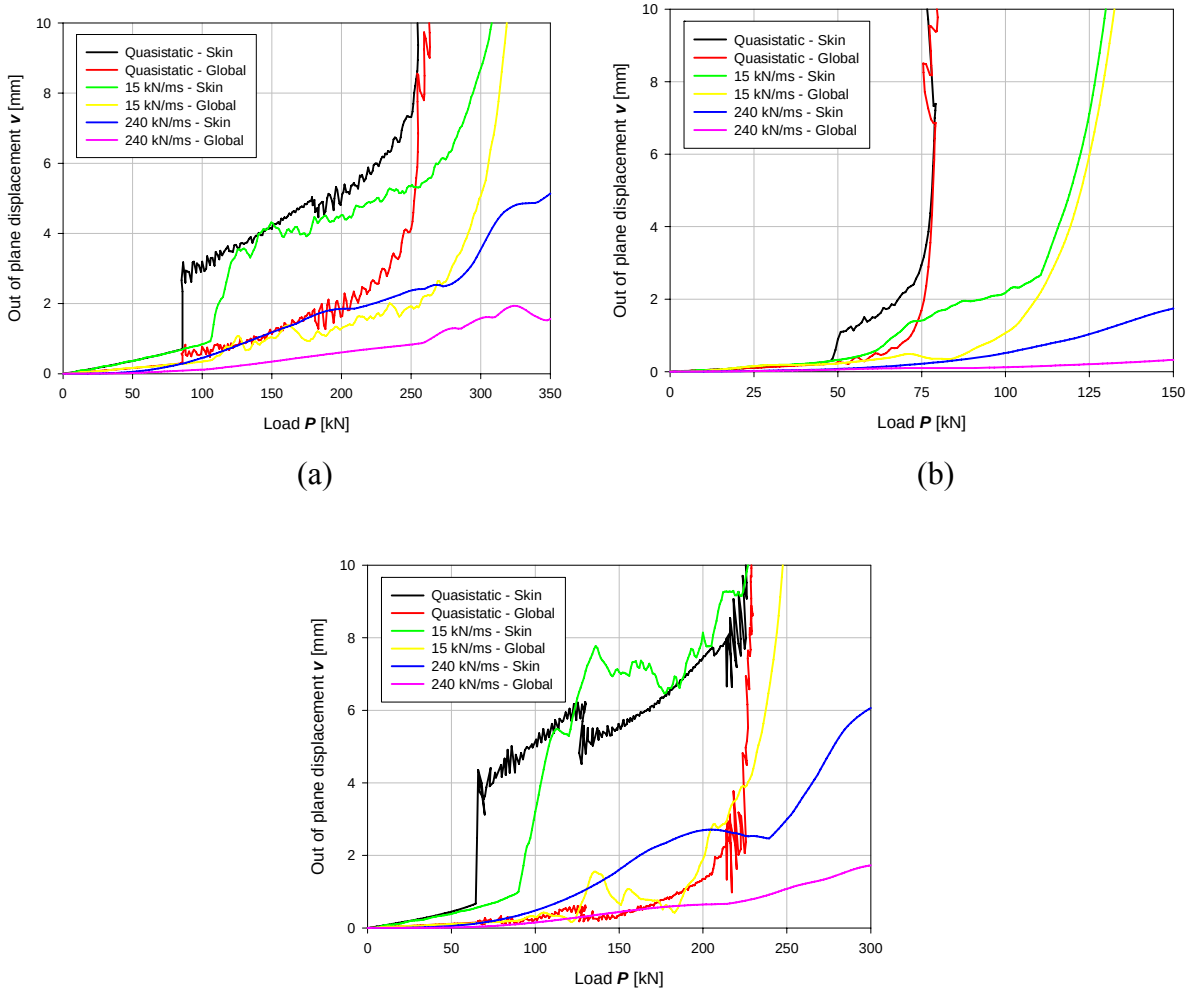

Figure 5.7. Budiansky-Hutchinson plots for the stiffened curved CFRP panels (a) – **Panel 1**; (b) – **Panel 2**; (c) – **Panel 3**

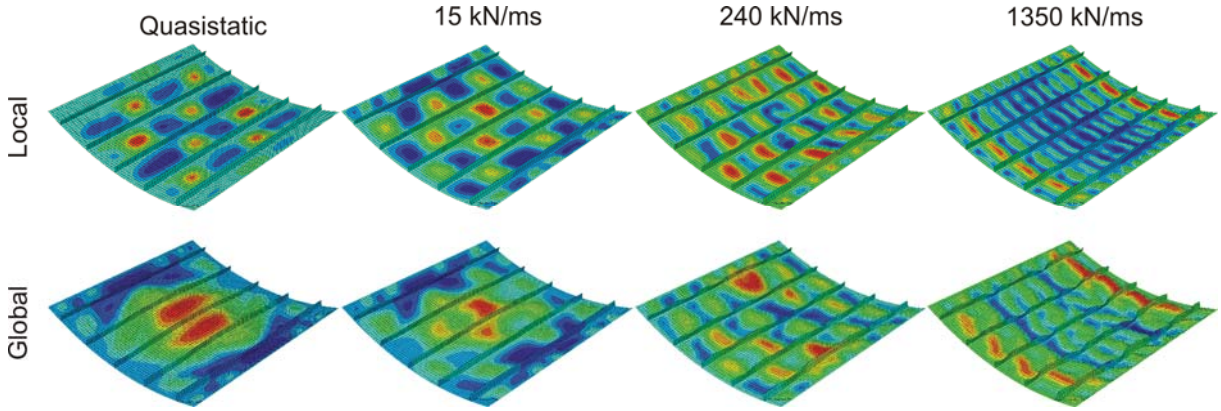

Figure 5.8. Buckling modes of **Panel 1** at different loading rates

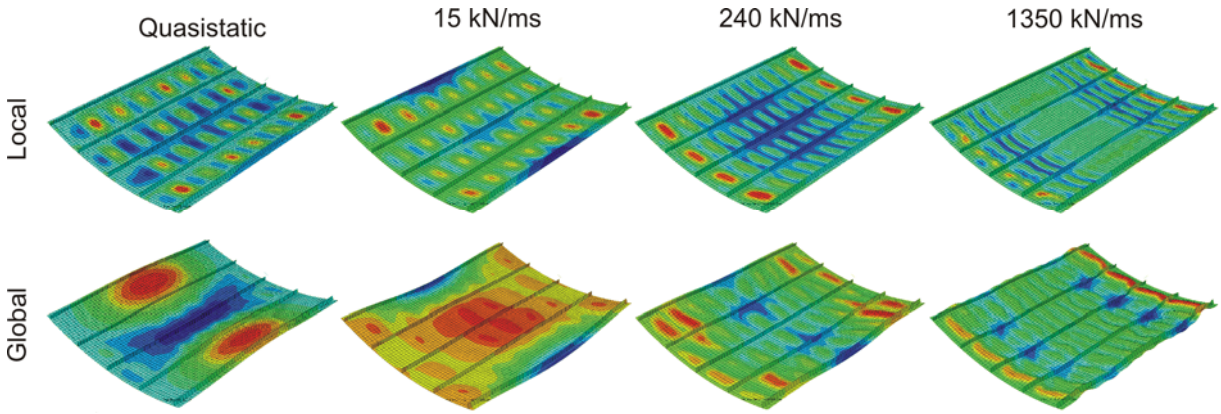

Figure 5.9. Buckling modes of **Panel 2** at different loading rates

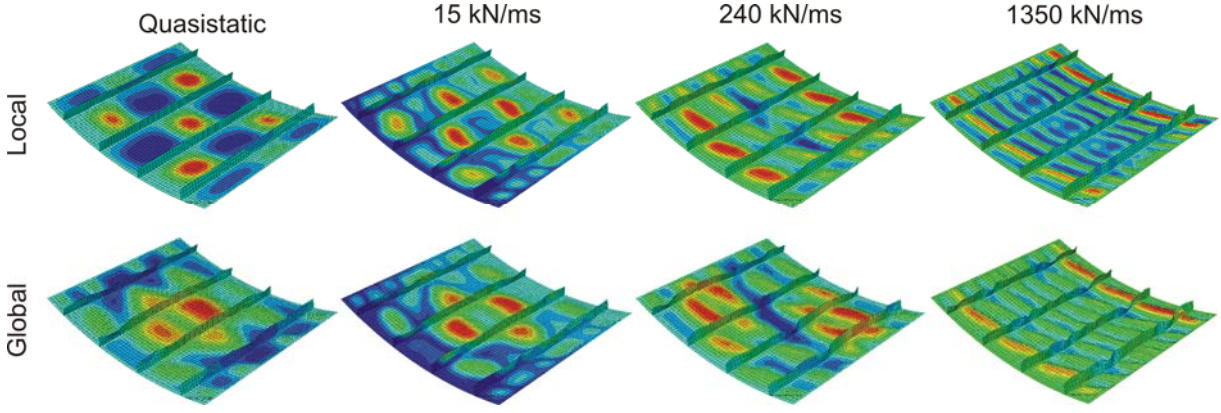

Figure 5.10. Buckling modes of **Panel 3** at different loading rates

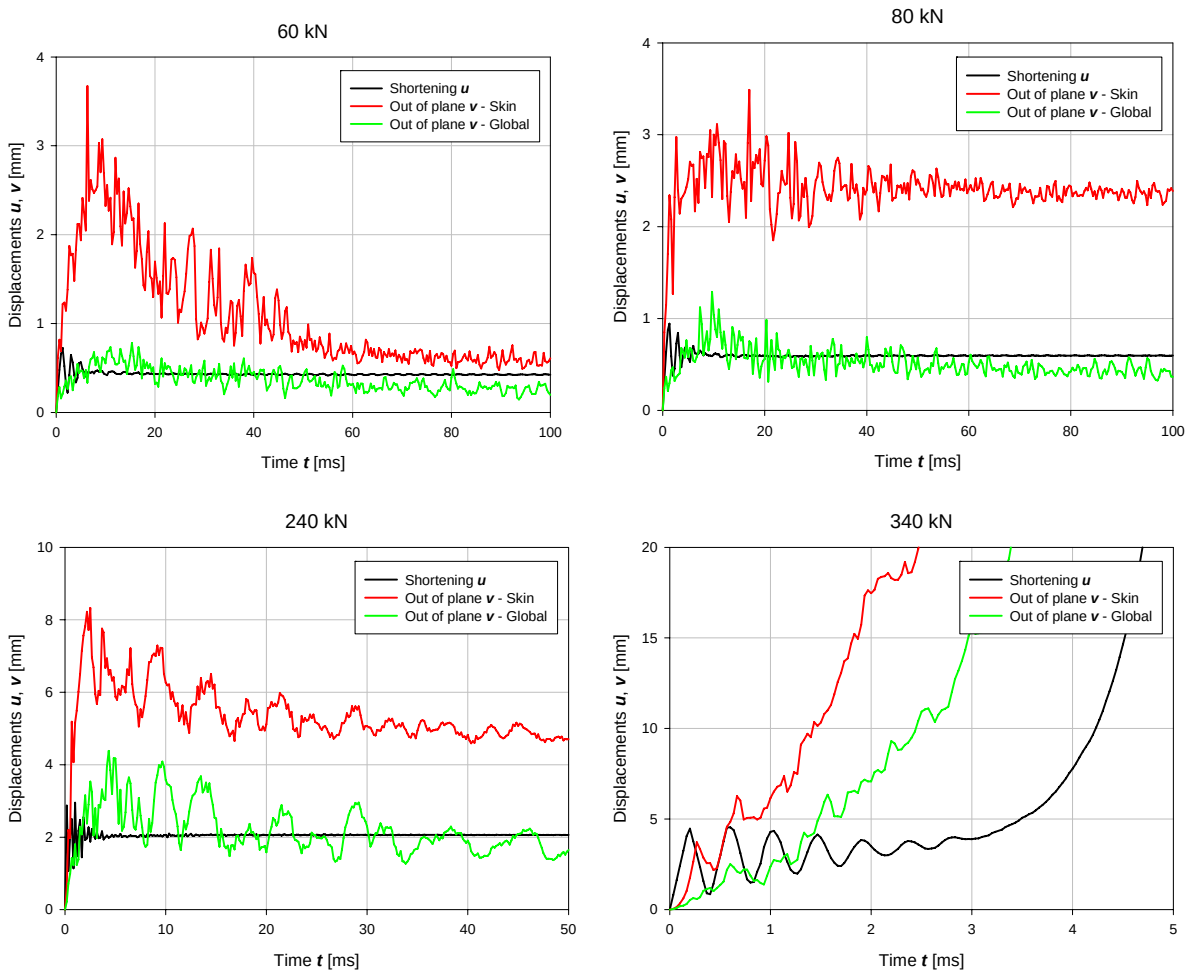

Figure 5.11. Displacement response of **Panel 1** under different sudden loads

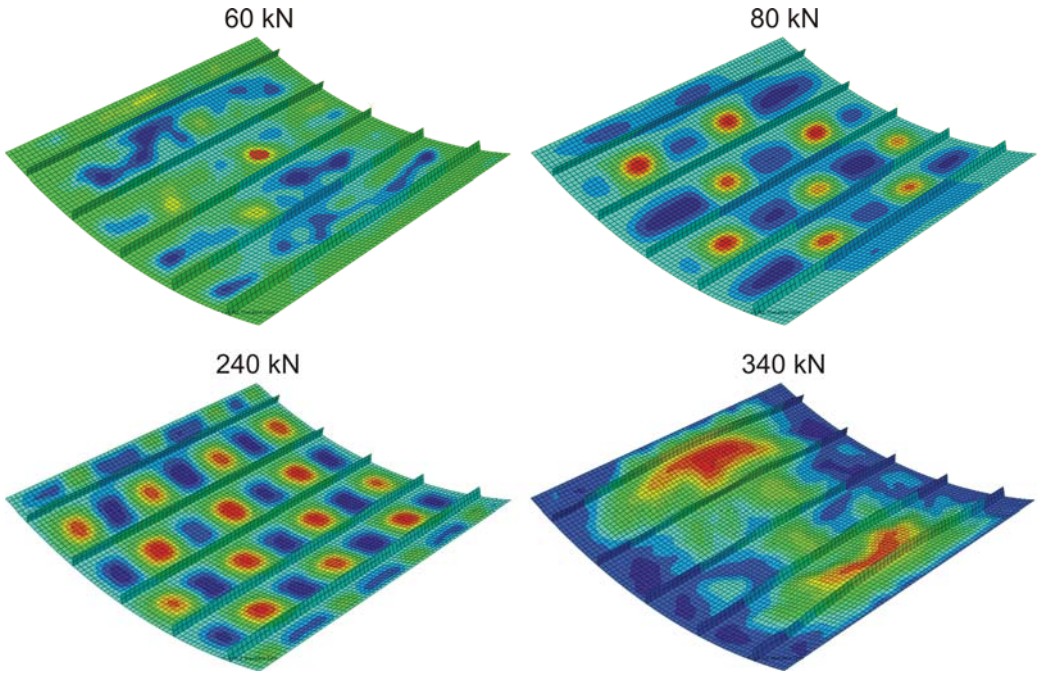

Figure 5.12. Buckling shapes of **Panel 1** under different sudden loads

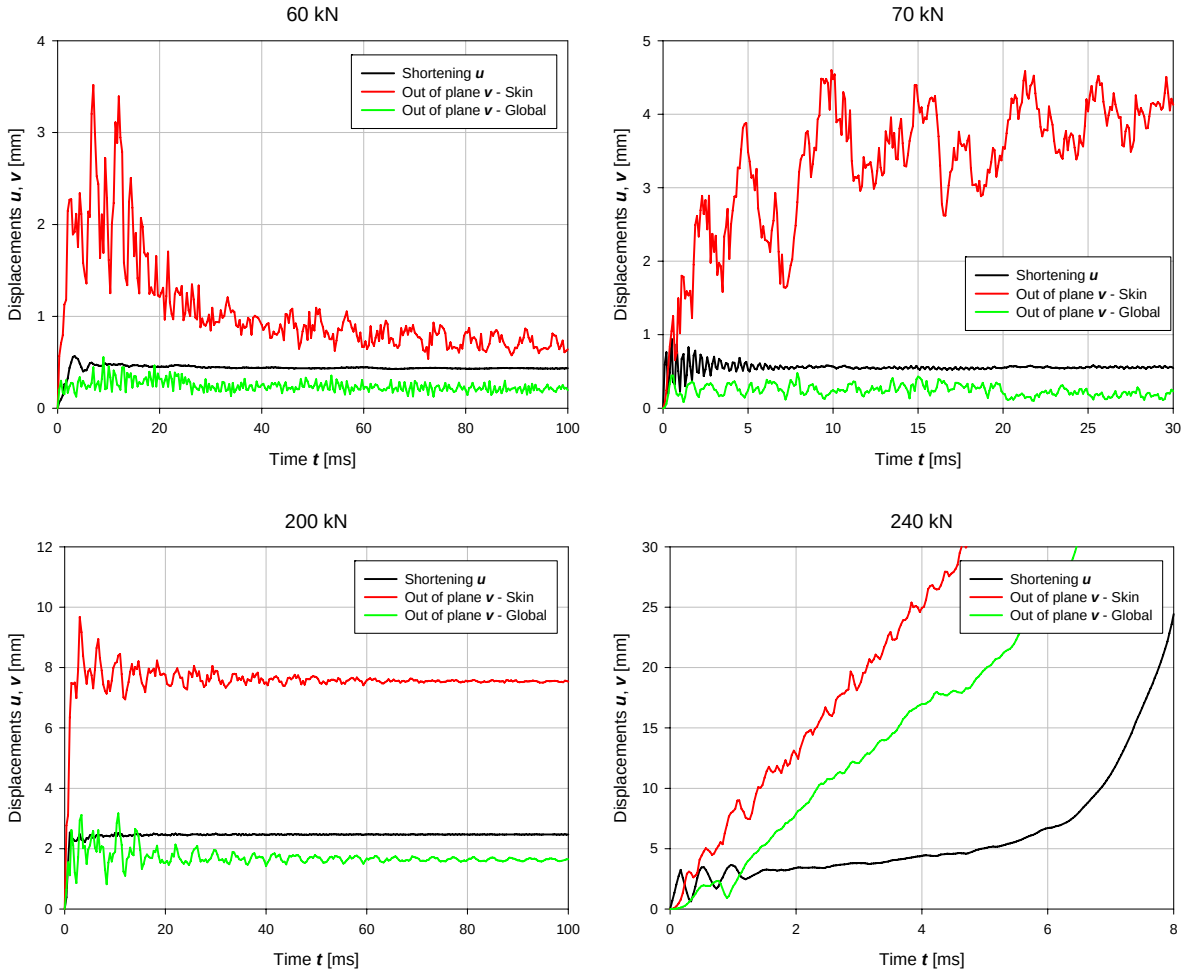

Figure 5.13. Displacement response of **Panel 3** under different sudden loads

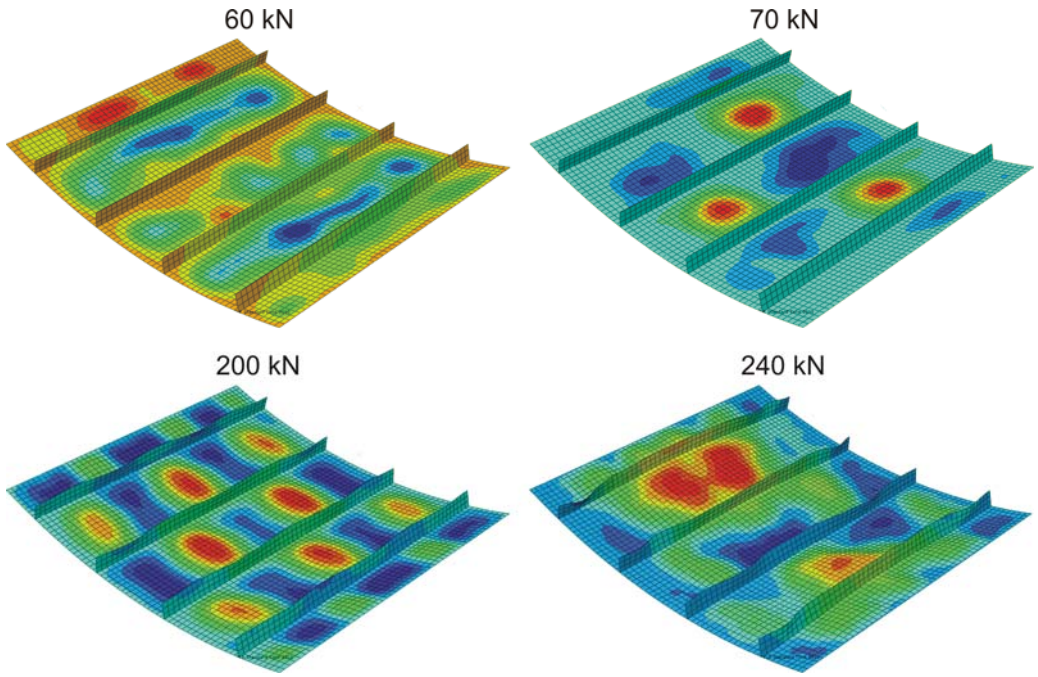

Figure 5.14. Buckling shapes of **Panel 3** under different sudden loads

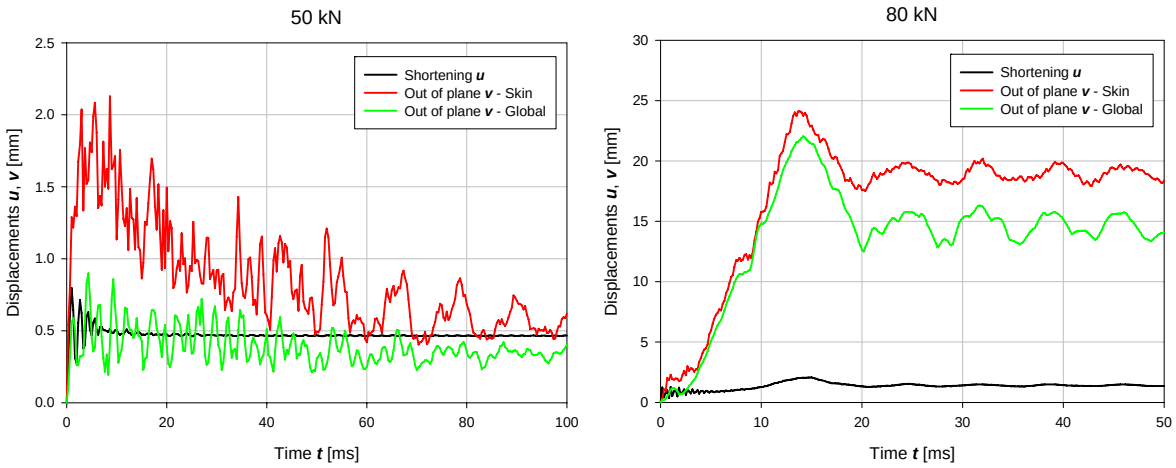

Figure 5.15. Displacement response of **Panel 2** under different sudden loads

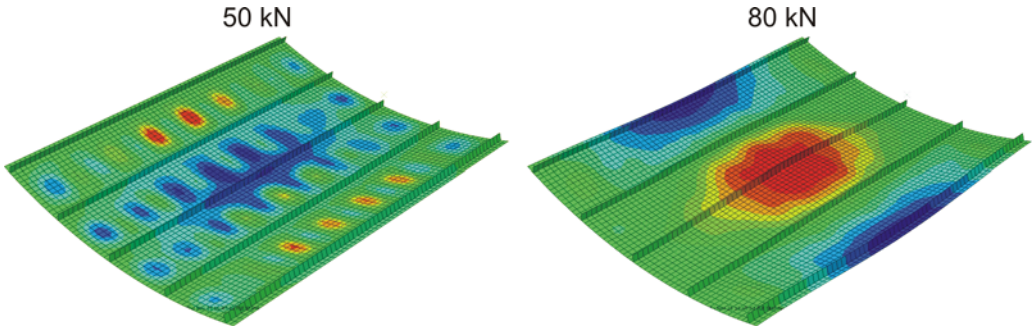

Figure 5.16. Buckling shapes of **Panel 2** under different sudden loads

Budiansky – Hutchinson plots have been used to determine the buckling loads of the stiffened CFRP panels under gradually increasing loads, in a similar manner as with the GFRP cylinders. The difference is that two different buckling modes have been monitored at the same time, first the skin buckling, which always occurs at lower loads, and then the global buckling, where the whole skin-stiffener assembly loses stability. The out-of-plane displacement tolerances for finding the buckling loads have been chosen for each panel and buckling mode to serve as a buckling criterion for both static and dynamic buckling tests. The tolerance values had to be diversified because of the differences between the three panels in terms of geometry and buckling behaviour. The values of these critical displacement values are summarized in Table 5.2.

Table 5.2. The arbitrary chosen critical displacement values

	Critical out-of-plane displacement *v* [mm]	
	Skin buckling	**Global buckling**
Panel 1	1.2	4.5
Panel 2	0.75	1.75
Panel 3	1.2	3

The approach used in the case of cylinders under sudden loads could be employed with stiffened CFRP panels because of the stable post-buckling behaviour of the panels: applying a buckling load does not result in virtually unbound axial shortening like in the case of cylinders. Therefore, an approach similar to Budiansky-Hutchinson criterion has been used in case of suddenly applied load. The displacements were plotted against time, not the load, because load is a constant in this case, and the critical load duration is considered the time when the out-of-plane displacements exceed the defined tolerance.

The use of the simple out-of-plane displacement tolerance criterion has its drawbacks, though. To compare the dynamic buckling loads to the static ones, the criterion has to be used for the static tests, too, and this is one constraint for the critical displacement value. This causes problem illustrated in Figure 5.17 (a). The critical displacement for finding the buckling load is dictated by the Budiansky-Hutchinson plot of the quasi-static case, and at this value, the buckling load at loading rate of 70 kN/ms is 8% higher than at loading rate of 75 kN. However, the buckling load would be higher at 75 kN/ms if the tolerance of 2.5 mm – 3.0 mm would be used. Similar problem can be observed on the example of Panel 2 in the Figure 5.17 (b): the growth of maximum out-of-plane displacement is not always uniform, and at some loading rates (85 kN/ms and 15 kN/ms in this case) it can have even negative slope. If the character of the curve does not change, a jump in DLF-load duration plot occurs when the local maximum of the Budiansky-Hutchinson plot exceeds the critical displacement. These inconsistencies of the DLF-load duration usually, but not always, occur at loading rates where the buckling modes change, as can be observed in Figure 5.18 that shows the buckling modes of the Panels 1 and 2 corresponding to the curves in Figure 5.17.

Despite the drawbacks of the critical out-of-plane displacement tolerance criterion, it serves well as a consistent criterion for comparison of buckling behaviour of the structure under different dynamic load conditions. The efforts to establish more sophisticated criteria for finding the buckling load, e.g. criteria based on finding maximum curvature in the Budiansky-Hutchinson plot, were not so successful because of the complexity of these plots in case of stiffened panels. The same out-of-plane displacement tolerances have been used to find the critical load durations at each value of suddenly applied load in order to have a reasonable comparison of DLF-load duration curves for gradually increasing and sudden loading.

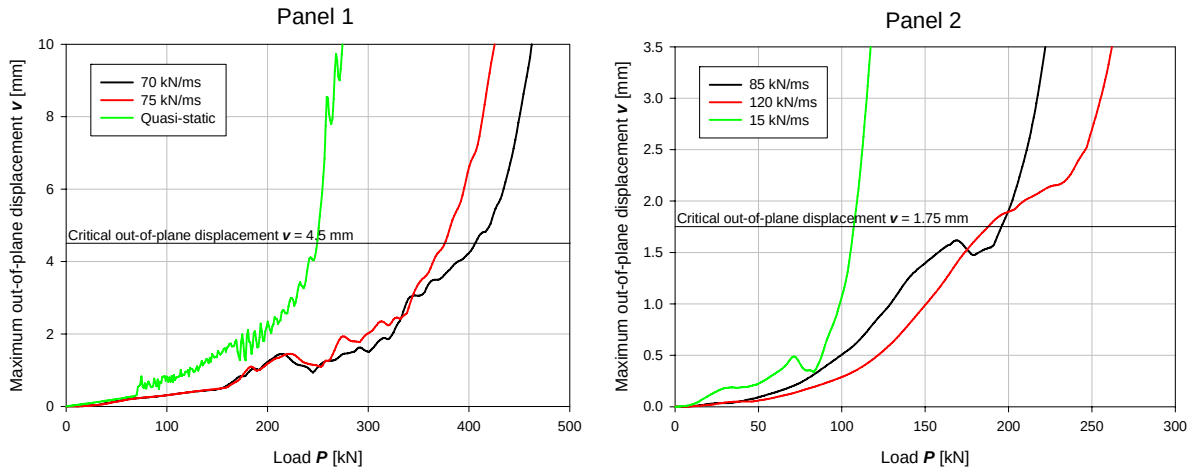

(a) (b)

Figure 5.17. Sample Budiansky-Hutchinson plots for global buckling
(a) – **Panel 1**; (b) – **Panel 2**

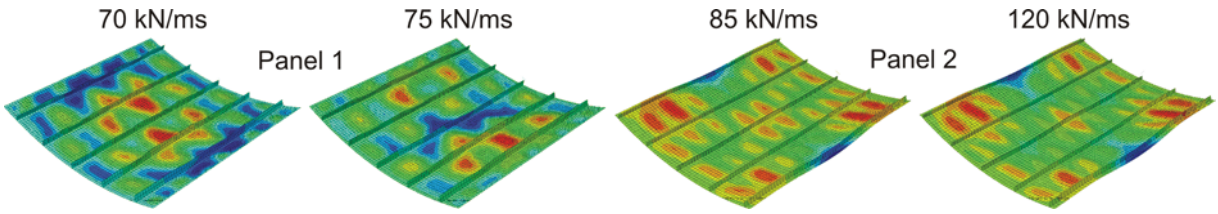

(a) (b)

Figure 5.18. Sample global buckling modes
(a) – **Panel 1**; (b) – **Panel 2**

The DLF-load duration curves for Panel 1, Panel 2 and Panel 3 are presented in Figure 5.19, Figure 5.20 and Figure 5.21, respectively. Separate curves for Skin buckling and Global buckling modes and for gradually and suddenly applied loads are given. These curves show a general trend of the DLF increase with the decreasing of the load duration, yet, there are some inconsistent regions in most of the curves. To understand the reasons for that, the natural periods of the panels are found numerically, just like in case of the GFRP cylinders, and the changes of the buckling modes are observed.

The natural periods of the panels are presented in Table 5.3. The inconsistencies and drops in the DLF-load duration curves do not directly coincide with any of these natural periods. However, it must be noted that there natural bending frequencies are closely spaced and the drops may be associated with bending modes that have higher frequencies.

Most of the inconsistent regions of the DLF-load duration curves can be explained by the change of the buckling modes. The drops in the global buckling curve for Panel 1 under gradually applied load at 11 ms, 5 ms and the sudden slope change at 0.9 ms all are associated

with buckling mode shape changes. However, the inconsistencies in the corresponding local buckling curve can be explained by buckling mode shape change only in the region around 1.5 ms, while the drop of DLF in the region of 0.8 ms does not coincide with buckling shape change. In case of Panel 1 under suddenly applied load, no buckling shape changes can be observed in the only inconsistent region. The change of buckling modes in the inconsistency regions is presented in Figure 5.22.

The DLF-load duration curves are more consistent in case of the Panel 2 comparing to the other panels, probably because of its distinct boundary conditions. However, neither the inconsistency in the global buckling curve for gradually applied load at 1.7 ms, neither the inconsistency in the skin buckling curve for suddenly applied load around 0.5 ms are coinciding with buckling mode changes.

The model of the Panel 3 is the only model that resulted in DLF < 1.00 in case of gradually applied loads, and both points on the DLF-load duration curves that are below 1.00 are associated with the change of buckling shape. The third inconsistent region on the global buckling curve for Panel 3 under gradually applied also features change in the buckling shape. These buckling shape changes are presented in Figure 5.23. All the other DLF-time duration curves for Panel 3 are relatively smooth and no significant jumps can be noted.

The low skin buckling DLFs under suddenly applied load (down to 0.30 in case of Panel 1) have to be noted. The numerical imperfection sensitivity studies of the stiffened CFRP panels in Chapter 5.1. show that the skin buckling load is strongly influenced by initial geometric imperfections, and the study of GFRP cylinders under sudden load in Chapter 4.4. proved that the harmonic response of the cylinders can act as initial imperfections and result in very low DLFs, especially when the structure is modelled with perfect geometry.

Table 5.3. Natural periods of the stiffened CFRP panels

Model	$T=\tau_{skin}/2$ **[ms]**	$T=\tau_{global}/2$ **[ms]**	$T = 2a/c$ **[ms]**
Panel 1	2.47	1.33	0.201
Panel 2	1.77	2.77	0.204
Panel 3	1.88	0.933	0.170

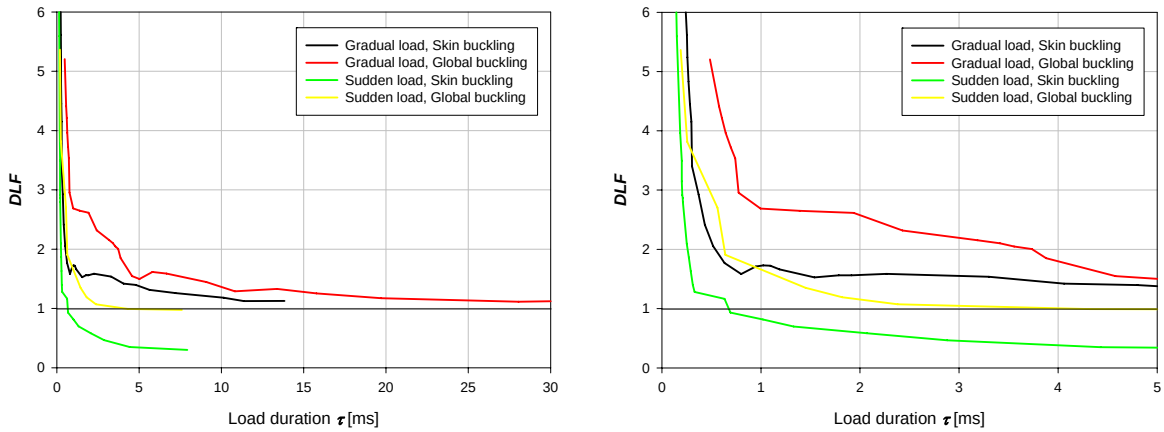

Figure 5.19. DLF versus load duration, **Panel 1**

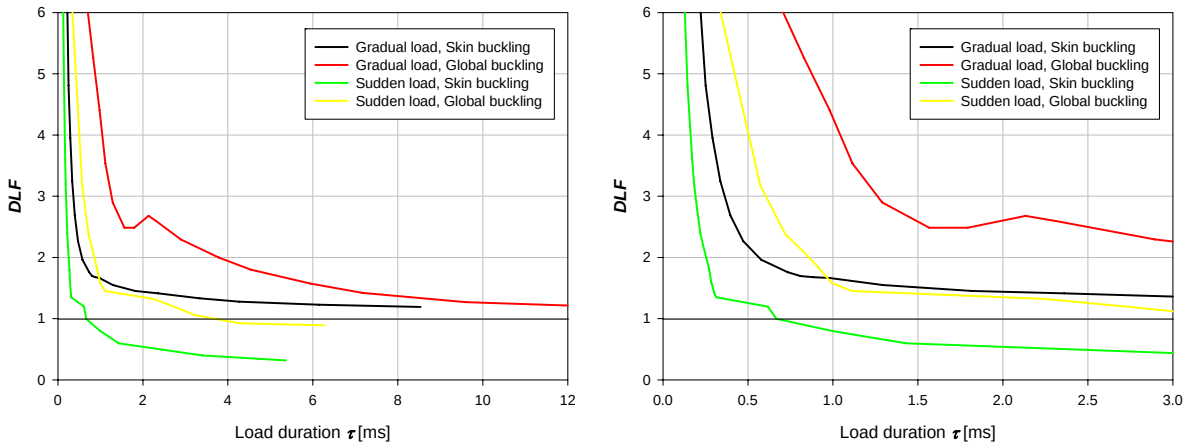

Figure 5.20. DLF versus load duration, **Panel 2**

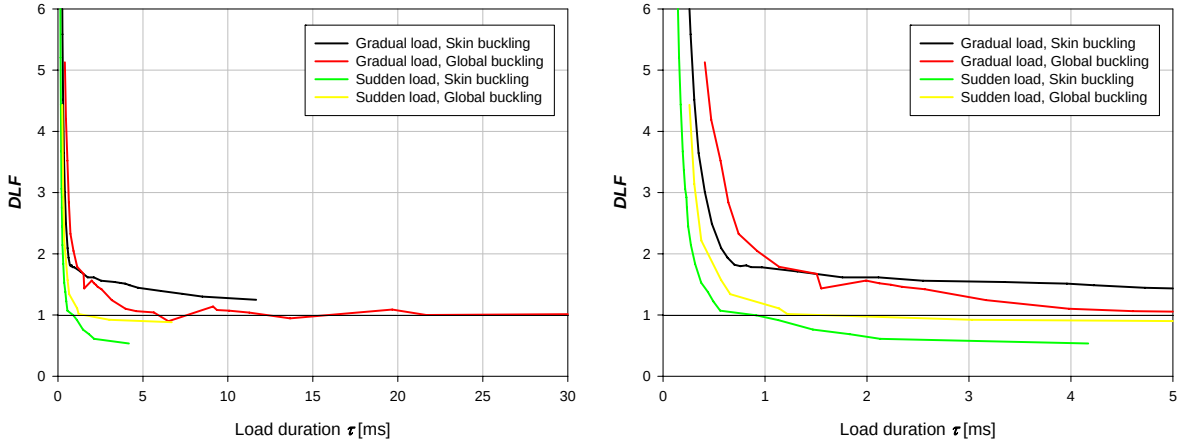

Figure 5.21. DLF versus load duration, **Panel 3**

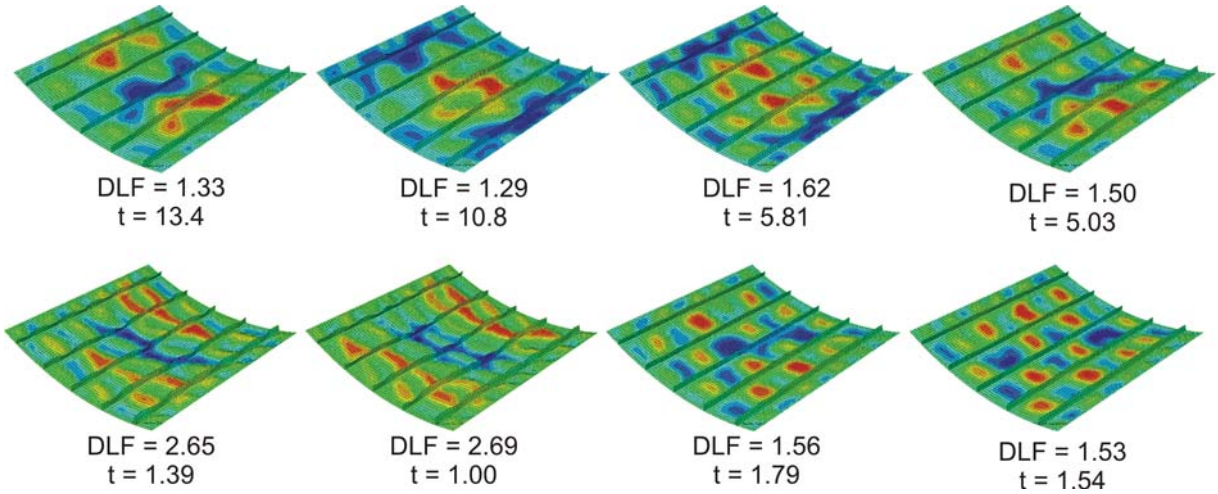

Figure 5.22. Buckling mode changes near inconsistencies in DLF curves for **Panel 1**

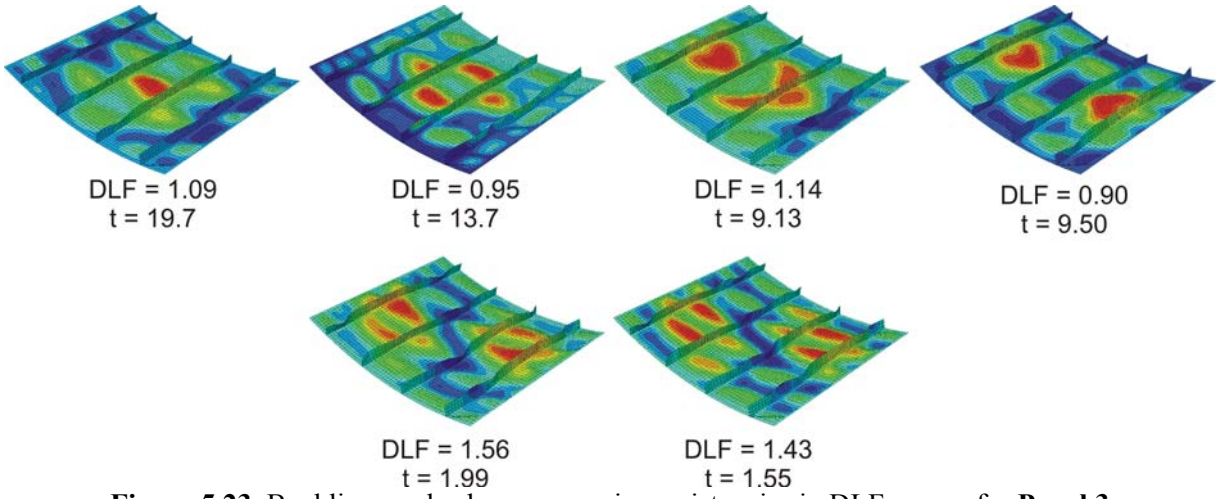

Figure 5.23. Buckling mode changes near inconsistencies in DLF curves for **Panel 3**

According to the aforementioned imperfection sensitivity study, the global buckling loads are less sensitive to the initial imperfections, and the lowest calculated global buckling DLF of 0.88 is in accordance with this finding.

However, the low skin buckling DLFs do not mean catastrophic failure of the stiffened CFRP panels in case of suddenly applied load because of the stable post-buckling behaviour of the panels. If a sudden load, which is lower than static skin buckling load, is applied to the structure and skin buckling occurs, the stiffened panel regains the equilibrium shape for the corresponding static load, as seen in the maximum out-of-plane displacement plots for the lowest sudden loads in Figure 5.11, Figure 5.13 and Figure 5.15.

5.4. Concluding remarks

The dynamic buckling of stiffened CFRP panels under gradually increasing and suddenly applied loads has been studied numerically using ABAQUS/Explicit. The numerical

models have been validated using static buckling experimental data obtained within the EC FP6 project COCOMAT.

The imperfection sensitivity study shows that the skin buckling load of curved, stiffened composite panel is as sensitive to the geometric imperfections as the buckling load of unstiffened shells. The global, stiffener-based buckling is affected by the initial imperfections to a smaller extent. The overall stiffness response of the panels does not change due to the initial imperfections, as the stiffeners support most of the compressive load at the given configurations. Thus, since the data on initial geometric imperfection was unavailable for the composite panels considered, no imperfections have been included in the further numerical studies.

Gradually increasing loads from 7 kN/ms to 2700 kN/ms have been considered, and DLFs from 1.12 to 9.30 have been obtained for skin buckling mode and from 0.90 to 12.65 for global buckling mode, yet the DLF < 1.00 has been observed in case of only one of the panels. The increase of the DLFs along with decrease of load duration is evident as in case of cylindrical shells, however, there are more inconsistencies and slight drops in the curves. Usually, but not always, these drops occurs at load durations where the buckling modes change.

Additionally, the buckling behaviour of stiffened CFRP panels under suddenly applied loads with magnitudes from 15 kN to 1350 kN has been studied using the same models. DLFs from 0.88 to 8.98 have been observed for global buckling mode and from 0.30 to 15.73 for the skin buckling mode. Similarly as in case of cylindrical shells, the low DLFs for the skin buckling mode arise from the imperfection sensitivity of the buckling load in this mode and the harmonic response of the panels to the sudden load, and use of models without initial geometrical imperfections.

In general, the dynamic buckling behaviour of the stiffened composite shells is similar to the behaviour of the composite cylinders. In both cases, the buckling load rises with the decrease of the load duration. In case of the stiffened CFRP panels, there are more inconsistencies in the DLF-time curves than in case of cylindrical shells because to the more complex buckling behaviour of the stiffened panels. The mode shape changes of the cylinders take place gradually, transforming from the diamond-shape pattern of the static buckling to the axisymmetric pattern at the highest loading rates considered. In contrary, the buckling modes of the curved, stiffened panels can change back and forth with the increase of the loading rate, and it affects the consistency of the DLF-time curves.

CONCLUSIONS AND RECCOMENDATIONS FOR FUTURE WORK

Dynamic buckling behaviour of unstiffened and stiffened composite shells under pulse, gradually increasing and suddenly applied loads has been studied numerically and experimentally within this thesis.

A total number of 34 cylindrical GFRP shell specimens with various dimensions have been produced while developing the fabrication and buckling testing technologies. Based on the statistically credible number of static and dynamic buckling tests and results of experimentally validated analyses, the following conclusions have been made:

I The high sensitivity of cylindrical shells to the geometrical imperfections has been confirmed. It has been demonstrated that the imperfection shape has greater influence on the buckling load than its magnitude.

II It is recommended to perform the geometric imperfection measurements on real shell specimens in order to model the buckling of a shell accurately and obtain reliable results.

III A testing procedure for static and dynamic buckling of cylindrical shells has been developed. This procedure provided consistent experimental results with 2.5% standard deviation and ensured the accordance of experimental and numerical results within 6% with a confidence of 95%.

IV It was found during the development of this procedure that particular attention has to be paid to assure strictly consistent boundary conditions and load distribution in order to obtain accurate results that could be used for the validation of the numerical methods.

V It has been demonstrated experimentally that the buckling load of cylindrical GFRP shells increases with the increase of the loading rate. This trend has been confirmed numerically using the validated finite element models.

VI A loading type has been identified which increases the buckling load of the composite structures comparing to the static buckling load across the whole dynamic loading range.

VII A modelling approach has been suggested for dynamic buckling simulations of composite structures to take advantage of the weight-saving potential created by the dynamic buckling phenomenon.

VII A worst-case dynamic loading type has been identified which lowers the buckling load of imperfection sensitive structures significantly comparing to the static buckling load.

IX It has been demonstrated that in case of suddenly applied load of infinite duration, the composite cylindrical structures are less sensitive to the initial geometrical imperfections than in cases of other loading types.

For the future studies it is recommended to expand the experimental research on dynamic buckling of composite shells in following ways:

- The dynamic buckling tests should be performed wider across the dynamic loading range, down to pulse durations of 0.2 ms, to improve the confidence in the numerical findings. Impact-based dynamic buckling testing procedures should be used due to the limited capabilities of hydraulically actuated systems.
- Dynamic loading histories of structures, experienced in yacht masts, aircraft structures during landing etc. should be determined and the buckling of structures subjected to these realistic loading histories should be investigated.
- Lateral oscillations should be induced in shells in addition to the compressive loads during buckling tests in order to assess the imperfection sensitivity and simulate some of the worst-case loadings.

REFERENCES

ABAQUS Online Documentation: Version 6.8 / Dassault Systèmes, 2008.

Abramovich H., Grunwald A. Stability of axially impacted composite plates. *Composite Structures*, Vol. 32, 1995, pp. 151-158.

Abramovich H., Grunwald A., Pevsner P., Weller T., David A., Ghilai G., Green T., Pekker N. Experiments on Axial Compression Postbuckling Behavior of Stiffened Cylindrical Composite Panels. *Proceedings of 44th AIAA/ASME/ASCE/AHS Structures, Structural Dynamics and Materials Conference*, -Norfolk, VI, AIAA paper no. 2003-1793 (2003).

Abramovich H., Singer J., Weller T. Repeated buckling and its influence on the geometrical imperfections of stiffened cylindrical shells under combined loading. *Int. J. of Non-Linear Mechanics*, Vol. 37, 2002, pp. 577-588.

Abramovich H., Weller T. Buckling until collapse of a damaged panel. *COOCMAT - Technion Technical Report*, -Tel Aviv, 2005. www.cocomat.de

Abramovich H., Weller T., Pevzner P. Dynamic buckling behavior of thin walled composite circular cylindrical shells under axial impulsive loading. *Proc. 12th Australian Aeronautical Conference,* Melbourne, Australia, 2007, pp. 647-666.

Abramovich H., Weller T. Repeated buckling and postbuckling behavior of laminated stringer-stiffened composite panels with and without damage. *Int. J. of Structural Stability and Dynamics*, Vol. 10, 2010, pp. 807-825.

Abumeri G.H., Chamis C.C. Dynamic buckling of adaptive composite shells. *Proceedings of 44th AIAA/ASME/ASCE/AHS Structures, Structural Dynamics, and Materials Conference*, 2003.

Abumeri G.H., Chamis C.C. Probabilistic dynamic buckling of smart composite shells. *NASA/TM-2003-212710*, 2003.

Agarwal B.L. Postbuckling behavior of composite-stiffened curved panels loaded in compression. *Experimental Mechanics*, Vol. 22, 1982, pp. 231-236.

Aiello R.A., Grady J.E. A NASTRAN DMAP Alter for Linear Buckling Analysis Under Dynamic Loading. *NASA TM-100832*, 1989.

Amazigo J. C. Buckling under Axial Compression of Long Cylindrical Shells with Random Axisymmetric Imperfections. *Quarterly of Applied Mathematics*, Vol. 26, 1969, pp. 537-566.

ANSYS Documentation Release 11.0 / Ansys, Inc., 2007.

Araico J.A., de Zarate I.O., Arribas F.R. Postbuckling degradation FE analysis of stiffened composite panels. *Int. J. of Structural Stability and Dynamics*, Vol. 10, 2010, pp. 645-668.

Arbocz J, Babcock C.D. The effect of general imperfections on the buckling of cylindrical shells. *Journal of Applied Mechanics*, Vol. 36, 1969, pp.28-38.

Arbocz J. The imperfection data bank, a means to obtain realistic buckling loads. In: Ramm E., editor. Buckling of shells, New York: Springer Verlag, 1982, pp. 535-567.

Arbocz J., Hol J.M. Collapse of axially compressed cylindrical shells with random imperfections. *Thin-Walled Structures*, Vol. 23, 1995, pp. 131-158.

Arbocz J., Williams J.G. Imperfection surveys on a 10 ft diameter shell structure. *AIAA Journal*, Vol. 15, No. 7, 1977, pp. 949-956.

Ari-Gur J., Elishakoff I. Dynamic instability of a transversely isotropic column subjected to a compression pulse. *Computers and Structures*, Vol. 62, 1996, pp. 811-815.

Ari-Gur J., Simonetta S.R. Dynamic pulse buckling of rectangular composite plates. *Composites Part B: Engineering*, Vol. 28, No. 3, 1997, pp. 301-308.

Ari-Gur J., Simonetta S.R. Pulse buckling of composite plates, *AIAA Paper No. AIAA-94-1435-CP*, 1994.

Ari-Gur J., Singer J. Composite Material Columns under Axial Impact. *TAE Report No. 462, Department of Aeronautical Engineering, Technion-Israel Institute of Technology, Haifa, Israel*, 1981

Ari-Gur J., Weller T., Singer J. Experimental and Theoretical Studies of Columns under Axial Impact. *International Journal of Solids and Structures*, Vol.18, 1982, pp. 619-641

Barkanov E., Gluhih S., Ozolinsh O., Eglitis E., Almeida F., Bowering M.C., Watson G. Optimal weight design of laminated composite panels with different stiffeners under buckling loads. *Proc. International Coucil of the Aeronautical Sciences 2010 Congress*, Nice, France, September 19-24, 2010

Bernard E.S., Coleman R., Bridge R.Q. Measurement and assessment of geometric imperfections in thin-walled panels. *Thin-Walled Structures*, Vol. 33, 1999, pp. 103-126.

Bisagni C. Dynamic buckling of fiber composite shells under impulsive axial compression. *Thin-Walled Structures*, Vol. 43, 2005, pp. 499-514.

Bisagni C. Dynamic buckling tests of cylindrical shells in composite materials. *Proc. of 24th international congress of the aeronautical sciences*, Yokohoma, Japan, 2004, 7 p.

Bisagni C., Cordisco P. An Experimental Investigation into the Buckling and Post-buckling of CFRP Shells under Combined Axial and Torsion Loading. *Composite Structures*, Vol. 60, 2003, pp. 391-402.

Bisagni C., Cordisco P. Post-buckling and collapse experiments of stiffened composite cylindrical shells subjected to axial loading and torque. *Composite Structures*, Vol. 73, 2006, pp. 138-149.

Bolotin V. V. Statistical Methods in the Nonlinear Theory of Shells. *NASA TT F-85* (Translation of a paper presented at a seminar in the Institute of Mechanics of the Academy of Sciences of the USSR, 1957), 1962.

Budiansky B. Dynamic buckling of elastic structures: criteria and estimates. *NASA Technical Report NASA-CR-66072* Jan. 1966.

Budiansky B, Hutchinson J.W. Dynamic buckling of imperfection sensitive structures. *Proc International Congress of Applied Mechanics*, Munich, Germany, Vol. 11, pp 637-651, 1964

Budiansky B., Roth R.S. Axisymmetric dynamic buckling of clamped shallow spherical shells. *Collected papers on instability of shell structures*, Dec. 1962 /SEE N63-10804 02-34, pp. 597-606

Byskov E., Hutchinson J. W. Mode interaction in axially stiffened cylindrical shells. *AIAA Journal*, Vol.15, 1977, pp. 941-948.

Chamis C.C. Assuring life in composite systems. NASA TM-2008-215452, 2008.

Chamis C.C., Abumeri G.H. Non-deterministic dynamic stability of composite shells. *Proceedings of 44th AIAA/ASME/ASCE/AHS Structures, Structural Dynamics, and Materials Conference*, 2003.

Chamis C.C., Abumeri G.H. Nonlinear dynamic buckling of a composite shell. Proceedings of *46th AIAA/ASME/ASCE/AHS Structures, Structural Dynamics, and Materials Conference,* 2005.

Chamis C.C., Abumeri G.H. Probabilistic dynamic buckling of composite shell structures. *Composites: Part A*, Vol. 36, 2005, pp. 1368-1380.

Cheng S. and Ho B.P.C. Stability of heterogenous aeolotropic cylindrical shells under combined loading. *AIAA Journal*, Vol. 1, 1963, pp. 892-898

Cheong H.K., Hao H., Cui S. Experimental investigation of dynamic post-buckling characteristics of rectangular plates under fluid-solid slamming. *Engineering Structures,* Vol. 22, 2000, pp. 947-960.

Chryssanthopoulos M.K. Probabilistic buckling analysis of plates and shells. *Thin-Walled Structures*, Vol. 30, Nos 1-4, 1998, pp. 135-157.

Chryssanthopoulos M.K., Elghazouli A.Y., Esong I.E. Compression tests on anti-symmetric two-ply GFRP cylinders. *Composites: Part B*, Vol. 30, 1999, pp. 335-350.

Chryssanthopoulos M.K., Elghazouli A.Y., Esong I.E. Validation of FE models for buckling analysis of woven GFRP shells. *Composite Structures*, Vol. 49, 2000, pp. 355-367.

Chryssanthopoulos M.K., Poggi C. Probabilistic imperfection sensitivity analysis of axially compressed composite cylinders. *Engineering Structures*, Vol. 17, No. 6, 1995, pp. 398-406.

Coan J.M. Large-deflection theory for plates with small initial curvatures loaded in edge compression. *ASME Journal of Applied Mechanics*, Vol. 18, 1951, pp. 143-151.

Cordisco P., Bisagni C. Design, testing and validation of a composite box under combined loading up to collapse. *Int. J. of Structural Stability and Dynamics*, Vol. 10, 2010, pp. 853-869.

Cui S., Cheong H.K., Hao H. Experimental study of dynamic buckling of plates under fluid–solid slamming. *Int. J. of Impact Engineering*, Vol. 22, 1999, pp. 675-691.

Cui S., Cheong H.K., Hao H. Experimental study of dynamic post-buckling characteristics of columns under fluid-solid slamming, *Engineering Structures*, Vol. 22, 2000. pp. 647-656.

Cui S., Hao H., Cheong H.K. Dynamic buckling and post-buckling of imperfect columns under fluid-solid interaction. *Int. J. of Solids and Structures*, Vol. 30, 2001, pp. 8879-8897.

Cui S., Hao H., Cheong H.K. Numerical analysis of dynamic buckling of rectangular plates. *Int. J. of Impact Engineering*, Vol. 25, 2001, pp. 147-167.

Cui S., Hao H., Cheong H.K. Theoretical study of dynamic elastic buckling of columns subjected to intermediate velocity impact loads. *Int. J. of Mechanical Sciences*, Vol. 44, 2002, pp. 687-702.

Degenhardt R., Kling A., Bethge A., Orf J., Karger L., Zimmermann R., Rohwel K., Calvi A. Investigations on imperfection sensitivity and deduction of improved knock-down factors for unstiffened CFRP cylindrical shells. *Composite Structures*, Vol. 92, 2010, pp. 1939-1946.

Degenhardt R., Kling A., Rohwer K., Orifici A.C., Thomson R.S. Design and analysis of stiffened composite panels including post-buckling and collapse. *Computers and Structures*, Vol. 86, 2008, pp. 919-929.

Degenhard R., Rolfes R., Zimmerman R., Rohwer K. COCOMAT – improved material exploitation of composite airframe structures by accurate simulation of postbuckling and collapse. *Composite Structures*, Vol. 73, 2006, pp. 175-178.

Dong S.B., Pister K.S., Taylor R.L. On the theory of laminated anisotropic shells and plates. *Journal of the Aerospace Sciences*, Vol. 29, 1962, pp. 969-975

Donnell L.H. A new theory for the buckling of thin cylinders under axial compression and bending. *Transactions of the American Society of Mechanical Engineers*, Vol. 56, (AER-56-12), 1934, pp. 795-806.

Eglitis E., Kalnins K., Bisagni C. Study on buckling behaviour of laminated shells under pulse loading. *Proc. International Coucil of the Aeronautical Sciences 2010 Congress*, Nice, France, September 19-24, 2010

Eglītis E., Kalniņš K., Ozoliņš O., Teters G., An experimental and numerical study on the dynamic buckling of cylindrical composite shells. *Proceedings of International Conference Mechanics of Composite Materials*, Riga, Latvia, May 2008, p. 76.

Eglitis E., Kalnins K. Benchmarking of FE post-buckling analysis of stiffened composite panels with experimental validation. *Proceedings of 4th Conference on Strength, Durability and Stability of Materials and structures* - Palanga, September 2007, pp. 32–38.

Eglītis E., Kalniņš K., Ozoliņš O. Experimental and numerical study on buckling of axially compressed cylinders. *RTU zinātniskie raksti. Būvzinātne*, Vol. 10, 2009, pp. 33-49.

Eglītis E., Kalniņš K., Ozoliņš O. The influence of loading eccentricity on buckling of axially compressed imperfect composite cylinders. *Mechanics of Composite Materials*, Vol. 46, 2010, pp. 483-492.

Eglītis E., Kalniņš K., Ozoliņš O., Rikards R. Numerical Study of Geometrical Imperfection Response on Composite Cylinders under Axial Loading. *Proceedings of 20th Nordic Seminar on Computational Mechanics*. Gothenburg, Sweden, November 2007, pp. 101-104.

Elghazouli A.Y., Chryssanthopoulos M.K., Esong I.E. Buckling of woven GFRP cylinders under concentric and eccentric compression. *Composite Structures*, Vol. 45, 1999, pp. 13-27.

European Standard / Plastics – Determination of tensile properties – Part 4 (EN ISO 527-4:1997)

Faser W. B., Budiansky B. The Buckling of a Column with Random Initial Deflections. *Journal of Applied Mechanics*, Vol. 36, 1969, pp. 233-240.

Gay D., Hoa S. V. Composite materials: Design and applications. - New York: CRC Press, 2007

Geier B., Klein H., Zimmermann R. Buckling Tests with Axially Compressed Unstiffened Cylindrical Shells Made from CFRP. *Proceedings of Buckling of Shell Structures, on Land, in the Sea and in the Air* - Lyon, September 1991, pp. 498-507

Giavotto V., Poggi C., Castano D., Guzzetti D., Fezzani M. Buckling Behavior of Composite Shells under Combined Loading. P*roceedings of 17th European Rotorcraft Forum* - Berlin, September 1991, pp. 84-1 – 84-13.

Gladden J.R., Handzy N.Z., Belmonte A., Villermaux E. Dynamic Buckling and Fragmentation in Brittle Rods. *Physical review letters*, Vol. 94, 2005.

Godoy L.A. Thin-walled structures with imperfections: Analysis and Behavior. – Elsevier, London, 1996.

Grady J.E., Chamis C.C., Aiello R.A. Dynamic delamination buckling in composite laminates under impact loading: Computational simulation. *NASA TM-100192*, 1987

Harris L.A., Suer H. S., Skene W. T., Benjamin R. J. The stability of thin-walled unstiffened circular cylinders under axial compression including the effects of internal pressure. *Journal of Aeronautical Science*, 24, 1957, pp. 587-596.

Hilburger M.W, Starnes J.H. Effects of imperfections of the buckling response of composite shells. *Thin-Walled Structures*, Vol. 42, 2004, pp. 369-397.

Hoff N. J. Thin Shells in Aerospace Structures. *Aeronautics and Astronautics*, Vol. 5, February 1967, pp.26-45.

Humphreys J.S., Sve C. Dynamic buckling of cylinders under axial shock-tube loading. *AIAA meeting*, January 1966, paper no. 66-82.

Humphreys, J.S., Zatlers J. Experiments on the Dynamic Response of Shells Under Shock Wave Loading. *RAD-S330-T-243*, February 25, 1965

Hutchinson J.W., Budiansky B. Dynamic buckling estimates. *AIAA Journal*, Vol. 4, No. 3, 1966, pp. 525-530.

Huyan X., Simitses G.J. Dynamic buckling of imperfect cylindrical shells under axial compression and bending moment. *Proceedings of 37th AIAA/ASME/ASCE/AHS/ASC Structures, Structural Dynamics, and Materials Conference and Exhibit*, 1996, pp. 1333-1343.

Hühne C., Rolfes R., Breitbach E., Teßmer J. Robust design of composite cylindrical shells under axial compression - Simulation and validation. *Thin-Walled Structures*, Vol. 46, 2008, pp. 947-962.

Johnson W., Mamalis A. G., Crashworthiness of Vehicles. – London: Mechanical Engineering Publications, 1978

Johnson W., Reid S. R. Metallic energy dissipation systems. *Applied Mechanics Reviews*, 31, 1978, pp. 277-287

Kadandale M., Ari-Gur J. Dynamic pulse buckling of viscoelastic columns. *38th AIAA/ASME/ASCE/AHS/ASC Structures, Structural Dynamics and Materials Conference*, Kissimmee, Florida, April 1997, AIAA Paper 97-1097, pp. 374-381.

Kalnins K., Rikards R., Auzins J., Bisagni C., Abramovich H., Degenhardt R. Metamodeling methodology for postbuckling simulation of damaged composite stiffened structures with physical validation. *Int. J. of Structural Stability and Dynamics*, Vol. 10, 2010, pp. 705-716.

Karachalios E., Vrettos C., Marioli-Riga Z., Bisagni C., Cordisco P., de Zarate I.O., Caruso A. Numerical simulation and testing of a composite-stiffened structure under combined buckling loads. *Int. J. of Structural Stability and Dynamics*, Vol. 10, 2010, pp. 871-884.

Karagiozova D., Alves M. Transition from progressive buckling to global bending of circular shells under axial impact - Part I: Experimental and numerical observations. *Int. J. of Solids and Structures*, Vol. 41, 2004, pp. 1656-1580.

Karagiozova D., Alves M. Transition from progressive buckling to global bending of circular shells under axial impact - Part II: Theoretical analysis. *Int. J. of Solids and Structures*, Vol. 41, 2004, pp. 1681-1604

Karagiozova D., Jones N. Influence of stress waves on the dynamic progressive and dynamic plastic buckling of cylindrical shells. *Int. J. of Solids and Structures*, Vol. 38, 2001, pp. 6723-6749.

Karagiozova D., Jones N. On dynamic buckling phenomena in axially loaded elastic-plastic cylindrical shells. *Int. J. of Non-linear Mechanics*, Vol. 37, 2002, pp.1223-1238.

Kaw A.K. Mechanics of Composite Materials: Second edition. - New York: CRC Press, 2006.

Kenny S., Pegg N., Taheri F. Finite element investigations on the dynamic plastic buckling of a slender beam subject to axial impact. *Int. J. of Impact Engineering*, Vol. 27, 2002, pp. 179-195.

Kenny S., Pegg N., Taheri F. Finite element investigations on the dynamic plastic buckling of a slender beam subject to axial impact. *Int. J. of Impact Engineering*, Vol. 27, 2002, pp. 179-195.

Kenny S., Taheri F., Pegg N. Experimental investigations on the dynamic plastic buckling of a slender beam subject to axial impact. *Int. J. of Impact Engineering*, Vol. 27, 2002, pp. 1-17.

Kling, A., Degenhardt, R., Zimmerman, R. A hybrid subspace analysis procedure for non-linear postbuckling calculation. *Composite Structures*, Vol. 73, 2006, pp. 162-170.

Knight N.F., Jr., Starnes J.H. Postbuckling behavior of selected curved stiffened graphite-epoxy panels loaded in axial compression. *AIAA Journal*, Vol. 26, 1988, pp. 344-352

Koning V. C., Taub J. Impactu Buckling of Thin Bars in the Elastic Range Hinged at Both Ends. *Luftfahrtforschung*, Vol. 10, 1933, pp. 55-64

Koval L.R., O'Neill J.P. Stability of axially-loaded thin cylindrical shells under dynamic lateral pressures. *NASA technical report NASA-CR-58949*, October, 1963.

Koval L.R., Oneill J.P. Structural responses to dynamic loading Stability of axially loaded thin cylindrical shells under dynamic lateral pressures. *AIAA annual meeting*, Washington, D.C., June 29 - July 2, 1964, Paper no. 64-485.

Kriegesmann B., Rolfes R., Hühne C., Tessmer J., Arbocz J. Probabilistic design of axially compressed composite cylinders with geometric and loading imperfections. *Int. J. of Structural Stability and Dynamics*, Vol. 10, 2010, pp. 623-644.

Lilly W. E. The Economic Design Of Columns. *Transactions of Institution of Civil Engineers of Ireland (Dublin)*, March 1906, pp. 67-93.

Lindberg H.E. Florence A.L. Dynamic pulse buckling. – Dordrecht: Martinus Njihoff Publishers, 1987.

Lindberg H.E., Rubin M.B., Schwer L.E. Dynamic buckling of cylindrical shells from oscillating waves following axial impact. *Int. J. of Solids and Structures*, Vol. 23, 1987, pp. 669-692.

Lorenz R. Buckling of cylindrical shell shell under axial compression. *Zeitschrift des Vereines Deutcher Ingenieure*, Vol. 52, 1908, p. 1766.

Lundquist E.E. Strength tests of thin-walled duralumin cylinders in compression. *NACA Report* No. 473, June 1933.

Mamalis, A.G. Manolakos, D.E. Ioannidis, M.B. Papapostolou D.P. The static and dynamic axial collapse of CFRP square tubes: Finite element modeling. *Composite Structures*, Vol. 74, 2006, pp. 213-225.

McGowan D.M., Young R.D., Swanson G.D., Waters W.A. Compression tests and non-linear analysis of a stringer- and frame-stiffened graphite-epoxy fuselage crown panel. *Proc. 5th NASA/Dod Advanced Composites Technology Conference*, 1994, Paper No. A94-33140.

Megson T.H.G, Hallak, G. Measurement of the geometric initial imperfections in diaphragms. *Thin-Walled Structures*, Vol. 14, 1992, pp. 381-394.

Meyer-Piening H. R., Farshad M., Geier B., Zimmermann R. Buckling Loads of CFRP Composite Cylinders under Combined Axial and Torsion Loading - Experiments and Computations. *Composite Structures*, Vol. 53, 2001, pp. 427-435.

NASA SP-8007: Buckling of thin walled circular cylinders. – National Aeronautics and Space Administration, 1965.

Orifici A.C., Thomson R.S., Degenhardt R., Kling A., Rohwer K., Bayandor J. Degradation investigation in a postbuckling composite stiffened panel. *Composite Structures*, Vol. 82, 2008, pp. 217-224.

Pegg N.G. A numerical study of dynamic pulse buckling of cylindrical structures. *Marine Structures*, Vol. 7, 1994, pp. 189-212.

Petry D., and Fahlbusch G. Dynamic buckling of thin isotropic plates subjected to in-plane impact. *Thin-Walled Structures*, Vol. 38, 2000, pp. 267-283.

Pircher M, Wheeler A. The measurement if imperfections in cylindrical thin-walled members. *Thin-Walled Structures*, Vol. 41, 2003, pp. 419-433.

Rahman T., Jansen E.L. A finite element based perturbation method for dynamic buckling analysis of shell structures. *Proceedings of 60th AIAA/ASME/ASCE/AHS/ASC Structures, Structural Dynamics, and Materials Conference*, 2009.

Roth R.S., Klosner J.M. Nonlinear response of cylindrical shells with initial imperfections subjected to dynamic axial loads. *Proc. Aerospace Sciences Meeting*, New York, N.Y., January 20-22, 1964, paper no. 64-76.

Shaw D., Shen Y.L., Tsai P. Dynamic buckling of an imperfect composite circular cylindrical shell. *Computers and Structures*, Vol. 48, 1993, pp. 467-472

Shover D.R. On the problem of geometric imperfections on thin circular cylindrical shells, PhD thesis, Stanford University, Stanford, California, 1968.

Simitses G.J. Dynamic stability of suddenly loaded structures. – New York: Springer-Verlag, 1990.

Simitses G.J., Tabiei A. Dynamic stability of shell structures. *Proceedings of 38th AIAA/ASME/ASCE/AHS/ASC Structures, Structural Dynamics, and Materials Conference and Exhibit*, 1997, pp. 2438-2445.

Singer J, Abramovich H. The development of shell imperfection measurement techniques. *Thin-Walled Structures*, Vol. 23, 1995, pp. 379-398.

Singer J. Vibration correlation techniques for improved buckling predictions of imperfect stiffened shells. in: Harding J.E., Dowling P.J., Agelidis N. (Eds.) Buckling of Shells in Offshore Structures, – Granada Publishing, London, 1982, pp. 285–330.

Singer J., Arbocz J., Weller T. Buckling Experiments: Experimental Methods in Buckling of Thin-Walled Structures. - New York: John Wiley and Sons, Inc., 2004.

Singer J., Ari-Gur J. Dynamic buckling of thin-walled structures under impact. *The DGLR Jahrbuch*, vol. 1, 1981

Sofiyev A.H. The buckling of functionally graded truncated conical shells under dynamic axial loading. *Journal of Sound and Vibration*, Vol. 305, 2007, pp. 808-826.

Southwell R.V. *Philosophical Transactions of the Royal Society*, Vol. 213, 1914, p. 187.

Spagnoli A., Elghazouli A.Y., Chryssanthopoulos M.K. Numerical simulation of glass-reinforced plastic cylinders under axial compression. *Marine Structures*, Vol. 14, 2001, pp. 353-374.

Tabiei A., Tanov R., Simitses G.J. Numerical simulation of cylindrical laminated shells under impulsive lateral pressure. *AIAA Journal*, Vol. 37, 1999, pp. 629-633.

Tanov R, Tabiei A., Simitses G.J. Effect of static preloading on dynamic buckling of laminated cylinders under sudden pressure. *Mechanics of Composite Materials and Structures*, Vol. 6, 1999, pp. 195-206.

Tanov R., Tabiei A. Static and dynamic buckling of laminated composite shells. *Proceedings of 5th International LS-DYNA Users Conference*, 1998

Teng J. G., Rotter J. M. Buckling of Thin Metal Shells. - London: Spon Press, 2004.

Teng J.G., Lin X., Rotter J.M., Ding X.L. Analysis of geometric imperfections in full-scale welded steel silos. *Engineering Structures*, Vol. 27, 2005, pp. 938-950.

Tennyson R.C. Buckling of laminated composite cylinders: A Review, *Composites*, Jan. 1975, pp. 17-24.

Tennyson R. C., Muggeridge D. B. Buckling of Laminated Anisotropic Imperfect Circular Cylinders under Axial Compression. *Journal of Spacecraft*, Vol. 10, February 1973, pp. 143-148.

Teter A. Static and dynamic interactive buckling of isotropic thin-walled closed columns with variable thickness. *Thin-Walled Structures*, Vol. 43, 2007, pp.936-640.

Timoshenko S. P., Einige Stabilitätsprobleme der Elasticitätstheorie. *Zeitschrift für Matematic und Physik*, Vol. 58, 1910, pp.378-385.

Tsai J., Sun C.T. Dynamic compressive strengths of polymeric composites*. Int. J. of Solids and Structures*, Vol. 42, 2005, pp. 5555-5567.

von Karman T., Tsien H. S. The buckling of thin cylindrical shells under axial compression, *Journal of the Aeronautical Sciences*, Vol. 8, 1941, pp. 303-312.

Wei Z.G., Yu J.L., Batra R.C. Dynamic buckling of thin cylindrical shells under axial impact. *Int. J. of Impact Engineering*, Vol. 32, 2005, pp. 575-592.

Weingarten V.I., Morgan E.J., Seide P. Elastic stability of thin-walled cylindrical and conical shells under axial compression. *AIAA journal*, Vol. 3, 1965, pp.500-505.

Weller T., Abramovich H., Yaffe R. Dynamic buckling of beams and plates subjected to axial impact. *Computers and Structures*, Vol. 32, Nos. 3-4, 1989, pp. 835-851.

Wilckens D., Degenhardt R., Rohwer K., Zimmermann R., Kepke M., Hildebrandt B., Zipfel A. Cyclic buckling tests of pre-damaged CFRP stringer-stiffened panels. *Int. J. of Structural Stability and Dynamics*, Vol. 10, 2010, pp. 827-851.

Wilson W.M., Newmark N.M. The strength of thin cylindrical shells and columns. *University of Illinois Engineering Experiment Station*, Bulletin No. 255, Feb. 1933.

Yaffe R., Abramovich H. Dynamic buckling of cylindrical stringer stiffened shells. *Computers and Structures*, Vol. 81, 2003, pp. 1031-1039

Zhang Z., Taheri F. Dynamic pulse-buckling behavior of quasi-ductile carbon/epoxy and E-glass/epoxy laminated composite beams. *Composite Structures*, Vol. 64, 2004, pp. 269-274.

Zimick D.G., Tennyson R.C. Stability of Circular Cylindrical Shells under Transient Axial Impulsive Loading. *AIAA Journal*, Vol. 18, 1980, pp. 691-699.

Zimmermann R. Buckling Research for Imperfection Tolerant Fiber Composite Structures. *Proceedings of Conference on Spacecraft Structures, Materials and Mechanical Testing - Noordwjik*, The Netherlands, March 1996, pp. 411-416.

Zimmermann R., Rolfes R. POSICOSS—improved postbuckling simulation for design of fibre composite stiffened fuselage structures. *Composite Structures*, Vol. 73, 2006, pp. 171-174.

LIST OF PUBLICATIONS

1. Eglitis E., Kalnins K., Ozolinsh O. The influence of loading eccentricity on buckling of axially compressed imperfect composite cylinders. *Mechanics of Composite Materials*, Vol. 46, 2010, pp. 483-492.
2. Eglitis E., Kalnins K., Bisagni C. Study on buckling behaviour of laminated shells under pulse loading. *Proc. International Coucil of the Aeronautical Sciences 2010 Congress*, Nice, France, September 19-24, 2010, 8 p. (CD edition)
3. Eglitis E., Bisagni C., Kalnins K., Ozolinsh O., Dzelzitis K. Dynamic buckling of axially impacted cylindrical composite shells. *Abstracts IV European Conference on Computational Mechanics*, Paris, France, May 16-21, 2010, 2 p. (available online at http://www.eccm2010.org)
4. Eglitis E., Kalnins K., Ozolinsh O., Teters G. An experimental and numerical study on the dynamic buckling of cylindrical composite shells. *Abstracts XV International Conference Mechanics of Composite Materials*, Riga, Latvia, May 26-30, 2008, p. 76.
5. Eglitis E., Kalnins K., Ozolinsh O. Experimental and numerical study on buckling of axially compressed cylinders. *Scientific proceedings of RTU, section "Construction science"*, 2nd series, 10th issue, 2009, pp. 33-49.
6. Eglitis E., Kalnins K. Benchmarking of FE post-buckling analysis of stiffened composite panels with experimental validation. *Proc. of 4th Conference on Strength, Durability and Stability of Materials and structures*, Palanga, Lithuania, September 11-13, 2007, pp. 32-38.
7. Eglitis E., Kalnins K., Ozolinsh O., Rikards R. Numerical study of geometrical imperfection response on composite cylinders under axial loading. *Proc. of 20th Nordic Seminar on Computational Mechanics*. Gothenburg, Sweden, November 23-24, 2007, pp. 101-104.
8. Eglitis E., Kalnins K., Ozolins O. The influence of loading ecentricity on buckling of axially compressed imperfect composite cylinders. *Abstracts XVI International Conference on Mechanics of Composite Materials*, Riga, Latvia, May 24-28, 2010, p. 64.
9. Eglitis E., Ozolinsh O., Gluhih S., Barkanov E. Finite element buckling analysis of stiffened composite panels. *Scientific proceedings of RTU, section "Construction science"*, 2nd series., 7th issue, 2006, pp. 105-112.

10. Barkanov E., Gluhih S., Ozolinsh O., Eglitis E., Almeida F., Bowering M.C., Watson G. Optimal weight design of laminated composite panels with different stiffeners under buckling loads. *Proc. International Coucil of the Aeronautical Sciences 2010 Congress*, Nice, France, September 19-24, 2010, 8 p. (CD edition)
11. Barkanov E., Gluhih S., Ozolinsh O., Eglitis E., Almeida F., Bowering M.C., Watson G. Optimal weight design of composite lateral wing upper covers. *Proc. of 29th Annual International Scientific-Practical Conference and Accompanying Exhibition "Composite Materials in the Industry"*, Yalta, Ukraine, June 1-5, 2009, pp. 349-352.
12. Barkanov E., Gluhih S., Ozolinsh O., Eglitis E., Almeida F., Bowering M., Watson G. Optimal design of composite lateral wing upper covers based on non-linear buckling analysis. *Proc. of the 9th International Conference on Computational Stuctures Technology*, Athens, Greece, September 2-5, 2008, pp. 295-308.
13. Kalnins K., Bisagni C., Rikards R., Eglitis E., Cordiso P., Chate A. Metamodels for the optimization of damage tolerant composite structures. *Proc. of 26th International Congress of the Aeronautical Sciences,* Anchorage, Alaska, USA, September 14-19, 2008, 7 p. (CD edition)
14. Kalnins K., Bisagni C., Abramovich H., Cordisco P., Eglitis E., Rikards R. Metamodels for optimum design of composite stiffened structures under torsion loading. *Proc. of 48th Israel Annual Conference on Aerospace Sciences*, Tel Aviv/Haifa, Israel, February 27-28, 2008, 4 p. (CD edition)
15. Kalnins K., Auzins J., Janushevskis J., Janushevskis A., Eglitis E., Rikards R. Sequential metamodeling for optimization of stiffened composite structures. *Proc. of 7th World Congress on Structural and Multidisciplinary Optimization*. Seoul, May 21-25, 2007, pp. 1145-1150.
16. Kalnins K., Eglitis E., Jekabsons G., Rikards R. Metamodels for optimum design of laser welded sandwich structures. *Proc. of International Conference on Welded Structures*, Miscolc, Hungary, April 24-26, 2008, pp. 119-126.
17. Ozolinsh O., Dzelzitis K., Eglitis E. Experimental Evaluation of Damage Influence on Buckling Performance of Stiffened CFRP Shells. *Scientific proceedings of RTU, section "Construction science"*, 2nd series, 10th issue, 2009, pp. 79-92.
18. Jekabsons G., Kalnins K., Eglitis E. Polynomials in metamodeling of glass fibre bar stability. *Scientific proceedings of RTU, section "Computer science"* 5th series, 24th issue, 2008, pp. 150-158.

19. Kalnins K., Jekabsons G., Janushevskis J., Eglitis E., Rikards R. Different approximation functions in surrogate modelling of sandwich structures. *Optimization and Engineering*, 11 lpp. (in review)

Presentations at Conferences, Project meetings etc.

1. International Coucil of the Aeronautical Sciences 2010 Congress, September 19-24, 2010, Nice, France. Presentation on *Study on buckling behaviour of laminated shells under pulse loading*.
2. IV European Conference on Computational Mechanics, May 16-21, 2010, Paris, France. Presentation on *Dynamic buckling of axially impacted cylindrical composite shells.*
3. 2nd International Conference on Buckling and Postbuckling Behaviour of Composite Laminated Shell Structures, September 3-5, 2008, Braunschweig, Germany.
4. XVI International Conference on Mechanics of Composite Materials, May 24-28, 2010, Riga, Latvia. Presentation on *The influence of loading eccentricity on buckling of axially compressed imperfect composite cylinders*.
5. International conference on Mechanics of Composite Materials, May 29, 2008, Jurmala, Latvia. Presentation on *An experimental and numerical study on the dynamic buckling of cylindrical composite shells.*
6. 20th Nordic Seminar on Computational Mechanics, November 23-24, 2007, Gothenburg, Sweden. Presentation on *Numerical Study of Geometrical Imperfection Response on Composite Cylinders under Axial Loading.*
7. 4th Conference on Strength, Durability and Stability of Materials and structures, September 11-13, 2007, Palanga, Lithuania. Presentation on *Benchmarking of FE post-buckling analysis of stiffened composite panels with experimental validation.*
8. Junior Euromat 2006, September 4-8, 2006, Lausanne, Switzerland. Presentation on *An optimum stacking sequence design procedure for carbon/epoxy composite stiffened panels.*
9. International conference Engineering Systems 2008, April 4-8, 2008, Moscow, Russia.
10. 51th RTU Scientific conference, October 12-14, 2006, Riga, Latvia. Presentation on *Finite element buckling analysis of stiffened composite panels.*
11. 47th RTU Scientific conference, October 12-14, 2006, Riga, Latvia. Presentation on *Finite element buckling analysis of stiffened composite panels.*
12. COCOMAT Project meeting. September 3-6, 2007, Milano, Italy.
13. ALCAS Project meeting, March 22, 2007, Riga, Latvia.

14. ALCAS Project meeting, June 8, 2006, Riga, Latvia.
15. Attended Ph.D. course on *Advanced Methods for Analysis and Design of Sandwich Structures*, at Department of Mechanical Engineering, Aalborg University, Denmark, August 28-29, 2007.
16. Visit of Politechnico di Milano, Faculty of Aerospace Engineering, May 16-18, 2007. Visit of Buckling test facilities.
17. Internship at Politecnico di Milano, Department of Aerospace Engineering, September 29, 2009 – February 26, 2010, Milan, Italy.

RESUME

Edgars Eglitis was born on June 7, 1984, in Riga, the capital of Latvia. In year 2005 he completed the B.S. degree in civil engineering in Riga Technical University. Continuing the education at Riga Technical University, Institute of Materials and Structures, he earned the M.S. degree in structural engineering and started his career as a research assistant, working on the EC 6th Framework project ALCAS. While as Ph.D. student, he worked as assistant in education of students and as a researcher for EC 6th Framework projects ALCAS and COCOMAT. A presented doctoral thesis was defended on 23th of March, 2011. The results of the thesis have been stated in 19 publications, 4 of which are cited in the EBSCO database and one is a *Springer Science+Business Media, Inc.* journal publication.